



**HIGH RESOLUTION MR SYSTEM
FOR DYNAMIC ARTERIAL IMAGING *IN VITRO***

by

Kenneth C. Chu

Department of Medical Biophysics

Submitted in partial fulfilment
of the requirements for the degree of
Doctor of Philosophy

Faculty of Graduate Studies
The University of Western Ontario
London, Ontario
May 1997

© Copyright by Kenneth C. Chu 1997



National Library
of Canada

Acquisitions and
Bibliographic Services

395 Wellington Street
Ottawa ON K1A 0N4
Canada

Bibliothèque nationale
du Canada

Acquisitions et
services bibliographiques

395, rue Wellington
Ottawa ON K1A 0N4
Canada

Your file Votre référence

Our file Notre référence

The author has granted a non-exclusive licence allowing the National Library of Canada to reproduce, loan, distribute or sell copies of this thesis in microform, paper or electronic formats.

The author retains ownership of the copyright in this thesis. Neither the thesis nor substantial extracts from it may be printed or otherwise reproduced without the author's permission.

L'auteur a accordé une licence non exclusive permettant à la Bibliothèque nationale du Canada de reproduire, prêter, distribuer ou vendre des copies de cette thèse sous la forme de microfiche/film, de reproduction sur papier ou sur format électronique.

L'auteur conserve la propriété du droit d'auteur qui protège cette thèse. Ni la thèse ni des extraits substantiels de celle-ci ne doivent être imprimés ou autrement reproduits sans son autorisation.

0-612-28481-6

Canada



The UNIVERSITY of WESTERN ONTARIO

Faculty of Graduate Studies

In the interests of facilitating research by others at this institution and elsewhere, I hereby grant a licence to:

THE UNIVERSITY OF WESTERN ONTARIO

to make copies of my thesis

HIGH RESOLUTION MR SYSTEM FOR DYNAMIC ARTERIAL IMAGING IN VITRO

or substantial parts thereof, the copyright which is invested in me, provided that the licence is subject to the following conditions:

1. Only single copies shall be made or authorized to be made at any one time, and only in response to a written request from the library of any University or similar institution on its own behalf or on behalf of one of its users.
2. This licence shall continue for the full term of the copyright, or for so long as may be legally permitted.
3. The Universal Copyright Notice shall appear on the title page of all copies of my thesis made under the authority of this licence.
4. This licence does not permit the sale of authorized copies at a profit, but does permit the collection by the institution or institutions concerned of charges covering actual costs.
5. All copies made under the authority of this licence shall bear a statement to the effect that the copy in question "is being made available in this form by the authority of the copyright owner solely for the purpose of private study and research and may not be copied or reproduced except as permitted by the copyright laws without written authority from the copyright owner."
6. The foregoing shall in no way preclude my granting to the National Library of Canada a licence to reproduce my thesis and to lend or sell copies of the same.

Mia Horakova
(signature of witness)

Kenneth Chiu
(signature of student)

MAY 23 , 1997
(date)

PHD
(degree)

MEDICAL BIOPHYSICS
(department of student)

THE UNIVERSITY OF WESTERN ONTARIO
FACULTY OF GRADUATE STUDIES

CERTIFICATE OF EXAMINATION

CHIEF ADVISOR

Dean Ritz

EXAMINING BOARD

R. Wil

ADVISORY COMMITTEE

Peter Canham

D. Holbrook

Ann Fung

J. Russell

D. Wood

The thesis by
Kenneth C. Chu

entitled

**HIGH RESOLUTION MR SYSTEM
FOR DYNAMIC ARTERIAL IMAGING *IN VITRO***

is accepted in partial fulfilment of the requirements for the degree of
Doctor of Philosophy

DATE *May 6, 1997*

S. D. Dunn
CHAIR OF EXAMINING BOARD

Abstract

The goal of this research is to develop a magnetic resonance (MR) imaging system for dynamic imaging of arteries and phantoms *in vitro*. The system is used to study differences in the local elastic properties which may be important in the *early* detection fibrous atherosclerotic plaques.

A clinical MR scanner was modified with a customized quadrupole gradient coil with optimized wire positions that increased the volume of 0.4% gradient uniformity by a factor of 4.7 larger than the Webster reference coil. Collected images did not need any corrections. The problem of heat dissipation was resolved by providing water cooling. A mathematical model predicted local coil temperatures to within $\pm 5^{\circ}\text{C}$ of measured values. Important parameters in minimizing coil temperature were small radius, large copper mass, and forced cooling. The gradient coil set permitted collection of 33 cardiac gated images in 64 seconds with no temperature change. The signal to noise ratio in the high resolution images (94 μm pixels x 2.5 mm thick) was increased by averaging 8 sets of data.

A hydrogenless fluid (1,1,2-trichloro-1,2,2-trifluoroethane) was found to be ideal as a pumping fluid since it does not introduce flow artifacts in MR imaging. The fluid was demonstrated to be compatible with arterial tissue for periods under 7 hours as assessed in terms of tensile stress-strain, MR relaxation times (T_1 and T_2), magnetic susceptibility, and histology.

A novel polyvinyl alcohol (PVA) cryogel material was developed as an elastic vascular phantom with circumferential stress-strain data nearly identical to that of porcine aortas at stress levels below 125 kPa. The T_1 and T_2 values of PVA cryogel were also similar to that of porcine aortas (500-650 ms and 50-75 ms, respectively).

An exponential model of tensile stress-strain curves demonstrated that the use of a single exponential parameter α was more descriptive in describing arterial stiffness compared to elastic modulus. A method of extrapolating *incremental* stress-strain data to *full* stress-strain data was derived using this model.

Incremental tensile tests demonstrated that α could be predicted to $\pm 30\%$ using incremental data with stresses under 75 kPa. Incremental experiments using a MR tagging method with aortic phantoms and intact porcine aortas showed that α could be predicted to $\pm 20\%$.

Keywords:

High resolution magnetic resonance imaging; MRI; quadrupole gradient coil; printed circuit board; numerical optimization; gradient coil power; heat dissipation; forced cooling; temperature response; arterial specimen; aortic segments; improved contrast; R-113; Freon-113; polyvinyl alcohol; PVA cryogel; MR phantoms; elastic arterial model; distensible hydrogel; tensile test; incremental elastic modulus; exponential stress-strain curve; extrapolation; local atherosclerotic plaque; lesion; material stiffness.

Acknowledgements

I would like to begin by thanking my supervisor, Dr. Brian K. Rutt, who had the courage to accept a working chemical engineer as a graduate student without knowing if I had a scholarship or not. Not only did Brian guide me through these past years, but he also stimulated my intellectual freedom, which resulted in the multi-disciplinary thesis presented here.

I would like to thank all of the members of the Imaging Research Laboratories who have provided not only constructive criticism, but open conversations and ideas, as well as solutions to mathematical, computer and machine shop related problems. Two of the key people, who deserve special thanks are R.Frayne, and S.Tong, who patiently explained medical physics to a person with little experience in this field. One other person who I must acknowledge as a great help is J.McKaig, Manager of Department of Physics Stores. Mr. McKaig permitted me to acquire much of the chemicals and equipment necessary for my experiments without having to deal with the usual bureaucracy and paper work. Of course, there were many other people who assisted me in different aspects of this project. Some of these people were (in alphabetical order): A.Alejski, E.Barberi, J.Brown, P.Canham, N.Cardinal, L.Carey, B.Chronik, I.Cunningham, M.Drangova, J.Dunmore, A.Fenster, B.Goodyear, D.Holdsworth, C.Jones, R.Kratky, L.Lauzon, T.Y.Lee, I.MacDonald, C.Maier, A.J.Martin, J.Miller, R.Mitchell, M.Moreau, H.Nicolov, P.Picot, D.Rickey, L.Rigutto, R.Smith, D.Steinman, S.Thielen, C.Thomas, and M.Westmore.

I am also grateful to P.Roemer (G.E.) and R.Rogers (Techron) for valuable discussions and suggestions on fabricating and safely implementing my gradient coils on the clinical MR scanners at University Hospital (London Health Sciences Centre). D.Gray and S.Whitworth (DuPont Canada) provided technical advice and samples of polyvinyl alcohol and Freon which are the basis of two chapters in this thesis.

I acknowledge personal financial support from the Medical Research Council of Canada, and Meloche-Monnex Insurance Brokers, as well as that of my

supervisor who received research grants from the Medical Research Council of Canada and University Hospital-Centre for the Advancement of Medical Device Technology. Without this funding none of the work here would have been possible.

Finally, I wish to thank my parents who had the foresight to always encourage their children to obtain the best education possible. But special thanks goes to Melanie, my fiancée, for saying yes! Especially after putting up with all the related problems that living with a financially strapped student has to offer. Without her, and her support, my graduate work would have not been nearly as enjoyable.

TABLE OF CONTENTS

	Page
CERTIFICATE OF EXAMINATION	ii
Abstract	iii
Acknowledgements	v
Table of Contents	vii
List of Figures	xii
List of Tables	xvi
Chapter 1 Introduction	1
1.1 Overview	1
1.2 Vascular Disease	1
1.2.1 Possible Mechanisms	1
1.2.2 Differences in Local Elastic Properties Hypothesis	5
1.2.3 Limitations of the Hypothesis	6
1.3 Elastic Measurements of Arteries	7
1.3.1 Tensile Tests	7
1.3.2 Mechanical Transducers to Measure Strain	8
1.3.3 Ultrasound Imaging	10
1.3.4 X-Ray Imaging of Vascular Geometries	11
1.3.5 Pulse Wave Velocity	12
1.3.6 Non-Tagging MR Methods	13
1.3.7 MR Tagging Methods	14
1.4 Magnetic Resonance Imaging	14
1.4.1 General Description	14
1.4.2 Relaxation Times T_1 and T_2	15
1.4.3 Spatial Encoding Using Gradients	16
1.4.4 Spin Echo Imaging	18
1.4.5 Inversion Recovery Imaging	20
1.4.6 Gradient Recalled Echoes	21
1.4.7 MR Gradients and Resolution	21
1.4.8 MR Tagging	22
1.5 Research Goal	23
1.6 Thesis Outline	25
1.6.1 Gradient Coil Design and Evaluation	25
1.6.2 Gradient Coil Heating	25

1.6.3	Trichlorotrifluoroethane as a Pumping Fluid	26
1.6.4	Polyvinyl Alcohol Cryogel	26
1.6.5	Stress-Strain Curves Extrapolated from Incremental Data	27
1.6.6	Summary and Future Applications	28
1.7	References	29
Chapter 2	Gradient Coil Design and Evaluation	34
2.1	Introduction	34
2.2	Methods	35
2.2.1	Design	35
2.2.2	Field Calculations	36
2.2.3	Numerical Optimization of Wire Positions	38
2.2.4	Construction	38
2.3	Results	42
2.4	Discussion	43
2.4.1	Gradient Uniformity	43
2.4.2	Implementation	52
2.5	Summary	53
2.6	References	53
Chapter 3	Gradient Coil Heating	55
3.1	Introduction	55
3.2	Methods	55
3.3	Theory	58
3.3.1	Cooling Parameter α_c	63
3.3.2	Average Temperature of Whole Coil	64
3.3.3	Local Temperature Rise	66
3.3.4	Transient Temperature Rise	67
3.3.5	Forced Cooling	67
3.4	Experimental Results and Discussion	72
3.5	Summary	75
3.6	References	77

Chapter 4	Trichlorotrifluoroethane as a Pumping Fluid	79
4.1	Introduction	79
4.2	Background and theory	81
4.3	Effect of R-113 on MR relaxation properties	82
	4.3.1 Methods	82
	4.3.2 Results	86
4.4	Contrast and signal to noise	88
	4.4.1 Methods	88
	4.4.2 Results	88
4.5	Tensile Properties	91
	4.5.1 Methods	91
	4.5.2 Results	92
4.6	Histology	92
	4.6.1 Methods	92
	4.6.2 Results	95
4.7	Safety concerns with R-113	95
4.8	Compatibility with other materials	96
4.9	Summary	96
4.10	References	97
Chapter 5	Polyvinyl Alcohol Cryogel	99
5.1	Introduction	99
5.2	Methods	101
	5.2.1 Physical Testing	102
	5.2.2 MR relaxation times	102
	5.2.3 Aortic phantom with stiff elastic plaque	103
5.3	Results and Discussion	103
	5.3.1 Tensile Testing	103
	5.3.2 MR relaxation times	107
	5.3.3 Aortic phantom with dual elastic modulus	109
5.4	Summary	111
5.5	References	112

Chapter 6	Stress-Strain Curves Extrapolated from Incremental Data . . .	116
6.1	Introduction	116
6.2	Theory	118
6.2.1	Incremental Modulus of Tubes	118
6.2.2	First Principles: Exponential Stress Strain Relationship	120
6.2.3	Elastic Modulus	122
6.2.4	Incremental Stress-Strain Data	125
6.2.5	Relating Incremental Data to the Exponential Stress-Strain Curve	126
6.2.6	Estimating α and ϵ_1	127
6.2.7	Slope and Error in the Fitted Exponential Curve	128
6.2.8	Stress Calculations for Thick Walled Tubes	129
6.3	Methods	130
6.3.A	Phantoms and Specimens	131
6.3.A.i	Straight PVA Cryogel Tubes	131
6.3.A.ii	PVA Cryogel Tube With Cosine Stenosis	131
6.3.A.iii	Aortic Phantom With Stiff Elastic Plaque (Dual PVA Phantoms)	132
6.3.A.iv	Porcine Thoracic Aortic Specimens	132
6.3.B	Tensile Testing to Determine β	132
6.3.B.1	PVA and Porcine Aortic Strips	132
6.3.C	Incremental Tensile Testing	134
6.3.D	MR Imaging System	134
6.3.D.i	MR Imaging	134
6.3.D.ii	MR Tags	134
6.3.D.iii	MR Compatible Pulsatile Pumping System	135
6.3.D.iv	Pressure Data	136
6.3.E	Post processing	136
6.3.E.i	Geometric Dimensions of Cylindrically Symmetric Vessels	136
6.3.E.ii	Dimensions of Dual PVA Phantoms	137
6.3.E.iii	Tag Intersections and Length of Lines	138
6.4	Results and Discussion	138
6.4.A	PVA Cryogel Phantoms	138
6.4.B	β From Tensile Tests	141

6.4.B.1	β For PVA	141
6.4.B.2	β From Tensile Tests of Porcine Aortas	141
6.4.C	Incremental Tensile Testing	144
6.4.C.1	Incremental Tensile Testing for PVA	144
6.4.C.2	Incremental Tensile Testing for Porcine Aorta	148
6.4.D.i	Incremental Data from Cosine Stenosis Phantom	151
6.4.D.ii	PVA phantom With Dual Elastic Properties	156
6.4.D.iii	Tagging method with Porcine aorta	160
6.5	General Discussion and Summary	162
6.6	References	165
Chapter 7	Summary and Future Applications	171
7.1	Overview	171
7.2	Gradient Coils	172
7.2.1	PC Boards	172
7.2.2	Accuracy of Current Paths	172
7.2.3	Heat Dissipation	173
7.2.4	Installation	174
7.2.5	Alternative Designs	174
7.3	Hydrogen Free Medium For Aortic Specimens	174
7.3.1	Practicality of using R-113	175
7.4	PVA Cryogel	176
7.5	Elastic Properties of Arteries	177
7.5.1	MR Tagging	177
7.5.2	Modelling Stress-Strain Data	178
7.5.3	Validation of Stress-Strain Model	178
7.5.4	Limitations	179
7.5.5	Future of Local Elasticity Measurements	179
7.6	Overall Conclusions	180
7.7	References	181
Appendix	Permission from co-authours and publisher	186
VITA		189

List of Figures

Figure 1.1	A schematic diagram of the structure of atherosclerotic plaque is shown	2
Figure 1.2	A sketch of a simplified stenosed arterial model; steady flow streamlines show that immediately after the stenosis there is a separation zone where flow may be reversed and residence times are long.	3
Figure 1.3.	A schematic diagram of how the digitized signal is stored in a 2-D array (16 x 16 in size) called k-space.	19
Figure 2.1.	The azimuthal angles of the 1 st and i th wires are shown for calculating the $\cos(2\theta)$ current distribution.	37
Figure 2.2a.	The PC board design for the 96 wire Webster design.	39
Figure 2.2b.	The PC board design for the optimized 192 wire design.	40
Figure 2.2c.	The PC board design for the optimized 16 wire optimized design.	41
Figure 2.3a	Contour plot of one quadrant of the central transverse gradient uniformity in units of % deviation from the central value for (a) the 96 wire Webster design.	45
Figure 2.3b	Contour plot of a quadrant of the central transverse gradient uniformity in units of % deviation from the central value for the optimized 192 wire design with the cost function calculated for a square region with side equal to the radius.	46
Figure 2.3c	Contour plot of one quadrant of the central transverse gradient uniformity in units of % deviation from the central value for the optimized 16 wire design with the cost function calculated for a square region with side equal to the radius.	47
Figure 2.3d	Longitudinal contour plot of the gradient uniformity for the central plane of the optimized 16 wire design.	48
Figure 2.4.	Two MR images (2 cm FOV) of a human iliac artery (ex-vivo) using the 16 wire gradient coil.	49

Figure 2.5.	Contour plot of the central transverse gradient uniformity (a) and an image of a 4.47 cm square grid phantom (b) using the Webster coil. (c) and (d) are the corresponding plot and image when each of the wire angles in the Z gradient are shifted by a factor of 0.995.	50
Figure 3.1a	PC board design of quadrupole gradient Coil "D". The coils longitudinal and azimuthal directions are the vertical and horizontal axis of the figure, respectively.	56
Figure 3.1b	Schematic showing various dimensions of a cylindrical gradient coil made from PC board construction.	57
Figure 3.2	Natural convective and radiative heat transfer coefficients are plotted as a function of coil temperatures.	69
Figure 3.4	The temperature response of various coils with different currents.	73
Figure 3.5	The theoretical temperature response of coil "A" mounted horizontally given various I_{rms} . Failure modes at 22 A and 71 A were experimentally determined.	76
Figure 4.1.	High resolution 1.5T MR images of an excised porcine aortic specimen submersed in 0.9% saline solution with a small air bubble on the right side of the container.	80
Figure 4.2.	High Resolution spin echo images (0.94 mm pixels, 1 mm thick, TE=16 ms, TR=416 ms, 4 NEX) of an excised porcine thoracic aortic specimen submersed in (A) saline, (B) air, (C) water, and (D) R-113.	90
Figure 4.3.	Circumferential stress-strain curve for porcine aortic rings submersed in R-113 or saline.	93
Figure 4.4.	Histological sections of porcine aortas submersed for 7 hours in saline (top) and R-113 (bottom) before being fixed in buffered formalin solution and stained Movat's trichrome stain system.	94
Figure 5.1.	Longitudinal stress-strain measurements of strips cut from PVA cryogel rings that underwent 1,2,3,4,5 and 10 freeze thaw cycles.	104

Figure 5.2.	PVA cryogel tube wall thickness measured as a function of freeze-thaw cycles.	106
Figure 5.3.	The T1 and T2 relaxation times (at 1.5T) for PVA cryogel tubes that underwent various freeze-thaw cycles.	108
Figure 5.4.	High resolution MR image of an aortic model with a dual PVA structure.	110
Figure 6.1.	A theoretical example of how stress-strain curves depend on the parameters α and β	123
Figure 6.2.	A schematic showing how an exponential stress-strain curve is linearized by taking small line segments.	124
Figure 6.3.	A schematic stress-strain curve showing four incremental data points plotted from $\epsilon_{inc,1}=0$. The inset shows the full stress-strain curve, compared to the incremental data.	124
Figure 6.4.	A schematic diagram of the cosine stenosed mold used to form a two diameter phantom.	133
Figure 6.5.	A schematic diagram of the equipment necessary to provide <i>in vitro</i> dynamic studies of aortic phantoms and arteries.	133
Figure 6.6.	A schematic diagram showing how the length of a line segment (thick line) defined by two points in a cartesian coordinate system can be described in a polar coordinates based on a reference point (i.e. lumen center).	139
Figure 6.7.	Stress-strain curves for PVA cryogel frozen 1, 2, 3, 4, and 10 times.	139
Figure 6.8.	Stress-strain curves from 28 samples of porcine aortas are shown by the dots. The solid line is the theoretical fit line using Eq. 6.5b with α and β equal to the average of the values from the 28 individual fits.	143
Figure 6.9.	Incremental tensile stress-strain data for PVA cryogel.	145
Figure 6.10.	Incremental tensile stress-strain data for porcine aorta.	149
Figure 6.11.	MR image of the longitudinal cross section of a PVA cryogel tube with a cosine stenosis (4.8 cm FOV).	152
Figure 6.12.	Circular cross sections of cosine stenosis phantom at the thick wall region in the centre of the stenosis (a and b), and in the thin wall region 2.5 cm upstream of the stenosis (c and d).	153

Figure 6.13.	A typical plot of mean L_r versus $\ln(T/\beta+1)$ for the thick and thin walled regions of a PVA stenosis phantom (a). The results from the thin wall section are given by squares, while the thick walled stenosed results are given by the circles. A linear least squares fit to each data set gives an intercept of L_0 and the slope is L_0/α . When the data is plotted as average T_{inc} versus ϵ_{inc} , the results are shown below in (b).	154
Figure 6.14.	Cross sectional MR image of a PVA tube two distinct stiffness regions. The stiff region has been frozen and thawed 12 times, and the flexible region has been frozen only twice. . . .	157
Figure 6.15	A typical stress-strain curve for the dual elastic phantom. The top graph shows the original incremental data. The slope of the linear least squares fit line (solid lines) is E_{inc} . The solid squares represent the average data from the stiff region, and the open circles represent the average data from the flexible region. The extrapolated data are also shown in the lower plot.	158
Figure 6.16.	Ex-vivo porcine aorta undergoing pulsatile motion. Horizontal DANTE tags were applied at diastole ($P_m=12.2$ kPa).	161
Figure 6.17.	Average stress-strain curve for porcine aorta. The incremental data are shown as solid circles, and E_{inc} is the slope of the solid straight line. The extrapolated data are shown as hollow circles.	161

List of Tables

Table 2.1.	Properties of 3 different quadrupole gradient coils designs. . .	44
Table 3.1.	Physical, electrical, and thermal properties of the five quadrupole gradient coils.	59
Table 3.2.	Constants for determining the natural convection heat transfer coefficients.	62
Table 3.3.	Typical thermal properties of several materials (at 20°C) that can be used in gradient coil fabrication. (Note the properties will vary depending on the additive types, amounts, chemistry, and manufacturing method).	68
Table 4.1.	Typical chemical properties of R-113 at 25°C and 101.3 kPa.	83
Table 4.2.	Relaxation properties of porcine upper thoracic aortae in various fluids measured at 20°C.	85
Table 4.3.	The ratio of $Q_{\text{loaded/unloaded}}$ for the RF coil used in this study and the corresponding increases in image SNR and CNR of arteries when surrounded with various fluid.	89
Table 6.1.	Stiffness parameter, α , for PVA cryogel as a function of freeze-thaw cycles. The scaling parameter, β , was assumed to be 64.759 kPa. The values in brackets are the percent deviation from the mean α	164
Table 6.2.	Typical incremental tensile data for PVA cryogel frozen twice. The values in brackets are percent deviation from the actual value.	165
Table 6.3.	Typical incremental tensile data for porcine aortas. The values in brackets are percent deviation from the actual value.	166

CHAPTER 1 INTRODUCTION

1.1 Overview

This chapter presents a brief background on vascular disease, measurements of elastic properties, and the motivation for this thesis. This is followed by a discussion of several MR imaging concepts relevant to the thesis. Finally, an outline of each chapter is given. Each chapter is presented as a separate entity with its own symbols, definitions, equations and references. Corresponding figures and tables are located at the end of each chapter. Chapters 2 through 5 describe tools developed and used to support my hypothesis. Chapter 6 describes and demonstrates the hypothesis that high resolution MR imaging can be used to distinguish local differences in elastic properties of arteries and phantoms *in vitro*. The importance of developing the technique is to provide a method to detect atherosclerotic plaques before the disease becomes symptomatic. Chapter 7 summarizes the different conclusions from each chapter and discusses future applications of the work presented here along with several recommendations. Throughout this thesis the term "local" is meant to describe different segmental sections when viewing a circular tube (see Fig. 1.1). The term "phantom" is used to describe a physical model made to mimic a specific tissue.

1.2 Vascular Disease

Cardiovascular disease, including heart attacks, strokes, and peripheral arterial occlusions, has a high incidence. For example, In the United States, there are approximately 500,000 cases of strokes per year with 30% of the cases resulting in deaths.¹ Of the 3 million survivors of stroke, 55% require special care and 15% are totally disabled. In 1994 more than 6 million people died from stroke world wide.^{1,2,3}

1.2.1 Possible Mechanisms

Atherosclerosis is one form of cardiovascular disease and results in local changes in the content, structure and function of vascular components such as elastin, smooth muscle cells, collagen, and glycosaminoglycan (see Fig. 1.1). It is hypothesized that, by having a high concentration of lipids within blood, there is a

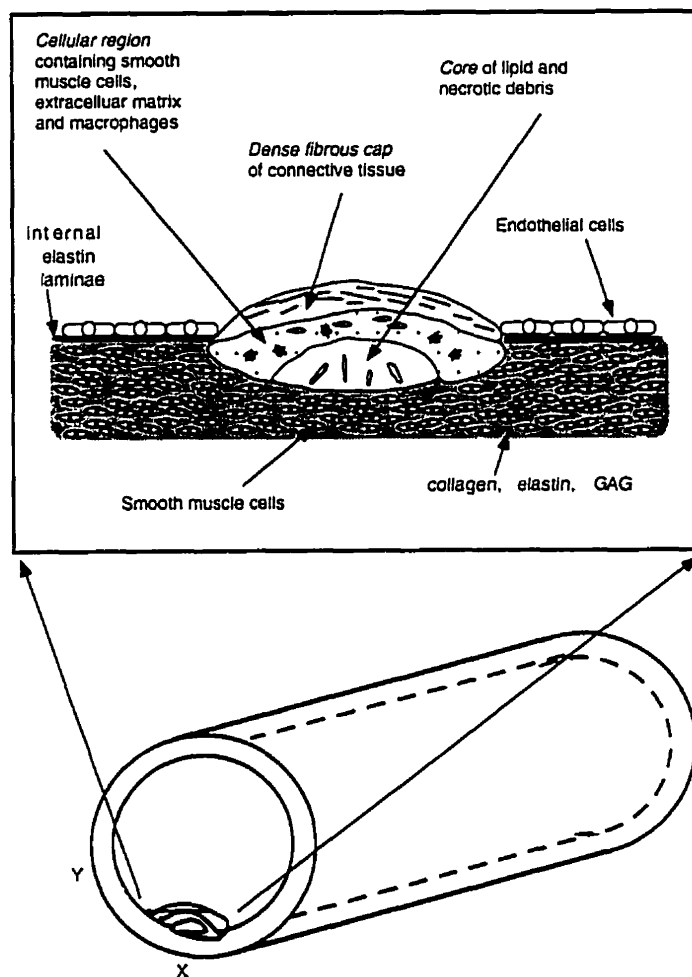


Figure 1.1 A schematic diagram of the structure of atherosclerotic plaque⁴ is shown on the top. Common features include a *core* of lipid and necrotic debris, a *cellular region* containing smooth muscle cells and macrophages, and a *dense fibrous cap*. In practice, plaques differ from this generalized model and may include thrombotic and calcified regions. The bottom diagram is a sketch of an artery with a raised lesion in the intima. The *local* elastic properties at points X and Y (in adjacent sectors of the artery cross section) are different because of the presence of the plaque.

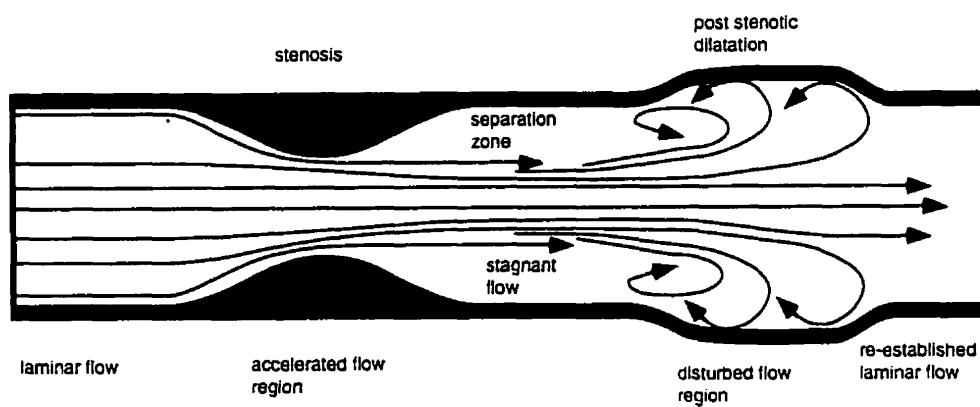


Figure 1.2 A sketch of a simplified stenosed arterial model; steady flow streamlines show that immediately after the stenosis there is a separation zone where flow may be reversed and residence times are long. Further downstream is the region of disturbed flow where the shear stress next to the endothelial cells are high. In practice, the flow patterns are much more complicated because the artery wall distends with pressure, the blood flow is pulsatile, and the geometry is not perfectly cylindrical.

high probability that lipids will infiltrate the vascular wall.^{4,5} Over time, a complicated cascade of events causes the lipid deposits to become fibrotic. In more advanced stages of the disease the lesion may eventually become thrombotic and/or calcified. An alternate mechanism for lesion formation may be injury to the vascular wall.⁴ In the case of injury, lipid and immune response cells, (such as monocytes/macrophages in blood) penetrate and accumulate in the intima. Smooth muscle cells may also penetrate the intima, and begin forming connective tissue leading to fibrotic plaques (see Fig. 1.1). However, the exact cause of the initial lesion formation is not clear⁶ since the mechanisms described above do not explain why atherosclerotic lesions form as localized patches near bends and bifurcations of arteries⁷ as shown by pathology studies.

The patchy distribution of atherosclerotic plaques suggests that local mechanical factors, such as hemodynamic forces and mechanical stresses within the artery wall, must have a strong influence on the lesion development.⁸ The geometric location of bifurcations, tapers and curves causes the blood flow patterns to experience fluid acceleration, fluid separation zones, and regions of disturbed or turbulent flow (see Fig. 1.2). In regions of disturbed flow, there is high fluid shear stresses near the vessel wall and the endothelial cells may be damaged or injured, which leads to plaque development.⁹ In the separation regions the blood velocity experience reverse flow and/or undergo near stagnant flow rates.¹⁰ In these regions lipids within in the blood have long residence times, and there is a potential physiological mechanism for the preferential localization of plaques. These simple explanations are further complicated by the pulsatility of the blood flow as well as the distensibility of the arterial wall. It is still unclear as to whether the hemodynamic factors are the cause or result of atherosclerotic disease.

Regardless, it is generally understood that healthy arteries are elastic because they act as a sophisticated energy storage device during systole, and during diastole the elastic energy is converted to energy of flow. This simplistic description of the Windkessel theory describes how the body is able to circulate several litres of blood per minute (with a mean aortic pressure of approximately 13

kPa) through billions of capillaries.¹¹

1.2.2 Differences in Local Elastic Properties Hypothesis

Since atherosclerotic lesions generally occur as localized patchy regions (as shown in Fig. 1.1), it is reasonable to expect that there are localized differences in the wall stiffness in both the circumferential and longitudinal directions as measured from excised arterial strips.¹² For *in vivo* situations, elastic properties in the circumferential directions can be determined from changes in the arterial cross-section due to the pressure changes throughout the cardiac cycle. With advances in medical imaging techniques such as MR imaging, it should be theoretically possible to detect *early* signs of fibrous and calcified plaque growth by distinguishing differences in the elastic properties of diseased regions and healthier regions in an artery. This thesis addresses some of the technical and theoretical issues related to proving this theory with current MR imaging technology.

Although this thesis is based on *in vitro* experiments, most of the concepts can be adapted to non-invasive *in vivo* studies since an effort was made to simulate *in vivo* conditions wherever possible. The tools and *in vitro* data presented here will aid in the long-term goal of being able to provide a method of early identification and management of people at high risk of vascular disease (i.e. people with risk factors such as genetic predisposition, hyperlipidaemia, hypertension, obesity, diabetes as well as lifestyle choices of cigarette smoking, poor diet, and lack of physical activity).⁴ In addition, such tools can be used to monitor the regression or progression of disease in people undergoing different drug therapies.

Another benefit of having high resolution MR imaging capabilities is the ability to perform both *in vitro* and *in vivo* studies of the morphology and geometry of both healthy and diseased arteries. Having this type of information along with the local elastic (or stress) properties of arteries, it may be possible to identify plaques prone to rupture which can cause acute stroke or myocardial infarction long before chronic stenotic symptoms occur.¹³ This important topic is not

addressed here and will be left to future researchers.

1.2.3 Limitations of the Hypothesis

The concept of measuring local elastic differences as a screening tool for atherosclerotic plaques assumes that patients are not in a state of hypertension. At high luminal pressures, the incremental strain of elastic arteries from systole to diastole is quite small due to the exponential stress-strain behaviour of arteries. The small changes in strain may not be detectable using current imaging techniques. The hypothesis also assumes that the development of the fibrous or calcified plaque is sufficient in size so that differences in strain can be properly resolved. It is assumed that "arteriosclerotic" disease, or the overall hardening of the arteries,^{3,4,6,14} has not developed. Several studies have shown that in the general population, arterial stiffening occurs with age.^{14,15} The importance of being able to measure local elastic properties is much more valuable for asymptomatic individuals with a genetic predisposition to atherosclerotic disease and who have made poor lifestyle choices while below the age of 30 (i.e. their arteries are still reasonably distensible¹⁴).

Arteriosclerosis can be diagnosed through the measurement of gross elastic properties of arteries as studied by numerous researchers using several different methods of characterizing the mechanical properties of arteries. Because several of the definitions for some of the various parameters have similar semantics, it is often difficult to compare results between different studies unless the definitions and testing procedures are made clear. My interpretations of these definitions are discussed in Section 1.3 and later in Chapter 6.

The next section is a brief discussion of reported methods that are utilized to measure the elastic properties of arteries. There is an emphasis on uniaxial tensile testing since this will be the basis of comparison for the work presented in Chapter 6. Presently, most medical diagnostic tools can only detect *gross* changes in elastic properties of arteries *after* they have become severely sclerosed or stenosed and the geometric motion or dimensions have been significantly altered with subsequent effects on the blood flow patterns.

1.3 Elastic Measurements of Arteries

Milnor¹¹ and Fung¹⁶ have summarized many of the methods used to estimate the elastic modulus of arteries since the 1950's. Below, is a brief outline of that research.

Throughout this thesis the terms "material stiffness" and "structural stiffness" is used sporadically, and I defined them here. "Material stiffness" is a property represented by the elastic modulus or slope of a stress-strain curve, and "structural stiffness" is dependent on both the elastic modulus **and** the artery wall thickness.¹⁷ The stress-strain behaviour of arteries is not linear and displays viscoelastic characteristics. Hysteresis is observed depending on whether the specimen is experiencing increasing or decreasing stress. To simplify the analysis of stress-strain data, researchers (including myself) have treated the increasing and decreasing stress states separately.

One fundamental measurement of material stiffness at a particular stress and strain level is the Young's modulus or elastic modulus, E , which is defined as the slope of the stress-strain curve.¹¹ Because *in vivo* experiments cannot yield a complete stress-strain curve, researchers have approximated E using different definitions as described in Sections 1.3.2, 1.3.5, and 6.2. *In vitro* experiments, on the other hand, can be designed to yield a complete stress-strain data from either strips of arteries (uniaxial testing) or intact sections of arteries (biaxial testing); thus these experiments provide a more complete understanding of the fundamental characteristics of a material.

1.3.1 Tensile Tests

In the case of arterial strips, the most basic quantitative physical measurement is obtained from the uniaxial tensile test.¹⁸ The force-length data from such a test can be converted to a stress-strain graph. Tensile tests have been performed on arterial strips^{12,19,20} to relate the artery's complex structure to its physical properties.²¹ It is generally agreed that the specimen must be kept moist during testing as the properties change significantly if it is allowed to dehydrate. In doing tensile tests at a fixed strain rate one assumes that: 1) the

strain rate has no significant effect on the stress-strain measurements, 2) there are no edge effects from the strips, 3) there are no residual stresses in the specimen, 4) the mechanical properties are not dependent on the elongation rate, and 5) the uniaxial test only reflects the properties in the test direction. Because the arterial properties are anisotropic, some researchers have separately measured artery strips in the longitudinal and circumferential directions.¹²

1.3.2 Mechanical Transducers to Measure Strain

In most methods that measure elasticity, the strain is obtained by recording some dimensional change in the specimen. Over the years, more sophisticated methods of strain detection have been reported. For example, *in vivo* studies^{22,23,24,25} required the physical attachment of light-weight strain gauges onto the outer wall of various arteries in anesthetized dogs. The lumen pressure was obtained through an intravascular catheter connected to a pressure transducer. With this information, the pressure elastic modulus, E_p , is defined as:²⁶

$$E_p = \frac{\Delta P}{(\Delta D / D_m)} \quad (1.1)$$

where D_m is the mean diameter, ΔD is the diameter change, and ΔP is the corresponding pressure change.

After the experiments, the dogs were euthanized so that the volume of the artery wall could be measured. Since artery volume is conserved²⁷ and specimen length kept constant, the inner diameter becomes a function of the outer diameter as given by:

$$D_i = \sqrt{(D_o^2 - \frac{4V_w}{\pi L})} \quad (1.2)$$

where D_i is the inner diameter, D_o is the outer diameter, V_w is the volume of the wall with a length L . Because the inner diameter is now determined, it is possible

to calculate the incremental elastic modulus, E_{inc} , at a mean pressure P_2 using²⁸

$$E_{inc} = \frac{P_3 - P_1}{D_{o_3} - D_{o_1}} \frac{2 (1 - \nu^2) D_i^2 D_{o_2}}{D_{o_2}^2 - D_i^2} \quad (1.3)$$

where P is the pressure, ν is Poisson's ratio, and the subscripts 1,2,3 represent successive measurements of pressure and radius. Because of the invasiveness of these studies, they are obviously not practical for *in vivo* human studies.

It should be noted an experiment of this type reveals biaxial properties and is different from the case of arterial strips being elongated in the one direction during tensile testing. In tensile tests, the material dimensions decrease in the two unconstrained directions. This is different from biaxial testing of intact arterial segments where the length of the artery is constrained, and the lumen pressure is increased. In this case, there are circumferential and radial forces acting directly on the artery wall. Since the volume of the artery wall is conserved²⁷, as the diameter increases, the wall thickness will decrease by the same factor.

Eq. 1.3 was used by Bergel²⁸ who measured D_o without attaching any mechanically devices; instead, he photoelectrically monitored the shadow of excised arteries as the lumen pressure was varied. The inner diameter was calculated using Eq. 1.2. Several researchers^{29,30,31} have modified Eq. 1.3 by assuming a circular geometry and replacing the internal and external diameter with internal and external circumference (c_i and c_o , respectively) to get

$$E_{inc} = 2 (1 - \nu^2) \frac{dp}{dc_o} \frac{c_i^2 c_o}{c_o^2 - c_i^2} \quad (1.4)$$

where dc_o is the change in outer circumference due to a change in the internal pressure, dp . By using CT imaging,²⁹ both the inner and outer circumferences could be measured directly without the need for Eq. 1.2. Both Eq. 1.3 and Eq. 1.4 were derived assuming the specimens were tethered and that specimens are thin walled circular geometries with isotropic properties.

1.3.3 Ultrasound Imaging

Ultrasound is commonly used to diagnose vascular disease because it is non-invasive, collects data in real time and is relatively inexpensive. However, ultrasound has a number of drawbacks which include its inability to penetrate past tissue-air and tissue-bone interfaces as well as being limited in its imaging depth. Even with these limitations, numerous ultrasound studies have been reported using superficial arteries and, more recently deep arteries have also been reported.²⁶

Vascular geometries can be obtained using B-mode or M-mode ultrasound imaging.³² B-mode imaging produces 2-D spatial images of the cross-section of arteries, and the time required to collect one image is directly proportional to the depth of the object being imaged and the number of lateral ultrasound elements.³³ A typical clinical image can be acquired in 30 to 60 ms range. The resolution of B-mode images, on the other hand, is limited by the size of the focal region produced from neighbouring ultrasound elements. Typical resolutions found in clinical images are in the 1 to 2 mm range.³⁴

Instead of collecting a 2-D spatial resolution image, it is possible to obtain an image of 1-D spatial resolution (with increased temporal resolution) as a function of time. This type of imaging is called M-mode ultrasound which can have temporal resolution in the 3 ms range. The principle of M-mode ultrasound assumes that a single ultrasound beam is directed through the center of an artery, and that the reflected signals are from the near and far lumen walls of the artery. These signals can be collected rapidly as a function of time, and hence, the image is typically displayed as diameter versus time.²⁵ Specialized M-mode ultrasound equipment with echo tracking features can measure the diameter of arteries with high precision (2-10 μ m); however, the accuracy of the diameter measurement is between 30 to 200 μ m due to variations in the cardiac output and errors in positioning the transducer.³⁵

The vessel compliance³⁵ can be measured (see below), and if the wall thickness is known, the elastic modulus can be calculated using Eq. 1.3. Numerous studies using M-mode ultrasound to monitor dimensional changes in

various arteries *in vivo* have been reported^{26,35,36} to measure the distensibility of superficial arteries³⁶ and the aorta.²⁶ The drawbacks of this method are in its assumptions: i) a single measured diameter is sufficient to describe the artery geometry (which would be true only for circular geometries), and ii) the ultrasound beam passes perpendicularly through the center of the artery. In all cases, it is necessary to determine the wall stress which is calculated from measuring the pressure either directly using a catheter²⁶ (invasive) or by inferring it through non-invasive monitoring of the pressure in external arteries.³⁵

1.3.4 X-Ray Imaging of Vascular Geometries

The sub-millimetre resolution of x-ray angiography has made it the "gold standard" in assessing in-vivo vascular geometries. X-ray angiography requires the injection of a bolus of radio-opaque contrast agent into the blood stream to increase the contrast between the blood and surrounding tissue. 2-D images are acquired as the bolus travels through the vessel. Digital subtraction³⁷ of the pre- and post-contrast agent images will yield a high resolution projection of the contrast agent in the vasculature. The disadvantages of using x-ray angiography are its invasiveness, the potential patient reactions to the contrast agent, and the potential harmfulness of using ionizing radiation.

X-ray computed tomography (CT) can be used to collect a series of 2-D slices through the object being imaged which then are assembled into a 3-D data set. CT-based imaging provides accurate representations in the vasculature and improved image contrast within the body. The drawback of CT imaging is that the dosage of ionizing radiation increases.

In order to accurately measure arterial wall motion, our laboratory has developed two specialized CT imagers^{29,38} for *in vitro* studies of vascular mechanics. One is optimized for high spatial resolution (150 μm) and the other for high temporal resolution (17 ms) by gating to the cardiac cycle. Average elastic properties can be obtained by using Eq. 1.4. Local elastic properties can be estimated by placing copper wires around the outer circumference of the vascular specimens and monitoring the circumferential strain between wires. Because of the

high x-ray dosage involved in collecting these images, these techniques are not likely to be used clinically.

1.3.5 Pulse Wave Velocity

Several researchers were able to estimate the pulse wave velocity, c_o , of arteries and show that it increases with stiffness.³⁹ Typical values of c_o for elastic arteries (such as the aortic arch and thoracic aorta) are in the range of 4 to 6 ms^{-1} and are different from more muscular arteries (such as the iliac and femoral) which have values in 8 to 12 ms^{-1} range.

There are two approaches in calculating c_o . The first method involves determining the volume elastic modulus E_v :

$$E_v = \frac{\Delta P}{\Delta A / A_m} \quad (1.5)$$

where ΔA is the change in the lumen area, A_m is the mean area, and ΔP is the change in pressure. The length of the artery segment does not appear in Eq. 1.5 because of the denominator is the relative change in volume. E_v can be measured using any technique that can report lumen areas (i.e. physical strain gages, M-mode ultrasound³⁵ of diameter changes, or MR imaging¹⁵ of lumen cross sectional images). The reciprocal of E_v is the volume distensibility and is sometimes incorrectly called compliance.⁴⁰ The arterial compliance^{15,11} C is equal to $\Delta V/\Delta P$, where ΔV is the change in lumen volume.

The pulse wave velocity, can be calculated as⁴¹

$$c_o = \sqrt{\frac{E_v}{\rho_f}} \quad (1.6)$$

where ρ_f is the fluid density. When the wall thickness is known, the incremental elastic modulus can be obtained from Eq. 1.3 or an alternative estimate of the elastic modulus can be obtained using the Moens-Korteweg equation⁴²

$$c_o = \sqrt{\frac{Eh}{2R\rho_f}} \quad (1.7)$$

where ρ_f is the fluid density, h is the wall thickness, and R is the mean radius. Eq 1.7 was derived for tubes undergoing progressive waves of radial motion of long wavelength and infinitesimal amplitude, propagating in an infinitely long circular cylinder filled with an inviscid fluid and having a linearly elastic wall.¹⁶ Caution must be used in reporting the results because of the many conditions imposed in the derivation of this equation.

Alternatively, the pulse wave velocity can be obtained by simultaneous monitoring of the lumen diameter (or blood velocity or pressure wave front as a function of time) at two different locations along the artery.¹¹ This will give the speed of the pulse wave between the two locations. There is no need to measure the pressure in this method. This techniques can only yield gross elastic properties over a large region.

1.3.6 Non-Tagging MR Methods

General tagging techniques are necessary for measuring local strains. For *in vivo* studies, MR tagging is much less invasive than physically attaching markers onto the elastic material to be studied.^{22,23,24,25,29} Other researchers have reported success in using MR phase contrast methods^{43,44} to estimate strain with the heart from a series of images containing pixel by pixel velocity. The principle behind this method is that the distance each pixel moves from one image to the next image can be calculated as the time between the adjacent images multiplied by the velocity of the pixel in the first image. Although phase contrast methods are not easily interpreted without significant post processing, they have an added advantage of being able to measure flow velocities within the lumen as well as the wall itself. These methods require high gradient strengths to be able to detect slow velocities found in arterial motion. This would allow direct measurements of fluid shear⁴⁵ as well as local wall motion.

A completely novel method of estimating the stress-strain curve of excised arteries was described by Vinee et al.⁴⁶ and Constantinesco et al.⁴⁷ They reported a mathematical correlation between MR relaxation times, T_1 and T_2 , and a single exponential parameter that described the longitudinal arterial stress-strain curve as measured by tensile tests. The concept is based on the fundamental principle that MR relaxation times are influenced by differences in the chemical composition of healthy and diseased tissues. Their findings revealed that a correlation does exist, but the correlation was weak ($r \approx 0.6$) due to sample dehydration and biological variations in T_1 and T_2 measurements of arterial sections.

1.3.7 MR Tagging Methods

I believe that it is possible to exploit a unique MR imaging method for non-invasive measurement of strain by tagging the artery using magnetic presaturation techniques.^{48,49,50} MR tagging techniques are described in detail by others;⁵¹ a short description is given in section 1.4.8. In brief, dark tag lines can be made to appear in MR images by flipping the net magnetization of selected protons into the transverse plane and then dephasing their magnetization prior to starting the MR imaging sequence. During MR imaging, these protons do not contribute to the measured signal because their longitudinal magnetization at the start of the imaging sequence is very small. Since the MR tags are applied during diastole and the protons are in the artery wall, the tags will move with the artery throughout the cardiac cycle. Depending upon the time at which the images are collected, the tags will have moved by a different amount. Hence, if a series of images are obtained throughout the cardiac cycle, the tagged lines will show the motion of the artery wall.

1.4 Magnetic Resonance Imaging

1.4.1 General Description

Although magnetic resonance (MR) imaging is a relatively new medical imaging modality there are several general references that explain how this technology works.^{52,53,54} The popularity of MR imaging is increasing because:

i) it does not use harmful ionizing radiation, *ii)* it has excellent resolution comparable to other medical modalities, and *iii)* it can provide excellent contrast between different soft tissues. Contrast in MR imaging is based upon the tissues' magnetic properties such as proton density (ρ_0) as well as T_1 and T_2 relaxation times. The following is a brief classical description of processes relevant to this thesis. For simplicity, the description assumes a Cartesian coordinate system.

When an object is placed in a strong magnetic field as found inside the bore of a superconducting MR scanner, the protons in the object will experience a torque. This causes their magnetic moments to align either parallel (low energy state) or anti-parallel (high energy state) to the main magnetic field, B_0 . By convention, the direction of B_0 is called the z-axis or the longitudinal direction. At thermal equilibrium, the net magnetic moment, M_0 , will be aligned parallel with B_0 and precesses at a frequency given by the Larmor equation:

$$f = \frac{\gamma}{2\pi} B_0 \quad (1.8)$$

where f is the frequency in MHz, and γ is the gyromagnetic ratio for hydrogen ($\gamma/2\pi$) = 42.58 MHz/T).

To produce a MR signal that can be measured, radio frequency (RF) energy at the Larmor frequency is applied to the object to flip (or nutate) M_0 away from the z-axis through an angle α_t . When the RF energy is turned off, this results in a transverse magnetic moment, M_t , in the plane perpendicular to B_0 such that $M_t = M_0 \sin(\alpha_t)$. The amount of remaining longitudinal magnetization, M_z , is $M_z = M_0 \cos(\alpha_t)$. Receiver coils placed near the object can be turned on to detect M_t .

1.4.2 Relaxation Times T_1 and T_2

The amplitudes of the net magnetic moments M_z and M_t do not remain constant. After the RF pulse is turned off, M_z eventually returns to its steady state value M_0 by transferring energy to the surrounding chemical lattice. The regrowth in the magnitude of M_z to M_0 is a function of time, t , and is dependent on the T_1 time constant as described by:

$$M_z(t) = M_0 \left(1 - \exp\left(-\frac{t}{T_1}\right) \right) \quad (1.9)$$

In the transverse plane, the net magnitude of M_t decreases due to a loss in phase coherence of the magnetic moments of each individual proton. This is attributed to local magnetic field disturbances caused by dipole-dipole interactions with neighbouring molecules which alters the precession rate of the individual proton spins. The effect on the magnitude of M_t is described by the equation

$$M_t(t) = M_t(0) \exp\left(-\frac{t}{T_2}\right) \quad (1.10)$$

When there are other magnetic field inhomogeneities specific to our MR system such as magnetic susceptibility gradients, eddy currents, and B_0 inhomogeneities, the observed rate of the loss in phase coherence increases and M_t can be described by:

$$M_t(t) = M_t(0) \exp\left(-\frac{t}{T_2^*}\right) \quad (1.11)$$

where

$$\frac{1}{T_2^*} = \frac{1}{T_2} + \frac{\gamma}{2\pi} |\delta\mathbf{B}| \quad (1.12)$$

and $\delta\mathbf{B}$ is the total magnetic field inhomogeneity from the experimental set up.

Although, there are several inter-related processes that govern the magnitude of the collected signal, specific MR parameters and procedures can be adjusted to extract the MR relaxation times T_1 and T_2 from a series of images. These techniques are described in sections 1.4.4 and 1.4.5.

1.4.3 Spatial Encoding Using Gradients

In order to obtain a 2-D image of an object, it is possible to encode spatial information into the magnetic spins by applying a linearly varying magnetic field gradient to the main magnetic field B_0 . Thus Eq. 1.8 becomes

$$f = \frac{\gamma}{2\pi} (B_0 + \mathbf{G} \cdot \mathbf{r}) \quad (1.13)$$

where $\mathbf{r}=(x,y,z)$; x,y,z is the location to which the spatial encoding is applied; $\mathbf{G}(G_x, G_y, G_z)$ is equal to the magnetic field gradients ($\partial B_z/\partial x, \partial B_z/\partial y, \partial B_z/\partial z$); and B_z is the z component of the gradient field in the z direction. Each of the three gradients serve a different purpose. For example, in a 2-D axial image, the slice thickness is governed by the slice encode gradient G_z ; G_y is often selected as the phase encode gradient; and the G_x , by default, becomes the read-out gradient which is turned on during data acquisition.

If the magnetic field gradients are uniform in space, then Eq. 1.13 reveals that the frequency components of a signal is a linear function of the spatial location of the magnetic spins. The G_z gradient in combination with an RF pulse can be used to limit the thickness of the 3-D object, thereby creating a thin 2-D object. The 2-D Inverse Fourier transform, FT^{-1} , may then be used to decompose the total signal as a function of amplitude and frequency (i.e. spatial location).

Because the FT^{-1} and 2-D Fourier transform, FT , can be used to convert the measured signal to an image and vice versa, it is often convenient to visualize the two domains of data as representing either "image-space" or "k-space" (also known as "frequency space").^{55,56} If one assumes: *i*) all signals originates from a 2-D plane, *ii*) the signal is demodulated from the Larmor frequency, *iii*) the detectors are phase sensitive, and *iv*) relaxation effects can be ignored, then the measured signal, $S(t)$ is:

$$S(t) = \iint_{x,y} M_0(x,y) e^{-2\pi i [k_x(t)x + k_y(t)y]} dy dx \quad (1.14)$$

$$= S(k_x(t), k_y(t))$$

where $M_0(x,y)$ is proportional to the net longitudinal magnetization (before the imaging sequence is started) at the location (x,y) , $i=\sqrt{-1}$, $S(k_x(t), k_y(t))$ is the spatial frequency content of the object at the k-space location $(k_x(t), k_y(t))$, and

$$k_x(t) = k_x = \frac{\gamma}{2\pi} \int_0^t G_x(t') dt' \quad (1.15)$$

and

$$k_y(t) = k_y = \frac{\gamma}{2\pi} \int_0^t G_y(t') dt' \quad (1.16)$$

where (k_x, k_y) are the Fourier conjugates of the Cartesian coordinates (x, y) of a thin slice of the object, t' is the integration variable, and G_x and G_y are the gradient waveforms.

For imaging purposes, the MR signal is acquired with k_y fixed and k_x increasing linearly throughout the signal acquisition. It is common to sample the measured signal (for digital processing purposes) with 256 points. These data points fill one k_x line in k -space. If the process is repeated after a time TR (time of repetition), but with k_y increased by Δk_y (achieved by increasing G_y), then this will fill another horizontal line in k -space (see Fig. 1.3). After 256 signal acquisitions (all with different k_y 's), a 2-D FT^{-1} on the k -space data will produce an image with intensities proportional to $M_o(x, y)$:

$$M_o(x, y) = FT^{-1} [S(k_x, k_y)] \quad (1.17)$$

In reality, relaxation effects cannot be ignored. These effects are dependent on the chemical environment of the protons and directly affects image contrast. The next section describes how image contrast is related to relaxation times as well as MR pulse sequence parameters.

1.4.4 Spin Echo Imaging

Clinical MR imaging typically utilizes differences in the ρ_o , T_1 , or T_2 to provide contrast between different tissues. One of the most common MR techniques is called the "spin echo" pulse sequence. This pulse sequence can be controlled so that the image contrast is solely dependant on either the T_1 or T_2

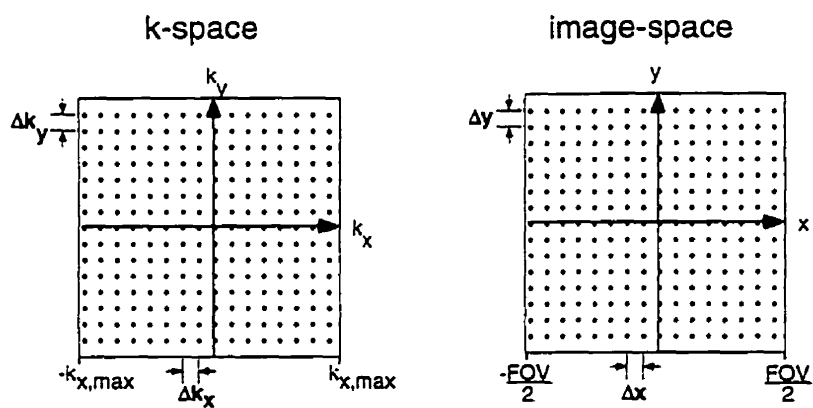


Figure 1.3. A schematic diagram of how the digitized signal is stored in a 2-D array (16 x 16 in size) called k-space. The k-space data and image are Fourier conjugates and can be converted to one another using the FT or FT^{-1} .

relaxation time within an object. The following is a description of how the magnetic moments are manipulated in a spin echo pulse sequence.

Spin echoes are formed by applying a series of RF pulses. The first RF pulse flips the longitudinal magnetization 90° into the transverse plane. Immediately after the RF pulse is removed, the individual spins begin to lose phase coherence as a result of their slightly different Larmor frequencies caused by local magnetic field variations. In order to regain phase coherence at a time TE (Time of Echo), another RF pulse is applied at time TE/2 to flip the transverse magnetization 180° . Hence, at time TE, the transverse magnetization will have regained its phase coherence (originally lost through T_2^* decay) and a spin echo is formed. Spatial information can be encoded in the k_x direction by turning on the x-gradient (G_x) during signal acquisition. The signal from the spin echo can now be measured. Spatial information from the y direction can also be encoded by repeating the spin echo process but with a different y-gradient amplitude applied after the 90° RF pulse. Eventually the k-space matrix is filled, and the 2-D FT^{-1} used to produce an image with intensities, $I(x,y)$, at the coordinate (x,y) approximated by:

$$I(x,y) = I_0 \exp\left(\frac{-TE}{T_2}\right) \left(1 - \exp\left(\frac{-TR}{T_1}\right)\right) \quad (1.18)$$

where I_0 is proportional to ρ_0 , and TR is the time of repetition of spin-echo experiments. If $TR \gg T_1$, Eq. 1.18 can be approximated as:

$$I_{TE}(x,y) \approx I_0 \exp\left(\frac{-TE}{T_2}\right) \quad (1.19)$$

where $I_{TE}(x,y)$ is the image intensity at time TE. I_{TE} is dependent on the material properties ρ_0 and T_2 , and also on the MR pulse sequence adjustable parameter TE. By obtaining a series of images at different TE's, it is possible to numerically calculate I_0 and T_2 .

1.4.5 Inversion Recovery Imaging

Another method of adjusting contrast in MR images is obtained by using an

inversion recovery (IR) pulse sequence. In this method, a 180° RF pulse is applied at a time T_I (time of inversion) prior to the start of the spin echo sequence. When $TR \gg T_1$ and $TE \ll T_2$, the image intensity at time T_I , $I_{TI}(x,y)$, can be described as

$$I_{TI}(x,y) = I_0 \left(1 - 2\exp\left(-\frac{T_I}{T_1}\right)\right) \quad (1.20)$$

The image intensity is now a function of the material properties ρ_0 and T_1 , as well as the MR pulse sequence adjustable parameter T_I . By obtaining a series of images at different T_I 's, it is possible to numerically calculate I_0 and T_1 .

1.4.6 Gradient Recalled Echoes

An alternative imaging pulse sequence to the spin echo sequence is the Gradient Recalled Echo (GRE) sequence. In this imaging sequence, there is only one RF pulse which tips the initial longitudinal magnetization by an angle less than 90° . Immediately after the RF pulse has ended, a negative G_x gradient is applied to force the transverse magnetization to dephase rapidly. Following this negative G_x gradient, a positive G_x gradient is turned on to rephase the transverse magnetization. The transverse magnetization will have regained its phase coherence at the time when the sum of these two gradients are zero. GRE pulse sequences are inherently faster than spin echo sequences, but GRE sequences are sensitive to magnetic inhomogeneities and may sacrifice contrast when compared to spin echo images.

1.4.7 MR Gradients and Resolution

It is often difficult to visualize in 3-D Cartesian space the three z-components of magnetic gradients used in MR imaging. This is complicated by the fact that there are 9 total independent components that describe a complete magnetic field. The following analogy is made as an aid in visualizing the three linear MR gradients: G_x , G_y , G_z . Recall that in clinical superconducting MR scanners, the magnetic bore axis is referred as the z-direction. The vertical direction is the y-axis, and the horizontal direction is the x-axis. If the G_x gradient was on, the measured z-component of the magnetic field varies only in the x-

direction. Similarly, if the G_y gradient was on, the measured magnetic field in the z-direction varies only in the y-direction. Finally, if the G_z gradient was on, the measured magnetic field in the z-direction varies only in the z-direction. In each case, the magnetic field is constant in the other two directions.

In order to understand how the gradient strength affects the MR spatial resolution, it is easiest to recall that the MR signal is collected in k-space (see Fig. 1.3). Because of the FT relationship between k-space and image space, it is understood that the field-of-view (FOV) in the image-space is

$$FOV = \frac{1}{\Delta k_x} \quad (1.21)$$

where Δk_x is the spacing between adjacent k_x points in k-space. Similarly, the spatial resolution, Δx , in image-space is

$$\Delta x = \frac{1}{2 k_{x,max}} \quad (1.22)$$

Using Eq. 1.15 with G_x set at a constant amplitude for a fixed time t_x , it can be shown that:

$$\Delta x = \frac{1}{\left(\frac{\gamma}{2\pi} G_x t_x \right)} \quad (1.23)$$

Thus the spatial resolution is inversely proportional to the gradient strength and the duration of the gradient. When t_x is fixed, higher gradient strengths will give a smaller pixel dimensions. A similar analogy can be derived for the resolution in the y direction (not shown).

1.4.8 MR Tagging

MR imaging has the unique ability to presaturate protons within an object so that they when the MR signal is collected, these protons do not contribute to any signal. This presaturation causes the longitudinal magnetic moment to become effectively zero at the start of an MR imaging pulse sequence. The presaturation

is temporary and the longitudinal magnetization will recover as given by Eq. 1.9.

The DANTE⁵¹ tagging technique is one such preparation pulse technique that is applied prior to standard MR imaging pulse sequences. The DANTE presaturation technique can be easily visualized by using an excitation k-space \leftrightarrow object-space analogy,⁵⁷ where each domain is related by the FT or FT⁻¹. Presaturation of magnetic spins means spatially *selecting* certain protons in the object and flipping their longitudinal magnetization 90° into the transverse plane **before** starting a MR imaging pulse sequence. If the *selected* protons in a 2-D plane object were chosen to be in a stripe pattern (e.g. vertical lines), then these *selected* protons will have no longitudinal magnetization when the imaging sequence starts. Since measured signal will be proportional to $M_t = M_0 \sin(\alpha_t)$ and the *selected* protons have M_0 equal to zero, M_t will also be zero (i.e. no signal).

For example, if a train of rectangular RF pulses are applied in the excitation k-space domain (with G_x turned on), then *selected* protons in object space would be presaturated as a series of stripes in the x direction. Since the duration of each RF pulse has a finite length, there will be a sinc apodization on the object saturation. Note that in order to saturate the *selected* protons, the total RF power deposited at the end of the RF train must be just enough to flip the longitudinal magnetization 90° before the imaging pulse sequence is started.

In reality, G_x is only turned on between each RF pulse, and the k_x 's (Eq. 1.15) will govern the tag spacing (i.e. spatially saturated protons) in the object domain. Because the train of RF pulses is not infinitely long, each of the selected stripes in the object domain has a sinc-like profile. To obtain stripe lines in the y-direction, the presaturation process can be repeated using G_y instead of G_x .

In the special case when the train of RF pulses consists of only two pulses (each with the power for a 45° flip), the resulting object space will have presaturation stripes in a sinusoidal pattern. This technique is given the acronym SPAMM⁴⁸ (Spatial Modulation of Magnetization).

1.5 Research Goal

Since atherosclerotic lesions occurs in localized patchy regions, one

possible method of detecting atherogenesis before the disease becomes symptomatic, is to be able to distinguish local differences in the elastic properties of diseased regions and the surrounding healthier regions in an artery. Hence, the specific goals of my research are to: i) modify a clinical MR scanner (1.5T GE Signa) to permit distortion free high resolution ($<100 \mu\text{m}$ pixels) images within a reasonable amount of time (<10 minutes), ii) design a pumping system to deliver reproducible pressure waveforms to *in vitro* specimens, and not introduce flow artifacts in the MR images, iii) develop a synthetic phantom material that mimics the properties of arteries in both biomechanical and MR properties iv) modify an GRE pulse sequence to permit non-invasive MR tagging of dynamic arterial specimens, v) measure the local elastic properties of pulsatile arteries and arterial phantoms *in vitro*, and vi) make an effort to simulate *in vivo* conditions in all experiments and to consider at all stages of the research how each development can be adapted to *in vivo* studies in the future.

To fulfil the objectives outlined above, I have developed a high resolution MR imaging method that uses DANTE tagging techniques to track the strain in pulsatile aortic specimens and phantoms. Since clinical MR gradient strengths do not permit high resolution imaging in short time periods, I have developed a method of designing and manufacturing MR gradient coils from printed circuit (PC) boards. When installed into the bore of a clinical MR scanner, these small gradient coils can deliver high gradient strengths to permit high resolution MR imaging with short imaging times. Because of the large electrical current requirements, it was necessary to model the amount of heat dissipation and cooling required to keep the gradient coil temperature at acceptable levels. Next, it was necessary to find a suitable pumping fluid that would not introduce any motion artifacts in MR images. Motion artifacts appear as ghosts in the phase encoding direction of MR images, and can mask a large portion of the imaged object. To evaluate my system, a novel distensible arterial phantom was developed. Its properties were reproducible, and could be measured in a tensile tester. Finally, I measured the incremental elastic properties of several phantoms and aortas. To compare these

results to that of full tensile test results, I present a new method of extrapolating incremental data to full exponential stress-strain curves.

1.6 Thesis Outline

1.6.1 Gradient Coil Design and Evaluation

Chapter 2 is based on the paper "Quadrupole gradient coil design and optimization: A printed circuit board approach" by K.C.Chu (the author) and Dr. B.K. Rutt (supervisor), which appeared in *Magnetic Resonance in Medicine*, Volume 31, pages 652-659 in 1994. Most of the research was performed by the author. Dr. Rutt provided guidance with the original optimization software and the concept of using PC boards for coil evaluation.

In Chapter 2, three different dual-axis quadrupole gradient coils for quantitative high resolution MR imaging of phantoms and specimens were designed and built using printed circuit board technology. Numerical optimization of the conductor positions was used to increase the volume of 0.4% gradient uniformity by up to a factor of four. In one coil, the volume of 5% gradient uniformity occupied 88% and 83% of the overall diameter and length of the coil, respectively. A systematic error of -0.5% in the wire placement was shown to cause a reduction in the volume of 0.4% gradient uniformity by a factor of two, although the region of 5% gradient uniformity was not significantly affected.

1.6.2 Gradient Coil Heating

Chapter 3 is based on the paper "MR gradient coil heat dissipation" by K.C. Chu (the author) and Dr. B.K. Rutt (supervisor), which appeared in *Magnetic Resonance in Medicine*, Volume 34, pages 125-132 in 1995. Most of the research was performed by the author. Dr. Rutt provided guidance to reorganize the theoretical equations to a sensible format.

In Chapter 3, the temperature responses of five different gradient coil designs were modeled using simplified engineering equations and verified through direct measurements. The model predicts that the coil temperature approaches a maximum as an inverse exponential function, and that the maximum temperature is governed by two parameters: a local power density and a cooling term. The

power density is a function of position and is highest where the current paths have minimum widths and are closely packed. The cooling parameter consists of convective, conductive, and radiative components which can be controlled by (1) providing forced cooling, (2) having a coil former with high thermal conductivity and thin walls, and (3) varying the emissivity of the coil surfaces.

For a given gradient strength, the *average* temperature rise is minimized by designing a coil with a small radius and thick copper. The coil temperature model predicted the *local* temperatures rise to within 5°C of the measured values.

1.6.3 Trichlorotrifluoroethane as a Pumping Fluid

Chapter 4 is based on the paper "Improved MR images of arterial specimens by submersion in trichlorotrifluoroethane" by K.C.Chu (the author), A.J.Martin (colleague), and B.K.Rutt (supervisor), which appeared in *Magnetic Resonance in Medicine*, Volume 35, pages 790-796 in 1996. Most of the research was performed by the author. Drs. A.J.Martin and B.K.Rutt provided guidance in understanding some of the implications of using 1,1,2-trichloro-1,2,2-trifluoroethane (also known as refrigerant R-113) with arterial specimens. J.Dunmore provided assistance with the histological portion of this work.

In Chapter 4, I show that MR images of ex-vivo arterial specimens surrounded with the fluid R-113 have improved signal-to-noise ratio (SNR) and contrast-to-noise ratio. R-113 has no hydrogen atoms, so it yields no proton signal; hence, the contrast between the specimen and its background is inherently maximized. SNR is maximized because (1) R-113 is non conductive so coil loading and inductive noise are minimized and (2) the volume susceptibility of R-113 closely matches that of water and tissue so that T_2^* effects are minimized.

Short term submersion of porcine aortas in R-113 was found to have no significant effect on the artery's hydration level, relaxation time, nor tensile strength. The structure and quantity of elastin, collagen and smooth muscle cells remain unchanged.

1.6.4 Polyvinyl Alcohol Cryogel

Chapter 5 is based on the paper "Polyvinyl alcohol cryogel: an ideal

phantom material for MR studies of arterial flow and elasticity" by K.C.Chu (the author) and B.K.Rutt (supervisor), which appeared in *Magnetic Resonance in Medicine*, Volume 37, pages 314-319 in 1997. All of the research was performed by the author. Dr. Rutt provided encouragement and freedom in the pursuit of an alternative material as the near perfect tissue mimic for medical imaging studies.

In this chapter, I present a unique application of polyvinyl alcohol (PVA) cryogel as an anthropomorphic, elastic, vascular phantom material that can be used in MR imaging. The composition consists of two non-toxic ingredients: water and PVA. The biomechanical and MR properties can be adjusted to be similar to those of excised porcine aortas by varying the number of freeze-thaw cycles of the PVA solution. I present the T_1 , T_2 , shrinkage, and tensile properties of PVA cryogel tubes as a function of freeze-thaw cycles. MR images of a dual elastic aortic phantom undergoing pulsatile motion are shown.

1.6.5 Stress-Strain Curves Extrapolated from Incremental Data

Chapter 6 is based on the two part paper "Stress-strain curves of arterial phantoms and arteries extrapolated from incremental data obtained from high resolution MRI" by K.C.Chu (the author) and B.K.Rutt (supervisor), which is being submitted to the *Journal of Biomechanics*. Most of the research was performed by the author. Dr. Rutt was instrumental in vastly improving my original MR software to provide DANTE tags in a fast gated gradient recalled echo pulse sequence. Dr. Rutt also helped to reorganize the theoretical equations in a more coherent format.

In Chapter 6, a two parameter exponential model is used to describe the stress-strain characteristics of arteries. A derivation is presented that permits the extrapolation of a full exponential arterial stress-strain curve from a limited amount of incremental stress-strain data. The method can be used to estimate the elastic modulus of arteries at different stress levels.

The method is proven using incremental tensile test data from arterial phantoms and porcine aortas. The elastic modulus can be estimated from incremental data using the extrapolation method with good accuracy ($\pm 28\%$) only for stress levels less than 75 kPa. At these same stress levels, the extrapolation

method is shown to be reasonably valid in estimating the exponential stiffness parameter α to $\pm 26\%$, which is reasonable given that there are biological variations in the aortic specimens. The errors are attributed to the limitations of using a single exponential model to fit the measured data.

The method is further demonstrated using a high resolution MR tagging method on two different elastic aortic phantoms where incremental elastic moduli reported by themselves can yield contradictory results. Only through local stress-strain measurements followed by the extrapolation method was it possible to obtain the full material stiffness properties (i.e. stress-strain curves) of the phantoms. This differs from previous authors who report multi-parameter models for describing the structural stiffness properties of arteries.^{17,58,59} A final demonstration of the extrapolation method using incremental data from MR images of pulsating porcine aortas resulted in full stress-strain curves similar to that obtained by direct tensile tests.

1.6.6 Summary and Future Applications

Chapter 7 summarizes the work described in this thesis and provides a discussion of recommendations for future applications of my work. The concept of gradient coil construction and cooling described in Chapters 2 and 3 has already been adapted to evaluate new MR gradient coil projects at the University of Western Ontario. The use of R-113 as a pumping fluid is fine for *in vitro* MR studies but cannot be used *in vivo*. The problem of flow artifacts for *in vivo* studies is addressed in Chapter 7. The introduction of the PVA cryogel (chapter 5) technology shows tremendous promise for medical researchers beyond being a phantom material. Finally our concept of extrapolating incremental elastic data to exponential stress strain curves is new and can be applied to any clinical imaging modality; its implications are described in Chapter 7.

1.7 References

1. J.E.Heiserman, The imaging evaluation of carotid arteriosclerosis, *Applied Radiology*, 30-40, November 1996.
 2. "Demographic Yearbook 1991, Special Issue: Population Aging and the Situation of Elderly Persons", United Nations, Department of Economics and Social Information and Policy Analysis, Statistical Division, 1993.
 3. R.Ross, The pathogenesis of atherosclerosis: a perspective for the 1990's, *Nature*, **362**, 801-809 (1993).
 4. N.J.Severs and H.Robenek, Constituents of the arterial wall and atherosclerotic plaque: an introduction to atherosclerosis, in "Cell Interactions in Atherosclerosis" (H.Robenek, N.J.Severs, Eds.), CRC Press, Boca Raton, 1992.
 5. J.F.Cornhill, M.R.Roach, Quantitative method for the evaluation of atherosclerotic lesions, *Atherosclerosis*, **20**, 131-136 (1974).
 6. C.J.Schwartz, A.J.Valente, E.A.Sprague, J.L.Kelley, R.M.Nerem, The pathogenesis of atherosclerosis: an overview, *Clinical Cardiology*, **14**, 1-1-16 (1991).
 7. Z.Lou, W.J.Yang, Biofluid dynamics at arterial bifurcations, *Critical Reviews in Biomedical Engineering*, **19**, 455-493 (1992).
 8. T.Asakura, T.Karino, Flow patterns and spatial distribution of atherosclerotic lesions in human coronary arteries, *Cir. Res.*, **66**, 1045-1066 (1990).
 9. M.H.Friedman, O.J.Peters, C.B.Bargeron, G.M.Hutchins, F.F.Mark, Shear dependent thickening of the human arterial intima, *Atherosclerosis*, **60**, 161-171 (1986).
 10. D.N.Ku, D.P.Giddens, C.K.Zaims, S.Glagov, Pulsatile flow atherosclerosis in the human carotid bifurcation: positive correlation between plaque localization and low and oscillating shear stress, *Arteriosclerosis*, **5**, 293-302 (1985).
 11. W.R.Milnor. "Hemodynamics", 2nd Ed., Williams & Wilkins, Baltimore, 1989.
 12. M.H.Sherebrin, H.A.Bernans, M.R.Roach, Extensibility changes of calcified soft tissue strips from human aorta, *Can. J. Physiol. Pharmacol.*, **65**, 1878-1883 (1987).
-

13. E.Falk, Why do plaques rupture?, *Circulation*, **86** (suppl. III), III-30 - III-42 (1992).
 14. M.R.Roach, A.C.Burton, The effect of age on the elasticity of human iliac arteries, *Can. J. Biochem. Physiol.*, **37**, 557-570 (1959).
 15. R.H.Mohiaddin, S.R.Underwood, H.G.Bogren, D.N.Firmin, R.H.Klipstein, R.S.O.Rees, D.B.Longmore, Regional aortic compliance studied by magnetic resonance imaging: the effects of age, training, and coronary artery disease, *Br. Heart J.*, **62**, 90-96 (1989).
 16. Y.C.Fung, "Biomechanics: Mechanical Properties of Living Tissues", 2nd Ed., Springer-Verlag, New York, 1993.
 17. K.Hayashi, Experimental approaches on measuring the mechanical properties and constitutive laws of arterial walls, *Journal of Biomechanical Engineering*, **115**, 481-488 (1993).
 18. Standard test method for tensile properties of plastics (metric), in "Annual Book of ASTM Standards", Vol 08.01, ASTM D 638M-91a, American Society for Testing and Materials, Philadelphia, 1993.
 19. Y.C.B.Fung, Elasticity of soft tissues in simple elongation, *American Journal of Physiology*, **213**, 1532-1544 (1967).
 20. D.H.Touw, M.H.Sherebin, and M.R.Roach, The elastic properties of canine abdominal aorta at its branches, *Can. J. Physiol. Pharmacol*, **63**, 1378-1383 (1985).
 21. C.M.He, M.R.Roach, The composition and mechanical properties of abdominal aorta aneurysms, *Journal of Vascular Surgery*, **20**, 6-13 (1994).
 22. L.H.Peterson, R.E.Jensen, and J.Parnell, Mechanical properties of arteries in vivo, *Circulation Research*, **8**, 622-639 (1960).
 23. B.S.Gow, C.D.Hadfield, The elasticity of canine and human coronary arteries with reference to postmortem changes, *Circulation Research*, **45**, 588-594 (1979).
 24. D.J.Patel, F.M.De Freitas, J.C.Greenfield Jr.,D.L.Fry, Relationship of radius to pressure along the aorta in living dogs, *J. Appl. Physiol.*, **18**, 1111-1117 (1963).
 25. R.H.Cox, Passive mechanics and connective tissue composition of canine arteries, **234**, H533-H541, *Am. J. Physiol.* (1978).
-

26. T.Imura, K.Yamamoto, T.Satoh, K.Kanamori, T.Mikami, H.Yasuda, In vivo viscoelastic behaviour in human aorta, *Circulation Research*, **66**, 1412-1419 (1990).
 27. T.E.Carew, R.N.Vaishnav, D.J.Patel, Compressibility of the artery wall, *Circulation Research*, **23**, 61-68 (July 1968).
 28. D.H.Bergel, The static elastic properties of the arterial wall, *J.Physiol*, **156**, 445-457 (1961).
 29. M.Drangova, "Computed Tomography Scanner for Dynamic Vascular Imaging In Vitro", Ph.D. Thesis, University of Western Ontario, 1993.
 30. M.Drangova, D.W.Holdsworth, C.J.Boyd, P.J.Dunmore, M.R.Roach, A.Fenster, Elasticity and geometry measurements of vascular specimens using a high-resolution laboratory CT scanner, *Physiological Measurement*, **14**, 277-90 (1993).
 31. C.J.Boyd, M.R.Roach, M.H.Sherebrin, R.N.Rankin, and A.Fenster, Demonstration of the need for the inclusion of parameter correlations in error estimation for non-linear curve fitting, *Med. & Biol. Eng. & Comput.*, **32**, 221-224 (1994).
 32. D.H.Evans, W.N.McDicken, R.Skidmore, J.P.Woodcock, "Doppler Ultrasound: Physics, Instrument, and Clinical Applications", pp.262-263, Wiley, Toronto, 1989.
 33. F.W.Kremkau, "Doppler Ultrasound Principles and Instruments", 2nd Ed., pg. 21, *W.B.Saunders*, Toronto, 1995.
 34. W.N.McDicken, "Diagnostic Ultrasonics: Principles and Use of Instruments", 2nd Ed., pp. 237-238, John Wiley & Sons, Toronto, 1981.
 35. Y.Tardy, J.J.Meister, F.Perret, H.R.Brunner, and M.Arditi, Non-invasive estimate of the mechanical properties of peripheral arteries from ultrasonic and photoplethysmographic measurements, *Clin. Phys. Physiol. Meas.*, **12**, 39-54 (1991).
 36. A.P.G.Hoeks, P.J.Brands, F.A.M.Smeets and R.S.Reneman, Assessment of the distensibility of superficial arteries, *Ultrasound in Med. & Bio.*, **16**, 121-128 (1990).
 37. C.A.Mistretta, A.B.Crummy, C.M.Strother, Digital angiography: a perspective, *Radiology*, **139**, 273-276 (1981).
-

38. D.W.Holdsworth, "A TDI-CCD System For Slot-Scanned Digital Radiography and Computer Tomography", Ph.D.Thesis, University of Toronto, 1992.
39. D.A.McDonald, Regional pulse-wave velocity in the arterial tree, *J.Appl. Physiol.*, **24**, 73-78 (1978).
40. S.N.Urchuk, D.B.Plewes, A velocity correlation method for measuring vascular compliance using MR imaging, *JMRI*, **5**, 628-634 (1995).
41. R.B.Hickler, Aortic and large artery stiffness: current methodology and clinical correlations, *Clin. Cardiol.*, **13**, 317-322 (1990).
42. D.H.Bergel, The dynamic elastic properties of the arterial wall, *J.Physiol.*, **156**, 458-469 (1961).
43. A.Lingamneni, P.A.Hardy, K.A.Powell, N.J.Pelc, R.D.White, Validation of cine phase-contrast MR imaging for motion analysis, *J. Magn. Resonance Imaging*, **5**, 331-338 (1995).
44. N.J.Pelc, M.Drangova, L.R.Pelc, Y.Zhu, D.C.Noll, B.S.Bowman, R.J.Herfkens, Tracking of cyclic motion with phase-contrast cine MR velocity data, *Journal of Magnetic Resonance Imaging*, **5**, 339-345 (1995).
45. J.N.Oshinski, D.N.Ku, S.Mukundan, F.Loeh, R.I.Pettigrew, Determination of wall shear stress in the aorta using MR phase velocity mapping, *JMRI*, **5**, 640-647 (1995).
46. P.Vinee, B.Meurer, A.Constantinesco, B.Kohlberger, K.Hauenstein, S.Petkov, Proton magnetic resonance relaxation times and biomechanical properties of human vascular wall: in vitro study at 4 MHz, *Invest. Radiol.*, **27**, 510-514 (1992).
47. A.Constantinesco, P.Gries, P.Vinee, B.Heckert, P.Carlier, In vitro 4 Mhz NMR proton relaxation times and in vitro mechanical behaviour at low extension of human common carotid arterial wall, *Magnetic Resonance Imaging*, **7**, 173-177 (1989).
48. L.Axel, L.Dougherty, MR imaging of motion with spatial modulation of magnetization, *Radiology*, **171**, 841-845 (1989).
49. J.L.Prince, E.R.McVeigh, Motion estimation from tagged MR image sequences, *IEEE transactions on Medical Imaging*, **11**, 238-249 (1992).
50. A.A.Young, L.Axel, L.Dougherty, D.K.Bogen, C.S.Parenteau, Validation of tagging with MR imaging to estimate material deformation, *Radiology*, **188**, 101-108 (1993).

51. T.J.Mosher, M.B.Smith, A DANTE tagging sequence for the evaluation of translational sample motion, *Mag. Res. Med.*, **15**, 334-339 (1990).
 52. P.Sprawls and M.J.Bronskill, Eds., "The Physics of MRI: 1992 AAPM Summer School Proceedings", American Institute of Physics, Woodbury, NY 1993.
 53. S.C.Bushong, "Magnetic Resonance Imaging: Physical and Biological Principles", *C.V. Mosby*, Toronto, 1988.
 54. L.E.Crooks, Image formation methods, *in* "Encyclopedia of Nuclear Magnetic Resonance", (D.M.Grant and R.K.Harris, Eds.), John Wiley & Sons, Toronto, 1996.
 55. D.B.Twieg, The k-trajectory formulation of the NMR imaging process with applications in analysis and synthesis of imaging methods, *Med. Phys.*, **10**, 610-621 (1983).
 56. M.L.Lauzon, B.K.Rutt, Generalized k-space analysis and correction of motion effects in MR imaging, *Magnetic Resonance in Medicine*, **30**, 438-446 (1993).
 57. J.Pauly, D.Nishimura, A.Macovski, A k-space analysis of small tip-angle excitation, *Journal of Magnetic Resonance*, **81**, 43-56 (1989).
 58. G.J.Langewouters, K.H.Wesseling, W.J.A.Goedhard, The static elastic properties of 45 human thoracic and 20 abdominal aortas in vitro and the parameters of a new model, *J.Biomechanics*, **17**, 425-435 (1984).
 59. F.Hansen, P.Mangell, B.Sonesson, T.Lanne, Diameter and compliance in the human common carotid artery - variations with age and sex, *Ultrasound in Med. & Biol.*, **21**, 1-9 (1995).
-

CHAPTER 2 GRADIENT COIL DESIGN AND EVALUATION

2.1 Introduction

Proper gradient coil design is vital in MR imaging. Parameters such as the efficiency, inductance and resistance of the gradient coil govern maximum gradient strength, transient characteristics, heat generation, and scan speed (duty cycle). The overall gradient strength directly affects the maximum spatial, velocity and diffusion resolution in images. A high degree of gradient accuracy and uniformity is desirable when accurate quantitative measurements are required. In such applications, the use of image warping algorithms to correct for gradient imperfections may be undesirable, as these may distort quantitative measurements. In an image with 256x256 pixels, the gradient uniformity should provide less than 1/256 or 0.4% deviation across the field of view in order that image warping algorithms not be needed to correct for spatial distortions.

The importance of not requiring the application of image warping algorithms cannot be over-emphasized. For example, the acquisition of MR images from custom gradient coils attached to clinical scanners is simplified because no post-processing is required. Since MR imaging is a 3-D process (i.e. dependent on all three gradients coils), any post-processing will be more complex than a just applying a simple 2-D warping algorithm. In addition, by having good gradient uniformity, quantitative phase contrast images can be obtained from the clinical imager without any need for corrections.

One type of cylindrical gradient coil that has a large region of uniformity and high gradient efficiency is the quadrupole design.^{1,2,3} In this design, a perfectly linear gradient field is produced on the interior of an infinitely long cylinder by a continuous current distribution oriented parallel to the cylinder axis and proportional to $\cos(2\theta)$, where θ is the azimuthal angle.¹ In practice, this current distribution is approximated by winding discrete wires and the volume of uniformity is reduced. Further loss in uniformity arises from any inaccuracies in the exact winding position. Traditionally, construction of gradient coils has involved winding wires into grooves cut into an insulating former.^{2,4,5,6} The disadvantage of this method is

that the milling of the grooves and the winding of the wires is often laborious and time consuming. In addition, complicated wire designs are almost impossible to fabricate without numerically controlled milling machines.

These issues were resolved by developing a *simple* design and fabrication technique for quadrupole gradient coils. The technique positions each wire using numerical optimization and a printed circuit (PC) board approach. With this method, researchers can design and construct a high strength dual-axis (X-Z or Y-Z) quadrupole gradient coil set within a few hours. The PC board method can be used to create complicated wire patterns that are tedious or expensive to build by winding wires.

Because the quadrupole coil axis must be placed transverse to the main magnetic field axis, this design is ideal for researchers who have access to clinical MR scanners but wish to perform high resolution imaging of small animals, in-vitro specimens, or phantoms. Although these coils are not well suited for full body imaging in conventional MR imagers, they have potential application in imaging systems in which the main magnetic field is naturally oriented orthogonal to the long axis of the body.

In this chapter the characteristics of three quadrupole coils constructed using the PC board method are described. Numerical optimization of wire positions was used in two of these designs to improve the region of gradient uniformity. Gradient field calculations are shown for each coil. The effect of a 0.5% error in the wire positions is shown by simulation and experiment for the third coil. Finally, coil properties from all three coils are presented, and images from one of the coils are shown.

2.2 Methods

2.2.1 Design

One quadrupole design evaluated was based on Webster's recommendation² of three wire clusters at 22.5°, 45° and 67.5° azimuthal angle in each quadrant with relative current densities of 7, 10, and 7, respectively. Two other designs discretely sampled the $\cos(2\theta)$ current distribution by varying the

placement of each individual wire. The angle of each wire was calculated iteratively (see Fig. 2.1) by solving for θ_i and $\Delta\theta_i$ in Eq. 2.1:

$$\cos(2\theta_i) = \frac{c}{\Delta\theta_i} \tag{2.1}$$

$$\theta_i = \theta_{i-1} + \frac{\Delta\theta_{i-1}}{2} + \frac{\Delta\theta_i}{2}$$

where θ_i is the angular position of the i^{th} wire, $(\Delta\theta_{i-1} + \Delta\theta_i)/2$ is the angle between the centre positions of the θ_{i-1}^{th} and θ_i^{th} wires, c = constant of proportionality, $\Delta\theta_i = (\text{wire width} + \text{wire gap})/(\text{coil radius})$ and $\theta_1 = \Delta\theta_1/2$ is the position of the first wire. My method of determining θ_i differs from that of Bolinger⁷ in the incorporation of constraints imposed by the finite wire width and wire gap and the implicit maximization of the total number of wires given these constraints.

Double-sided 71 μm (2 oz.) thick copper PC boards were used with a minimum spacing between tracings of 0.38 mm. Using these dimensions, the fusing current, I_{max} (applied for 20 ms), for flat copper conductors could be estimated.⁸ To maintain a good margin of safety so that the copper does not melt, my *maximum* operating current never exceeded $I_{\text{max}}/20$. However, if one were to consider the maximum temperature rise in continuous current applications, a safe limit for the *mean* current that can be applied with no forced cooling is approximately $I_{\text{max}}/200$. Chapter 3 describes a mathematical model that accurately predicts the temperature rise in gradient coils.

2.2.2 Field Calculations

Given the precise location of each wire, an accurate representation of the magnetic field, B_z (i.e. the component parallel to the main magnetic field) was determined by integration of the Biot-Savart law⁶ along a straight wire at each of the locations θ_i . A B_z field map for the gradient coil was produced for the central transverse plane⁶ and the central longitudinal plane by summation of the B_z contributions from all wires. The gradient field was estimated numerically using finite differences. Contour plots of the gradient uniformity show the $\pm 0.4, 5, 10$, and

25% deviation from the central value. The magnetic field contribution from the return paths (i.e. the wires connecting different longitudinal wires in the quadrupole design) were also included, though to simplify calculations, they were assumed to be straight wires rather than arcs. In making this approximation, the maximum error in the gradient mean and variance over a square ROI with sides equal to the radius in any transverse plane within the coil was less than 0.04%.

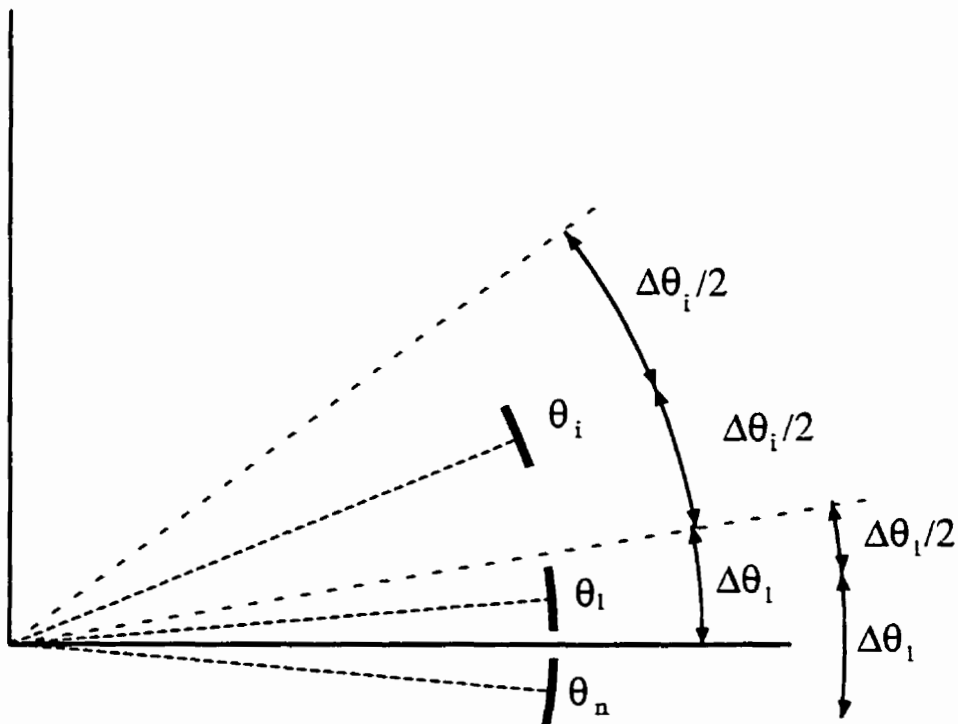


Figure 2.1. The azimuthal angles of the 1st and ith wires are shown for calculating the $\cos(2\theta)$ current distribution. The conducting paths are shown as thick bars \blacksquare .

2.2.3 Numerical Optimization of Wire Positions

Because of the physical limitations (finite number of wires and finite width) in PC board construction, it was not possible to provide a perfect $\cos(2\theta)$ current distribution on a cylindrical surface. However, it was possible to optimize⁹ the angular positions of a finite set of wires to maximize the volume over which gradient uniformity was better than 0.4%. The optimum wire angles were numerically determined using the constrained minimization routine in the MATLAB Optimization Toolbox.¹⁰ This minimization technique was based on a sequential (i.e. recursive) quadratic programming method¹¹ where the general problem is reformulated into a quadratic approximation of the Lagrangian function which is solved numerically. The initial starting points for the optimization were obtained from the Webster² design or from Eq. 2.1. The standard error of the mean gradient field over either a square or circular region in the central transverse plane was chosen as the cost function to be minimized.

2.2.4 Construction

Three different dual axis quadrupole gradient coil sets (9.5 cm dia. x 25cm long) were constructed. The first design was the design proposed by Webster² with 1.24 mm wide conductor traces; the second and third designs both sampled the $\cos(2\theta)$ current distribution, as described in Eq. 2.1, with 0.62 and 4.38 mm wide conductor traces which resulted in a maximum of 192 and 16 wires, respectively. The final wire positions for the second and third designs were numerically optimized. The coordinates of these wires were plotted onto paper from which two negatives were made. These negatives, with a 45° azimuthal offset from each other, were used to photosensitize Y and Z gradient coils onto opposite sides of a double sided PC board. The PC board was developed and etched, leaving the wire tracings precisely at the desired locations. Figs. 2.2a, b and c show the circuit board designs for each of the coils designs. After the PC board was glued onto the circumference of an acrylic cylinder, it was mounted in the X-direction of a whole

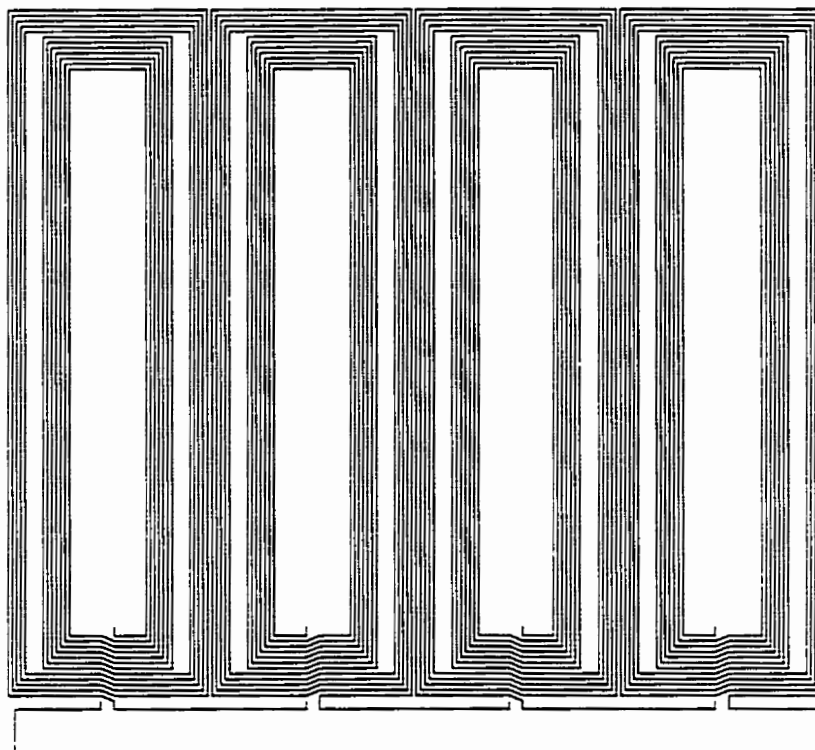


Figure 2.2a. The PC board design for the 96 wire Webster² design. The horizontal axis is the azimuthal direction, and the vertical axis is the longitudinal direction of the coil.

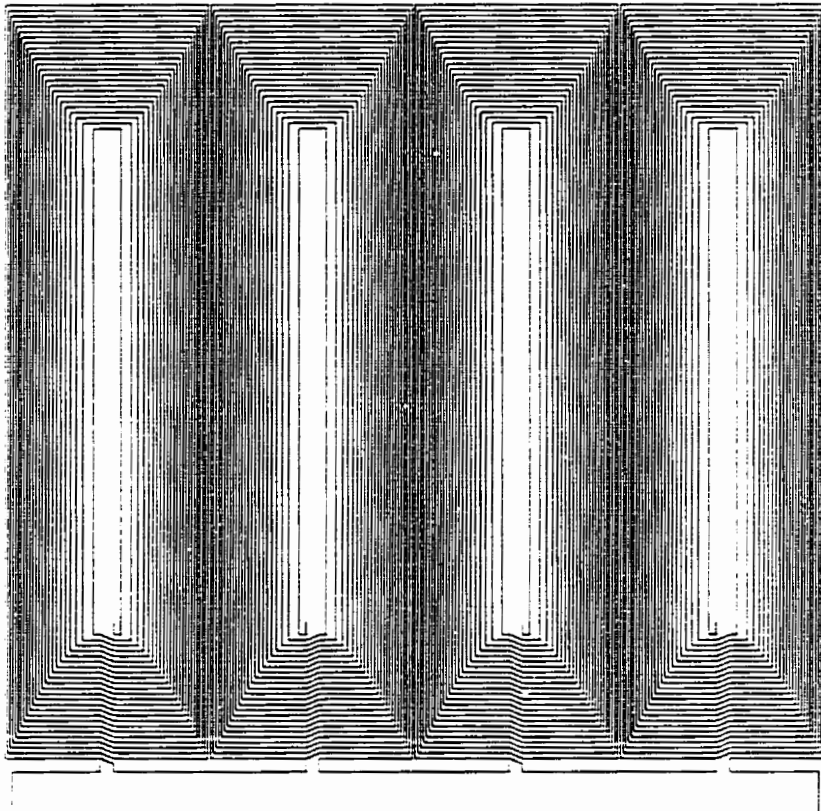


Figure 2.2b. The PC board design for the optimized 192 wire design. The horizontal axis is the azimuthal direction, and the vertical axis is the longitudinal direction of the coil.

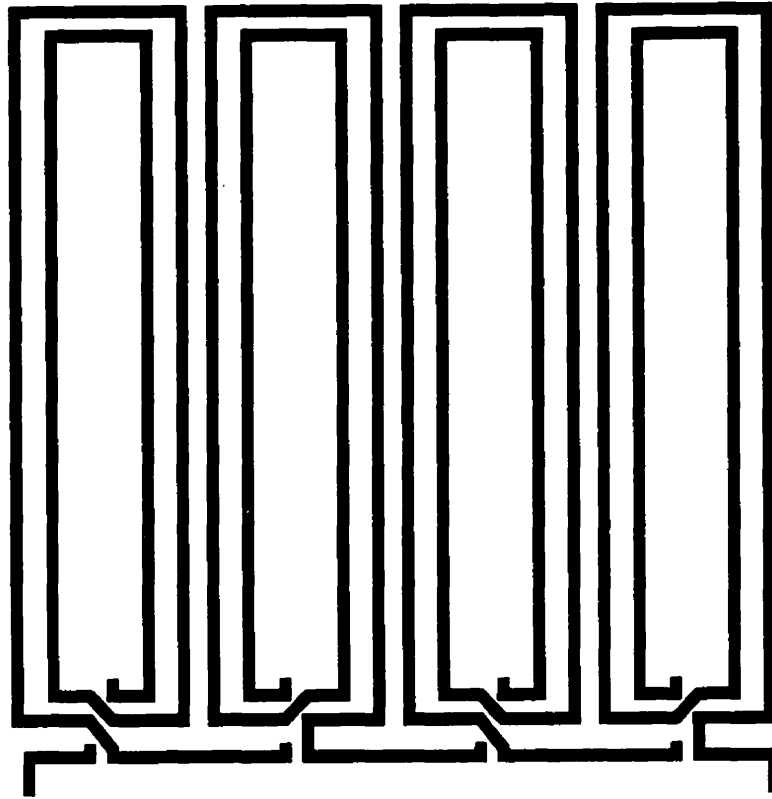


Figure 2.2c. The PCB board design for the optimized 16 wire optimized design. The horizontal axis is the azimuthal direction, and the vertical axis is the longitudinal direction of the coil.

body GE Signa scanner. *Special precautions were taken to guard against the dangers of electric shock during installation and motion of the coil during imaging.* To compare the measured gradient strength and uniformity to the theoretical values, a square phantom (44.7 mm side) with cartesian channels (1.59 mm wide and 3.30 mm centre to centre) milled into its plane was filled with CuSO_4 solution and placed inside a single turn 7.0 cm diameter x 11.1 cm long transmit/receive coil. Images from spin echo sequences showed the relative gradient uniformity.

2.3 Results

Table 2.1 summarizes the properties of the three coils. The measured inductances (at 1 kHz) and resistances were obtained from a HP 4262A LCR meter, and were within 7 μH and 2 Ω of the theoretical values,^{12,13} respectively. My inductance calculations included the self and mutual inductances of the main wires as well as the return wires (which were assumed to be straight). The gradient strength was determined by varying the current to each of the coils and comparing the measured dimensions in the MR image with the actual overall size of the square phantom. The theoretical gradient strengths from my field calculations were within 2.5% of the measured values. Since the three coil designs described in this chapter had equal dimensions, and the wire angles were near optimum, the coil gradient efficiencies were found to be approximately proportional to the number of windings ($6.77 \times 10^{-3} \text{ Gcm}^{-1} \text{A}^{-1} \text{winding}^{-1}$). A gradient strength of 4 G/cm could be easily obtained in each of the coils to produce a resolution of 78 $\mu\text{m}/\text{pixel}$ from a 2 cm FOV image (256x256, 16 kHz bandwidth).

A measure of the gradient uniformity was derived from the calculated field maps by measuring the minimum distance between the 0.4 or 5% deviation contours from the longitudinal and transverse uniformity plots. All results are presented as a percentage of coil length or diameter. Images of my square grid phantom (Fig. 2.5) confirmed that the gradient uniformity in the central plane covered at least the area of the phantom by producing straight grid lines to within 1 pixel.

Figs. 2.3a, b, and c show example maps of the gradient uniformity from the

96 wire Webster² design, the optimized 192 wire design, and the optimized 16 wire design. Fig. 2.3d is a longitudinal field plot for the 16 wire design. A high resolution (2 cm FOV) fast spin echo MR image of an excised human iliac artery using the optimized 16 wire coil is shown in Fig. 2.4. Figs. 2.5a and b show the transverse field plot and corresponding square phantom imaged using the Webster² coil design. When the wires in the Z gradient are misplaced by a factor of 0.995, the field plot and image are distorted as shown in Figs. 2.5c and d.

2.4 Discussion

2.4.1 Gradient Uniformity

The contour plots of the transverse gradient uniformity (Fig. 2.3) show that the size of the regions with better than 0.4% and 5% uniformity can be significantly improved using numerical optimization of the wire positions. In Fig. 2.3a, the Webster² design was approximated by placing the 3 clusters of wires as close as physically possible to the 22.5°, 45.0° and 67.5° positions using the PC board method. In the ideal situation, where each wire is infinitely thin, my results would approach those reported by Webster.² Although not shown, numerical optimization of the angles in Fig. 2.3a would increase the region of 0.4% and 5.0% gradient uniformity to 71% and 78% of the coil diameter. This compares well with more traditional gradient coil designs where the ROI with better than 5% deviation is typically 70% of the diameter.¹⁴

Even by using as few as 16 wires, numerical optimization will produce a region of 0.4 and 5.0 % gradient uniformity as large as 49 and 63% of the diameter. By using 192 wires, these regions increase to 77 and 88% of the coil diameter, respectively. Depending on its application, the designer must balance the number of wires with inductance, gradient strength, gradient rise time, and current carrying capacity. In using Eq. 2.1 without numerical optimization, the region of gradient uniformity is highly dependent on the total number of wires used to sample the $\cos(2\theta)$ current distribution, and at least 40 wires are needed to obtain a gradient uniformity similar to that in Fig. 2.3a. Increasing the number of wires

Table 2.1. Properties of 3 different quadrupole gradient coils designs.

Coil Design	Webster ²	Cos(2 θ) Optimized	Cos(2 θ) Optimized
Total Number of Wires	96	192	16
Wire Width (mm)	1.24	0.62	4.38
20 ms Fusing Current I_{\max} : copper [solder] (A)	180 [99]	90 [49]	639 [351]
Inductance: measured [theoretical] (μ H)	150 [157]	580 [580]	6.3 [6.0]
Resistance: measured [theoretical] (Ω)	6.7 [4.7]	25 [23]	0.5 [0.3]
Time Constant τ (μ s)	22	23	13
0.4% [5%] Transverse Uniformity (% of total diameter)	36 [70]	78 [88]	49 [63]
0.4% [5%] Longitudinal Uniformity (% of length)	29 [83]	29 [83]	29 [82]
Gradient Efficiency: measured [theoretical] ($\text{Gcm}^{-1}\text{A}^{-1}$)	0.69 [0.68]	1.30 [1.3]	0.12 [0.12]

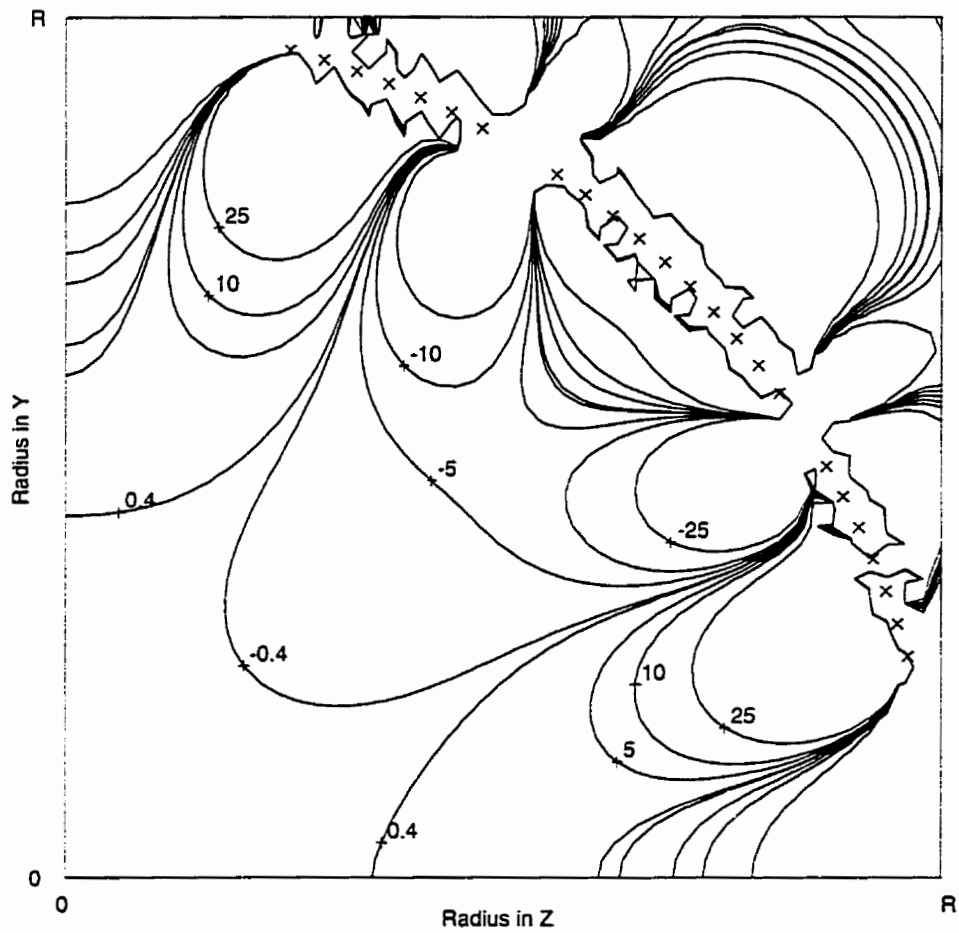


Figure 2.3a Contour plot of one quadrant of the central transverse gradient uniformity in units of % deviation from the central value for (a) the 96 wire Webster² design. Wire positions are indicated by 'x'.

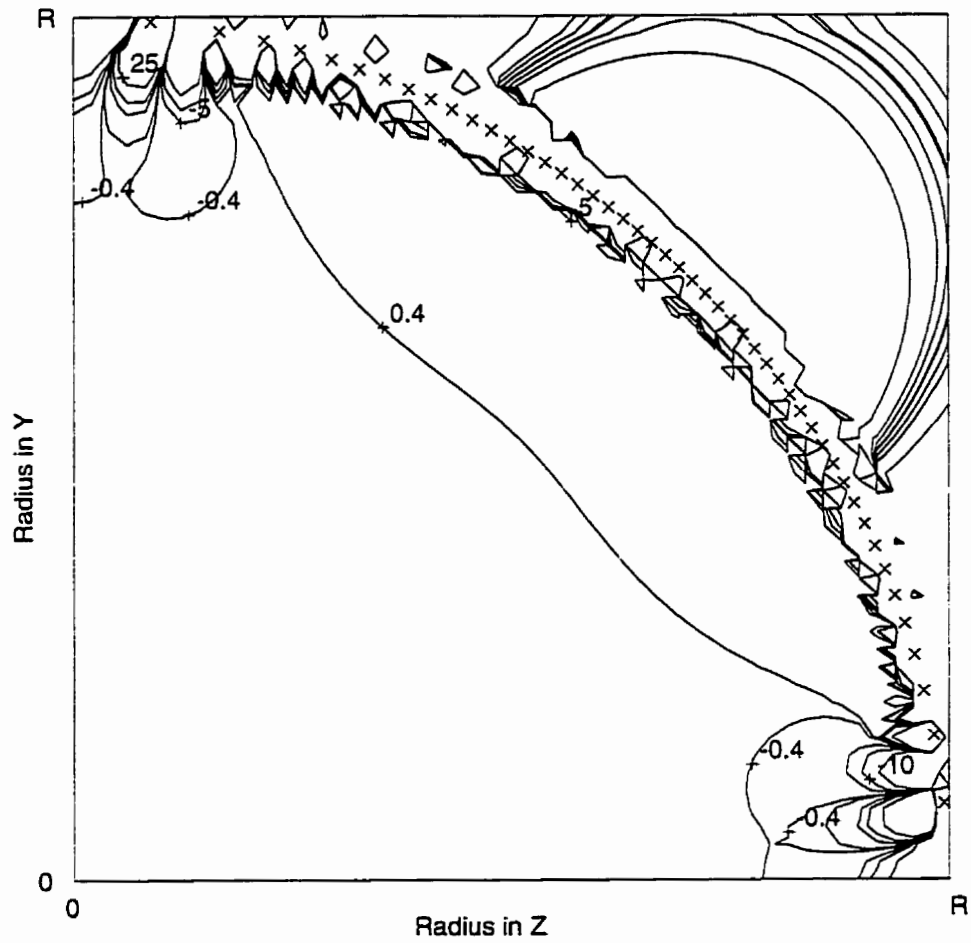


Figure 2.3b Contour plot of a quadrant of the central transverse gradient uniformity in units of % deviation from the central value for the optimized 192 wire design with the cost function calculated for a square region with side equal to the radius.

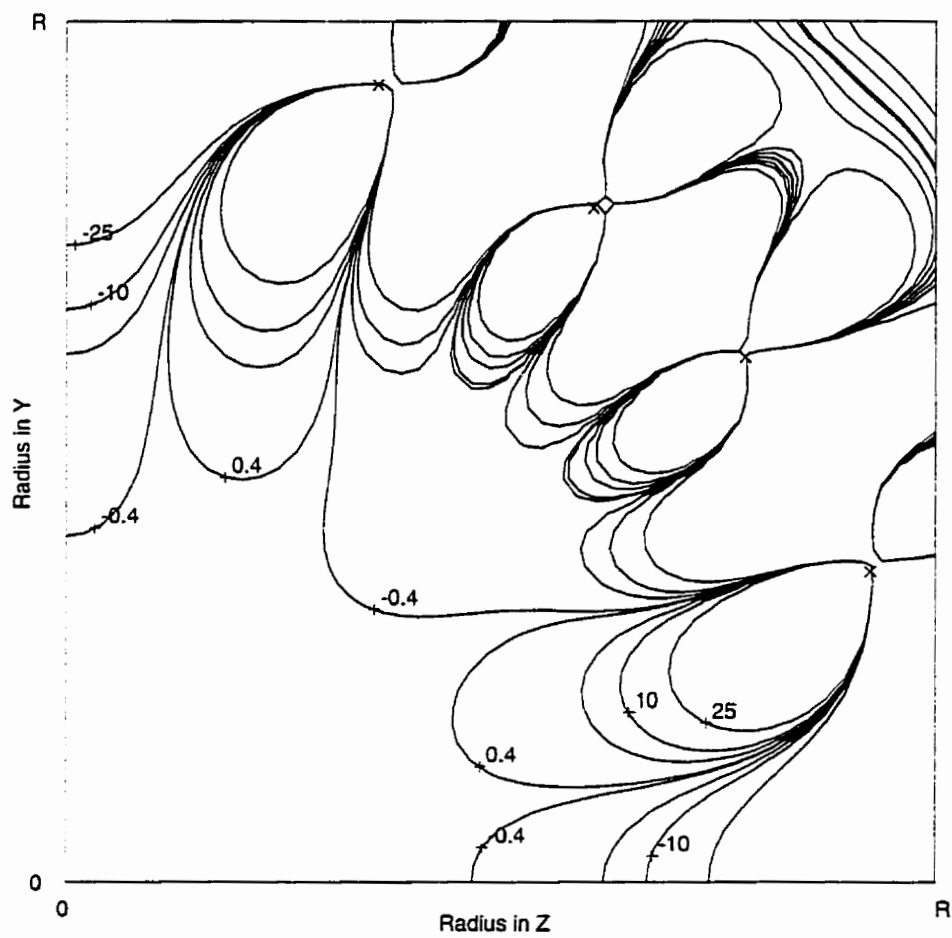


Figure 2.3c Contour plot of one quadrant of the central transverse gradient uniformity in units of % deviation from the central value for the optimized 16 wire design with the cost function calculated for a square region with side equal to the radius. Wire positions are indicated by 'x'.

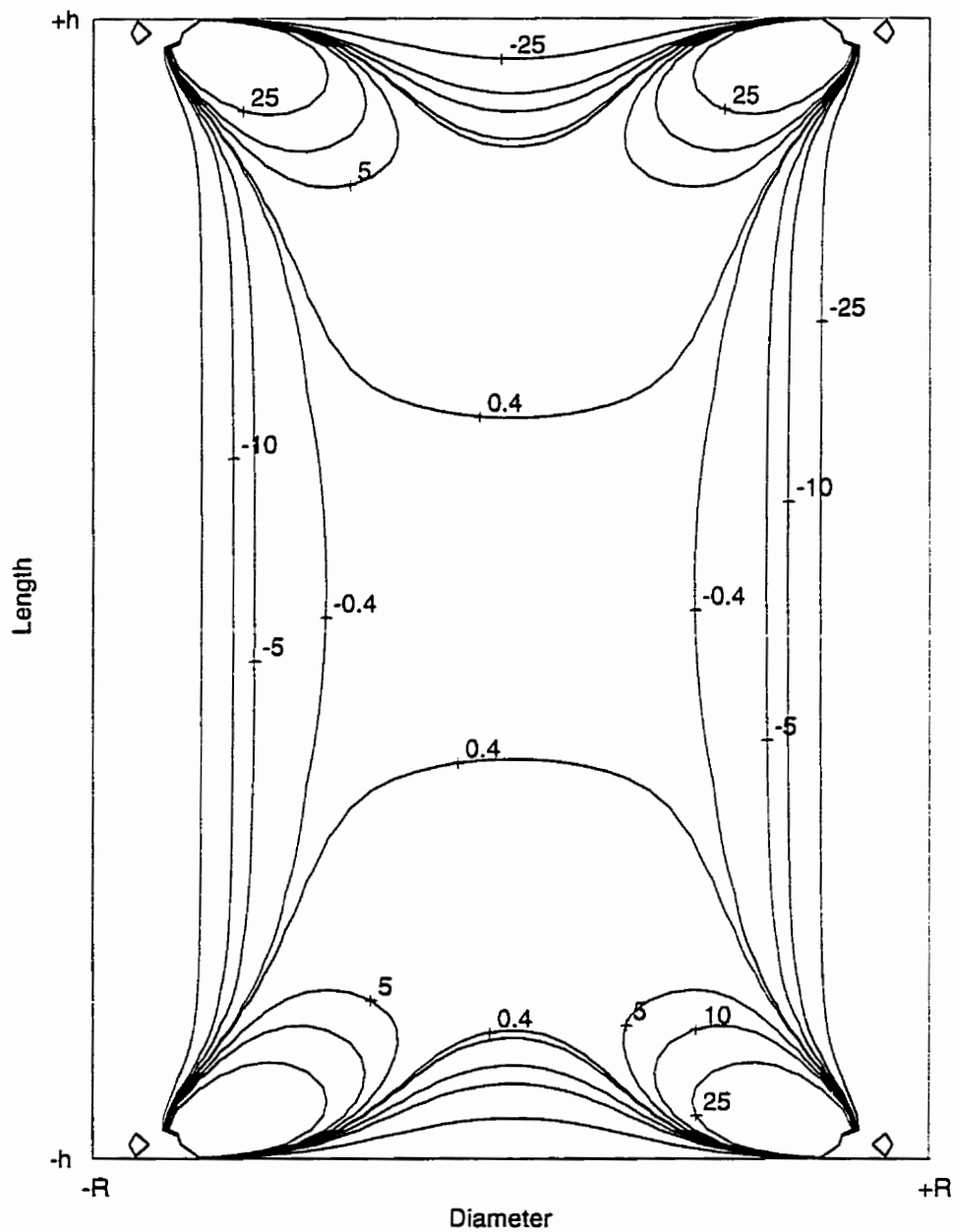


Figure 2.3d Longitudinal contour plot of the gradient uniformity for the central plane of the optimized 16 wire design.



Figure 2.4. Two MR images (2 cm FOV) of a human iliac artery (ex-vivo) using the 16 wire gradient coil.

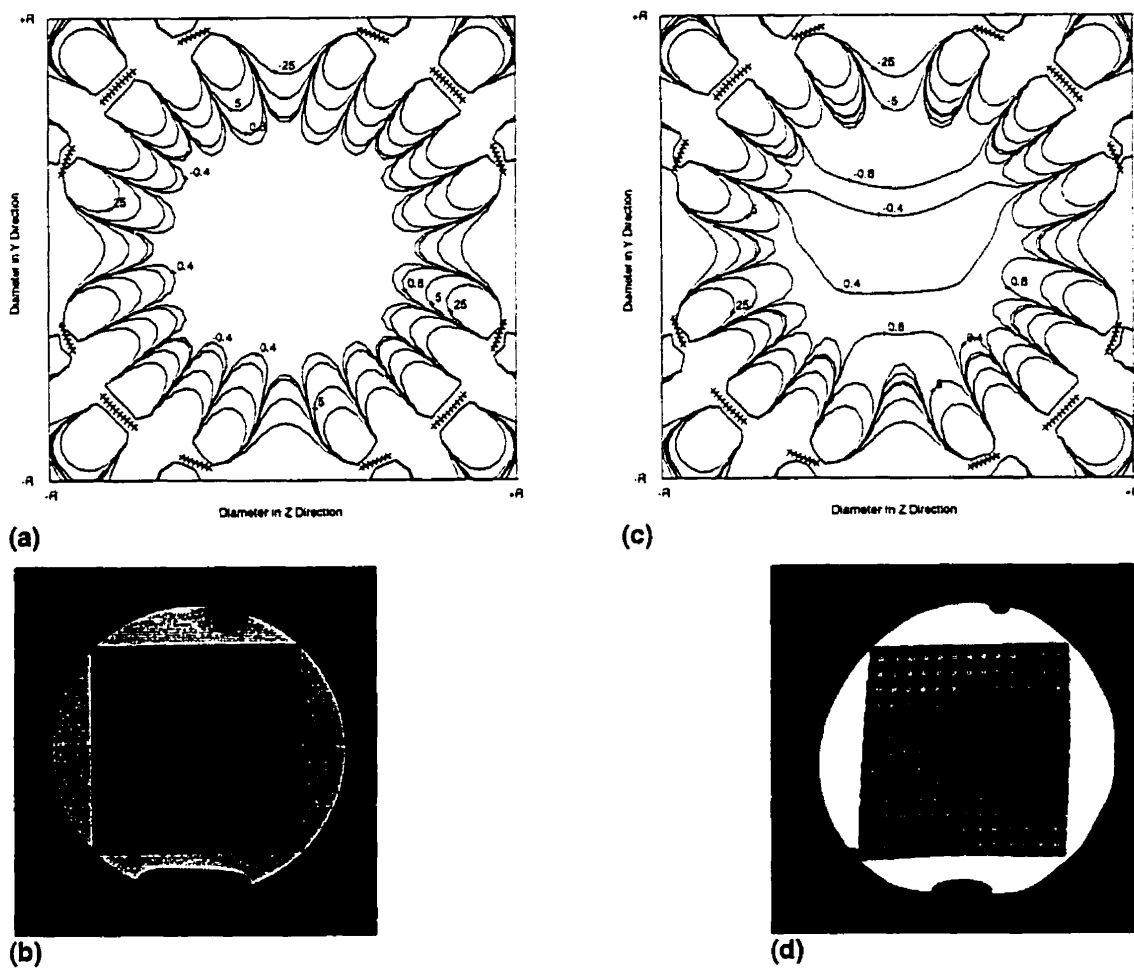


Figure 2.5. Contour plot of the central transverse gradient uniformity (a) and an image of a 4.47 cm square grid phantom (b) using the Webster² coil. (c) and (d) are the corresponding plot and image when each of the wire angles in the Z gradient are shifted by a factor of 0.995. When the gradient uniformity is not within $\pm 0.4\%$ (i.e. ± 1 pixel in 256) images will appear distorted (d) and will require warp correction algorithms.

increases the gradient uniformity at the cost of increasing the inductance. For a fixed inductance, the gradient uniformity is improved through optimization of the wire positions.

There is no guarantee that any numerical optimization method will find the global minimum. The chosen numerical optimization technique finds one of many local minima satisfying the cost function. It was observed that the initial wire locations, as well as the size and shape of the cost function region, influences the final wire positions. However, the size and shape of the region of 0.4% gradient uniformity does not change significantly; therefore, finding the global minimum will not produce a significantly larger region of gradient uniformity.

Independent of wire location and number of wires, the longitudinal uniformity is limited by the overall wire length. As shown in Table 2.1, the 0.4% and 5% deviation contours for all designs are 29% and 83% of the overall coil length, respectively.

To compare gradient efficiency of the quadrupole design with a more conventional design, I have theoretically modelled an optimized 96 wire quadrupole coil with overall dimensions (66 cm dia., 132 cm length) and inductance (1000 μH) similar to the transverse gradient coil on a GE Signa. The quadrupole coil gradient efficiency was found to be $0.0143 \text{ Gcm}^{-1}\text{A}^{-1}$ with a region of 0.4% (and 5%) gradient uniformity covering 72% (and 78%) of the diameter and 33% (and 83%) of the length, which compares favourably with the GE gradient coil design.

Using the PC board method, the most common type of manufacturing error would be making the PC board too short due to mis-accounting for the space necessary for gluing the coil or too long due to an undersized former. The effect of these errors was investigated by simulating and constructing a coil with an intentional systematic error in wire placement of -0.5%. Fig. 2.5c is the central transverse gradient deviation contour plot of such a coil. Fig. 2.5d is an MR image of a square grid phantom with the Z gradient constructed with the angles shifted by a factor of 0.995. Theoretical analysis shows that this small error in the wire positioning during construction will reduce the region of 0.4% gradient uniformity

by more than a factor of 2.

2.4.2 Implementation

Gradient coil optimization often includes a minimum inductance constraint¹⁴ which could have been added to the optimization program; however this was not necessary for these small diameter gradient coils. Instead, I report the measured and calculated inductances (L) and resistances (R) in Table 2.1. Using a first order resistance-inductance circuit model,^{6,15} an ideal voltage step of amplitude V_s produces a current response $I(t) = V_s (1 - \exp(-t/\tau)) / R$. The time constant, $\tau = L/R$, is the time it takes the gradient coil current to reach 63% of full strength (assuming a constant applied voltage) and governs the rate at which the gradients can switch on and off. The initial rate of current increase at time $t=0$ is $dI(0)/dt = V_s/L$, and can be increased by applying higher voltages during gradient ramping. In each of the quadrupole designs, τ was a factor of at least 85 times less than the existing whole body GE Signa gradient coils, resulting in a theoretical switching time that is shorter by the same factor. The 192 wire coil achieved a decreased τ by an increase in R, which is not desirable as it causes the coil heat loading (power= I^2R) to increase proportionally. The 16 wire design achieved fast rise times through a decrease in L compared to the GE Signa whole body coil.

It is important to know the inductance and resistance values for each design so that the compensation networks in the gradient amplifiers can be matched to the new gradient coils. *A mismatch in the compensation values could cause the amplifier to oscillate.* It is recommended that the amplifier manufacturer be contacted to confirm compatibility.

The theoretical copper fusing current in Table 2.1 is the current at which a 20 ms applied current pulse will melt the copper tracing. Since the limiting factor of coil integrity can also be the 185°C melting point of solder, its fusing current is also included.

In addition to the fusing current, it is also important to determine the root mean squared current, I_{rms} that can be continuously applied to the coil without exceeding a wire temperature of 185°C. This topic is addressed in the next

chapter, where I theoretically derive the governing equations that calculates the maximum gradient coil temperature based on how the gradient coil is cooled.

2.5 Summary

I have developed a simple technique for accurately constructing a dual axis quadrupole gradient coil set. By numerical optimization of the wire angles, one can improve the volume of gradient uniformity for MR imaging. With 192 wires, an optimized design showed the size of the 0.4% uniformity volume to be 78% in diameter by 29% in length. This 0.4% uniformity volume is a factor of 4.7 larger than the Webster² quadrupole design.

The effect of imprecision of wire placement was investigated by comparing computer simulation with an image made from a coil constructed with a small error. Theoretical analysis shows that an error of -0.5% in all of the wire positions during construction will asymmetrically reduce the volume of 0.4% gradient uniformity by half.

The time constants of these gradient coils were at least 85 times shorter than the existing GE Signa gradient coils. Considerations for the fusing current and coil heat loading play an important role in selecting and implementing the final gradient design.

I have found that the numerically optimized quadrupole design is an excellent choice where high strength or high speed, small diameter gradient coils are required for research applications.

2.6 References

1. D.E.Lobb, Properties of some useful two-dimensional magnetic fields. *Nuclear Instruments and Methods*. **64**, 251-267 (1968).
2. D.S.Webster, K.H.Marsden, Improved apparatus for the NMR measurement of self-diffusion coefficients using pulsed field gradients. *Rev. Sci. Instruments*. **45**, 1232-1234 (1974).
3. W.G.O'Dell, J.S. Schoeniger, S.J.Blackband, E.R.McVeigh, A modified quadrupole gradient set for use in high resolution MRI tagging, *Magn. Reson. Med*. **32**, 246-250 (1994).

4. A.Jasinski, T.Jakubowski, M.Rydy, P.Morris, I.C.Smith, P.Kozłowski, J.K.Saunders, Shielded gradient coils and radio frequency probes for high resolution imaging of rat brains. *Magn. Reson. Med.* **24**, 29-41 (1992).
5. J.S.Schoeniger, "Theory and Equipment Design for Nuclear Magnetic Resonance Microscopy and its Application to the Study of Water Properties in Isolated Neurons," PhD Thesis, The Johns Hopkins University, 1992.
6. C.D.Eccles, "Microscopic NMR Imaging", PhD Thesis, Massey University, 1987.
7. L.Bolinger, M.G.Prammer, J.S.Leigh Jr., A multiple-frequency coil with a highly uniform B₁ field. *J. Magn. Resonance.* **81**, 162-166 (1988).
8. E.R.Stauffacher, Short-time current carrying capacity of copper wire, *General Electric Review.* **31**, 326-327 (1928).
9. E.C.Wong, A.Jesmanowicz, J.S.Hyde, Coil optimization for MRI by conjugate gradient descent, *Magn. Reson. Med.* **21**, 39-48 (1991).
10. A.Grace, "Optimization ToolBox: For Use with MATLAB," The MathWorks, Natick, 1992.
11. W.Hock, K.Schittowski, A comparative performance evaluation of 27 nonlinear programming codes", *Computing.* **30**, 335-358 (1983).
12. F.W.Grover, "Inductance Calculations: Working Formulas and Tables," p. 31-35, Dover, New York, 1946.
13. L.H. VanVlack, "Materials for Engineering: Concepts and Applications," p. 470, Addison-Wesley, Don Mills, 1982.
14. R.Turner, Gradient coil design: a review of methods. *Magn. Reson. Imaging.* **11**, 903-920 (1993).
15. J.W.Nilsson, "Electric Circuits," pp.178-179, Addison-Wesley, Don Mills, 1984.

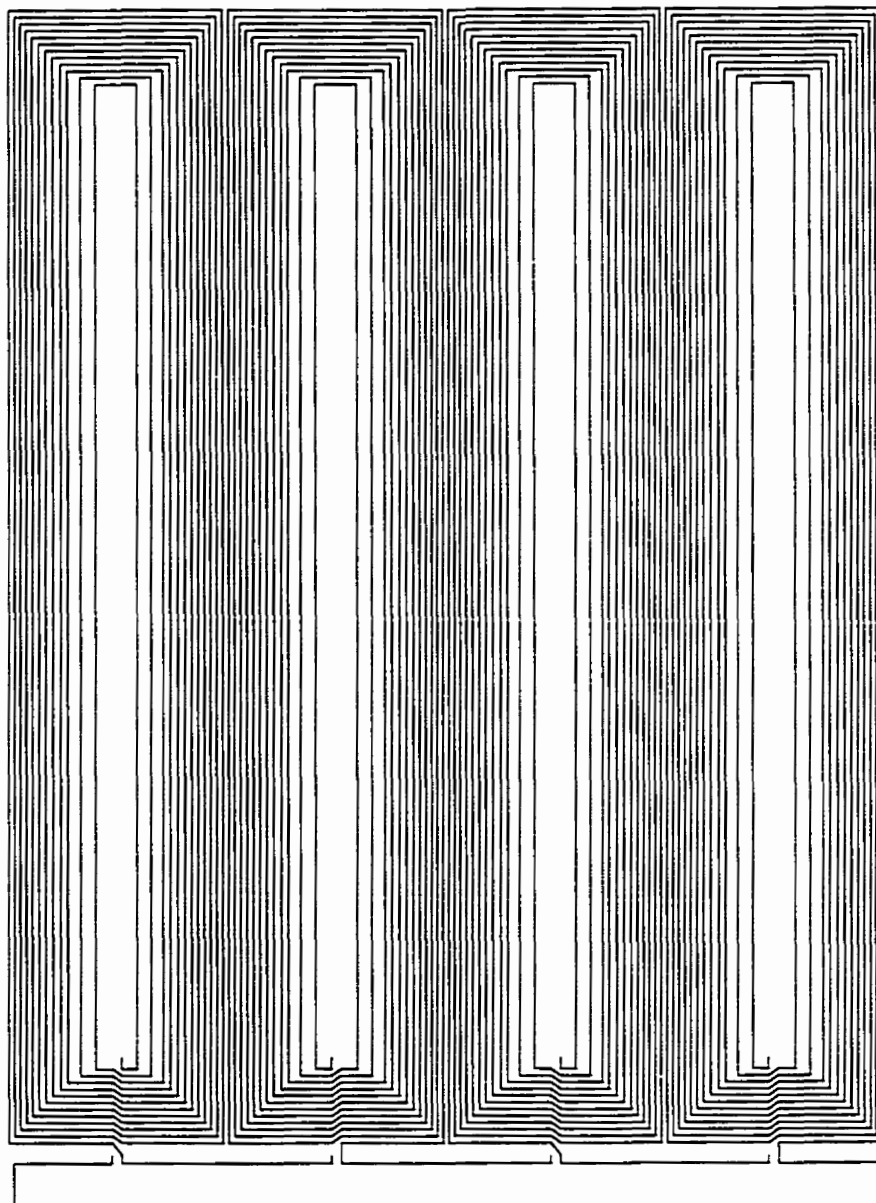
CHAPTER 3 GRADIENT COIL HEATING

3.1 Introduction

Customized gradient coils^{1,2,3,4,5} for head,⁶ extremity, breast^{7,8,9} or specimen^{1,10} imaging on clinical MR machines can provide higher resolution and shorter scan times since these coils generally have increased gradient strength, switching speed and/or region of gradient uniformity. As the duty cycle of these gradient coils is often pushed to their maximum, heat dissipation becomes important since (1) the comfort and safety of the patient being imaged is paramount in any MR protocol, (2) the structural integrity of the coil may be compromised, and (3) the precise current path locations may be altered due to local heating and thermal expansion differences. In this chapter a model based on heat transport theory that describes the temperature response of cylindrical gradient coils mounted either horizontally or vertically is presented. The coil orientation is important for natural convective cooling since the mechanism by which the heat is removed is based on fluid flow due to differences in fluid density with temperature. A discussion of how each of the parameters in the model affects the coil temperature response is followed by experimental results. The experimental data were collected from five different experimental quadrupole gradient coils with a range of applied currents under different cooling conditions. The maximum root-mean-squared current (I_{rms}), and hence, the repetition time (TR) that can be applied to a gradient coil is demonstrated. This methodology can be applied to other gradient coil designs. Suggestions for increasing the heat dissipation are also addressed.

3.2 Methods

The conductor positions of four different quadrupole gradient coil designs were optimized by the method described by Chu and Rutt.¹⁰ The conductor positions of a fifth gradient coil (coil "B" in Table 3.1) were based on the design by Webster and Marsden.¹¹ A representative coil design (Coil "D") is shown in Fig. 3.1a, and reveals that the current densities of the main gradient conductors vary around a cylinder to follow a $\cos(2\theta)$ distribution, where θ is the azimuthal angle.



(a)

Figure 3.1a PC board design of quadrupole gradient Coil "D". The coils longitudinal and azimuthal directions are the vertical and horizontal axis of the figure, respectively.

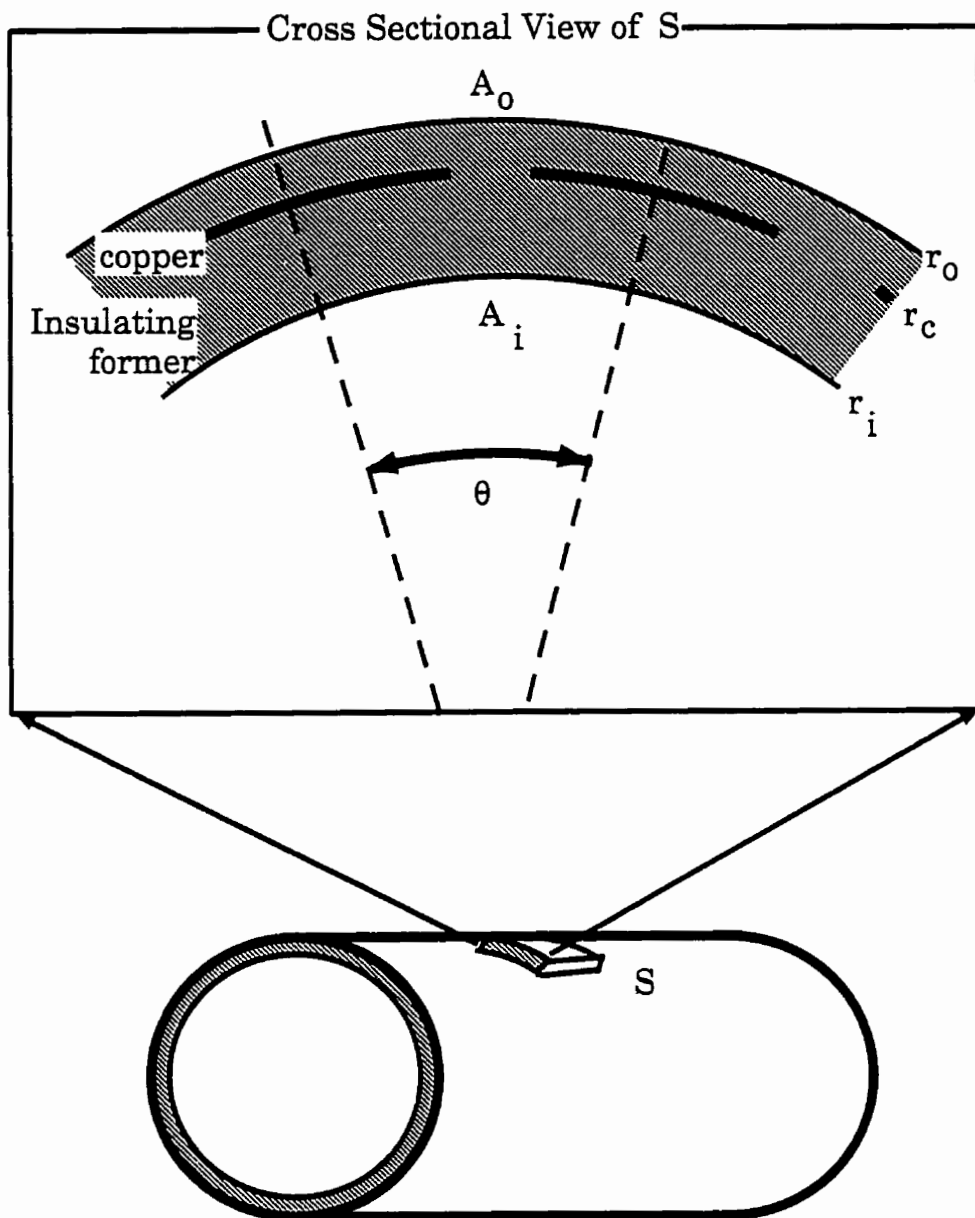


Figure 3.1b Schematic showing various dimensions of a cylindrical gradient coil made from PC board construction.

For simplicity, the conductor widths within each coil were kept constant. The conductor patterns from each design were etched onto flexible printed circuit (PC) boards and glued onto the surface of acrylic cylinders (6 mm wall thickness). A polyethylene heat-shrink (1.2 mm thick) was used to insulate the outer surface of the small diameter coils. For larger diameter coils, the outer surface was insulated using a thin layer of fibreglass and epoxy glue. The coil dimensions, number of conductors, conductor widths, inductance, resistance and gradient efficiency are reported in Table 3.1. Other parameters found in Table 3.1 are explained in the theory section.

The temperature of each gradient coil was measured with thermocouples attached to the inside and outside surfaces of the central portion of the gradient coil where the conductor density was highest. A constant current was applied to each of the coils and the temperature was monitored until the temperature reached an equilibrium state or until the outer temperature reached 90° C. The coils were mounted with their longitudinal axes either horizontal or vertical. In some of the experiments where the coils were mounted horizontally, the coils were cooled by (a) circulating 2.8 m³/min air along the inside and outside surfaces of the coil, or (b) evenly distributing 20°C water flowing at a rate of 0.9 l/min. over the outer coil surface.

3.3 Theory

Here the governing equations describing the average local wall temperature of a gradient coil as a function of time are developed. Within the derivation, a method of determining the heat transfer parameters is shown for the case of cooling by natural convection in air.¹²

In a small section S of a cylindrical gradient coil (see Fig. 3.1b), the incremental heat rise (assuming isotropic properties) is $\rho_s V C_{p,s} dT$, where ρ_s , V , $C_{p,s}$, and dT are the density, volume, specific heat capacity, and incremental temperature rise of S , respectively. This heat rise can also be described as the difference between the heat generated and the total heat dissipated in an infinitesimal time period dt .

Table 3.1. Physical, electrical, and thermal properties of the five quadrupole gradient coils.

Coil	A	B	C	D	E	
Number of windings, N	16	96	192	96	40	
Inner radius, r_i (m)	4.13×10^{-2}	4.13×10^{-2}	4.13×10^{-2}	10.8×10^{-2}	10.8×10^{-2}	
Copper radius, r_c (m)	4.79×10^{-2}	4.79×10^{-2}	4.79×10^{-2}	11.6×10^{-2}	11.5×10^{-2}	
Outer radius, r_o (m)	4.91×10^{-2}	4.91×10^{-2}	4.91×10^{-2}	11.8×10^{-2}	11.7×10^{-2}	
Conductor width, w (m)	4.38×10^{-3}	1.51×10^{-3}	0.62×10^{-3}	4.2×10^{-3}	11×10^{-3}	
Copper thickness, δ (m)	7.1×10^{-5}	7.1×10^{-5}	7.1×10^{-5}	24.9×10^{-5}	24.9×10^{-5}	
Conductor length, D (m)	25.4×10^{-2}	25.4×10^{-2}	25.4×10^{-2}	40.6×10^{-2}	40.6×10^{-2}	
Inductance (μ H)	6.0	157	580	225	41	
Total Coil Resistance, R_{coil} (Ω)	0.5	6.5	32.7	0.92	0.46	
Gradient efficiency ($\text{mTm}^{-1}\text{A}^{-1}$)	1.2	6.9	13	1.2	0.49	
h_r ($\text{WK}^{-1}\text{m}^{-2}$)	6.4	6.4	6.4	6.4	6.4	
$h_{c,i}$ ($\text{WK}^{-1}\text{m}^{-2}$)	Horizontal Vertical	3.0 5.0	3.0 5.0	3.0 5.0	2.0 4.5	2.0 4.5
$h_{c,o}$ ($\text{W}^{-1}\text{m}^{-2}$)	Horizontal Vertical	5.7 5.0	5.7 5.0	5.7 5.0	4.6 4.5	4.6 4.5
Local Resistance R (Ω)	26×10^{-3}	56.7×10^{-3}	143×10^{-3}	7.45×10^{-3}	8.92×10^{-3}	
A_c (m^2)	2.92×10^{-3}	0.475×10^{-3}	0.256×10^{-3}	1.98×10^{-3}	4.62×10^{-3}	

Thus, one can write:¹²

$$\rho_s V C_{p,s} dT = [P - (q_c + q_r)] dt \quad (3.1)$$

where P =power generated inside the section S ; q_c and q_r are the total convective and radiative heat transfer rates from S , respectively.

In order to get a first approximation of q_c , it can be assumed that a pseudo-steady state condition exists, and that there is a linear temperature change from the location of the copper paths to the inner and outer surfaces of S . If one also assumes heat conduction is only in the radial direction, then the convective heat transfer rate from S consists of inside and outside terms as follows:^{12,13}

$$q_c \approx \frac{(T - T_o) A_i}{\frac{-r_i \ln(r_i / r_c)}{k_s} + \frac{1}{h_{c,i}}} + \frac{(T - T_o) A_o}{\frac{r_o \ln(r_o / r_c)}{k_s} + \frac{1}{h_{c,o}}} \quad (3.2)$$

where T is the average temperature in Kelvin of section S ; T_o is the air temperature at a distance not influenced by the coil; r_i and r_o are the inner and outer radii of the insulating former, respectively; r_c is the radius at which the current paths are located within the former; k_s is the thermal conductivity of the former; A_i and A_o are the inner and outer surface areas of S , respectively; and $h_{c,i}$ and $h_{c,o}$ are, respectively, the inner and outer surface heat transfer coefficients due to convection.

By assuming S is small compared to the whole coil, (that is, S can be approximated as a small flat section in a larger flat surface of equal temperature) then $h_{c,i}$ and $h_{c,o}$ can be *estimated* for the case of natural convection when S is in a horizontal or vertical position by using the relation:^{12,13}

$$h_c = \frac{k_f}{L} a (N_{Gr} N_{Pr})^m \quad (3.3)$$

where h_c =convective heat transfer coefficient; k_f =thermal conductivity of the cooling fluid; L ="vertical length" of the coil (i.e. L =coil length if oriented vertically; or L =coil diameter if oriented horizontally); a and m are correlation constants¹² that depend on orientation and N_{Gr} , N_{Pr} (see Table 3.2); and N_{Gr} , N_{Pr} is the product of the dimensionless Grashof and Prantal numbers¹² describing the heat transfer characteristics of the fluid as shown:

where ρ_f , $C_{p,f}$, μ_f , and β_f are respectively: the density, heat capacity, viscosity, and volumetric

$$N_{Gr} N_{Pr} = \frac{L^3 \rho_f^2 g \beta_f (T - T_o)}{\mu_f^2} \frac{C_{p,f} \mu_f}{k_f} \quad (3.4)$$

coefficient of expansion of the fluid at an intermediate temperature estimated to be equal to $(T+T_o)/2$; and g =acceleration due to gravity.

The rate of heat loss due to radiation can be expressed as:^{12,13}

$$\begin{aligned} q_r &= \sigma (T^4 - T_o^4) e_i A_i + \sigma (T^4 - T_o^4) e_o A_o \\ &= h_r (T - T_o) (e_i A_i + e_o A_o) \end{aligned} \quad (3.5)$$

where the heat transfer coefficient due to radiation is

$$h_r = \sigma \frac{(T^4 - T_o^4)}{(T - T_o)} \quad (3.6)$$

and σ = the Stefan-Boltzmann constant= $5.67 \times 10^{-8} \text{ Wm}^{-2}\text{K}^{-4}$; e_i and e_o are the emissivities of the inner and outer coil surfaces, and can vary from 0 to 1 depending on colour. For the dark coloured¹⁴ gradient coils used in my experiments it is reasonable to assume that e_i and e_o are approximately 0.96. For simplicity, $h_{c,i}$, $h_{c,o}$, and h_r can be assumed to be constant over the temperature range of 20 to 60°C. This assumption will be addressed later.

Table 3.2. Constants for determining the natural convection heat transfer coefficients.

Cylindrical Coil Orientation	$N_{Gr}N_{Pr}$	a	m
Vertical plate in air (L=height and L < 3m)	10^4-10^9	0.59	0.25
	$>10^9$	0.13	0.333
Horizontal plate with air above it	$10^5-2 \times 10^7$	0.54	0.25
	$2 \times 10^7-3 \times 10^{10}$	0.14	0.333
Horizontal plate with air below it	10^5-10^{11}	0.58	0.2

Substituting Eqs. 3.2 and 3.5 into Eq. 3.1, and using $A_i=A_c r_i/r_c$ and $A_o=A_c r_o/r_c$, where A_c is the circumferential area of S at the copper radius r_c , produces:

$$dt = \frac{\rho_s V C_{\rho,s} dT}{P + \alpha_c A_c T_o - \alpha_c A_c T} \quad (3.7)$$

where α_c =cooling parameter as described by:

$$\alpha_c = \frac{\frac{r_i / r_c}{-r_i \ln (r_i / r_c)} + \frac{1}{h_{ci}}}{\frac{k_s}{k_s} + \frac{1}{h_{ci}}} + \frac{\frac{r_o / r_c}{r_o \ln (r_o / r_c)} + \frac{1}{h_{co}}}{\frac{k_s}{k_s} + \frac{1}{h_{co}}} + h_r \left(e_i \frac{r_i}{r_c} + e_o \frac{r_o}{r_c} \right) \quad (3.8)$$

Because of my simplifying assumption of constant thermal properties, and since it can be shown that $V=A_c \Delta r \bar{r}/r_c$, where $\Delta r=r_o-r_i$, and $\bar{r}=(r_o+r_i)/2$, Eq. 3.7 can be integrated from time 0 to t, and temperature T_o to T to give the temperature rise as:

$$\Delta T = T - T_o = \frac{(P / A_c)}{\alpha_c} \left[1 - \exp \left(\frac{-t}{C_{\rho,s} \rho_s \frac{\Delta r \bar{r}}{\alpha_c r_c}} \right) \right] \quad (3.9)$$

3.3.1 Cooling Parameter α_c

By defining $\Delta r_i=r_c-r_i$ and $\Delta r_o=r_o-r_c$, the cooling parameter in Eq. 3.8 can be simplified for *thin walled* formers (i.e. $\Delta r_i \ll r_c$ and $\Delta r_o \ll r_c$) to be:

$$\alpha_c \approx \frac{1}{\frac{\Delta r_i}{k_s} + \frac{r_c}{h_{ci} r_i}} + \frac{1}{\frac{\Delta r_o}{k_s} + \frac{r_c}{h_{co} r_o}} + h_r \left(e_i \frac{r_i}{r_c} + e_o \frac{r_o}{r_c} \right) \quad (3.10)$$

I can now examine two extreme cases: 1) convection limited and 2) conduction limited.

Case 1) means that $r_c/(h_{ci} r_i) \gg \Delta r_i/k_s$, and $r_c/(h_{co} r_o) \gg \Delta r_o/k_s$, and Eq. 3.10

reduces to

$$\alpha_c \approx (h_r e_i + h_{c,i}) \frac{r_i}{r_c} + (h_r e_o + h_{c,o}) \frac{r_o}{r_c} . \quad (3.11)$$

This means that the total cooling rate is limited by convection and radiation rates rather than the conduction rate through the former material.

Case 2) means $r_i/(h_{c,i}r_i) \ll \Delta r/k_s$, and $r_o/(h_{c,o}r_o) \ll \Delta r/k_s$, and Eq. 3.10 reduces to

$$\alpha_c \approx k_s \left(\frac{1}{\Delta r_i} + \frac{1}{\Delta r_o} \right) + h_r \left(e_i \frac{r_i}{r_c} + e_o \frac{r_o}{r_c} \right) \quad (3.12)$$

This means that the cooling rate is limited by the conduction rate through the former material and the radiation rate, rather than the convection rate.

3.3.2 Average Temperature of Whole Coil

Upon examination of Eq. 3.9, it can be seen that the temperature rise of a cylindrical gradient coil is an inverse exponential function of time. The equilibrium (i.e. maximum) temperature rise is given by:

$$\Delta T_{eq} = \frac{(P / A_c)}{\alpha_c} \quad (3.13)$$

where P/A_c is the power density. To gain physical insight into the dependence of ΔT_{eq} on gradient strength, geometry, and cooling, let me consider a *hypothetical* situation where the conductors of a gradient coil are axially oriented and *evenly distributed* around a cylinder. The following discussion examines how each of P , A_c , and α_c separately affect the temperature change.

The average power deposited in the coil can be written as:

$$P = I^2 R_{coil} \quad (3.14)$$

where I =current, and R_{coil} =resistance of the entire coil. For etched PC board circuits with a constant copper thickness, δ , the coil resistance can be expressed as:

$$R_{coil} = \frac{\rho_{copper} N D}{\delta w_{avg}} = \frac{\rho_{copper} N D}{\delta (2 \pi r_c / N)} \quad (3.15)$$

where ρ_{copper} =resistivity of copper ($17.7 \times 10^{-9} \Omega m$); N =number of current paths; D =average length of one current path; and w_{avg} =average conductor width. From the Biot-Savart law, it can be shown that¹⁵

$$G \propto \frac{N I}{r_c^2} \quad (3.16)$$

where G =gradient strength. Combining Eqs. 3.14 to 3.16 gives:

$$P \propto \frac{\rho_{copper} G^2 D r_c^3}{\delta} \quad (3.17)$$

Eq. 3.17 shows that for a constant gradient strength and constant aspect ratio ($D \propto r_c$), the average power deposited varies as r_c^4/δ . This demonstrates the importance of minimizing the coil radius and maximizing the copper thickness. It is important to realize that the current and the number of windings do not appear in Eq. 3.17. This means that in terms of average power deposited, it makes no difference if one uses a few wide current paths with high current or many narrow current paths with low current to obtain the same gradient strength. However, there is a benefit to using a sufficient number of current paths to (1) assure high gradient uniformity, and (2) provide adequate gradient strength when the researcher's amplifiers are current limited.

To see how these parameters affect the equilibrium temperature rise averaged over the whole coil, $\Delta T_{eq,avg}$, let's define $A_c = 2\pi r_c D$, and combine Eqs. 3.13 and 3.17 to get:

$$\Delta T_{eq,avg} \propto \frac{\rho_{copper} G^2 r_c^2}{\alpha_c \delta} \quad (3.18)$$

Examination of Eq. 3.18 shows that $\Delta T_{eq,avg}$ is independent of number of

current paths, but a strong function of the coil radius. In order to maintain a constant $\Delta T_{eq,avg}$ with a fixed δ and G , I must scale the cooling parameter α_c with r_c^2 . For example, in moving from a head coil size ($r_c \sim 16\text{cm}$) to a body coil size ($r_c \sim 32\text{cm}$), α_c would have to increase by a factor of 4 to maintain the same $\Delta T_{eq,avg}$. In this example, even though natural convection may have sufficed for the head size coil, forced cooling may be required for the body size coil.

3.3.3 Local Temperature Rise

Because *real* gradient coils never have evenly distributed current paths, Eq. 3.18 does not fully describe the local equilibrium temperature rise at a given location on the coil surface. Edelstein¹⁶ described a technique where thin gaps were etched onto the PC board to produce a coil with variable conductor width. In this case, the maximum temperature rise is at a region where the power density is highest. Thus, to determine this maximum temperature rise, A_c is redefined as a minimum local area:

$$A_c = (w_{min} + w_{gap}) d \quad (3.19)$$

where w_{min} =minimum conductor width, w_{gap} =width of space between conductors, and d =short length of conductor within A_c . The resistance within A_c becomes:

$$R = \frac{\rho_{copper} d}{\delta w_{min}} \quad (3.20)$$

By assuming $w_{min} + w_{gap} = w_{min}$, and that $w_{avg} = 2\pi r_c / N$ for gradient coils with axially oriented conductors, I can combine Eqs. 3.13, 3.14, 3.16, 3.18, 3.19, and 3.20 to get the local maximum temperature rise, $\Delta T_{eq,max}$ as:

$$\Delta T_{eq,max} = \left[\frac{w_{avg}}{w_{min}} \right]^2 \Delta T_{eq,avg} \quad (3.21)$$

Eq. 3.21 implies that the $\Delta T_{eq,max}$ can be minimized by minimizing the ratio w_{avg}/w_{min} ; hence, $\Delta T_{eq,max}$ is highly dependent on the variations in the conductor density around the coil surface. For example, if $w_{min} = w_{avg}/2$ and $\Delta T_{eq,avg} = 25^\circ\text{C}$, then

$\Delta T_{\text{eq,max}}=100^{\circ}\text{C}$, which could mean that local heating is excessive, even though the average temperature rise is in a safe range. In such cases, it may be important to optimize the coil conductor pattern to give the lowest $w_{\text{avg}}/w_{\text{min}}$.

3.3.4 Transient Temperature Rise

An alternate strategy for minimizing the temperature of a gradient coil is to slow down the rate of approach to equilibrium temperature by maximizing the temperature time constant $C_{p,s}\rho_s(\Delta r \bar{r})/(\alpha_c r_c)$ found in Eq. 3.9. This can be accomplished by increasing the specific heat capacity and density product ($C_{p,s}\rho_s$), which may not always be practical when using common former materials^{17,18,19,20,21,22,23} as shown in Table 3.3. Alternatively, $\Delta r/\alpha_c$ can be maximized by increasing the thickness Δr . A complication with this latter strategy is that under some circumstances (such as Eq. 3.12 with Δr_i and $\Delta r_o = 0.006$ m; $k_s=0.2$ $\text{WK}^{-1}\text{m}^{-1}$, $h_r=6.4$ $\text{WK}^{-1}\text{m}^{-2}$, and $r_i=r_c=r_o$) it is possible to have $\alpha_c \propto 1/\Delta r$. This means that the temperature time constant will increase with Δr^2 . However, the equilibrium temperature ΔT_{eq} will increase linearly with Δr . Thus, the gradient coil temperature rise may be less in the transient state (short term), but will be higher in the equilibrium state (long term). A second complication with the overall strategy of maximizing the temperature time constant is that the cooling time constant will also be maximized. In effect, more heat is being stored in the coil compared to the amount being dissipated. If there is not sufficient time between scans for adequate cooling, then the gradient coil temperature will gradually increase.

3.3.5 Forced Cooling

Once a gradient coil is designed and built, the only term in Eq. 3.9 that can be adjusted is the cooling parameter α_c through the manipulation of the heat transfer coefficients $h_{c,i}$ and $h_{c,o}$ as discussed below.

Fig. 3.2 is a plot of the radiative and natural convective heat transfer coefficients (in air) as a function of temperature for the coils reported in Table 3.1. Even though $h_{c,i}$ and $h_{c,o}$ are functions of orientation and dimension, Fig. 3.2 shows that their variation with temperature is not large over the temperature range of

Table 3.3. Typical thermal properties of several materials (at 20°C) that can be used in gradient coil fabrication. (Note the properties will vary depending on the additive types, amounts, chemistry, and manufacturing method).

Material	Density (kgm ⁻³)	Thermal Conductivity (WK ⁻¹ m ⁻¹)	Specific Heat Capacity (Jkg ⁻¹ K ⁻¹)
Polyethylene ^{17,18}	917-965	0.35-0.50	2000-2300
Nylon ¹⁷	1130	0.28-0.30	2300
Acrylic ¹⁸	1170-1200	0.17-0.25	1440
Polyvinyl Chloride ^{17,18} (rigid)	1380	0.15-0.21	960
Epoxy Resin ^{19,20}	1080	0.16-0.33	1050-1170
Epoxy Resin ^{18,19} + 73% (of total wt) Al ₂ O ₃	1400-2400	0.63-1.05	-
Epoxy Resin + Glass fiber ¹⁸	1600-2000	0.17-0.42	-
Glass Fiber ²¹ (E type, low alkali)	2550	1.04	795
Glass Fiber ²¹ (A type, alkali)	2460	0.94	837
Aluminum Oxide ^{22,23}	2400-3980	40	1274-1836
Graphite ¹⁷ (firm, natural)	2000-2500	155	610

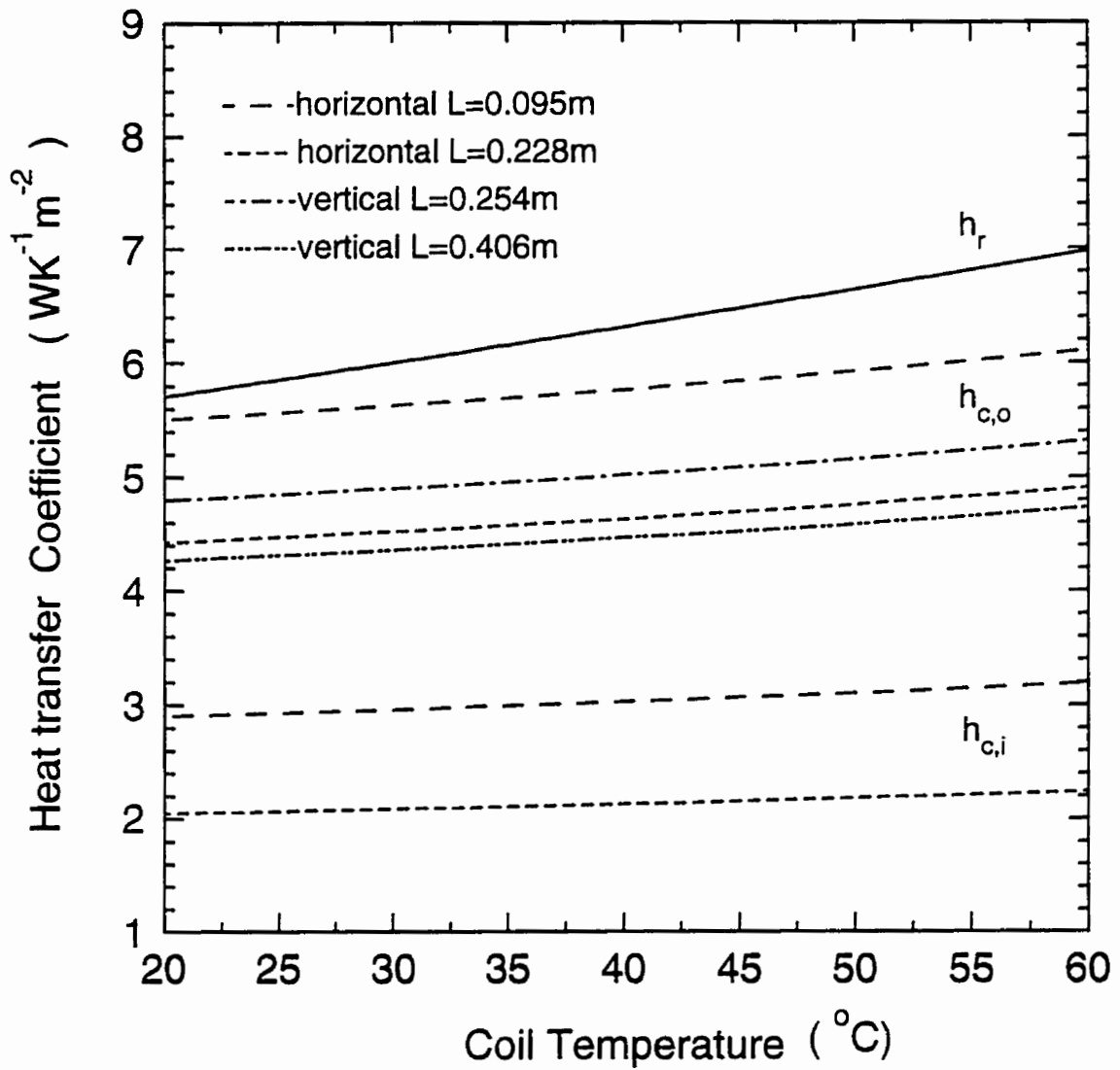


Figure 3.2 Natural convective and radiative heat transfer coefficients are plotted as a function of coil temperatures. The top curve is h_r and applies to all coils. The lower two curves apply to $h_{c,i}$ in the horizontal position. In the vertical position, $h_{c,i}=h_{c,o}$. The remaining four curves describe $h_{c,o}$ for different coil dimensions and orientation.

interest. Between 20 and 60°C, h_r ranges from 5.7 to 7.0 $\text{WK}^{-1}\text{m}^{-2}$; $h_{c,i}$ ranges from 2.9 to 3.2 $\text{WK}^{-1}\text{m}^{-2}$ for $L=0.095$ m, and 2.0 to 2.2 $\text{WK}^{-1}\text{m}^{-2}$ for $L=0.22$ m; and $h_{c,o}$ ranges from 5.5 to 6.1 $\text{WK}^{-1}\text{m}^{-2}$ for $L=0.095$ m, and 4.4 to 4.9 $\text{WK}^{-1}\text{m}^{-2}$ for $L=0.22$ m. Hence, for a given coil configuration, h_r , $h_{c,i}$, and $h_{c,o}$ can each be approximated by a different constant. For example, in this temperature range (with a horizontal coil and $L=0.095$ m), h_r is approximately 6.4 $\text{WK}^{-1}\text{m}^{-2}$, $h_{c,i}$ is 3.0 $\text{WK}^{-1}\text{m}^{-2}$, and $h_{c,o}$ is 5.7 $\text{WK}^{-1}\text{m}^{-2}$.

High values of h_r , $h_{c,i}$, and $h_{c,o}$ are desirable as they increase α_c . The values of $h_{c,i}$ and $h_{c,o}$ found in Fig. 3.2 are minimum values, and can be increased by using forced convection,¹² although it is much more difficult to predict their exact values without knowing the exact conditions and geometry being used. As a first approximation, $h_{c,i}$ and $h_{c,o}$ are in the range of 11-55 $\text{WK}^{-1}\text{m}^{-2}$ for moving air, 55-1700 $\text{WK}^{-1}\text{m}^{-2}$ for moving oil, and 280-17,000 $\text{WK}^{-1}\text{m}^{-2}$ for moving water.¹² Thus water is the preferred coolant. The value of $h_{c,i}$ and $h_{c,o}$ for natural convection in water can be calculated to be approximately 530 $\text{WK}^{-1}\text{m}^{-2}$ and 3400 $\text{WK}^{-1}\text{m}^{-2}$, respectively, by using water properties as the fluid parameters in Eq. 3.3 and 3.4 with $L=0.095$ m.

For coils with $r_c=4.79$ cm (coils "A", "B", and "C"), the cooling parameter α_c is plotted as a function of $h_{c,o}$ in Fig. 3.3a. For this plot, air cooling was assumed to be only on the outside surface of the coil and $h_{c,i}$ was held constant at 3 $\text{WK}^{-1}\text{m}^{-2}$. Three different thickness ratios ($r_o/r_c=1.02$, 1.1 and 1.2) are plotted with two different k_s values of 0.2 $\text{WK}^{-1}\text{m}^{-1}$ and 0.6 $\text{WK}^{-1}\text{m}^{-1}$ which are representative of pure epoxy and Al_2O_3 doped epoxy, respectively. (For the rest of the discussion below, it is assumed that r_i is fixed. The benefits of increasing $h_{c,i}$ will be similar to that of $h_{c,o}$ and can be calculated using Eq. 3.8). From Fig. 3.3a, it is evident that as forced cooling causes $h_{c,o}$ to increase, α_c will eventually reach an equilibrium value for each thickness ratio as described by Eq. 3.12. The equilibrium α_c is lower for coils with larger thickness ratios. Increasing k_s from 0.2 $\text{WK}^{-1}\text{m}^{-1}$ to 0.6 $\text{WK}^{-1}\text{m}^{-1}$ will increase the equilibrium α_c by approximately a factor of two for each thickness ratio. If one were to provide equal cooling to both the inside and outside surfaces

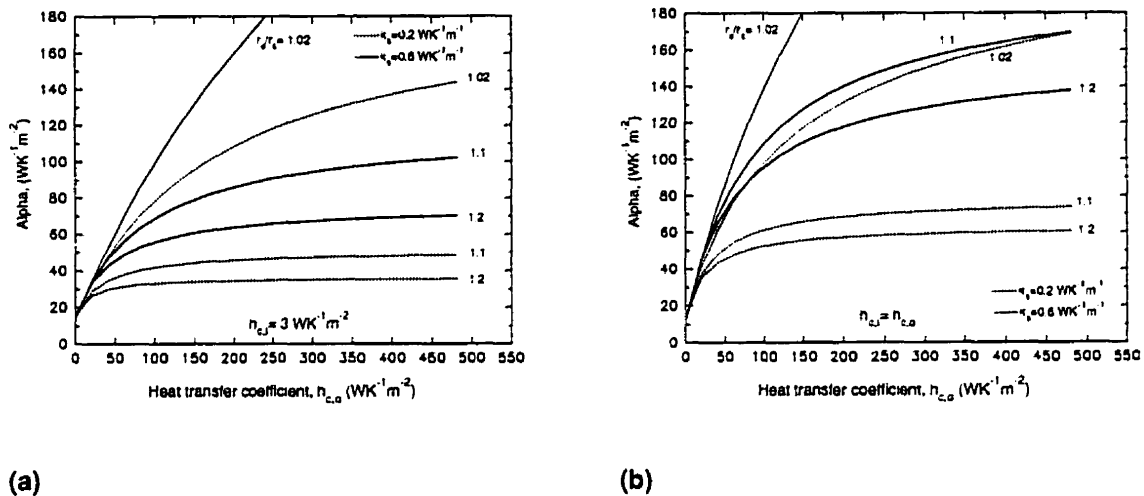


Figure 3.3 The cooling parameter α_c is plotted as a function of h_c for coils "A", "B", and "C". The dotted lines are for $k_s = 0.2 \text{ WK}^{-1}\text{m}^{-1}$, and the solid lines are for $k_s = 0.6 \text{ WK}^{-1}\text{m}^{-1}$. For each thermal conductivity, there are three different thickness ratios $r_o/r_c = 1.02, 1.1, \text{ and } 1.2$. The coil is assumed to be oriented horizontally with $r_c = 4.79 \text{ cm}$ and $D = 25.4 \text{ cm}$. (a) is when forced cooling is only on the outside surface, and $h_{c,i} = 3 \text{ WK}^{-1}\text{m}^{-2}$. (b) is when both the inside and outside surfaces are cooled and $h_{c,i} = h_{c,o}$.

(i.e. $h_{c,i}=h_{c,o}$), then the result would be as shown in Fig. 3.3b. The equilibrium α_c values in Fig. 3.3b are approximately 1.2 to 2 times higher than when cooling is only on one surface (Fig. 3.3a). Again, by increasing k_s the equilibrium α_c almost doubled at each thickness ratio; this represents the conduction limited case (Eq. 3.12). At low values of $h_{c,o}$, such as for natural convection ($h_{c,o}\sim 5$), increasing the thermal conductivity does not increase α_c , and hence, has little influence on the equilibrium temperature of the coil; this represents the convection limited condition.

If it is vital that the subject being imaged not be radiatively heated, then the constant h_r can be influenced by adjusting the emissivities e_i and e_o . For example,¹⁴ if the inner surface of the coil is coated with polished copper ($e_i=0.018$) or aluminium paint ($e_i=0.27$), and the outer surface painted black ($e_o=0.96$), then radiative heat occurs primarily on the outer surface of the coil. At the same time, it would be ideal to have the outer gradient coil section constructed with a high thermal conductivity material, and the inner section constructed with a low thermal conductivity material to retard conductive temperature increases to the subject being imaged. Unfortunately, these changes in e_i , e_o , and k_s will decrease the total value of α_c , and thus cause the average coil temperature to increase.

3.4 Experimental Results and Discussion

Fig. 3.4a shows both the experimental and theoretical temperature responses of coils "D" and "E" placed horizontally with an applied current of approximately 10A. The theoretical curve was calculated by solving for T in Eq. 3.9 with the thermal parameters presented in Tables 1 and 3. A_c was defined in Eq. 3.19 and calculated in the area where the conductors were most densely packed. The power was set equal to $I_{rms}^2 R$, where R was the fraction of the total measured resistance in A_c . There was no forced convection, and hence $h_{c,i}$ and $h_{c,o}$ were calculated to be 2.0 and 4.6 $WK^{-1}m^{-2}$, respectively. The agreement between experiment and theory was excellent with a deviation of no more than $\pm 2^\circ C$. The temperature measurements were accurate to $\pm 1^\circ C$. The model was sensitive enough to distinguish the difference in temperature responses of coil "D" with 9.2 A and 10.5 A.

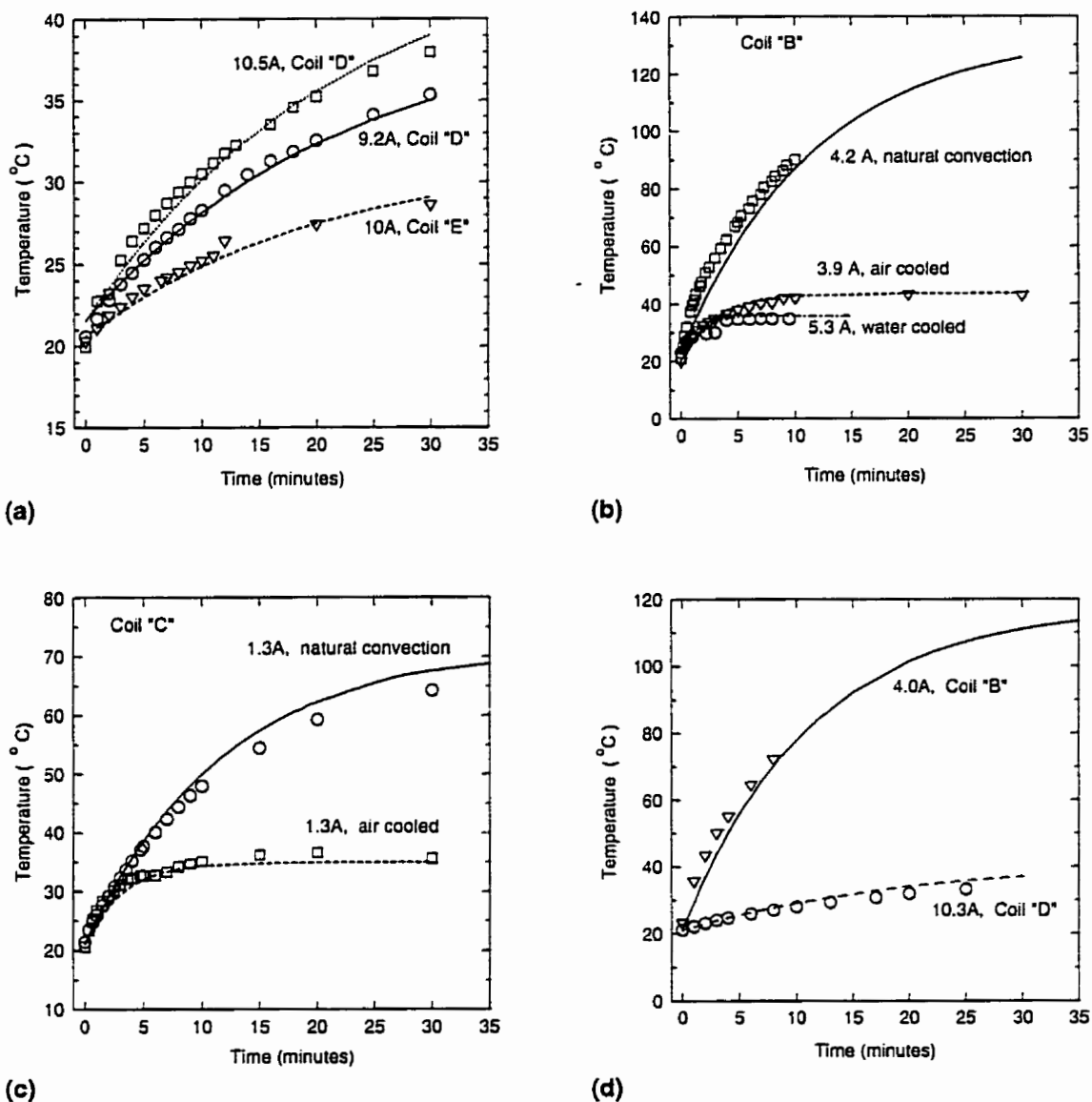


Figure 3.4 The temperature response of various coils with different currents. The theoretical curves are shown as lines, whereas the experimental data are shown as symbols. (a) is for coils "D" and "E" with only convective cooling. (b) and (c) show the effect of forced cooling on coils "B" and "C", respectively. All coils were oriented horizontally, except for (d) which shows the temperature response of coils "B" and "D" oriented vertically with only convective cooling. α_c was estimated for the air and water cooled coils by matching the maximum measured temperature rise to Eq. 3.13. In all other cases, α_c was calculated using Eq. 3.8.

Fig. 3.4b shows the effect of forced cooling on coil "B" lying horizontally. Air cooling lowered the equilibrium temperature from 130°C to 43°C through the increase of $h_{c,i}$ and $h_{c,o}$ to 36 $\text{WK}^{-1}\text{m}^{-2}$ and 72 $\text{WK}^{-1}\text{m}^{-2}$, respectively; (this was determined by adjusting both $h_{c,i}$ and $h_{c,o}$ by a constant factor in Eqs. 3.8 and 3.9 so that the equilibrium temperatures were matched). Water cooling resulted in an equilibrium temperature of 35°C through an increase in $h_{c,o}$ to 1350 $\text{WK}^{-1}\text{m}^{-2}$. Hence, with the aid of either forced air or water cooling, this coil can operate at a continuous current of 4.2 A (to deliver a gradient strength of 29 mT/m), and still maintain a temperature less than 43°C. Without cooling, the coil integrity would be jeopardized with an equilibrium temperature of 130°C.

Fig. 3.4c shows a similar result for coil "C". Air cooling lowered the equilibrium temperature from 70°C to 35°C because both $h_{c,i}$ and $h_{c,o}$ increased by a factor of 10.

Results from gradient coils "B" and "D" mounted vertically with natural convection are shown in Fig. 3.4d. In both cases, the theoretical results were within $\pm 5^\circ\text{C}$ of the measured values. Thus, the model predicts the temperature response of vertically oriented coils nearly as well as it does for horizontal coils.

Three different failure modes are shown for coil "A" on Fig. 3.5 along with the theoretical temperature responses with I_{rms} at 15.5 A, 22 A, and 71 A. The theory was confirmed in an MR experiment with $I_{\text{rms}}=15.5$ A applied for 25 minutes. The coil was found to be extremely hot, but still operational since the equilibrium temperature (120°C) did not exceed the PC board adhesive failure temperature of 125°C. During a second MR scan with the TR reduced by 1/2, so that $I_{\text{rms}}=22$ A (since $I_{\text{rms}} \propto \text{TR}^{-1/2}$), the PC board adhesive failed and allowed the copper traces to vibrate after 10 minutes. This was observed as severe motion artifact in the collected image. Upon physical examination of the coil, it was observed that the heat-shrink on the outer surface could not contain the vibrating copper traces. In a similar experiment but with a 20 minute total scan time, the image was completely ruined as one of the solder joints was found to have failed (185°C). On a third experiment with an identical coil, a mismatch in the amplifier compensation

network caused the amplifiers to oscillate sinusoidally with an I_{rms} of 71 A. In this case, the coil started to burn and smoke within the first two minutes as predicted in Fig. 3.5 since the heat-shrink has a combustion temperature of $\sim 300^{\circ}\text{C}$ in air. Hence, the theory is in excellent agreement with the experimentally observed failure modes.

3.5 Summary

The problem of heat dissipation must be addressed when using customized high strength gradient coils. In small gradient coils where the subject may be in close proximity to the coil, it is vital that the temperature of the coil be maintained at a comfortable level. Although the temperature of the gradient coils can be monitored with a safety shut off, a properly engineered coil should **never** require this during any pulse sequence.

The model presented here allows gradient coil designers to quickly determine the temperature response of their coils. The model suggests that to minimize the temperature rise in gradient coils, the coil radius should be minimized and the copper thickness maximized. The use of a high thermal conductivity coil former along with circulating water will significantly enhance cooling of the coil. Oil and air are less effective cooling fluids. When no forced cooling is used, both natural convection and radiation play significant roles in cooling.

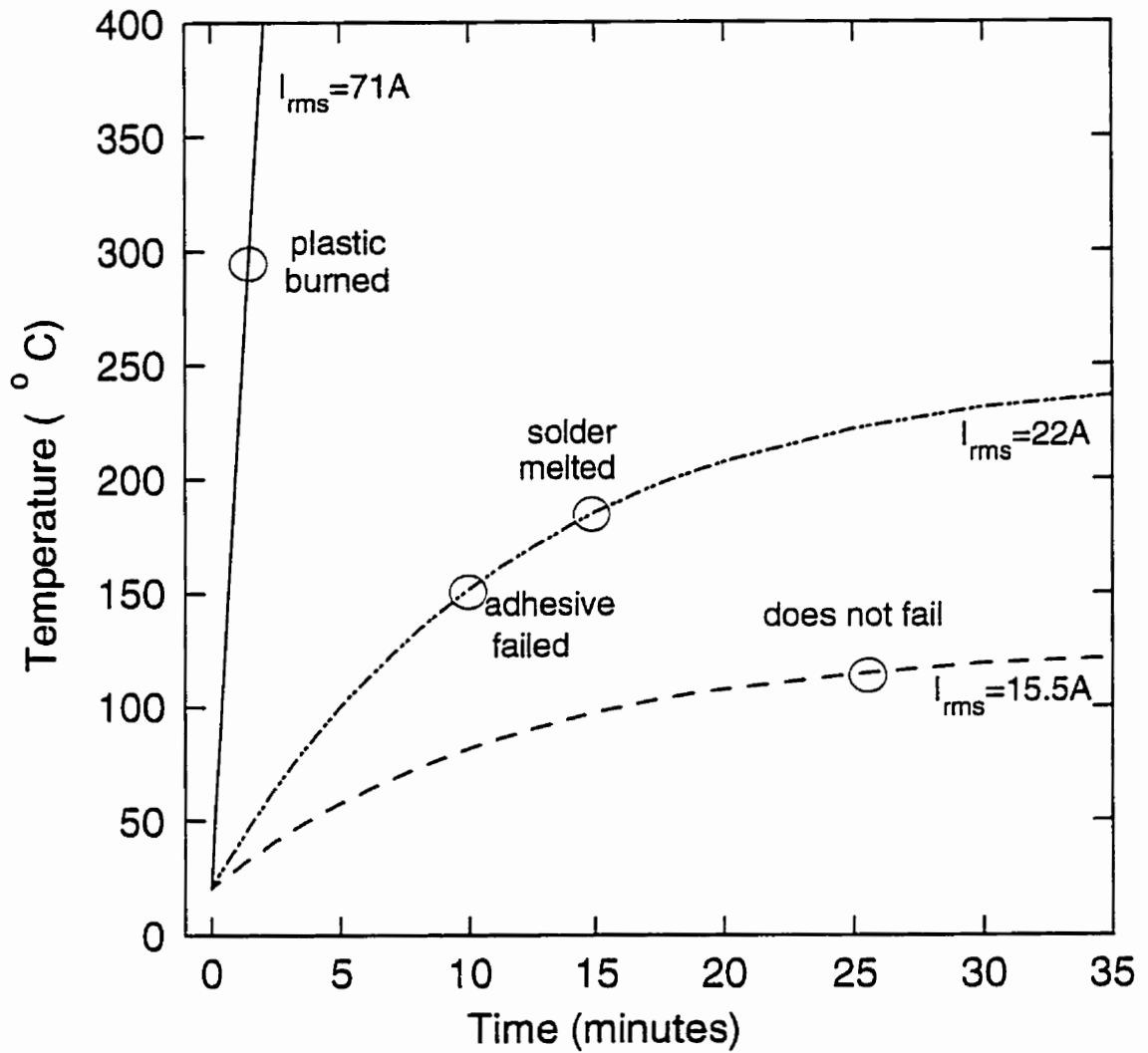


Figure 3.5 The theoretical temperature response of coil "A" mounted horizontally given various I_{rms} . Failure modes at 22 A and 71 A were experimentally determined.

3.6 References

1. W.G.O'Dell, J.S. Schoeniger, S.J.Blackband, E.R.McVeigh, A modified quadrupole gradient set for use in high resolution MRI tagging, *Magn. Reson. Med.* **32**, 246-250 (1994).
2. A.Jasinski, T.Jakubowski, M.Rydzy, P.Morris, I.C.Smith, P.Kozlowski, J.K.Saunders, Shielded gradient coils and radio frequency probes for high resolution imaging of rat brains. *Magn. Reson. Med.* **24**, 29-41 (1992).
3. J.S.Schoeniger, "Theory and Equipment Design for Nuclear Magnetic Resonance Microscopy and its Application to the Study of Water Properties in Isolated Neurons," PhD Thesis, The Johns Hopkins University, 1992.
4. E.C.Wong, A.Jesmanowicz, J.S.Hyde, Coil optimization for MRI by conjugate gradient descent. *Magn. Reson. Med.* **21**, 39-48 (1991).
5. R.Turner, Gradient coil design: a review of methods. *Magn. Reson. Imaging.* **11**, 903-920 (1993).
6. P.B.Roemer, Transverse Gradient Coils for Imaging the Head. U.S. Patent 5,177,442, Jan. 5, 1993.
7. C.F.Maier, K.C.Chu, B.K.Rutt, Design of local gradient coils for breast imaging, in "Proc. 2nd SMR Ann. Meeting, 1994", **1**, p.93.
8. S.Pissanetzky, M.R.Teodorescu, Compact magnet and gradient system for breast imaging, in "Proc. 12th SMRM Ann. Meeting, 1993", **3**, p.1304.
9. E.K.Insko, M.D.Schnall, J.S.Leigh, Biplanar gradients for high resolution mri of the breast, in " Proc. 2nd SMR Ann. Meeting, 1994" **2**, p.1072.
10. K.C.Chu, B.K.Rutt, Quadrupole gradient coil design and optimization: a printed circuit board approach, *Magn. Reson. Med.*, **31**, 652-659 (1994).
11. D.S.Webster, K.H.Marsden, Improved apparatus for the NMR measurement of self diffusion coefficients using pulsed field gradients. *Rev. Sci. Instrum.* **45**, 1232-1234 (1974).
12. C.J.Geankoplis, "Transport Processes and Unit Operations", Allyn and Bacon, Toronto, 1978.
13. L.C.Thomas, "Heat Transfer - Professional version", PTR Prentice Hall, Englewood Cliffs, 1993.

14. R.B. Bird, W.E. Steward, E.N. Lightfoot, "Transport Phenomena", John Wiley & Sons, Toronto, 1960.
 15. C.D. Eccles, "Microscopic NMR Imaging", Ph.D. Thesis, Massey University, 1987.
 16. W.A. Edelstein, Current Streamline Method for Coil Construction, U.S. Patent 4,840,700, Jun. 20, 1989.
 17. U. Grigull and H. Sandner, "Heat Conduction", Springer-Verlag (Hemisphere Publishing), New York, 1984.
 18. Engineering Data Bank, "Modern Plastics Encyclopedia", p. 512-546, McGraw-Hill, New York, 1983.
 19. Dexter Electronic Materials Division, "Hysol EE1087 High Thermal Conductivity Casting Resin Bulletin E3-249D", Dexter Corporation, Olean, New York, 1988.
 20. G. Lubin, "Handbook of Fibreglass and Advanced Plastics Composites", p.882, Van Nostrand Reinhold, Toronto, 1969.
 21. A. deDani, "Glass Fiber Reinforced Plastics", p.7, John Wiley & Sons, New York, 1960.
 22. A. Cezairliyan, "Specific Heat of Solids", p.461, Hemisphere Publishing, New York, 1988.
 23. Kirk-Othmer, "Encyclopedia of Chemical Technology", 3rd Ed., 5, p.273-275, John Wiley & Sons, Toronto, 1979.
-

CHAPTER 4. TRICHLOROTRIFLUOROETHANE AS A PUMPING FLUID

4.1 Introduction

Arterial specimens are often analyzed using high resolution magnetic resonance imaging^{1,2,3,4,5} to study their internal structure and overall geometric boundaries. This information is useful for *in vitro* studies in hemodynamics⁶ and wall compliance.⁴ However, excised arteries must be kept moist to prevent dehydration, otherwise the MR properties may be significantly different from the *in vivo* situation. Hence, specimens are frequently submersed in an aqueous solution³ or embedded into aqueous gels.² This results in a decreased contrast-to-noise ratio (CNR) since the surrounding fluid also yields an MR signal. It is preferable to submerge the specimen in a fluid or gel that does not provide a hydrogen MR signal. Such a fluid would be beneficial in *in vitro* MR wall compliance studies since flow artifacts would be non-existent, thus giving the best possible image.

In addition, inductive coupling of the RF coil with an aqueous solution causes increased noise. Any loss in signal-to-noise ratio (SNR) and CNR ($\frac{\text{signal in tissue} - \text{signal in fluid}}{\text{noise}}$) makes distinguishing the exact geometric boundaries more difficult. For example, the MR parameters (TE=40ms, TR=2000ms, 94 μ m pixels, 1000 μ m thick, 1 NEX) used to create Fig. 4.1 exaggerates the poor SNR and CNR that may be found in high resolution images of an excised porcine aortic section submersed in 0.9% saline solution. (Fig. 4.1b is a spin echo image with SNR=3.4, and CNR=0). To obtain the highest SNR and CNR, and hence, highest accuracy and precision in geometric boundary definition, a non-conductive surrounding medium which does not load the RF coil would be advantageous.

One method to achieve a non-conductive background with no MR signal is to place the specimen in 100% relative humidity air.⁷ Unfortunately, this leads to susceptibility artifacts at the specimen-air interface, which can be quite severe in gradient echo imaging (Fig. 4.1a). Geometric distortions may also occur due to a) small droplets of water condensing onto (or exuding from) the specimen and b) the

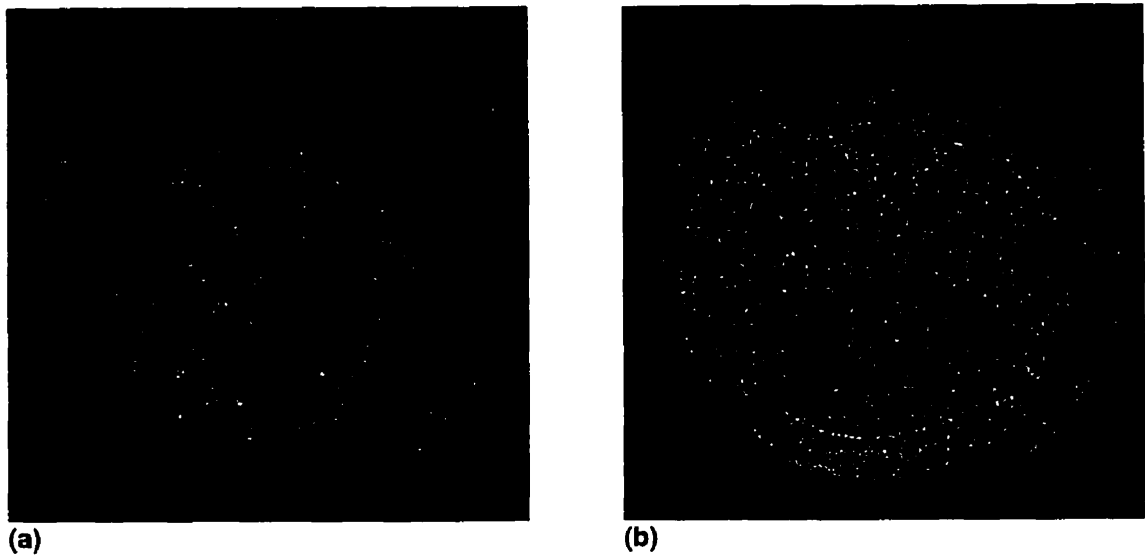


Figure 4.1. High resolution 1.5T MR images of an excised porcine aortic specimen submersed in 0.9% saline solution with a small air bubble on the right side of the container. The gradient echo image (A) reveals a large void, whereas the spin echo image (B) shows the same air bubble to be much smaller. MR parameters: TE=40ms, TR=2000ms, 94 μ m pixels, 1000 μ m thick slice, 256x256 matrix, 30 $^\circ$ flip angle for gradient echo image, and 1 NEX.

tissue collapsing under its own weight. Thus humid air would not produce geometries useful for either *in vitro* modelling or numerical flow simulations. Hence, there is a need to find an alternative medium for surrounding specimens for MR imaging.

I have found that the refrigerant R-113, which has no hydrogen atoms and is non-conductive, is one possible medium that is compatible with arterial specimens. The purpose of this chapter is to discuss the advantages and disadvantages of using R-113 as a method of improving MR images of arterial specimens. Specifically, the dependence of MR relaxation values, SNR and CNR, tensile properties, and histology of porcine aortic sections on R-113 immersion is examined. Because R-113 is a suspected contributor to atmospheric ozone reduction, special handling procedures are also described.

Although not addressed in this paper, R-113 can be used in other *in vitro* MR studies such as high resolution imaging of human tissue, animal, and certain agricultural specimens. Arterial specimens submersed in R-113 have also been shown to have advantages⁸ in x-ray imaging.

4.2 Background and theory

R-113 has no hydrogen atoms; thus R-113 yields no signal at the hydrogen resonance frequency, and hence, maximizes the contrast between the specimen and its background. In addition, because R-113 is non-conductive, the inductive noise and coil loading are both minimized. The RF coil energy is directed to the specimen and not the surrounding fluid.

Because the magnetic susceptibility of R-113 was not readily available, it was estimated using the additivity of atomic constants method described by Pascal.⁹ The magnetic volume susceptibility in S.I. units (χ_v) of R-113 was calculated to be -9.12×10^{-6} , which closely matches that of water or 0.9% saline solution (both calculated to be -9.05×10^{-6}). Based on calculations of molar susceptibility for a similar fluorocarbon (1,2-dichloro-1,1,2-trifluoroethane) with a known magnetic susceptibility,¹⁰ the accuracy of Pascal's method was estimated to be within 5%.

Biological samples do not dehydrate while submersed in R-113 because of the immiscibility of water in R-113. The solubility of water in R-113 is less than 0.011% by weight, and the solubility of R-113 in water is less than 0.017% by weight.¹¹ Because R-113 is immiscible in aqueous specimens, I do not expect it to diffuse into the specimen and cause chemical shift artifacts.

Another advantage in using R-113 over water or saline solution is that there are fewer air bubbles adhering to the specimen. This is attributed to the extra buoyancy of the air bubbles in the denser and less viscous R-113. Since the density of R-113 is 57% higher than that of water, biological specimens need to be held down to prevent them from floating. Some of the chemical properties of R-113 are reported in Table 4.1.

Since R-113 is an excellent non-polar solvent, it can potentially dissolve low molecular weight fats and oils from tissue. For these materials, R-113 may not be the optimum choice. However, other common liquids with no hydrogen atoms (carbon tetrachloride, methylene chloride, and fluorocarbon lubricants) can have prohibitive factors such as cost, toxicity, solubility, compatibility, or flammability problems.

4.3 Effect of R-113 on MR relaxation properties

4.3.1 Methods

Relaxation times of materials can be extremely sensitive to even the smallest chemical imbalances. Thus, in order to show that R-113 does not chemically alter *ex vivo* specimens, the change in MR relaxation properties in porcine descending thoracic aortas was monitored. It can be debated how such specimens should be stored, but for this purpose, I wanted to show *relative* changes between samples, and thus all samples were handled in an identical fashion. Four different arteries (labelled A, B, C, D) were received 11 hours after excision. During this time all arteries were stored in moist air at 4°C. The surrounding connective tissue was removed and the straight portion was rinsed with saline solution for 5 minutes. Each artery was cut into five annular sections 3 cm long (and sub-labelled 1,2,3,4,5). Each piece was placed in a separate

Table 4.1. Typical chemical properties of R-113 at 25°C and 101.3 kPa.

Chemical formula	$ \begin{array}{c} \text{Cl} \quad \text{F} \\ \quad \\ \text{F} - \text{C} - \text{C} - \text{Cl} \\ \quad \\ \text{Cl} \quad \text{F} \end{array} $
Boiling point	47.6°C
Vapour pressure	44.5 kPa
Density	1.57 g cm ⁻³
Viscosity	0.68 cp
Solubility of water in R-113	0.011 wt %
Solubility of R-113 in water	0.017 wt %
Dielectric constant	2.41
Volume susceptibility (χ_v)	-9.12x10 ⁻⁶ (dimensionless, S.I. units)
CT number ^a @90 kVp, 3mm Al	1600 HU

plastic vial with humid air, distilled water, 0.9% saline solution, or R-113. Details of all subsequent preconditioning for a total of either 7 or 74 hours at 4°C, are shown in Table 4.2. Briefly, the preconditioning experiments described in Table 4.2 can be categorized into 5 sections:

- (a) eight different arterial rings were stored for 7 hours in moist air before being MR imaged. To include intra- and inter-sample variations, five rings were from one aorta and three other rings were from three different aortas. For comparison, the relaxation times from an arterial ring submersed in R-113 for 7 hours was obtained.
- (b) one sample was stored only in R-113. The sample was MR imaged after 7 and 74 hours of submersion.
- (c) the eight samples from (a) were re-imaged after a total of 74 hours. For comparison, there were two specimens stored in water, and two specimens in saline solution. One specimen with each liquid was frozen for 74 hours and thawed before imaging.
- (d) two different specimens were stored in saline for 7 hours. One specimen was imaged as is, while the other specimen was submersed in R-113 (1 hour) for MR imaging.
- (e) one specimen was placed in saline solution for 7 hours before replacing with R-113. The specimen was imaged in R-113 at 1 and 67 hours later.

All imaging was performed at 20°C on a 1.5T General Electric Signa (Milwaukee, Wisconsin) imager with a 50 mT/m 10cm diameter gradient coil set¹² and a solenoidal transmit-receive(T/R) RF coil (4.5 cm diam x 9.5 cm long). A slice thickness of 4 mm, FOV of 24 mm, 256x128 matrix, 1 NEX, and a TR of 4 seconds were used for all scans. To get an average T_1 measurement of the artery pieces, an inversion recovery spin echo imaging sequence was used and repeated using 7 different inversion times (TI). A T_1 map was made by performing pixel by pixel non-linear least squared fit to the equation $I_{TI} = I_0(1 - 2\exp(-TI/T_1))$, where I_{TI} is the pixel intensity at the time TI, and I_0 is estimated by the fitting routine to be the

Table 4.2. Relaxation properties of porcine upper thoracic aortae in various fluids measured at 20°C. After sacrificing the animal, the aorta was immediately excised and stored in moist air for 11 hours at 4°C. The times indicated below refer to the period thereafter, just before MR imaging. MR imaging always occurred after 7 or 74 hours of pre-conditioning.

Experiment	Specimen Code	Preconditioning of specimen	T ₁ (ms)	T ₂ (ms)	Number of points averaged	Significance at P=0.05
a	A1,A2,A3, A4,A5,B4, C4,D4	moist air measured at 7 hr	511±71	51±7	80	None
	D1	R-113 (7 hr)	492±8	54±4	10	
b	D1	R-113 (7 hr)	492±8	54±4	10	T ₁ is different
	D1	R-113 (74 hr)	423±10	59±8	10	
c	A1,A2,A3, A4,A5,B4, C4,D4	moist air measured at 7 hr, and then at 74 hr	494±64	50±7	160	T ₁ and T ₂ are different
	B2,C2, B3,C3	water measured at 7 hr & at 74 hr; saline measured at 7 hr & at 74 hr; frozen in water 74 hr & thawed; frozen in saline 74 hr & thawed	622±55	70±11	60	
d	C2	saline measured at 7 hr	594±73	56±7	10	None
	D2	saline (7 hr), drained & replaced with R-113 (1 hr)	599±39	60±8	10	
e	D2	saline (7 hr), drained & replaced with R-113 (1 hr)	599±39	60±8	10	T ₁ is different
	D2	saline (7 hr), drained & replaced with R-113 (67 hr)	511±16	62±7	10	

maximum possible intensity. Similarly, an average T_2 measurement was determined by using a set of six spin echo imaging sequences each only differing in the TE value. A T_2 map was created by non-linear least squared fitting the pixel elements to the equation $I_{TE}=I_0 \exp(-TE/T_2)$, where I_{TE} is the pixel value in the image at time TE. Measurements were averaged from 10 pixels located in the medial portion of the arteries at various points around its circumference. The mean T_1 and T_2 values along with their standard deviations are reported in Table 4.2. A pooled t-test¹³ was performed on each pair of experiments listed in Table 4.2 to determine the significance ($P < 0.05$) in the differences in the means.

4.3.2 Results

Table 4.2 reveals that measured T_1 and T_2 can be correlated with the 5 different preconditioning categories described above. Some of the experiments used only a few specimens since I was not interested in biological heterogeneity, but rather gross systematic changes due to preconditioning. The results can be summarized as follows:

- a) samples that were stored in moist air for 7 hours have a T_1 range of 511 ± 71 ms and a T_2 range of 51 ± 7 ms. Their standard deviations reflect both intra- and inter- sample errors as well as errors in the fit to real data. These values were obtained by averaging 80 data points from 8 different arterial rings. When compared to a sample placed in R-113 for the same amount of time, the relaxation times were not significantly different.
- (b) a sample submersed in R-113 for 7 hours compared to 74 hours shows a significant decrease in T_1 from 492 ± 8 ms to 423 ± 10 ms. There was no significant change in T_2 .
- c) samples submersed for either 7 or 74 hours in saline solution or water, and regardless of being frozen or not, have a T_1 range of 622 ± 55 ms, and a T_2 range of 70 ± 11 ms. These relaxation times were significantly higher than for specimens stored in moist air for either 7 or 74 hours.
- d) a sample that was stored in saline for 7 hours followed by R-113 (1 hour) has a T_1 range of 599 ± 39 ms, and a T_2 range of 60 ± 8 ms. These relaxation

times were not significantly different from a specimen stored in saline solution for 7 hours.

e) a sample that was stored in saline solution (7 hours) followed by R-113 and MR imaged at hours 7 and 74, respectively, shows a significant decrease in the mean T_1 value (from 599 ± 39 ms to 511 ± 16 ms). There were no significant changes in the T_2 values.

Samples stored in R-113 for 7 hours, and imaged in R-113 have T_1 and T_2 values similar to samples stored and imaged in air (7 hours). The sample stored in saline solution (7 hours) and imaged in R-113 (1 hour), has T_1 and T_2 values similar to samples stored and imaged in saline (7 hours). Hence, we deduce that short term exposure to R-113 does not significantly affect the T_1 and T_2 times of arterial specimens. However, long term exposure (greater than 67 hours) to R-113 appears to decrease the average T_1 times by as much 15%. This may be attributed to dehydration, or cellular defatting, and/or absorption of R-113 over long periods of time. It is recommended that specimens be submersed in R-113 only during imaging and that the time period be less than 7 hours exposure.

Those samples stored in either distilled water or saline solution (for 7 hours and 74 hours, or frozen 74 hours) and imaged in the same fluid have average T_1 and T_2 values that are enhanced by 26% and 40%, respectively, when compared to samples stored and measured in air (for 7 and 74 hours). This suggests that the storage of all arteries in moist air for 11 hours (prior to receiving the specimens) caused (1) the samples to dehydrate modestly, and were re-hydrated to their proper level by submersion in water or saline solution; or (2) the specimens to hyper-hydrated upon submersion in water or saline.

We cannot conclusively state which T_1 and T_2 values are closest to the *in vivo* situation since the measurements were made *ex vivo* at 20°C. However, my results show that when *ex vivo* arterial specimens are exposed to R-113 for less than 7 hours, the relaxation times are not significantly affected when compared to fresh specimens handled in a similar manner. Hence the values presented here can only be compared relative to other specimens preconditioned in a similar

fashion. Measurements made *in vivo* (37°C) will produce lower relaxation times.

Although not shown in detail, my data suggests that freezing does not significantly affect the relaxation data; however, we must keep in mind that cellular damage may occur due to ruptured cell membranes. Since repeated handling of the tissue can cause dehydration and changes in relaxation times,¹⁴ all samples should be treated in the same manner with minimum handling.

4.4 Contrast and signal to noise

4.4.1 Methods

The coil quality (Q) of the T/R RF coil was measured using an HP 4195A Network-Spectrum Analyzer in transmit-receive spectrum mode to monitor the frequency response (to within 2.5 kHz) when unloaded and loaded with arterial specimens submersed in air, water, saline solution, and R-113. All measurements were made with the RF coil inside the gradient coil set. The ratios of loaded to unloaded Q's are reported in Table 4.3.

Two porcine aortic specimens were obtained after being stored in moist air for 11 hours at 4°C. Each specimen was cut into three sections and placed in separate vials with 0.9% saline solution for 24 hours at 4°C. Each vial was then MR imaged (spin echo, TE=16 ms, TR=416 ms, ±16kHz receive bandwidth, 24 mm FOV, 1 mm thick, 1 NEX, 256x256 matrix) with each specimen surrounded by saline solution. Immediately after imaging, pairs of vials were randomly drained and filled with (i) moist air, (ii) water, or (iii) R-113. Within minutes of filling, another MR image was obtained. Since the mass of hydrogen protons in each of the samples were different, the transmitter and receiver gains were optimized by using the Auto-PreScan sequence on the GE Signa imager. The images are shown in Figs. 4.2a-d.

The SNR and CNR was measured from 10 different regions throughout each of the images, and the results are shown in Table 4.3.

4.4.2 Results

The $Q_{\text{loaded/unloaded}}$ values for the samples in air, water, and R-113 were not significantly different; whereas the samples in saline solution had a 5% lower

Table 4.3. The ratio of $Q_{\text{loaded/unloaded}}$ for the RF coil used in this study and the corresponding increases in image SNR and CNR of arteries when surrounded with various fluid.

	$Q_{\text{loaded/unloaded}}$	% increase in SNR compared to saline	% increase CNR compared to saline
unloaded	1.00±0.01	-	-
artery in air	1.00±0.01	2.6±0.1	38.1±0.1
artery in water	0.99±0.01	2.8±0.1	0.0±0.1
artery in saline solution	0.95±0.01	0.0±0.1	0.0±0.1
artery in R-113	0.99±0.01	10.8±0.1	60±0.1

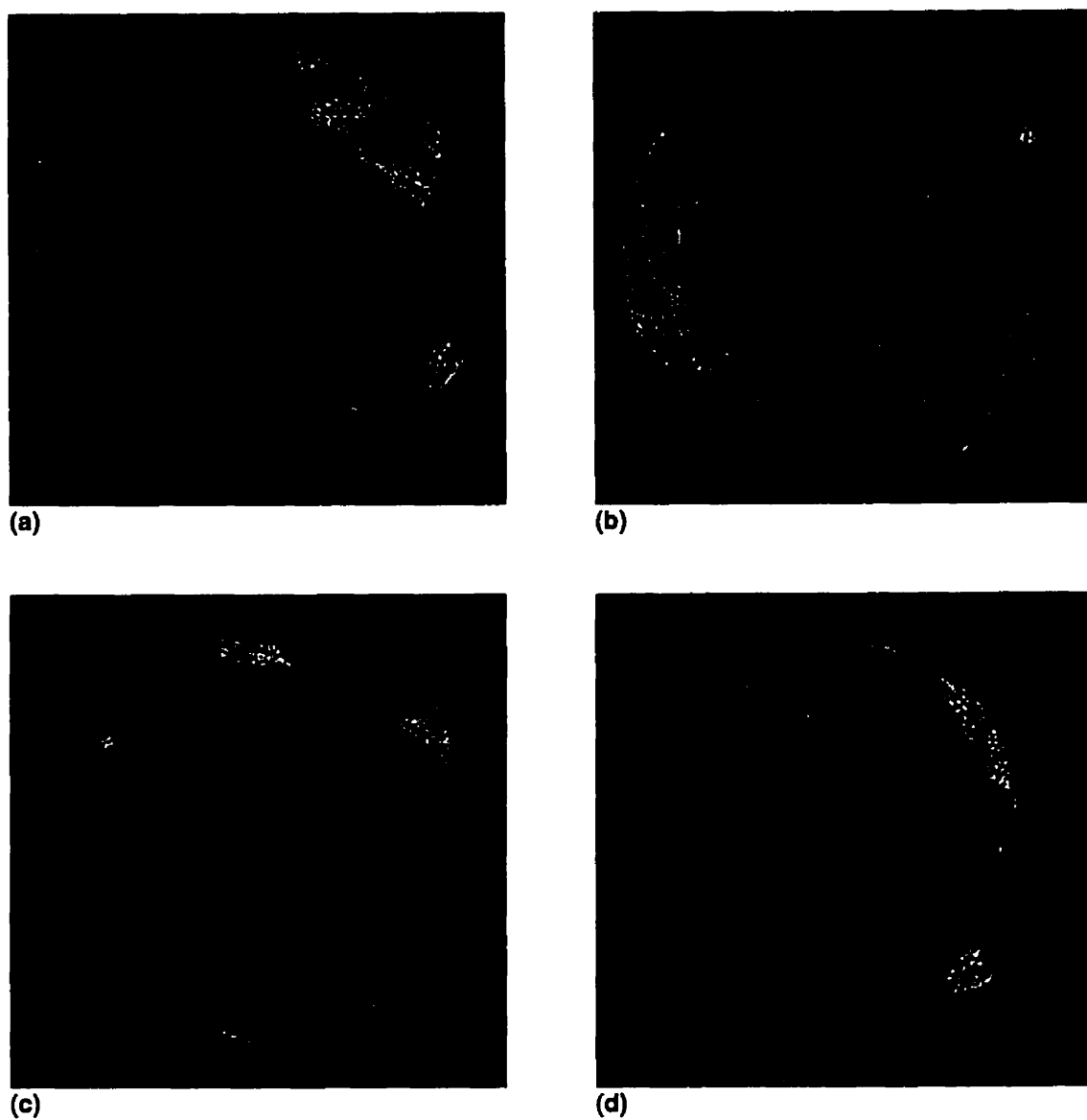


Figure 4.2. High Resolution spin echo images (0.94 mm pixels, 1 mm thick, TE=16 ms, TR=416 ms, 4 NEX) of an excised porcine thoracic aortic specimen submerged in (A) saline, (B) air, (C) water, and (D) R-113.

$Q_{\text{loaded/unloaded}}$ value. Since the SNR of spin echo images¹⁵ is proportional to \sqrt{Q} one would expect the SNR to decrease by 2.2% by imaging specimens in saline solution. The measurements reflect this since the SNR benefits of using air or water rather than saline solution was approximately 2.7%. An unexpected increased in SNR of 10.8 % was measured when the specimen was submersed in R-113. In these MR images, the noise level remained the same, while the signal increased. It is unclear why this benefit was observed.

Although high contrast can be obtained by surrounding the artery in air, the geometry may not be accurate. This is attributed to a) a decrease in B_0 homogeneity because the magnetic susceptibility difference at the air-tissue interface (χ_v for air is $+0.364 \times 10^{-6}$); and b) a modest amount of dehydration can cause the artery to shrink. For these reasons, we do not recommend increasing the CNR of arterial specimens by imaging in air. In addition, the artery may collapse under its own weight.

The average CNR was measured for each fluid, and we have found that specimens submersed in R-113 inherently had the highest CNR (60% more than that of specimens in saline solution). Specimens in moist air showed a 38% increase in CNR compared to specimens in saline solution. This increase is not as high as that found with R-113, and may be attributed to susceptibility differences at the air-artery interface. There was no difference in CNR between samples placed in water or saline solution. Thus, it is recommended that specimen be submersed in R-113 since this fluid gives no signal and the CNR is inherently maximized. With the SNR and CNR maximized, MR parameters such as TE and TR can be optimized to reveal structural differences within the artery wall.

4.5 Tensile Properties

4.5.1 Methods

The straight portion of another excised porcine aorta was cut into 10 adjacent circular rings each 7 mm in width. The rings were numbered consecutively, and the odd numbered rings were submersed in 0.9% saline solution while the even numbered rings were submersed in R-113. After 48 hours,

each of these rings were cut longitudinally to form strips. Thickness measurements of the aortic wall were made using callipers with a 12 gram load. After the dimensions were measured, each end of the aortic strip was mounted onto separate grips so that the circumferential tensile properties could be measured while submersed in saline solution. A strain rate of 2 mm/min was used. All specimens were pre-stressed by cycling the load from 0 to 400 grams four times before the tensile data was collected. The true stress (load/[actual area]) was estimated by multiplying the engineering stress (load/[initial area]) by the factor (1+strain).

4.5.2 Results

The tensile stress-strain curves for aortic sections submersed in saline solution or R-113 are shown in Fig. 4.3. Qualitatively, there are no major differences in the shapes of the stress-strain curves. Small differences in the individual curves can be attributed to biological variations between samples. This suggests that the R-113 does not attack or dissolve the elastin or collagen structure which govern the physical properties of the artery wall.¹⁶

4.6 Histology

4.6.1 Methods

To study the effect of R-113 on aortic tissue at a cellular level, another porcine aorta was cut into 10 adjacent rings each 1 cm in width. The rings were numbered consecutively, and the odd numbered rings were submersed in R-113, while the even numbered rings were stored in saline solution. After a time period of 0.5, 1, 2, 3 and 7 hours at 4°C, one set of bottles with each of the solutions was removed. The arterial rings were removed and fixed in buffered formalin solution. Each ring was embedded in paraffin wax and 7 µm thick microtomed sections were mounted on slides to be exposed to Movat's trichrome stain system with alcohol rinsing between stains. Fig. 4.4 shows typical microscopy images at 100X magnification.

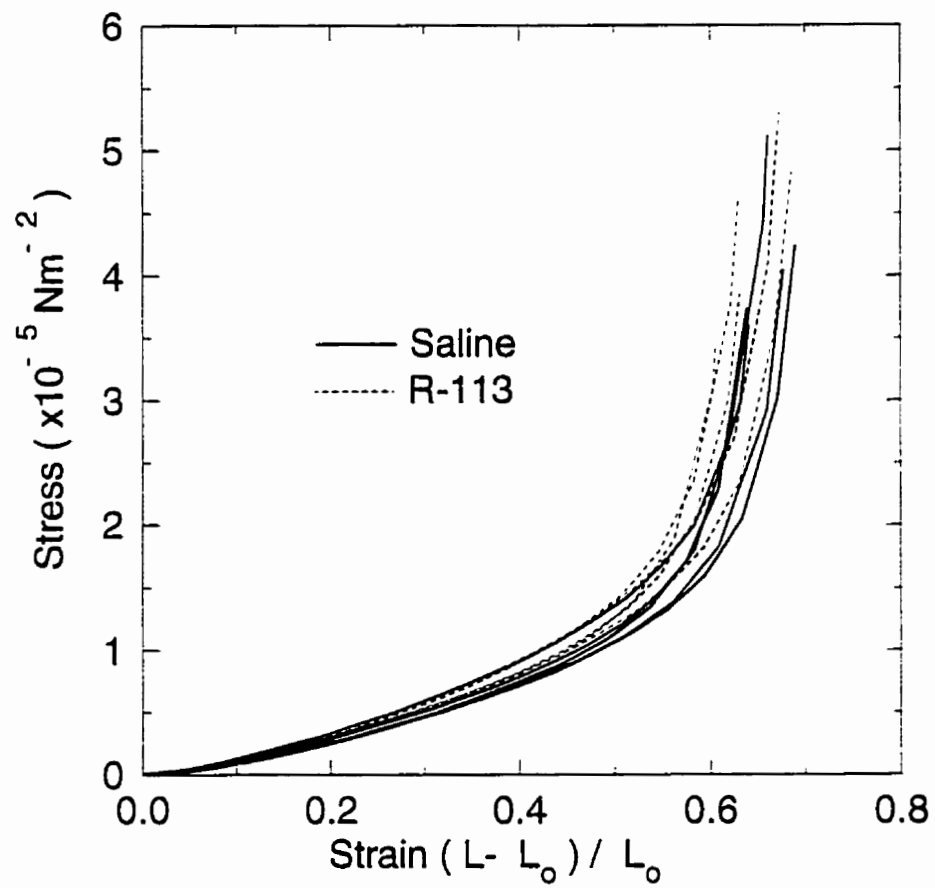


Figure 4.3. Circumferential stress-strain curve for porcine aortic rings submerged in R-113 or saline.

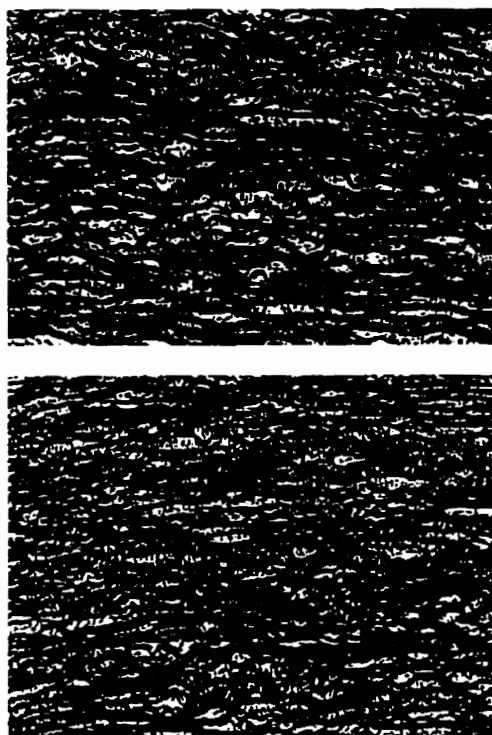


Figure 4.4. Histological sections of porcine aortas submersed for 7 hours in saline (top) and R-113 (bottom) before being fixed in buffered formalin solution and stained Movat's trichrome stain system. The grayscale image shown here does not reveal the purple-black, green-yellow, and pink-red colors from the original slide. Elastin is shown as wavy horizontal lines; collagen and GAG are the white regions; and smooth muscle cells are the greyish tick marks regions within the GAG.

4.6.2 Results

Qualitative comparisons by an experienced technician in examining histology slides of arterial specimens reported that porcine aortas exposed to R-113 for 7 hours showed no major effect on the structure and packing density of the elastin, collagen, glycosaminoglycan (GAG), and smooth muscle cells when compared to similar specimens submersed in saline solution. No gross differences in wall thickness could be observed. Automated image analysis programs that measure total areas of a single colour in histological slides were not used since biological and location differences of the specimens may account for some of the variations. It was more important to observe that the elastic laminae, collagen fibres, and smooth muscle cell membranes were not dissolved or attacked.

Even though R-113 is an excellent solvent for non-polar liquids, the histologist did not observe any unusual regions of defatting on the tissue. Fatty plaques and tri-lipids found on arteries generally consist of high molecular weight molecules, and may not necessarily be soluble in R-113, especially with short exposure times. These findings are in agreement with those of Martin et al.⁵

It should be noted that it is possible to incur sub-cellular damage as reported by McKnight¹⁷ who observed that R-113 applied to the backs of live mice for 10 minutes per day over a period of 20 days caused mitochondrial damage in liver cells when revealed by electron microscopy. Hence, when imaging specimens other than arteries, caution must be used to confirm that R-113 does not substantially affect the sample.

4.7 Safety concerns with R-113

R-113 can be considered to be low in toxicity for both inhalation (rat LD₅₀ 52,000 ppm/4 hour exposure¹⁸) and skin contact (rabbit, approximate lethal dose > 10,000 mg/kg). Inhalation of R-113 vapour can have an anaesthetic effect; and at high concentrations, it can cause suffocation by reducing the oxygen available for breathing. Because it is an excellent defatting agent, it can cause dermatitis on long exposure.

R-113 is suspected to be an ozone destroying chemical when released into

the atmosphere. It is recommended that waste R-113 be recycled by simple distillation at 100°C followed by condensation. Evaporation of R-113 in open containers can be minimized by floating a thin layer of water on top of the R-113.

4.8 Compatibility with other materials

Sealable glass or metal containers are ideal for storing and handling R-113. However, for MR imaging experiments, it is often more appropriate to use plastic containers. Polymers such as polyethylene or polypropylene have low permeability rates and are non-reactive with R-113. Other common plastics such as acrylic and polystyrene may be damaged by R-113. For sealing purposes, the best o-rings to use are made from Buna N (butadiene / acrylonitrile) or Polysulphide, which swell the least (1%) of all elastomers.¹¹ Since R-113 is an excellent solvent for oils and greases, lubricated parts in pumps, for example, should not be exposed to R-113.

4.9 Summary

Submersion of excised arterial specimens in R-113 has been shown to provide several benefits in high resolution MR imaging. Images have higher SNR and inherently maximized CNR. MR images of arteries with R-113 as the surrounding fluid do not appear distorted as a result of the nearly perfect match between χ_v values of R-113 and water. The relaxation times of porcine arteries were not significantly affected by R-113 when exposed for less than 7 hours. However, at longer periods of time, the arterial T_1 starts to decrease.

In general, the relaxation times of arteries are dependent on whether the specimen is surrounded in air or aqueous solution. My data suggests that storage in (1) air causes dehydration and/or water and saline solution causes hydration, and (2) short term storage in R-113 reflects the fluid it was previously in. In addition, submersion of arteries in R-113 compared to saline solution shows very little difference in tensile properties of the arteries. Histology confirms that at the cellular level, there are no apparent differences.

Signal to noise improvements and contrast enhancement of specimens, insects, phantoms, etc. can be obtained by utilizing R-113 as a surrounding medium.

4.10 References

1. L.Arnder, X.Zhou, G.P.Cofer, L.W.Hedlund, and G.A. Johnson, Magnetic resonance microscopy of the rat carotid artery at 300 megahertz, *Investigative Radiology*, **29**, 822-6 (1994).
2. G.E.Gold, J.M. Pauly, G.H.Glover, J.C. Moretto, A.Macovski, and R.J.Herfkens, Characterization of atherosclerosis with a 1.5-T imaging system, *JMRI*, **3**, 399-407 (1993).
3. C.Yuan, J.S.Tsuruda, K.N.Beach, C.E.Hayes, M.S.Ferguson, C.E.Alpers, T.K.Foo, and D.E.Strandness, Techniques for high-resolution MR imaging of atherosclerotic plaque, *JMRI*, **4**, 43-49 (1994).
4. K.C.Chu and B.K.Rutt, An in-vitro method of measuring local arterial elasticity under pulsatile motion, in "Proc of the 11th SMRM Ann. Meeting, 1992", p.829.
5. A.J.Martin, A.I.Gottlieb, and R.M.Henkelman, High-resolution MR imaging of human arteries, *JMRI*, **5**, 93-100 (1995).
6. I.M.Katz, E.J.Shaughnessy, B.B.Cress, A technical problem in the calculation of laminar flow near irregular surfaces described by sampled geometric data, *J.Biomechanics*, **28**, 461-464 (1995).
7. M.Drangova, D.W.Holdsworth, C.J.Boyd, P.J.Dunmore, M.R.Roach, and A.Fenster, Elasticity and geometry measurements of vascular specimens using a high-resolution laboratory CT scanner, *Physiological Measurement*, **14**, 277-90 (1993).
8. M.Drangova, "Computed Tomography Scanner for Dynamic Vascular Imaging In Vitro", Ph.D. Thesis, University of Western Ontario, 1993.
9. L.N. Mulay, E.A. Boudreaux, "Theory and Applications of Molecular Diamagnetism", Wiley-Interscience, New York, 1976.
10. R.C. Weast, Ed., "CRC Handbook of Chemistry and Physics", 68th Ed., p. E-129, CRC Press, Boca Raton, 1987.
11. Freon Product Information G-1, "Freon Fluorocarbons: Properties and applications", E.I.DuPont Demours & Co., Wilmington, DE, 1985.
12. K.Chu and B.K.Rutt, Quadrupole gradient coil design and optimization: a printed circuit board approach, *Mag. Res. Med.*, **31**, 652-659 (1994).

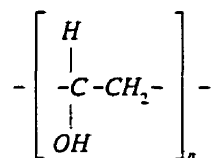
13. J.L.Devore, "Probability and Statistics for Engineering and the Sciences", 2nd Ed., Brooks/Cole, Monterey, 1987.
 14. K. Soila, P.Nummi, T.Ekfors, M.Viamonte, and M.Kormano, Proton relaxation times in arterial wall and atheromatous lesions in man. *Invest. Radiol.*, **21**, 411-415 (1986).
 15. W.A.Edelstein, G.H.Glover, C.J.Hardy, and R.W.Redington, The intrinsic signal-to-noise ratio in NMR imaging, *Mag. Res. Med.*, **3**, 604-618 (1986).
 16. M.R.Roach and A.C.Burton, The reason for the shape of the distensibility curves of arteries, *Can. J.Biochem. Physiol.*, **35**, 681-690, (1957).
 17. J.E.McKnight and J.L.McGraw Jr., Ultrastructural study of the effects of trichlorotrifluoroethane on the liver of hairless mice, *J.Submicrosc. Cytol.*, **15**, 447-451 (1983).
 18. F.A.Gartrell, "Freon TF Solvent: Material Safety Data Sheet", DuPont Canada, Inc., Mississauga, Ontario, May 1989.
-

CHAPTER 5 POLYVINYL ALCOHOL CRYOGEL

5.1 Introduction

It is recognized that arterial geometry and wall distensibility are involved in atherosclerotic disease development.¹ In-vitro studies have been limited to either rigid models that do not provide an MR signal (glass², acrylic³, polyester⁴) or flexible models (silicones⁵, latex rubber⁶) which do not have anthropomorphic properties (such as proton density, T_1 , T_2 , chemical shift, and elastic modulus). Materials such as hydrogels (polymers that retain more than 20% water within their structure) have generally not been used for flow or elasticity studies due to their poor inherent breaking strengths or non-realistic imaging properties. Examples of simple hydrogels are gelatin⁷, agar⁴, agarose⁸, and polysaccharides⁹ which have been used for MR quality control phantoms.^{10,11} In many cases, the MR properties are adjusted by using various additives (such as graphite⁷ or paramagnetic ions¹⁰). The physical strength can also be adjusted by chemically cross-linking the gel.¹¹ The recipes can often be very complex, and compromises in some of the desired properties are generally accepted.

One specific type of hydrogel that is formed by freezing and thawing an aqueous PVA solution^{12,13} has been shown to have rubber-like properties. The freeze-thaw process causes the PVA mixture to cross-link through hydrogen bonding¹⁴ with hydroxyl groups on PVA molecules. A material made by this process is defined as a *PVA cryogel*. For reference purposes, the chemical structure of the PVA molecule is shown below:



PVA cryogels are quite different from PVA hydrogels that are chemically cross-linked¹⁵ by addition of compounds such as aldehydes or borates to a PVA solution. Chemical cross-linking creates a gel with very low modulus and yield strength, and can be described as having an appearance and strength similar to

that of common gelatin. Therefore, a chemically cross-linked PVA hydrogel is not suitable as a distensible phantom material.

The first report of PVA cryogel's crystalline behaviour was reported in 1975 by Peppas.¹⁶ Nambu¹³ independently discovered the gel and recognized its potential applications. In Tanabe's and Nambu's patent claim,¹⁷ they found that the "strength of the gel is remarkably enhanced and properties such as non-stickiness and water resistance are improved..." by partial dehydration while the gel is in its initial frozen state. Variations of the Tanabe and Nambu patent are now extensively reported in the patent literature for specific uses. The material has been reported to be ideal as an MR quality control phantom;^{18,19,20} as a skin marker in MR²¹ and X-ray imaging;^{22,23} as an ultrasound or radio frequency thermal therapy transmission pad;²⁴ as a conductive membrane to be used in electroretinography;^{25,26,27} as a substitute for an ice bag;^{28,29} as a wound covering and bandage for burn victims;^{30,31} as a denture base;³² and in other medical applications.¹⁷

Several published papers have reported some of the properties of PVA cryogel^{12,18,33} after varying the number of freeze-thaw cycles. More recent research has shown that although the number of freeze-thaw cycles can affect the elastic modulus, it is not nearly as important as the rate of thawing³⁴ since the physical cross-linking process can be described as an entropic reordering phenomena. Cross-linking may occur by several mechanisms.¹² Inter- and intramolecular hydrogen bonding between hydroxyl groups can provide some cross-linking. However, it is more likely that crystal nuclei are generated by freezing, and upon thawing these sites grow into crystals which act as cross-linking sites for the polymer. Subsequent freezing produces regions of pure ice crystals to form and forces sections of polymer molecules to come into "closer proximity". The thawing process allows the "close proximity" molecules to realign and hydrogen bond to form crystallites. Larger and/or more numerous crystallite sites form to produce a rubber-like gel. It is unclear whether the length of time frozen has a large influence on the properties;¹² however, higher concentrations of PVA require lower freezing

temperatures. There is some evidence that a monolayer of water is bonded between each PVA molecule in the crystallites.³⁵

PVA cryogel has been reported to be ideal as an MR quality control phantom material since the relaxation properties are stable over a 6 month period of time and can be easily reproduced.¹⁸ However, other researchers challenged that a material with a stability period of 6 months is too short to be used as MR quality control phantom.^{10,11}

In this chapter, experimental data indicate that PVA cryogel is a near ideal material for the fabrication of distensible phantoms. Because of the simplicity of the manufacturing process, phantoms are made and used before long term stability problems arise. The tensile strength, dimensional changes, and MR relaxation times of PVA cryogels made with varying number of freeze-thaw cycles are examined. In addition, aortic phantoms with and without artificial *plaques* were made and imaged using a spin echo sequence. Pulsatile motion was studied using a gated fast gradient echo pulse sequence modified to apply DANTE tags to the cross-section of the phantom.

Although not discussed here, this phantom technology can be adapted to more complicated geometries and can also be used in ultrasound and X-ray imaging studies.

5.2 Methods

A sealed container of aqueous solution of $15.0 \pm 0.2\%$ by weight PVA (available from Business Development Office, London Health Sciences Centre, London, Ontario N6A 4G5) was heated in boiling water for 30 minutes. The hot PVA solution was poured into eleven pairs of annular polycarbonate molds. The time the PVA solution was exposed to air was minimized to less than 2 minutes to prevent evaporation of water. Each pair of molds was designed to create two PVA cryogel tubes with 3.175 mm wall thickness, 15.2 cm long. One of the tubes had a 9.53 mm inside diameter (I.D.) while the other had a 12.7 mm I.D. The annulus was sealed at both ends using rubber O-rings. Air space was deliberately maintained to allow for expansion while the aqueous solution froze. All of the tubes

were stored vertically at room temperature for 24 hours to allow small air bubbles to rise out. Following which, each tube was air cooled at a rate of $0.5^{\circ}/\text{minute}$ to -20°C ; then after 10.5 hours at -20°C , they were thawed by raising the air temperature by $0.27^{\circ}/\text{min}$ to 25°C and held at that temperature for 9.2 hours. (Freezing and thawing of samples was accomplished using a programmable temperature controller, an electric heater and commercial freezer with air circulation). Each of the eleven sets of tubes were given a different number of freeze-thaw cycles ranging from 1 to 11.

5.2.1 Physical Testing

A circular ring 7 mm wide was cut from tubes with a 12.7 mm I.D. Each ring was then cut along the longitudinal axis to form strips. Thickness and width measurements were made using calipers. Each end of the strip was mounted to grips so that the circumferential tensile properties could be measured while submerged in water. An elongation rate of 2 mm/min was used and specimens were pre-stressed before the tensile data was collected.

5.2.2 MR relaxation times

The relaxation times of all 22 tubes were measured on a 1.5T GE Signa imager. The T_1 was obtained by using an inversion recovery spin echo imaging sequence that was repeated using 7 different inversion times (TI). The imaging conditions were: body coil transmit, spine surface coil receive, 24 cm FOV, 256x128 matrix, ± 12.8 kHz RBW, TR=4 s, TE=12 ms, TI=50, 100, 200, 400, 800, 1600, and 3200 ms. The T_1 and I_0 values were calculated by performing non-linear least squared fit to the equation $I_{TI}=I_0(1-2\exp(-TI/T_1))$, where I_{TI} is the pixel intensity at time TI. Similarly, T_2 was determined by using a set of six spin echo imaging sequences each differing only in echo time (TE). The imaging conditions were: body coil transmit, spine surface coil receive, 24 cm FOV, 256x128 matrix, ± 12.8 kHz RBW, TR=4 s, TE= 12, 24, 48, 96, 192, 384 ms. T_2 and I_0 was estimated from non-linear least squared fitting to the equation $I_{TE}=I_0\exp(-TE/T_2)$, where I_{TE} is the pixel value at time TE.

5.2.3 Aortic phantom with stiff elastic plaque

A PVA tube that underwent ten freeze-thaw cycles was split longitudinally into four equal pieces. One of the pieces was placed longitudinally in a mould and the surrounding volume filled with PVA solution. This mould was then frozen and thawed twice. A high resolution MR spin echo image was obtained with the phantom in its mold. Another image was obtained with the tube removed from its mold and mounted in air and its internal pressure increased to 47mm Hg pressure using water. The imaging conditions were 3 cm FOV, 256x192 pixels, 2.5 mm thick, TE=30 ms, TR=1 s, 1 NEX, BW = ± 16 kHz.

A computer controlled pump³⁶ filled with trichlorotrifluoroethane³⁷ was used to pulsate the mounted specimen. A gated fast gradient echo pulse sequence modified to apply DANTE tags during diastole was used to create images at equally spaced phases throughout the cardiac cycle. The transmural pressure at the scan location was transferred to a solid state pressure transducer using 45 cm of 1.56 mm I.D. catheter tubing.

5.3 Results and Discussion

5.3.1 Tensile Testing

The solid lines in Fig. 5.1 are the stress-strain curves for strips cut from PVA tubes that under went 1,2,3,4,5 and 10 freeze-thaw cycles. After 5 freeze-thaw cycles, the shape of the stress-strain curves no longer changes. The dashed lines are stress-strain curves of porcine aortas measured under similar conditions.³⁷ At low stress levels (20 to 50 kPa) where typical strains values are less than 0.2, the elastic modulus was calculated to be 175 ± 6 kPa for the porcine aorta, and 190 ± 30 kPa for PVA cryogel with two freeze-thaw cycles. The errors reported are the inter-sample standard deviations. An unpaired t-test ($p=0.005$) on the data does not show any significant difference in the two means.

Fig. 5.1 shows that the porcine aorta's elastic modulus (i.e. slope) increases drastically above a strain of approximately 0.5. This occurs because the collagen matrix in the aorta limits further elongation. A similar behaviour was not observed with the PVA cryogel tube; but since strains above 20% are generally not observed

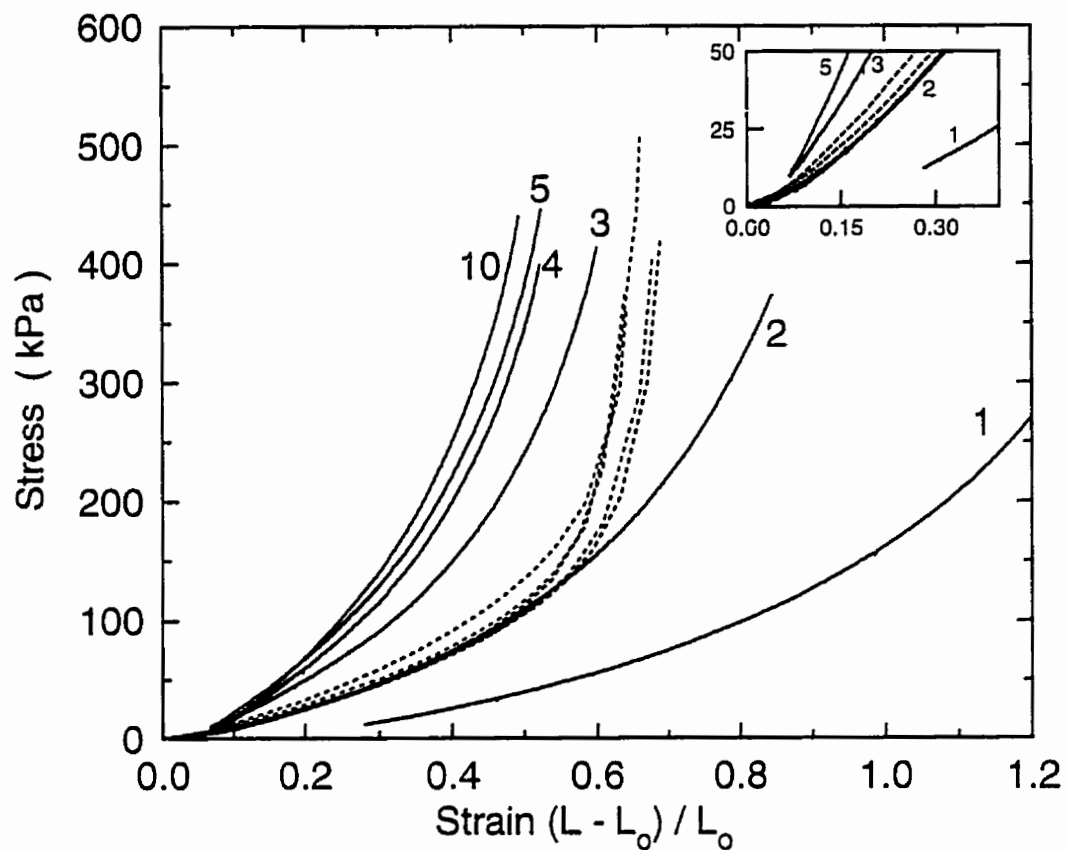


Figure 5.1. Longitudinal stress-strain measurements of strips cut from PVA cryogel rings that underwent 1,2,3,4,5 and 10 freeze thaw cycles. Data from a fresh Porcine aorta are plotted on the same graph for comparison (dashed lines). To compensate for the cross section area reduction during extension of the strips, the stress was calculated as $[(1+\text{strain}) \cdot \text{force}] / (\text{original cross-sectional area})$. The inset is a magnified view of the stress-strain curves at low stress and strain values.

in vivo, this difference in biomechanical properties was not a concern for my *in vitro* studies with physiological pressures. At high stress levels of 300 to 350 kPa, where the collagen matrix is bearing most of the load, the average elastic modulus for porcine aortas was measured to be 5900 ± 1100 kPa. This value is significantly higher than the elastic moduli (1840 ± 60 kPa at the same stress levels) of PVA cryogels tubes that underwent 4 to 10 freeze-thaw cycles (unpaired t-test with $p=0.005$). The values of elastic modulus (at high stress) levels are within the magnitude of moduli (at high stress) reported for excised human abdominal aortas³⁸ ($E=2600 \pm 800$ kPa, from 5 normal aortas with mean age= 66 ± 11 ; $E=3600 \pm 1000$ kPa, from 7 aortas with aneurysms with mean age= 63 ± 13).

Since cryogel stiffness varies directly with PVA concentration, thawing time,³⁴ number of freeze-thaw cycles, and amount of dehydration,¹⁷ it is theoretically possible to create an aortic phantom with stress-strain characteristics similar to that of real aortas by constructing the phantom in a composite fashion using different PVA cryogels. The concept can be visualized through the following example: a very thin walled PVA cryogel tube with a star (or crimped) shaped cross-section (instead of a circular cross section) is frozen and thawed at least 12 times. The star shaped PVA cryogel tube is placed into a larger annular mold and the surrounding space is filled with PVA solution. After this mold is frozen twice, one can visualize how the PVA tube will expand until the star shaped layer is fully expanded into a circular form. At this point, the stress-strain properties will be dominated by the PVA frozen many times. The dual stress-strain properties of this mold will mimic that of real arteries.

PVA cryogel can also be used to mimic other organs or tissues since the cryogel's elastic moduli is controllable (approximately 100 to 1000 kPa) by varying the number of freeze thaw cycles or the PVA concentration (not shown).

It should be noted that my method of tensile testing provides data for relative comparisons. The cryogel volume was assumed to be conserved during testing, and hence, a factor of $(1+\text{strain})$ was applied to the nominal stress [$=\text{force}/(\text{original cross-sectional area})$] and the resultant product is shown in Fig.

5.1. This assumption is appropriate at low strains where the specimen cross-section decreases proportionally to the elongation. More accurate and precise tensile test results can be obtained by using standardized material test methods³⁹ which require dog-bone shaped specimens with markers placed on the narrow section of the dog-bone.

Fig. 5.2 reveals that the thickness of the PVA-cryogel tube changes with increasing number of freeze-thaw cycles, and reaches an equilibrium after 5 cycles. The error bars represent the measurement error in using vernier calipers on soft materials. The dotted line represents the nominal tube thickness defined

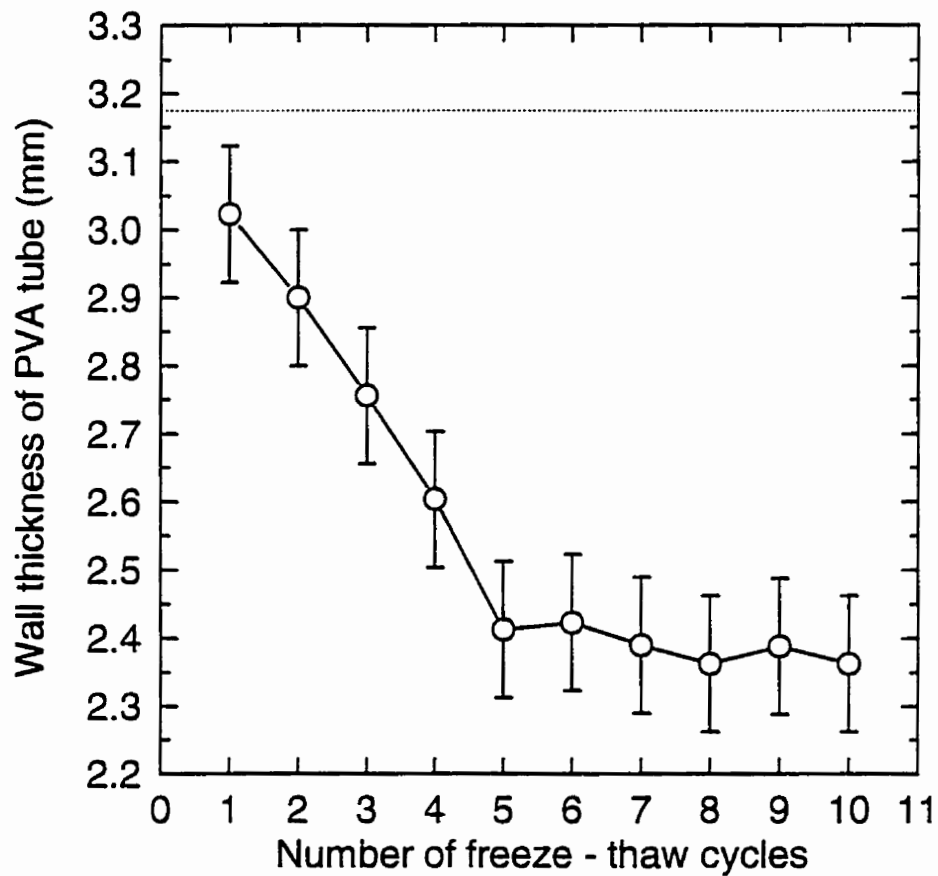


Figure 5.2. PVA cryogel tube wall thickness measured as a function of freeze-thaw cycles. The nominal mold wall dimension was 3.125 mm (dashed line).

by the mould. The manufacturing tolerances on the polycarbonate parts were accurate to ± 0.38 mm. Increased accuracy can be obtained by custom machining each piece to a specific dimension and taking into account any dimensional changes that may occur during the freezing and thawing of the PVA solution.

From Fig. 5.2, it can be observed that the wall thickness decreased by a total of approximately 25% after five freeze-thaw cycles. This is attributed to an increase in PVA cryogel density after each freeze-thaw cycle because free water is expelled from the gel as the crystallinity increases. It should be noted that the final concentration of the PVA cryogel becomes higher, and the quoted PVA content is correct only for the initial concentration. Although, it is reported that the PVA cryogel wall thickness decreases with freeze-thaw cycles, it must be emphasized that aqueous PVA solution expands during freezing just as pure water would. Hence, creating an aortic phantom with exact dimensions is possible only after characterizing the amount of expansion during freezing and the amount of shrinkage after removal from the mold. It must be kept in mind that a slow thaw rates will increase the amount of PVA cross-linking and shrinkage. For example, Nambu³⁴ reported that the PVA cryogel elastic modulus can be increased by several factors by thawing samples at 1°C instead of 37°C . Hence, to obtain reproducible PVA cryogel specimens regardless of the freeze-thaw conditions, the manufacturing conditions should be kept identical for each specimen.

A drawback of manufacturing PVA cryogel phantoms, compared to agar or gelatin based phantoms that set immediately when cooled, is that cryogel based phantoms may take a few days to form depending on the required number of freeze-thaw cycles.

5.3.2 MR relaxation times

T_1 and T_2 relaxation times of the PVA cryogel are shown in Fig. 5.3, and their values decrease rapidly for the first five freeze-thaw cycles. Thereafter, the T_1 and T_2 relaxation times slowly reach equilibrium values of approximately 473 ± 5 ms and 41 ± 1 ms, respectively. The error bars in Fig. 5.3 represent the standard deviations of relaxation values taken from 20 pixels in each pair of tubes with

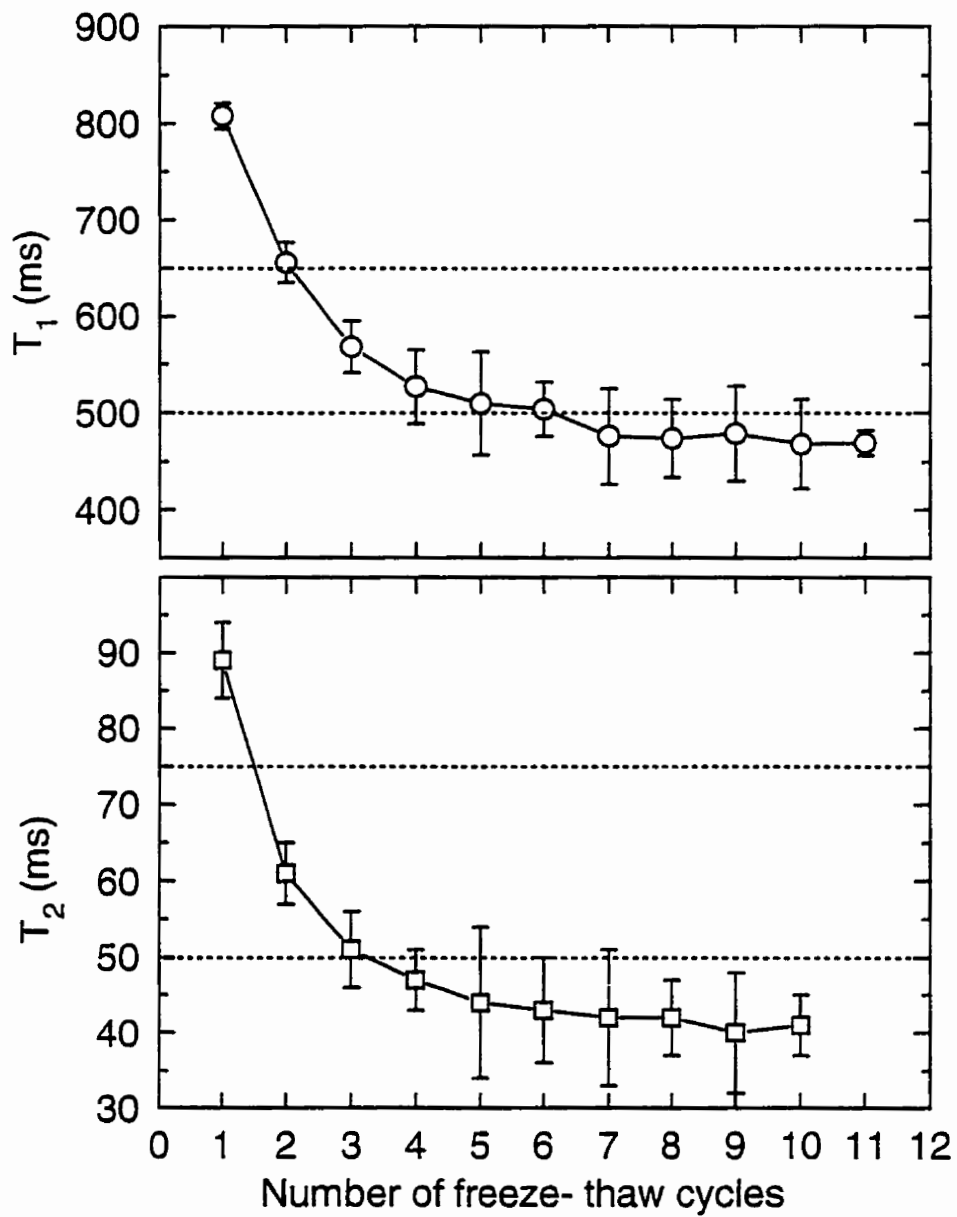


Figure 5.3. The T_1 and T_2 relaxation times (at 1.5T) for PVA cryogel tubes that underwent various freeze-thaw cycles. The dashed lines indicate upper and lower bounds of measured relaxation times for excised porcine aortas.

identical freeze-thaw cycles. Although not shown, a single exponential fit to the relaxation data was found to be appropriate for calculating T_1 and T_2 times of PVA cryogels.¹⁸

For comparison purposes, Fig. 5.3 also includes the upper and lower bounds of relaxation times for excised porcine aortas measured in a similar fashion.³⁷ The range of healthy porcine aortic T_1 and T_2 relaxation times can be obtained with PVA cryogels by using 2 to 5 freeze-thaw cycles, or 2 to 3 freeze-thaw cycles, respectively. When taking the elastic modulus into account, an ideal number of freeze-thaw cycles is 2. This will produce a phantom with relaxation times and elastic modulus that is similar to that of porcine aortas. Although the T_1 and T_2 times can be modified (i.e. decreased) by the addition of paramagnetic particles,¹⁰ there was no need to do so in this study.

Since the PVA gels have a high viscosity, and their T_2 values are less than 100 ms, I am confident that the measurements using our clinical MR imagers are not susceptible to various errors reported by other authors.^{40,41} Because the cryogel properties can be affected by the thawing rate,³⁴ different T_1 and T_2 values can be obtained even though the same PVA concentration and number of freeze-thaw cycles are used. Since many grades of PVA are available through several manufacturers, the exact structure, molecular weight, percent hydrolysis and impurities will affect the final relaxation times and properties. It is recommended that researchers be consistent in choosing their PVA.

5.3.3 Aortic phantom with dual elastic modulus

Fig. 5.4a is a high resolution spin echo image of my aortic model with a dual PVA structure. The phantom is inside its acrylic mold. The image clearly shows the PVA plaque structure due to differences in the MR properties of the two PVA cryogels where the plaque underwent 12 freeze-thaw cycles versus 2 freeze-thaw cycles for the bulk of the PVA tube. Since the PVA cryogel's outer diameter shrinks, a small layer of pure water can be seen surrounding the PVA cryogel tube. In Fig. 5.4b, the same phantom is mounted in air and its internal pressure increased to 47mm Hg pressure using water. Small air bubbles can be seen at the

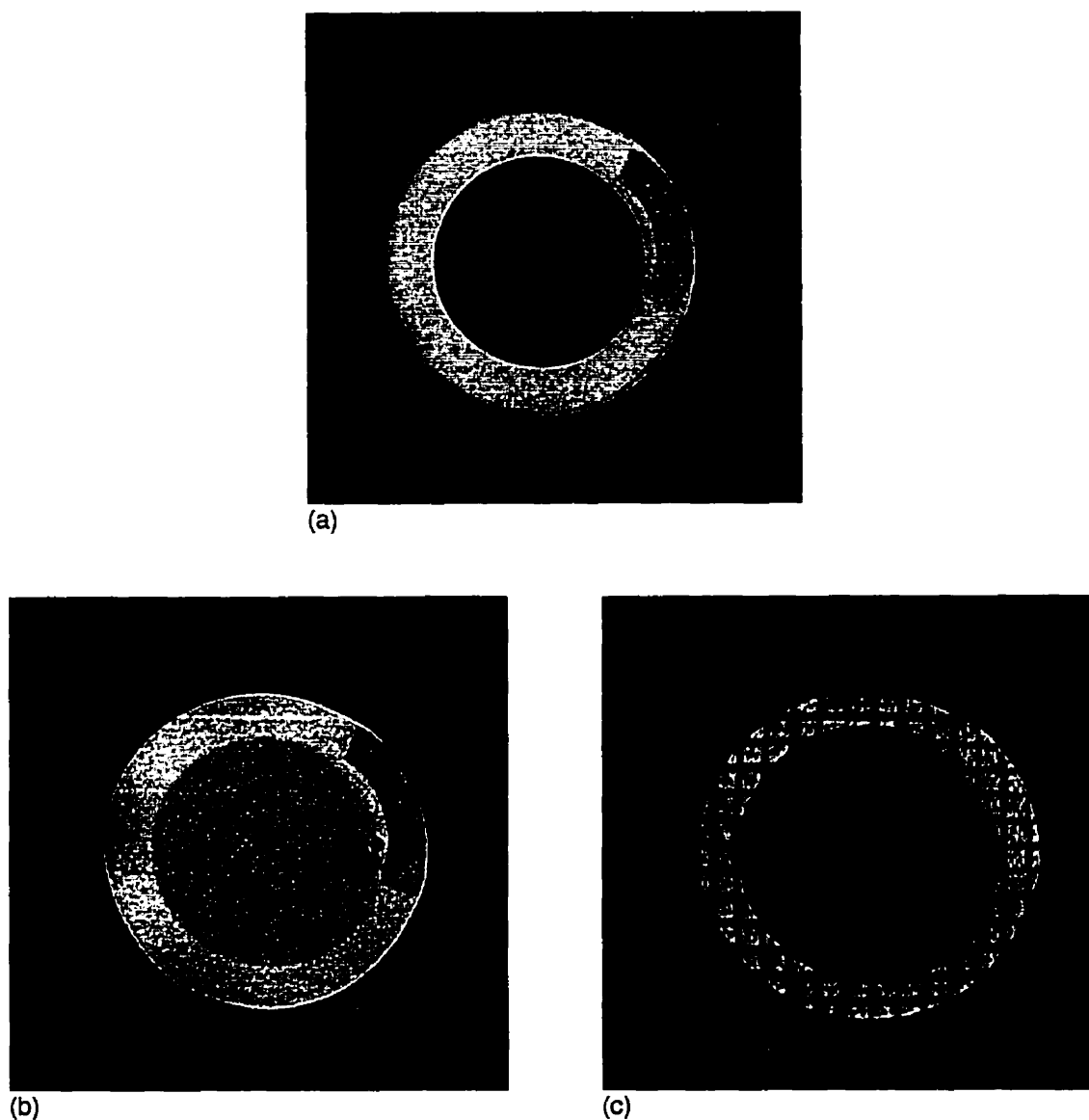


Figure 5.4. High resolution MR image of an aortic model with a dual PVA structure. (a) The phantom is inside its acrylic mold. The image conditions were spin echo, 3 cm FOV, 256x192 pixels, 2.5 mm thick, TE=30 ms, TR=1 s, 1 NEX, BW = ± 16 KHz. (b) The same phantom mounted in air and its internal pressure increased to 47mm Hg pressure using water. The imaging parameters are identical to that in Fig. 5.4a. (c) The same phantom undergoing sinusoidal motion at 1 Hz. A gated fast gradient echo pulse sequence modified to apply DANTE tags during the pressure wave minima was used to obtain this image. The image shown is 285 ms after the tags were applied, and the transmural pressure was 100 mm Hg. The imaging parameters were 20° flip angle, 3 cm FOV, 256x128 pixels, 2.5 mm thick, TE=3.4 ms, TR=12 ms, 4 NEX, BW= ± 16 kHz, 34 phases.

water-PVA cryogel interface. A small film of water on the lower left still adheres to the outer wall of the cryogel tube. On the right side of Fig. 5.4b, it can be observed that the stiff cryogel region does not become significantly thinner as the tube diameter expands. It is apparent that there are shear stresses at the stiff PVA-flexible PVA boundaries. At zero lumen pressure, these stresses are not present. Although it is unclear whether this stress situation is representative of human plaques, the phantom motion is probably similar to that of a health artery embedded with a stiff atherosclerotic plaque. Fig. 5.4c shows the same phantom while undergoing sinusoidal motion at 1 Hz. A gated fast gradient echo pulse sequence modified to apply DANTE tags during the pressure wave minima was used to obtain this image. The image shown was collected 285 ms after the tags were applied, and the transmural pressure was 100 mm Hg.

Qualitatively, the elastic behaviour of the dual PVA cryogel tube is as expected. The stiffer PVA cryogel does not distend or compress compared to the lower elastic modulus material. Although not shown here, quantitative analysis of the exact strain behaviour can be determined from a series of images obtained at various phases of the pressure wave by methods proposed by other researchers.^{42,43}

5.4 Summary

I have developed an elastic vascular phantom using PVA cryogel technology. The phantom (1) is inherently flexible and tough, (2) has similar elastic properties to that of porcine aortas, and (3) has MR relaxation times that are similar to porcine aortas. Regions of varying elastic moduli can be placed throughout the phantom, and under pulsatile flow, MR imaging techniques can reveal different strains in different regions.

The simplicity of the PVA cryogel recipe along with its excellent properties such as signal intensity, relaxation times, elasticity, and strength makes PVA a near-ideal phantom material. A drawback of using PVA cryogel is that its outer dimensions expands upon freezing and shrinks with subsequent freeze-thaw cycles; however, this shrinkage is reproducible and can be compensated for.

Although this study was limited to aortic phantoms, it is possible to create larger distensible phantoms such as those for studying cardiac motion and flow. The elastic properties can be adjusted to be similar to that of most tissues.

5.5 References

1. R.H.Mohiaddin, S.R.Underwood, H.G.Bogren, D.N.Firmin, R.H.Klipstein, R.S.O.Rees, D.B.Longmore, Regional aortic compliance studied by magnetic resonance imaging: the effects of age, training, and coronary artery disease, *Br. Heart J.* **62**, 90-96 (1989).
2. D.N.Ku, D.Liepsch, The effects of non-newtonian viscoelasticity and wall elasticity on flow at 90° bifurcation, *Biorheology*, **23**, 359-370 (1986).
3. A.J.Evans, F.Iwai, T.A.Grist, H.D.Sostman, L.W.Hedlund, C.E.Spritzer, R.Negro-Vilar, C.A.Beam, N.J.Pelc, Magnetic resonance imaging of blood flow with a phase subtraction technique: in vitro and in vivo validation, *Invest. Radiology*, **28**, 109-115 (1993).
4. R.Frayne, L.M.Gowman, D.W.Rickey, D.W.Holdsworth, P.A.Picot, M.Drangova, K.Chu, C.B.Caldwell, A.Fenster, B.K.Rutt., A geometrically accurate vascular phantom for in-vitro x-ray, ultrasound and MR flow studies: construction and geometric verification, *Med. Phys.* **20**, 415-425 (1993).
5. D.C.Goldstein, H.L.Kundel, M.E.Dube-Witherspoon, L.E.Thibault, E.J.Goldstein, A silicone gel phantom suitable for multimodality imaging, *Investigative Radiology*, **22**, 153-157 (1987).
6. S.N.Urchuk, D.B.Plewes, A velocity correlation method for measuring vascular compliance using MR imaging, *JMRI*, **5**, 628-634 (1995).
7. E.L.Madsen, Prospective tissue-mimicking materials for use in NMR imaging phantoms, *Mag. Res. Imaging*, **1**, 135-141 (1982).
8. M.D.Mitchell, H.L.Kundel, L.Axel, P.M.Joseph, Agarose as a tissue equivalent phantom material for NMR imaging, *Mag. Res. Imaging*, **4**, 263-266 (1986).
9. M.W.Groch, J.A.Urbon, W.D.Erwin, S.Al-Doohan, An MRI tissue equivalent lesion phantom using a novel polysaccharide material, *Mag. Res. Imaging*, **9**, 417-421 (1991).
10. K.A.Kraft, P.P.Fatouros, G.D.Clarke, P.R.S.Kishore, An MRI phantom material for quantitative relaxometry, *Mag.Res.Med.*, **5**, 555-562 (1987).

11. J.C.Blechinger, E.L.Madsen, G.R.Frank, Tissue-mimicking gelatin-agar gels for use in magnetic resonance imaging phantoms, *Med. Phys.*, **15**, 629-636 (1988).
 12. N.A.Peppas, S.R.Stauffer, Reinforced uncrosslinked poly(vinyl alcohol) gels produced by cyclic freezing-thawing process: a short review, *J.Controlled Release*, **16**, 302-310 (1991).
 13. M.Nambu, A hydrogel, Japanese Patent Kokai, No. 57/130543, 1982.
 14. M.Watase, K.Nishinari, M.Nambu, Rheological properties of an anomalous poly(vinyl alcohol) gel, *Polymer Communications*, **24**, 52-54 (1983).
 15. P.K.Watler, C.H.Cholaklis, M.V.Sefton, Water content and compression modulus of some heparin-PVA hydrogels, *Biomaterials*, **9**, 150-154 (1988).
 16. N.A.Peppas, Turbidimetric studies of aqueous poly(vinyl alcohol) solutions, *Makromol. Chem.*, **176**, 3433-3440 (1975).
 17. T.Tanabe, M.Nambu, Medical material of polyvinyl alcohol and process of making, U.S. Patent no. 4,734,097, March 29, 1988.
 18. I.Mano, H.Goshima, M.Nambu, M.Ito, New polyvinyl alcohol gel material for MRI phantoms, *Mag. Res. in Med.* **3**, 921-926 (1986).
 19. M.Nambu, H.Goshima, I.Mano, Material for diagnostic NMR imaging (in German), Ger. Offen. DE 3,614,142, 06 November 1986.
 20. M.Nambu, N.Yamada, Method for determining resolution power or discrimination capacity of an NMR imaging apparatus, U.S.Patent 5,023,185, June 11, 1991.
 21. M.Nambu, H.Goshima, I.Mano, Material for diagnosis by nuclear magnetic imaging, U.S.Patent 4,774,957, October 4, 1988.
 22. M.Nambu, N.Makino, Skin markers for NMR and x-ray imaging, Eur. Pat. Appl. EP 228,692, 15 July 1987.
 23. M.Nambu, N.Makino, Process for making skin marker, U.S.Patent 4,916,170, April 10, 1990.
 24. M.Nambu, T.Watari, T.Sakamoto, K.Akojima, Method for applying electromagnetic wave and ultrasonic wave therapies, U.S.Patent 4,958,626, 25 September 1990.
-

25. M.Nambu, Y.Honda, N.Naoi, S.Y.Kim, E.Sakaue, Electrode containing polyvinyl alcohol hydrogel membrane for use in electroretinography, Eur. Pat. Appl. EP 194,598, 17 September 1986.
26. Y.Honda, N.Nao-i, S.Y.Kim, E.Sakaue, M.Nambu, New disposable ERG electrode made of anomalous polyvinyl alcohol gel, *Documenta Ophthalmologica*, **63**, 205-207 (1986).
27. M.Nambu, Y.Honda, N.Naoi, S.Y.Kim, E.Sakaue, Electrode for use in electroretinography, U.S. Patent 4,735,207, April 5, 1988.
28. M.Nambu, Gel for use as a cooling medium, Eur.Pat.Appl. EP 70,986, 09 February 1983.
29. M.Nambu, T.Kinoshita, Hydrogel and its use as a cooling medium, Eur. Pat.Appl. EP 101,068, 22 Feb 1984.
30. M.Nambu, Porous hydrogel wound covering, Eup.Pat.Appl. EP 95,892, 07 December 1983.
31. L.L.Wood, G.J.Calton, Cryogel bandage containing therapeutic agent, U.S.Patent 5,260,066, November 9, 1993.
32. M.Nambu, O.Kuwabara, Y.Okuno, T.Ohban, Denture Base, U.S. Patent 4,828,493, May 9, 1989.
33. M.Watase, K.Nishinari, and M.Nambu, Anomalous increase of the elastic modulus of frozen poly (vinyl alcohol) gels, *Cryo-Letters*, **7**, 197-200 (1983).
34. M.Nambu, Rubber-like poly(vinyl alcohol) gel, *Kobunshi Ronbunshu* (In Japanese), **47**, 695-703 (1990).
35. M.Nagura, T.Hamano, H.Ishikawa, Structure of poly(vinyl alcohol) hydrogel prepared by repeated freezing and melting, *Polymer*, **30**, 762-765 (1989).
36. D.W.Holdsworth, D.W.Rickey, M.Drangova, D.J.M.Miller, A.Fenster, A computer-controlled positive displacement pump for physiological flow simulation, *Med. Biol. Eng. Comput.*, **29**, 565-570 (1991).
37. K.C.Chu, A.J.Martin, B.K.Rutt, Improved MR images of arterial specimens by submersion in trichlorotrifluoroethane, *Mag.Res.Med.*, **35**, 790-796 (1996).
38. C.M.He, M.R.Roach, The composition and mechanical properties of abdominal aorta aneurysms, *Journal of Vascular Surgery*, **20**, 6-13 (1994).

39. Standard test method for tensile properties of plastics (metric), in "Annual Book of ASTM Standards", Vol 08.01, ASTM D 638M-91a, American society for testing and materials, Philadelphia, 1993.
40. H.Y.Carr, E.M.Purcell, Effects of diffusion on free precession in nuclear magnetic resonance experiments, *Physical Review*, **94**(3), 630-638 (1954).
41. C.S.Poon, R.M.Henkelman, Practical T2 quantization for clinical applications, *JMRI*, **2**, 541-553 (1992).
42. E.Atalar, E.R.McVeigh, Optimization of tag thickness for measuring position with magnetic resonance imaging, *IEEE Transactions on Medical Imaging*, **13**, 152-160 (1994).
43. L.Axel, R.C.Goncalves, D.Bloomgarden, Regional heart wall motion: two-dimensional analysis and functional imaging with MR imaging, *Radiology*, **183**, 745-750 (1992).

CHAPTER 6 STRESS-STRAIN CURVES EXTRAPOLATED FROM INCREMENTAL DATA

6.1 Introduction

Atherosclerosis is one form of cardiovascular disease and results in the formation of lesions or plaques in the artery wall. The lesions form in localized patches and eventually develop into fibrous or calcified structures. Over a long period of time, some patients display chronic health problems related to plaque growth as the artery becomes almost fully stenosed. However, it is more serious when the plaque unexpectedly ruptures to induce the onset of acute stroke or myocardial infarction which can result in varying degrees of paralysis or death.¹ Hence, it is important to understand the fundamental stress-strain characteristics of atherosclerotic plaques so that it may be possible to determine which plaques have characteristic signs of occluding or rupturing.

Since the elastic properties of plaques and healthy arterial tissue are different, it should be theoretically possible to detect *early* signs of fibrous and calcified plaque growth by distinguishing differences in the elastic properties of diseased regions and healthier regions in an artery. This chapter addresses some of the issues related to demonstrating this theory using tensile testing and MR imaging. Although the procedures are based on *in vitro* experiments, an effort was made to simulate *in vivo* conditions wherever possible so that most of the concepts can be adapted to non-invasive *in vivo* studies of the carotid or aorta-iliac arteries in the future.

The long-term goal is to be able to provide a technique that is capable of measuring the elastic properties of arteries so that it can be used as early identification tool of young people with a high risk of vascular disease (i.e. people under the age of 30 with risk factors such as genetic predisposition, hyperlipidaemia, hypertension, obesity, diabetes as well as lifestyle choices of cigarette smoking, poor diet, and lack of physical activity).² In addition, the development of such a technique can be used to monitor the regression or progression of atherosclerotic and arteriosclerotic disease in people undergoing different drug therapies.

The technique presented in this chapter is demonstrated using *in vitro* samples, and involves the procedures and equipment described in the previous chapters.^{3,4,5,6} An important mathematical relationship that correlates incremental stress-strain data with exponential uniaxial stress-strain curves is also presented. This relationship will provide researchers who are measuring incremental elastic modulus with 1) an improved fundamental understanding of the behaviour of arteries in dynamic motion, and 2) a technique to compare incremental elastic properties measured by different researchers, independent of the experimental conditions from which they were obtained. To the best of my knowledge this is the first application and demonstration of a technique correlating incremental properties with material stiffness data (i.e. stress-strain curves). This work differs from other researchers who have studied the structural stiffness of arteries (which is dependent of pressure level and wall thickness) by modelling the pressure-radius⁷ or tension-radius curves.⁸

In order to present this information in a logical fashion, this chapter is separated into four sections:

1. The theory section describes an existing method of measuring gross incremental properties and show its limitations for detecting local elastic properties. An explanation is given on why incremental data from one set of experiments may not be compared to other data unless they were performed under similar conditions. An exponential model that can be used to describe arterial stress-strain curves is presented, and by modifying the exponential model it is possible to use incremental data to extrapolate a complete exponential stress-strain curve.

2. The experimental methodology is described in Section 6.3. First a description of specimen preparation is given. Next, I describe how tensile tests are performed to determine the two parameters in the exponential model. Incremental tensile tests were also performed to validate the proposed extrapolation model. This is followed by the description of experiments using *in vitro* high resolution MR imaging to measure arterial displacement in pulsatile specimens. To follow the local strain within the sample wall, a description of image processing is given.

3. In the results section, the parameters for the exponential model are obtained for PVA cryogel and porcine aortas from tensile stress-strain curves. Incremental tensile tests demonstrate the success of the extrapolation model as well as its limitations. Incremental tests on PVA phantoms and aortic segments measured using MR tagging^{9,10,11,12,13,14} were obtained to measure of the local elastic properties. I demonstrate through one simple experiment that paradoxical results can arise from incremental moduli data when the stresses are not known. The inconsistency was resolved by using the extrapolation method derived earlier.

4. I discuss and summarize my work as well as present some of the limitations in using my technique. Suggestions for future improvements and quantitative analysis are also described. A short discussion is also made on the potential of extending this theory to other imaging modalities which are currently being used to measure incremental moduli.

6.2 Theory

6.2.1 Incremental Modulus of Tubes

In the field of material science, the elastic properties of a material are commonly represented through the uniaxial stress-strain curve. The definitions for stress and strain are, unfortunately, not consistent in the literature. Often the definitions of strain are chosen to simplify a particular mathematical model, and only in the low strain regime do the different strain formulae produce similar values.^{15,16} Hence, one should be clear on the definitions of the terms and the specific reasons for these definitions.

Materials that have a linear stress-strain relationship are considered to obey Hooke's Law of elasticity. In such cases, the slope of the stress-strain line is defined as the elastic modulus and is one quantitative measure of material stiffness. Most stiff solids at very low strains do exhibit a linear elastic relationship. However, for the case of complex biological materials such as arteries, the stress-strain relationship is non-linear, and it is impossible to quantify the modulus with a single quantity. Despite this fact, many researchers have chosen to use an

incremental modulus at a specific stress level as one method of describing the material stiffness. The incremental modulus for samples that have a tubular shape such as arteries, is given by Bergel^{17,18} as

$$E_{inc}|_{p_2} = \frac{P_3 - P_1}{R_{o_3} - R_{o_1}} \frac{2 (1 - \nu^2) R_{i_2}^2 R_{o_2}}{R_{o_2}^2 - R_{i_2}^2} \quad (6.1)$$

where P is the pressure, ν is Poisson's ratio, R_i is the internal radius, R_o is the outer radius, and the subscripts 1,2,3 represent successive measurements of pressure and radius. For Example, if R_i and R_o were measured at three different pressure levels, the middle value of R_i and R_o is given the subscript 2 while the first and last measurements are given the subscripts 1 and 3 for P , R_i , and R_o .

It is possible to simplify Eq. 6.1 by replacing the radius measurements with the subscript 2 by the average of the radius measurements with subscripts 1 and 3. One should be cautious in using Eq. 6.1 because the assumptions for the vessel include (1) circular symmetry with respect to geometry and material properties, (2) linear elastic behaviour, (3) thin wall, (4) homogeneous and isotropic properties, (5) undergoing low strain, and (6) no longitudinal strain. For samples that do not follow these assumptions, the calculated E_{inc} may have limited value. A full appreciation for the assumptions required in deriving Eq. 6.1 can be obtained through the geometric derivation of this equation.^{19,20,21}

Several researchers^{22,23,24} have modified Eq. 6.1 by replacing the internal and external radii measurements with internal and external circumferential (c_i and c_o , respectively) measurements to get

$$E_{inc} = 2 (1 - \nu^2) \frac{dp}{dc_o} \frac{c_i^2 c_o}{c_o^2 - c_i^2} \quad (6.2)$$

where dc_o is the change in outer circumference due to a change in the internal pressure dp . The advantage of making this substitution is to increase the measurement accuracy when the exact centre of the vessel cannot be determined

accurately. Eq. 6.2 is also less sensitive than Eq. 6.1 to inhomogeneities and non-circularities around the circumference of the vessel wall. On the other hand, Eq. 6.1 has the advantage of representing the properties at the specific angular location at which the radii are actually measured.

Even if the samples meet all of the assumptions, E_{inc} does not represent the behaviour of the vessel wall at other stress levels because the stress-strain behaviour is not linear. In fact, E_{inc} does not even represent the slope of the stress-strain curve at the same stress level. Fung et al^{25,15} reported that the incremental modulus is determined by incremental experiments and "is not equal to the tangent of the loading or unloading tensile curve" at equivalent stress levels. Fung²⁵ also noted that some researchers "carelessly identify" E_{inc} with the tangent, E , (i.e. elastic modulus)²⁶ of the stress-strain curve at the same stress level.²⁷ Milnor²⁶ explicitly states that E_{inc} "gives results quite different from calculations in which unstressed length is the strain denominator". It can be debated whether E or E_{inc} is the more important modulus; however, these two quantities can be related to each other through a simple mathematical formula as shown in Section 6.2.4. For now, it is sufficient to say that E_{inc} should only be compared to incremental modulus data derived from incremental experiments performed and calculated in a similar fashion.

The next section defines stress and strain from first principles, and presents one exponential model to represent the full uniaxial tensile stress-strain curve. By using the definitions of E_{inc} and E , the mathematical model is modified to permit incremental data to be extrapolated to obtain a full exponential stress-strain curve. The exponential stress-strain curve can be used subsequently to describe the elastic behaviour of the blood vessel wall at all stress levels.

6.2.2 First Principles: Exponential Stress Strain Relationship

In general, a uniaxial stress-strain curve can be generated from tensile testing of artery specimens. This type of testing consists of mounting strips of arterial material between two grips. One of the grips is fixed to a load cell, while the other grip moves at a constant rate away from the fixed grip. The total distance

between the jaws is measured as well as the load. This basic *ex vivo* test has been used innumerable times over decades of research into arterial biomechanics and has yielded fundamental knowledge about the elastic behaviour of arteries.

The following are some basic definitions of stress, strain, and modulus. A few major references are included; however, it should be kept in mind that different symbols and terminology can be found in the literature to define the same quantities. In the work presented here, the dimensions of all quantities are in SI units, except when specified otherwise.

In a stress-strain curve, the tensile stress²⁸ (i.e. engineering stress) is defined as

$$T = \frac{F}{A_o} \quad (6.3)$$

where F = applied force, and A_o is the original cross-sectional area with no load applied. (A_o is measured in a plane perpendicular to the direction of the applied force.)

The strain^{28,29} (also known as engineering or absolute strain) is defined as

$$\varepsilon = \frac{L - L_o}{L_o} = \frac{L}{L_o} - 1 \quad (6.4)$$

where L is the total length of the specimen at some applied load T , and L_o is the original length at no applied load.

For arteries, one simple physiological model used to describe uniaxial tensile data is given by:^{7,15,30,31}

$$T = (\beta + T^*) \exp(\alpha (\varepsilon - \varepsilon^*)) - \beta \quad (6.5a)$$

where α and β are characteristic parameters of the material and (ε^*, T^*) is a point that the stress-strain curve is constrained to include. When ε^* and T^* are both zero,

Eq. 6.5a can be re-written as

$$T = \beta (\exp(\alpha\varepsilon) - 1) \quad (6.5b)$$

Fig. 6.1 shows that α can be thought of as an exponential stiffness parameter since higher values of α (varying typically from 1 to 10 for artery walls) reflect a material with a more rapidly rising stress-strain curve. β on the other hand, can be defined as a scaling parameter as revealed in Eq. 6.5b. Fig. 6.1b shows that the initial slopes of the stress-strain curves are strongly dependent on β .

Improvements to Eq. 6.5a may be obtained by using a set of two exponential equations^{15,30} where one equation represents the lower stress data, and the other equation represents that higher stress data. However, for this work, Eq. 6.5b is sufficient as long as the stress T is maintained within a normal physiological range.

6.2.3 Elastic Modulus

The next three sections are provided for background purposes only. More advanced readers will see that the value and application of Eq. 6.5b continues in Section 6.2.6. For linear stress-strain relationships, the material stiffness has traditionally been characterized by the elastic modulus (i.e. slope of the stress-strain plot). Medical researchers have often made several simplifications to the non-linear arterial stress strain curve in attempts to report a single value to represent the artery wall stiffness. The following describes some of these simplifications.

Since any non-linear curve can be divided into small linear segments. As shown in Fig. 6.2, the slope of the j^{th} linear segment, $E_{\text{seg},j}$, can be defined as:

$$E_{\text{seg},j}(\varepsilon_j) = \frac{T_j - T_{j-1}}{\varepsilon_j - \varepsilon_{j-1}} , \quad \text{where } j=1,2,3,\dots,n \quad (6.6)$$

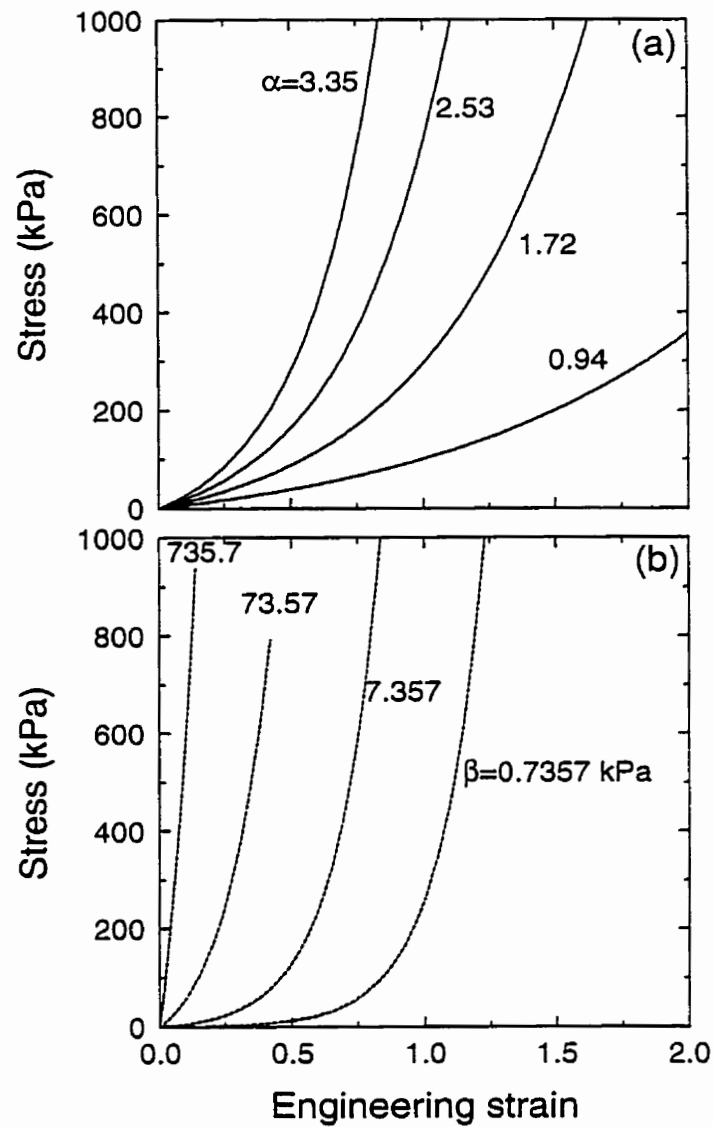


Figure 6.1. A theoretical example of how stress-strain curves depend on the parameters α and β . In (a), α is varied from 0.94 to 3.35 with β fixed at 64.759 kPa. The bottom plot (b) varies β by factors of 10 with a fixed $\alpha=5.87$.

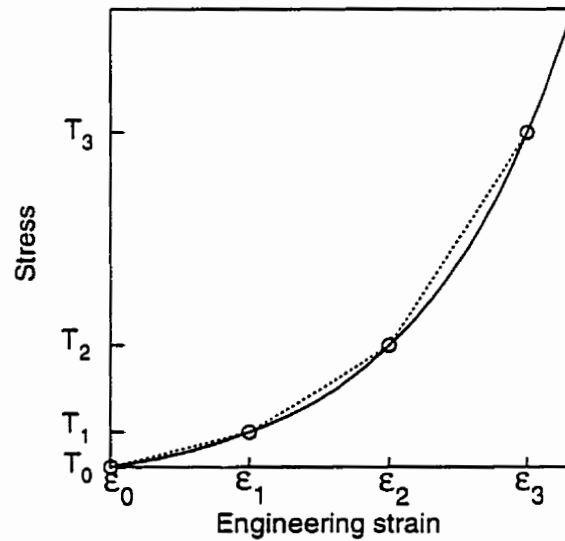


Figure 6.2. A schematic showing how an exponential stress-strain curve is linearized by taking small line segments.

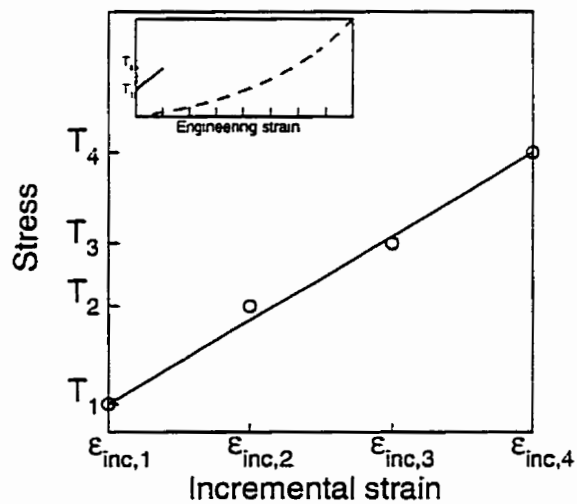


Figure 6.3. A schematic stress-strain curve showing four incremental data points plotted from $\epsilon_{inc,1}=0$. The inset shows the full stress-strain curve, compared to the incremental data. Note that the slope of the incremental data is higher than the slope of the full stress-strain curve at the same stress level.

Note that $E_{seg,i}(\epsilon_j)$ is approximately equal to the elastic modulus E (i.e. tangent to the stress-strain curve):

$$E_{seg}(\epsilon_j) \approx E \left(\frac{\epsilon_j + \epsilon_{j-1}}{2} \right) = \left. \frac{dT}{d\epsilon} \right|_{\epsilon = \frac{\epsilon_j + \epsilon_{j-1}}{2}} \quad (6.7)$$

Hence, if one calculates $E_{seg,i}(\epsilon_j)$, this can be considered as a measure of the material stiffness at a strain of $(\epsilon_j + \epsilon_{j-1})/2$. This information is useful to know especially if $(\epsilon_j + \epsilon_{j-1})/2$ is within the typical strain range which the material normally experiences.^a

Measuring $E_{seg,i}(\epsilon_j)$ is relatively simple in *ex vivo* or *in vitro* experiments since ϵ_j can be determined by applying Eq. 6.4 with L_0 measured with no external load. However, from *in vivo* experiments, it is usually impossible to measure $E_{seg,i}(\epsilon_j)$ because the zero load length L_0 is not known.³² The implications of this fact are discussed further in the next section.

6.2.4 Incremental Stress-Strain Data

The diameter or cross sectional area of a pulsating artery can be obtained using ultrasound,^{33,34,35} MR^{36,37,38} or X-ray²² imaging modalities. One generally obtains a series of images of the artery cross section at different stages of the cardiac cycle. Assuming there are two identifiable points that can be used to track local dimensional changes, then the incremental strain can be written as³²

$$\epsilon_{inc, i} = \frac{L_i - L_1}{L_1} = \frac{L_i}{L_1} - 1 \quad (6.8)$$

where i is the image number, L_1 refers to the total distance (i.e length) between the

^aAside: Because E_{seg} is the ratio of stress and strain, and stress is a function of strain (see Eq. 6.5b), the modulus is also a function of strain. However, modulus is traditionally not reported with an associated strain level, rather it is reported with an associated stress level. Hence for consistency of reporting modulus values, we will also report modulus with an associated stress level, and only for our mathematical analysis will we express E as a function of ϵ .

two identifiable points in the i_{th} image, and L_1 is the length measured in the first image. Eq. 6.8 differs slightly from the definition used by Milnor²⁶ and Bergel¹⁷, who used the mean length as the denominator of the incremental strain term. If the incremental tests are performed over increasingly smaller strain ranges, Eq. 6.8 will approach that of Milnor's definition.²⁶

Note that $\epsilon_{inc,i}$ for $i=1$ will always equal zero by definition. Assuming that the stress T_i at a point mid-way between the two identifiable points can be calculated for each image, then as shown in Fig. 6.3, a plot of T_i verses $\epsilon_{inc,i}$ will produce an approximately straight line (for a small range of ϵ_{inc}) with a slope equal to the incremental modulus

$$E_{inc} = E_{inc,i} \equiv \frac{T_i - T_1}{\epsilon_{inc,i} - \epsilon_{inc,1}} \quad (6.9)$$

$$= \frac{T_i - T_1}{(L_i - L_1)} L_1$$

where the subscript i is the image number and ranges from 1,2,3,...,n.

Combining, Eqs. 6.4, 6.6 and 6.7 gives $E_{seg,i} = L_o(T_i - T_{i-1}) / (L_i - L_{i-1}) \approx E$. If we let $j=2$, and compare the result with Eq. 6.9 with $i=2$, we get $E_{inc} = E(L_1/L_o)$ for equal stress levels. The same results can be obtained by using infinitesimally small steps. Note that E_{inc} is always higher than E , and that as L_1 becomes much larger than L_o , the difference between E_{inc} and E becomes larger. These results emphasize the importance of using E , and not E_{inc} for accurate estimation of the slope of the stress-strain curve.

6.2.5 Relating Incremental Data to the Exponential Stress-Strain Curve

As explained earlier, *in vivo* imaging can be used to calculate $\epsilon_{inc,i}$ data. To derive a full stress-strain curve from incremental data, it is necessary to convert $\epsilon_{inc,i}$ to ϵ_i . This can be accomplished by combining Eq. 6.4 and Eq. 6.8 to obtain

$$\varepsilon_{inc,i} = \frac{1 + \varepsilon_i}{1 + \varepsilon_1} - 1 \quad (6.10)$$

or rearranging:

$$\varepsilon_i = (1 + \varepsilon_1) (1 + \varepsilon_{inc,i}) - 1 \quad (6.11a)$$

$$\text{where } \varepsilon_1 = \frac{L_1 - L_o}{L_o} = \frac{L_1}{L_o} - 1 \quad (6.11b)$$

and ε_1 is generally unknown. Fortunately, ε_1 can be approximated if the material's stress-strain relationship can be described by Eq. 6.5b and the constant β is known. (The implication of using an incorrect β is described in the Results and Discussion).

6.2.6 Estimating α and ε_1

In imaging experiments, one calculates incremental strain by measuring some specific length L_i as a function of pressure P_i . Thus, substituting Eq. 6.4 (with $L=L_i$) into Eq. 6.5b gives:

$$T_i = \beta \exp \left(\alpha \frac{L_i - L_o}{L_o} \right) - \beta \quad (6.12)$$

Eq. 6.12 can be rearranged as

$$L_i = \frac{L_o}{\alpha} \ln \left(\frac{T_i}{\beta} + 1 \right) + L_o \quad (6.13)$$

It is clear from Eq. 6.13, that a plot of L_i versus $\ln(T_i/\beta+1)$ will yield an intercept equal to L_o , and a slope of L_o/α . Because L_o has been determined, ε_1 can be directly calculated from Eq. 6.11b.

When re-analyzing other research papers, the original L_i data may not be available, but instead only $\varepsilon_{inc,i}$ is available. In this scenario, it is still possible to

calculate α and ε_1 by substituting Eq. 6.11a into Eq. 6.5b, and rearranging to get:

$$\varepsilon_{inc,i} = \frac{1}{\alpha (1 + \varepsilon_1)} \ln \left(\frac{T_i}{\beta} + 1 \right) + \left(\frac{1}{1 + \varepsilon_1} - 1 \right) \quad (6.14)$$

Now a plot of $\varepsilon_{inc,i}$ versus $\ln(T_i/\beta+1)$, yields an intercept of $(1/(1+\varepsilon_1)-1)$ and a slope of $1/(\alpha(1+\varepsilon_1))$.

Thus, given a set of T_i and $\varepsilon_{inc,i}$ (or L_i) data, it is possible to determine α and ε_1 assuming *a priori* knowledge of the material scaling parameter β . A full exponential stress-strain curve can then be plotted (see Fig. 6.1). Thus by calculating α , one obtains a complete description of the material stiffness which is more valuable than just a single modulus value, such as E_{inc} or $E_{seg,i}$, at a corresponding stress level, T_i .

6.2.7 Slope and Error in the Fitted Exponential Curve

For comparison purposes, it is often desirable to calculate the slope of the *fit* stress-strain curve, E_{fit} , at a stress T . This can be accomplished by taking the derivative of Eq. 6.5b as:

$$E_{fit} = \frac{dT}{d\varepsilon} = \alpha\beta \exp(\alpha\varepsilon) \quad (6.15a)$$

By rearranging Eq. 6.5b to obtain ε , and substituting it into Eq. 6.15a, one can show that:

$$\begin{aligned} E_{fit} &= \alpha\beta \exp\left(\alpha \frac{1}{\alpha} \ln\left(\frac{T}{\beta} + 1\right)\right) \\ &= \alpha (T + \beta) \end{aligned} \quad (6.15b)$$

From Eq. 6.15b, the slope of the stress-strain curve can be calculated at any stress level, T . For example, at high stresses (i.e. $T \gg \beta$), E_{fit} is proportional to αT . Similarly, it can be seen that the initial slope at $T=0$, is $E_{fit,T=0}=\alpha\beta$. It will be shown later that for arteries, $\alpha\beta$ is dependent on elastin-collagen matrix at zero load and can be considered as a constant.

It is possible to estimate the percent error in α calculated using incremental data compared to α calculated from having a full stress-strain curve. By modifying Eq. 6.15b for a constant T , and assuming β is a perfect fit to the actual data, it can be shown that:

$$\% \alpha_{err} = 100 \frac{\alpha - \alpha_{full}}{\alpha_{full}} = 100 \frac{\Delta E_{fit}}{\alpha_{full} (T + \beta)} \quad (6.16)$$

where $\% \alpha_{err}$ is the percent error in α , α_{full} is the best fit exponential stiffness parameter to the full tensile stress-strain data, and ΔE_{fit} is the absolute difference between E_{fit} and E at the stress level T . Thus it is clear that errors in α are proportional to the difference in the slopes of the fit curve and the real data at the same stress level. Eq. 6.16 assumes that β is a perfect fit and the full data is exponential as described by Eq. 6.5b. In reality, Eq. 6.5b only approximates the data so that β is only an estimate and hence, this is another source of error for α .

Although α can be used to describe a full exponential stress-strain curve, it should be kept in mind that α was calculated from a limited amount of incremental data. Hence, α should be considered as being *extrapolated* from the incremental data.

6.2.8 Stress Calculations for Thick Walled Tubes

In the Section 6.2.2, I described how the stress is calculated in uniaxial tensile testing. To compare the uniaxial tensile data with incremental stress-strain data from tubular phantoms or arteries, one needs to be able to calculate the stress within the artery wall. Since this thesis only deals with the stress and strain in the circumferential direction, it can be shown that at a radius r in a pressurized, cylindrical, isotropic, thick walled, elastic tube, the circumferential stress, T_θ , is given by:^{20,21,19}

$$T_\theta = \frac{P_i R_i^2}{R_o^2 - R_i^2} \left(1 + \frac{R_o^2}{r^2} \right) \quad (6.17)$$

Because the material was assumed to be isotropic, this equation is only

valid away from any discontinuities where shear stresses must be considered. I will use Eq. 6.17 to obtain stress from pressure and radius measurements to determine the exponential stiffness parameter. Although Eq. 6.17 was derived for a linearly elastic body, I assume that it is a reasonable estimate of circumferential stress in the exponential model for the somewhat linear region below the heel of the stress strain curve. Improvements in Eq. 6.17 can be made by using Eq. 6.5b instead of Hooke's law of linear elasticity^{20,21,19} in its derivation. However, the analytic solution becomes more difficult, and numerical methods must be applied.

In using Eq. 6.17, it is necessary to have a center reference point so that radial distances can be obtained. In real specimens, the wall thickness is not generally constant, and thus the center is not well defined. In this work, the center was arbitrarily chosen as the best fit circle to the inner lumen wall. For stress calculations this choice is acceptable since it is not necessary to accurately know the precise center. For example, the radial distances in high resolution MR images are typically 60 to 80 pixels and thus an error of 1 or 2 pixels in the center location results in a small stress error of approximately 1 to 3%.

6.3 Methods

In order to validate the proposed theory, the methods section is sub-divided in to five different parts. In Part A, the preparation of the samples is described. These include fabrication of PVA cryogel phantoms into tubes that (i) are straight, (ii) have a cosine stenosis, and (iii) have dual elastic properties. In section (iv), the preparation of intact porcine aortic sections are described. In Part B, full uniaxial tensile tests were performed on strips of PVA cryogel and porcine aortas so that the average β could be determined for each of the material types. In Part C, some of the specimens used in Part B were also subjected to incremental tensile tests. These experiments permitted us to validate the extrapolation method. In Part D, I describe a specialized MR imaging system required to image dynamic arterial specimens and phantoms *in vitro*. In Part E, post processing techniques required to determine the geometric dimensions of (i) cylindrically symmetric PVA phantoms and intact porcine aortic sections, and (ii) PVA phantoms with dual elastic

properties are explained. Finally we describe how MR tag lines are used to measure length (and hence strain) from image to image.

6.3.A Phantoms and Specimens

6.3.A.i Straight PVA Cryogel Tubes

An aqueous solution of $15.0 \pm 0.2\%$ by weight PVA (available from Business Development Office, London Health Sciences Centre, London, Ontario N6A 4G5) was poured into annular polycarbonate molds to produce phantoms with dimensions 15.2 cm long, 19.1 mm O.D. and 12.7 mm I.D. Each tube was air cooled to -20°C for 10.5 hours and then thawed using an air temperature of 25°C for 9.2 hours. Each tubes was given a different number of freeze-thaw cycles^b ranging from 1 to 10.

6.3.A.ii PVA Cryogel Tube With Cosine Stenosis

In this section a technique of manufacturing a distensible tube phantom with a cosine stenosis is described. This tube will be used in MR experiments to verify that incremental elastic measurements can be extrapolated to give exponential stress-strain curves.

An aluminum rod 9.52 mm diameter by 28.2 cm long was lathed in such a way that a cosine shaped narrowing was formed into the rod. The exact shape of the narrowing can be described using the following equation for the rod radius in units of mm: $r_{\text{rod}} = 4.07 + 0.69 \cos(2\pi(x-202)/16.7)$, where x is the longitudinal distance along the rod and ranges from 202 mm to 218.7 mm. This rod was placed inside a polycarbonate tube (15.9 mm I.D., 22.2 mm O.D., and 22.8 cm long) and centred using rubber O-rings. The space between the tube and rod was filled with a 15% PVA solution. The complete mold assembly was frozen twice. This created a phantom with a cosine stenosis near the distal end of the mold. Fig. 6.4 is a schematic of the mold shape. A total of four phantoms were made and tested.

^b Chapter 5 reported that the elastic properties of PVA cryogel can be adjusted by freezing and thawing, and that 2 freeze-thaw cycles produced a material that has similar properties to porcine aortas.⁶

6.3.A.iii Aortic Phantom With Stiff Elastic Plaque (Dual PVA Phantoms)

A straight PVA tube (from Section 6.3.A.i) that underwent ten freeze-thaw cycles was split longitudinally into two equal pieces. One of the pieces was placed longitudinally into another mold of the same dimensions, and the surrounding volume filled with 15% PVA solution. This mold was then frozen and thawed twice. The new phantom had approximately half of its circumference made with 15% PVA cryogel frozen twice, and the remainder was a stiffer PVA cryogel frozen 12 times. A total of four tubes were made.

6.3.A.iv Porcine Thoracic Aortic Specimens

Porcine aortas were excised from 6 month old pigs at a local abattoir. The specimens were stored in moist air for approximately 11 hours at 4°C. After this time, the surrounding connective tissue from the thoracic aortas were removed. Only sections from intercostals 3 to 6 were used due to the straightness of this region. The specimens were then stored in 0.9% saline solution for another 74 hours before MR imaging or tensile testing as described below.

6.3.B Tensile Testing to Determine β

6.3.B.1 PVA and Porcine Aortic Strips

Circular rings approximately 7 mm wide were cut from porcine upper thoracic aortas (between intercostals 3 to 6) or straight PVA cryogel tubes. Each ring was cut longitudinally to form a strip 7 mm wide. Thickness and width measurements were made using calipers. Each end of the strip was mounted to grips so that the tensile properties in the circumferential direction³⁹ could be measured. The PVA cryogel samples were tested while submersed in water to prevent dehydration. For this same reason, the aortic strips were submersed in 0.9% saline solution during testing. Differences in the stress-strain properties of arteries as a function of test speed have been reported to be insignificant.⁴⁰ Hence, in this work, an elongation rate of either 2 or 10 mm/min was used. The specimens were pre-conditioned by cycling the applied load at least four cycles before any tensile data were collected. For complete stress-strain curves, the load was cycled from 0 to 400 g.

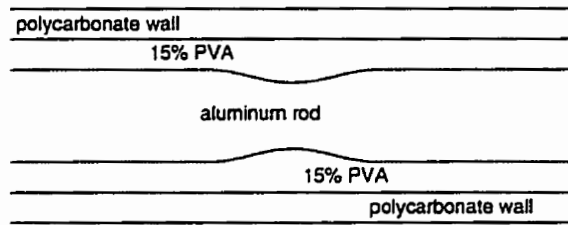


Figure 6.4. A schematic diagram of the cosine stenosed mold used to form a two diameter phantom.

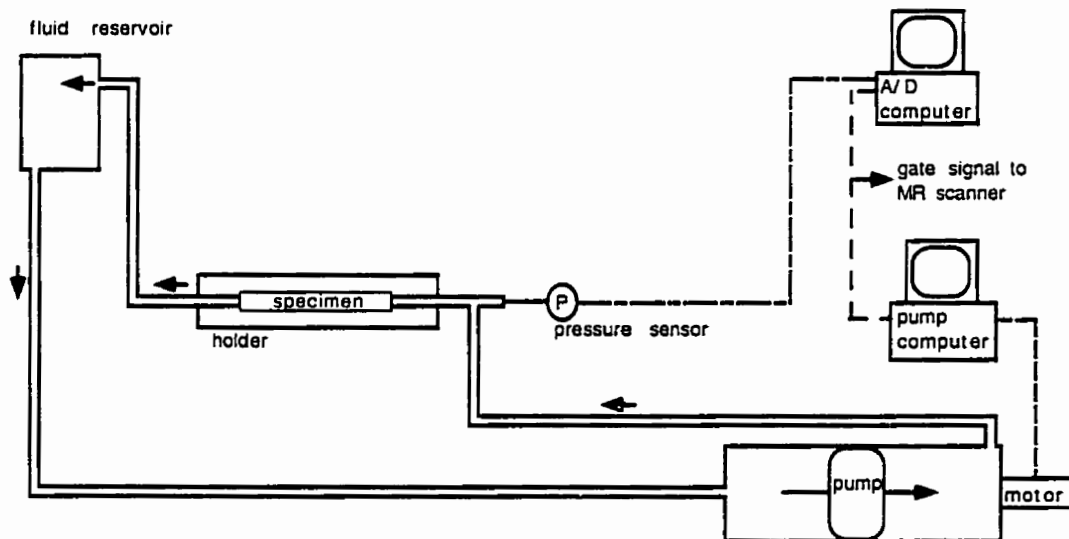


Figure 6.5. A schematic diagram of the equipment necessary to provide *in vitro* dynamic studies of aortic phantoms and arteries. In the diagram, everything to the left of the pressure sensor is inside the MR room. The specimen holder is mounted in an RF coil and placed inside a high resolution gradient coil set centered in the bore of the 1.5T GE Signa MR magnet (not shown).

6.3.C Incremental Tensile Testing

Some of the PVA and porcine aorta specimens tested in section 6.3.B were also tensile tested by increasing the load from 0 g to a preset maximum, and then cycling from the maximum load to 50 g less than the maximum load. Eight different maximum loads were used: 50, 100, 150, 200, 250, 300, 350, and 400 g. An elongation rate of 10 mm/min was used. The specimens were pre-conditioned by cycling the applied load at least four cycles before any tensile data were collected. In all cases the complete stress-strain curves from 0 to 400 g was also recorded.

6.3.D MR Imaging System

6.3.D.i MR Imaging

All imaging was performed inside a water cooled gradient coil with a peak strength of 50 mT/m. A gated fast gradient echo pulse sequence (G.E. Signa 5.4) was modified to allow the option of applying DANTE (Delays Alternating with Nutations for Tailored Excitations¹³) tags after detecting a trigger signal from the computerized pump. The trigger was set to occur when the diameter of the pulsating specimen was at its minimum. The MR imaging parameters were: 20° flip angle; 3.4 ms TE; ± 16 kHz receive bandwidth; 2 k-space lines collected per segment, 33 images per cardiac cycle, 8 NEX; 2.4 cm FOV, 2.5 mm thick slices; 256x128 pixel resolution. Total scan time was 8 minutes and 34 seconds.

6.3.D.ii MR Tags

The DANTE preparation parameters were: 4 hard RF pulses, with pulse spacings of 1500 μ s (250 μ s on and 1250 μ s off). The RF power was adjusted to give a total of 90° flip after the fourth RF pulse. The tag spacing in the image (chosen to be 2 mm over a 24 mm FOV) was controlled by adjusting the amplitude of trapezoidal gradient pulses applied between each RF pulse. After the last RF pulse was applied, a full strength crusher gradient was used to dephase any remaining transverse magnetization. Although tags in two directions could be applied, I chose to use unidirectional tags in the frequency encoding direction only.⁴¹ Each experiment was performed twice, with the frequency encoding and the phase encoding directions swapped for the second set of images. This yielded

sharper tags and permitted simpler tag locating algorithms to be implemented. In addition, the time required to apply one directional tags is half of that required to apply two directional tags. Superposition of the two orthogonal tag locations yields tag intersections that can be tracked precisely. Because this method requires 2 sets of images at a resolution 256x128, the imaging time is the same as that of a 256x256 image, yet the post processing is significantly simplified.⁴¹ The drawback in using two sets of orthogonal directional tags to form a cartesian grid is in the assumption that the motion is reproducible between the two sets of collected images, and that there are no phase errors in swapping the frequency and phase encode gradients. This drawback was not a concern in this study since the intersection of the outer boundaries of the arterial specimens (and phantoms) with the one directional tags were chosen for the length (and strain) measurements.

6.3.D.iii MR Compatible Pulsatile Pumping System

A schematic diagram of the system is shown in Fig. 6.5. A computer controlled pump filled with trichlorotrifluoroethane⁵ (R-113) was used to generate sinusoidal pressure waves with an amplitude of approximately 4 to 5.3 kPa (30 to 40 mm Hg) at 1 Hz. The height of the pump reservoir was adjusted to provide mean pressures near 13.3 kPa (100 mm Hg). To obtain the proper pressure waveform, the optimum flow rate, Q_t , for the pump was set to deliver $Q_t = (6 - 6\cos(2\pi t))$ ml/s, where t is the time. R-113 was used because it has no hydrogen protons, and thus did not contribute to any flow artifacts in the *in vitro* experiments.

The transmural pressure at the centre of the specimen was transferred to a solid state pressure transducer (Model PX26-005GV, Omega Engineering, Stamford, CT) using 45 cm of 1.56 mm I.D. polyethylene catheter tubing. The pump computer program was programmed to provide a trigger signal to the MR scanner to indicate when the specimen was near "diastole" (i.e. minimum diameter). All specimens were mounted horizontally and surrounded with 100% humid air at 20°C.

6.3.D.iv Pressure Data

The gated pressure data were collected before and after MR imaging and averaged and fit to a cosine waveform by using a least squares fitting routine. The cosine waveform equation was

$$P = P_{DC} - P_A \cos(\omega t + \phi_p) \quad (6.18)$$

where P is the measured pressure, P_{DC} is the mean pressure, P_A is the amplitude of the pressure wave, ω is the frequency of the pressure wave in radians per second, and ϕ_p is the phase shift. The pressure at the time of the image data collection was calculated from the fit equation.

In phantoms where the imaged inner diameter was different from the diameter where the catheter probe was located, the pressure at the imaging location was estimated by applying a modified Bernoulli's Equation:

$$P_i = P + \frac{\rho_f V^2}{2} \left(1 - \frac{A}{A_i} \right) \quad (6.19)$$

where P_i is the lumen pressure at the imaging plane, A_i is the lumen cross sectional area at the imaging plane, A is the cross sectional area of the lumen where the catheter is located (not including the catheter itself), ρ_f is the density of the fluid, and V is the average fluid velocity at the catheter location. V is calculated as the pump flow delivery rate Q_f divided by A . In general, these corrections were always less than 2% of the actual pressure.

6.3.E Post processing

6.3.E.i Geometric Dimensions of Cylindrically Symmetric Vessels

All MR images underwent post-processing so that the inner and outer edges of the specimen cross-sections could be accurately determined. The procedure for each image was as follows. 1) All pixels with intensities less than the mean noise level were set to zero. 2) A Sobel operator edge detection algorithm⁴² was used to create a binary image which assigned a value of one to all edges in the original MR image. Pixel growing techniques could not be used to find the inner and outer

walls in the binary image because the DANTE tag lines caused the lumen wall to have discontinuities. The binary image was superimposed onto the original image so that 3) a semi-automated process could be used for finding the locations of 12 points around the circumference of the binary image. I manually picked 12 points *near* the edge of the binary circumference, and the computer determined the exact pixel location of the nearest edge point. This process was repeated for both the lumen and outer walls in the image. 4) The inner and outer picked points were fit separately to a rotated ellipse in a least squares minimization program to find (with sub-pixel accuracy) the centre coordinates X_0 and Y_0 , the ellipse dimensions a and b , and the major axis rotation angle Θ based on the equation:

$$\left(\frac{X''}{a}\right)^2 + \left(\frac{Y''}{b}\right)^2 = 1 \quad (6.20)$$

where $X''=R\cos(-\Theta)$, $Y''=R\sin(-\Theta)$, and $R=[(X-X_0)^2+(Y-Y_0)^2]^{1/2}$, and X and Y are the corresponding cartesian coordinates from the 12 picked points. I chose ellipses rather than circles so that any non-circularities could be accounted for. Most data sets showed a nearly circular form. 5) From the ellipse parameters, the boundaries of both inner and outer walls were interpolated back to X-Y coordinates at regular angular intervals of 0.05 radians (2.86°) with respect to each ellipses' centre coordinates (from the fitting routine). This produced 125 points (with sub-pixel accuracy) describing the inner and outer boundaries. 6) Before any radius measurement could be made, it was necessary to pick one reference point in each image. This point was arbitrarily picked as the centre of the best least squares fit *circle* to the twelve inner wall points picked in step 3. 7) With this reference centre, the 125 X-Y points of the inner and outer walls were converted to polar coordinates, and the corresponding inner and outer radii recorded at 125 equal intervals.

6.3.E.ii Dimensions of Dual PVA Phantoms

Samples with a dual PVA structure were treated slightly differently than the more homogeneous samples. For these phantoms, there were essentially four

different surfaces that had to be fitted: The inner and outer walls of the *flexible* PVA cryogel (frozen twice), and the inner and outer walls of the *stiff* PVA cryogel (frozen 12 times). Hence, four different rotated ellipses were fitted to the semi-manually picked points described above. To separate points belonging to the *stiff* or *flexible* PVA, the program asked that the boundary of the stiff material be selected. With this information, the complete boundary in cartesian coordinates could be reconstructed with sub-pixel accuracy. To measure the radius of this non-symmetrical boundary, the reference center point in each image was the centre of the circle that best fit all of the picked points of the inner wall.

6.3.E.iii Tag Intersections and Length of Lines

Although sophisticated tag locating algorithms have been developed as the basis of several major studies,^{43,44,45,46,47} I chose to simplify this study by magnifying the images and manually selecting a vertical tag centre *near* either the inner and outer boundaries. A simple algorithm interpolated the fitted X-Y boundary to locate the exact intersection with the selected vertical tag. Images with horizontal tags were first rotated 90° and then treated in the same fashion.

Fig. 6.6 shows a schematic of how a line AB with length L_1 can be decomposed into radial and circumferential components. If the angle of line AB is Φ_L , and the angle of the radial axis is Ψ , then line AB can be projected to have a radial length $L_r = L_1 \cdot \cos(\Psi - \Phi_L)$ and a circumferential length $L_\theta = L_1 \cdot \sin(\Psi - \Phi_L)$. The radial axis is defined as the line from the centre reference point to the midpoint of line AB. This methodology ignores any changes in length due to shearing.

6.4 Results and Discussion

6.4.A PVA Cryogel Phantoms

The fabricated PVA phantoms were found to (1) be flexible and tough, (2) have similar elastic properties to that of porcine aortas, (3) be fully compatible with the pumping fluid R-113, and (4) have MR image intensities similar to porcine aortas. The PVA cryogel was found to be easily adaptable to pumping systems without leaking; thus the PVA cryogel was considered as the ideal phantom material for this study.

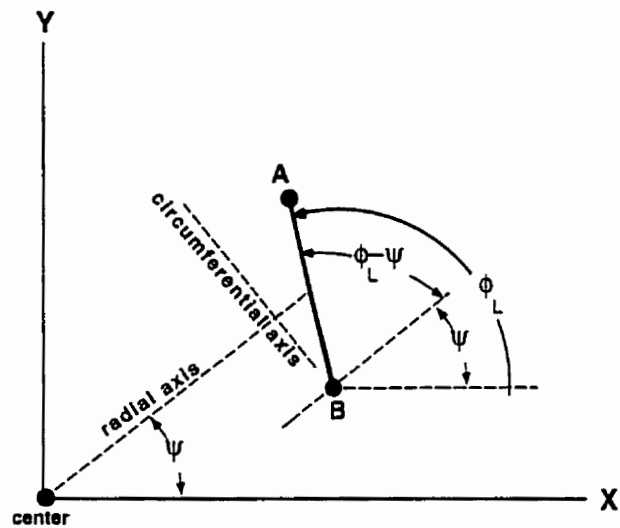


Figure 6.6. A schematic diagram showing how the length of a line segment (thick line) defined by two points in a cartesian coordinate system can be described in a polar coordinates based on a reference point (i.e. lumen center).

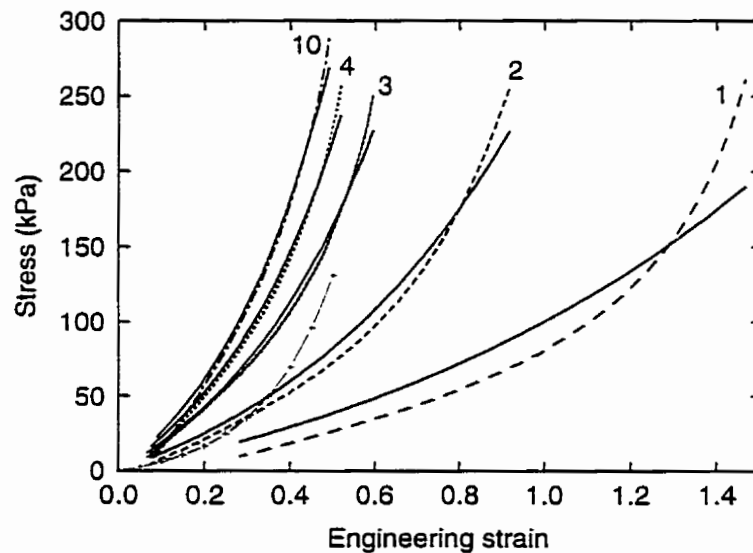


Figure 6.7. Stress-strain curves for PVA cryogel frozen 1, 2, 3, 4, and 10 times. The measured data are the dashed lines and the least squares fitted data (with β fixed at 64.759 kPa) are the solid lines. The + symbol is the best fit line representing porcine aortas as described in the next section.

Table 6.1. Stiffness parameter, α , for PVA cryogel as a function of freeze-thaw cycles. The scaling parameter, β , was assumed to be 64.759 kPa. The values in brackets are the percent deviation from the mean α .

15% PVA Cryogel, times frozen	mean α	$\alpha_{z\beta,max}$ (% from mean α)	Range of $\alpha_{z\beta}$
1	0.94	0.49 (52)	1.43-0.71
2	1.72	0.74 (43)	2.44-1.26
3	2.53	1.22 (48)	3.75-1.94
4	3.00	1.38 (46)	4.38-2.28
5	3.14	1.43 (46)	4.57-2.44
10	3.35	1.52 (45)	4.87-2.60

6.4.B β From Tensile Tests

As described in the theory section, my hypothesis depends on knowing the scaling parameter β for various classes of materials. For these reasons, β was measured for 15% PVA cryogel and for porcine thoracic aorta.

6.4.B.1 β For PVA

Fig. 6.7 shows typical stress-strain curves for PVA cryogel frozen 1, 2, 3, 4, and 10 times. A non-linear least squares fit to Eq. 6.5b was performed on these samples as well as 8 other stress-strain curves from 15% PVA cryogel (frozen twice) samples. After the optimum α and β for each sample were determined, the average β and its standard deviation were calculated to be 64.759 ± 35.017 kPa. Using this average β for PVA cryogel, all of the stress-strain data were fit to Eq. 6.5b with α allowed to vary. The results are shown in Table 6.1. For example, the 15% PVA cryogel frozen twice had an average α of 1.72 and a standard deviation in α of ± 0.37 ($n=9$).

An alternative estimate of the error in the α parameter is obtained by calculating the best fit α given a fixed β increased or decreased by one standard deviation compared to the average (i.e. 99.776 or 29.742 kPa). The maximum difference between these new α values and the original α (with average $\beta=64.759$ kPa) is reported in Table 6.1 as $\alpha_{-\beta, \max}$, the error due to β . As shown in Table 6.1, $\alpha_{-\beta, \max}$ was approximately 43 to 52% of the average α value for all PVA samples. Hence the error in α can be quite substantial; however, because $\alpha_{-\beta, \max}$ is known, it is possible to estimate a lower and upper bound to the estimated α due to having an incorrect β . To gain a full appreciation of the true errors, a full quantitative error analysis should be performed.

6.4.B.2 β From Tensile Tests of Porcine Aortas

A similar procedure was used to determine β for porcine aortas. The stress-strain data from 28 samples (four pieces of aortic rings from 7 different aortas) were fit to Eq. 6.5b and values for α and β extracted from the fit. The average β was determined to be 7.357 ± 3.935 kPa. Using a fixed β of 7.357 kPa, all of the stress-strain data were then fit to Eq. 6.5b to find the best α . The average α and

standard deviation from all 28 porcine stress-strain curves was 5.87 ± 0.72 . Typical tensile testing data from the porcine aortas are shown in Fig. 6.8. The numerically best fit line falls within the range of most of the experimental data. At low strain levels ($\epsilon=0$ to 0.3), the fit curve underestimates the stress. Qualitatively, it is apparent that the single exponential model is not ideal for porcine aortas, and should only be considered as a first approximation to the data.

Regardless of the shortcomings of the exponential model, I propose that at low stresses, i.e. below the heel of the stress-strain curve (i.e. 75 kPa), the application of Eq. 6.5b is adequate. This is a reasonable assumption because at higher stresses, the specimen would be in a state of hypertension and the strain on the artery would be limited by the collagen matrix within its wall. This higher stress range is not the normal physiological regime that I wish to study.

In addition, improved methods of choosing the average β may be needed. I arbitrarily took the average β of 28 different stress-strain curves. It may be more appropriate to subdivide¹⁵ the stress-strain data into a high stress region and a low stress region, and then determine a β for each region separately. Or perhaps a more sophisticated multi-parameter model can be used to fit the actual data.^{48,8} Unfortunately, the parameters in such models have no direct physical meaning. Although Wuyts et al⁴⁹ proposed a sophisticated mathematical model with each of its 8 parameters representing different physical properties of the structural components found in arteries, 4 of the parameters had to be measured from histological studies of the individual specimens, and the other 4 parameters were numerical fit from experimental tension-radius curves performed using *ex vivo* segments.

Physiologically, it is reasonable to assume that the product $\alpha\beta$ is nearly constant for arteries from the same age group. Arteries with similar compositions have similar initial slopes in a stress-strain curve because the elastic behaviour of arteries at low stress is controlled by the energy required to strain a composite mixture of elastin and collagen above its zero-load state. For example, the 28 porcine aortic stress-strain curves in this study had an average initial slope, $\alpha\beta$, of

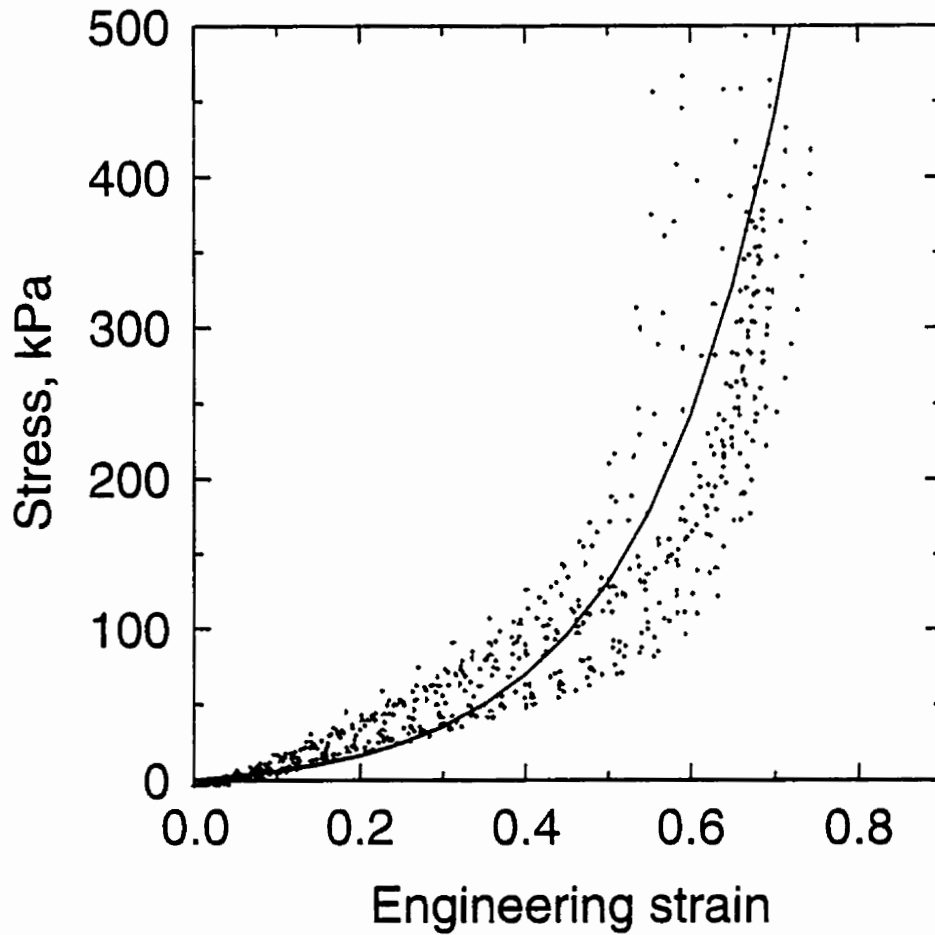


Figure 6.8. Stress-strain curves from 28 samples of porcine aortas are shown by the dots. The solid line is the theoretical fit line using Eq. 6.5b with α and β equal to the average of the values from the 28 individual fits. Since the theoretical line does not closely mimic the true stress-strain data, it is apparent that the single exponential model may not be the best model to use.

43 kPa. This compares favourably with the initial slopes of stress-strain curves of aortas measured from data extracted from He et al⁵⁰ ($E_{T=0} \approx 37$ to 75 kPa); Storkholm et al⁵¹ ($E_{T=0} \approx 58$ to 104 kPa); and Roach and Burton⁵² ($E_{T=0}$ 14 to 65 kPa).

6.4.C Incremental Tensile Testing

6.4.C.1 Incremental Tensile Testing for PVA

In order to evaluate how well incremental tensile data can be used to obtain an estimate of the full uniaxial tensile curve, I performed incremental tensile tests (with different average stress levels) on samples of PVA cryogel (frozen twice). A full stress-strain curve was also obtained by cycling the load from 0 g to 400 g. Typical results are shown in Table 6.2 and Fig. 6.9.

Figure 6.9a shows the data from the original incremental experiments plotted on the left; on the right side of the same plot is the same data with the strain linearly shifted so that the incremental data for each experiment starts from the full stress-strain curve. It is clear that slopes of the incremental data are not equal to the tangents of the full stress-strain curve at any stress level (Table 6.2). Fig. 6.9b shows the incremental strain adjusted by applying Eq. 6.11a with ϵ_1 set equal to the linear shift used in Fig. 6.9a. Fig. 6.9b shows that there is good agreement between the adjusted incremental data and the full stress-strain curve.

However, ϵ_1 is not normally known, and it is necessary to estimate it using the procedures described in section 6.2.6. These results are shown in Fig. 6.9c. Qualitatively, it is apparent from Fig. 6.9c. that the extrapolation method does not accurately predict the proper stress-strain curves when the stress level is higher than approximately 75 kPa. From Table 6.2, it can be seen that at the highest stress level, ϵ_1 is severely underestimated (by as much as 75%) which causes α to be over estimated by a factor of 2.7. The error in predicting α is caused by the single exponential fit with a single fixed β to the actual stress-strain curve. The dashed line in Fig. 6.9c is the best single exponential fit to the actual data. Qualitatively, the dashed line appears to be a reasonable fit to the actual data. However, it is apparent that the dashed line starts to deviate at the high stress

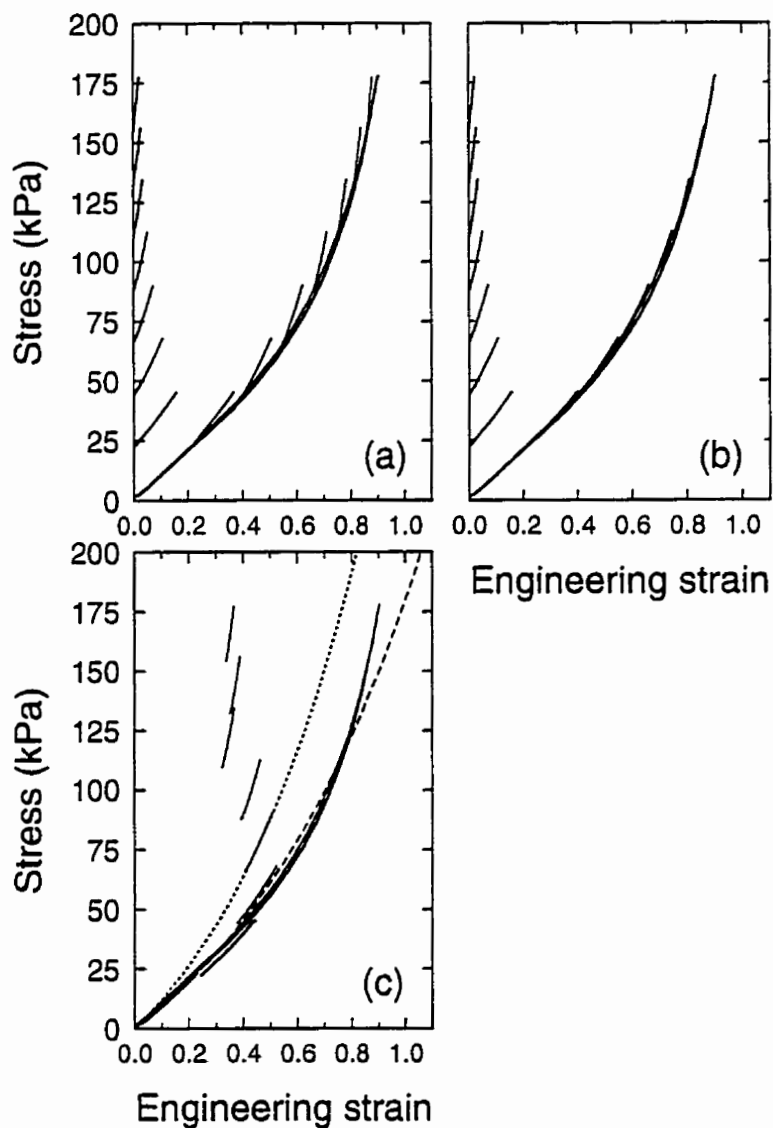


Figure 6.9. Incremental tensile stress-strain data for PVA cryogel. In (a), the strain of incremental data always starts at zero. A linear shift applied to ϵ_{inc} reveals that the slope of the incremental data is always higher than the slope of the full stress-strain curve at similar stress levels. By using Eq. 6.11a with ϵ_i chosen as the linear shift value used in (a), the results in (b) match closely to the stress-strain curve. The results from using Eq. 6.13 are reported in (c). The solid lines are the actual data. The dashed line is the best fit by Eq. 6.5b to the full stress-strain data; and the dotted line is from Eq. 6.5b with $\alpha=1.72$ (i.e. PVA cryogel frozen twice).

Table 6.2. Typical incremental tensile data for PVA cryogel frozen twice.
The values in brackets are percent deviation from the actual value.

Load range, g	Mean Stress, kPa	E_{inc} , kPa, (% from E)	E, kPa, from full stress-strain curve	E_m , kPa, (% from E)	estimated α	actual % error in α relative to $\alpha_{theor}=1.33$	% α_m as predicted by Eq. 6.16	ϵ_1 , fitted (% from theoretical value)	ϵ_1 , theory
0-50	11.7	102 (-4)	106	102 (-4)	1.34	1	-16	0.01 (1)	0.00
50-100	33.4	146 (33)	110	118 (7)	1.20	-10	15	0.25 (-14)	0.29
100-150	55.3	225 (54)	146	164 (12)	1.37	3	22	0.38 (-22)	0.49
150-200	77.4	343 (74)	197	244 (24)	1.72	29	42	0.41 (-37)	0.65
200-250	99.1	484 (87)	264	356 (35)	2.17	63	65	0.39 (-49)	0.76
250-300	120.8	749 (118)	343	586 (71)	3.06	130	143	0.32 (-62)	0.85
300-350	142.9	884 (106)	430	655 (52)	3.16	138	113	0.35 (-62)	0.91
350-400	164.6	1105 (120)	503	827 (64)	3.60	171	142	0.24 (-75)	0.96

levels (above 75 kPa), and the slope of the dashed curve at these stress levels is significantly lower than that of the actual data. In general, large differences between the slope of the fit curve (E_{fit}) and the slope of the real stress-strain curve results in large errors in α as shown in Table 6.2 and Figure 6.9c. Table 6.2 also compares the measured percent error in the estimated α 's with the theoretical error (Eq. 6.16). The theoretical errors do not accurately reflect the actual measured errors. However, they do provide a guide on how the order of magnitude in the errors escalates with the absolute differences in the slope of the fit stress-strain curve and the real data. Since the differences in slopes increase at high stress levels, improved estimates of α can be obtained for the high stress regime only if the mathematical model could be adjusted so that the fit is more accurate at higher stress levels.

At stress levels below 75 kPa, Table 6.2 show that the error in the calculated α varies from -10 to +29% which is reasonable for extrapolation methods. Hence, the concept of extrapolating incremental data to a full exponential stress-strain curve represented by a single α value (with a fixed β) is feasible.

In terms of elastic modulus, Table 6.2 shows that E_{inc} varies from -4 to +120% of E . After applying the extrapolation, the difference between E_{fit} and E is reduced to -4 to +64%. If I consider only data corresponding to stresses below 75 Kpa, the error in E_{fit} is less than 24%. Hence, compared to the E_{inc} , E_{fit} can be considered as an improved estimate of E . Remaining differences between E and E_{fit} can be explained by the single exponential model not being able to fit the real data accurately at higher stress levels.

It is unclear as to whether the extrapolation method can be improved by using a double exponential model since incremental data from *in vivo* studies do not cover a large range of strain values and the strain data may contain a significant amount of noise. In addition, by using a more sophisticated model, the simplicity of having a single stiffness parameter to represent a complete stress-strain curve is lost. It may be more useful to use two single exponential models to represent the low and high stress ranges separately.¹⁵

The importance of using the α rather than E_{inc} is now clear. The exponential stiffness parameter gives the full stress-strain curve from which the slope can be calculated at any stress-strain level; whereas, E_{inc} only gives a single over-estimate of E at one particular stress level. However, caution should be used as in any extrapolation method, the errors can be significant.

6.4.C.2 Incremental Tensile Testing for Porcine Aorta

An experiment was performed to determine how well incremental tensile data from porcine aortas could be used to estimate the α parameter of their full uniaxial tensile curve. Typical results are shown in Table 6.3 and Fig. 6.10.

Figure 6.10a shows the data from original incremental experiments plotted on the left; on the right side of the same plot is the same data with the strain linearly shifted so that the incremental data for each experiment starts from the full stress-strain curve. It is clear that slopes of the incremental data are not equal to the tangent of the full stress-strain curve at the same stress levels except for the lowest stress levels. Fig. 6.10b shows the incremental strain adjusted by applying Eq. 6.11a with ϵ_1 set equal to the linear shift used in Fig. 6.10a. In Fig. 6.10b there is good agreement between the adjusted incremental data and the full stress-strain curve. However, the agreement is not perfect. The remaining differences in the slopes are attributed to the ability of the arterial specimen to react differently depending on its previous stress-strain history.

Since ϵ_1 is not normally known, I must calculate it using the procedure described in section 6.2.6. These results are shown in Fig. 6.10c and Table 6.3. At the highest stress level, ϵ_1 is severely underestimated by as much as 71% which causes α to be over estimated by a factor greater than 4. Qualitatively, it is apparent from Fig. 6.10c that the extrapolation method does not accurately predict the proper stress-strain curves at stress levels above 75 kPa. The dashed line in Fig. 6.10 is the best single exponential fit to the actual data, and it is apparent that the slope of the dashed curve deviates significantly from the actual data at stress levels above 75 kPa. Table 6.3 also compares the measured percent error in the estimated α 's with the theoretical error (Eq. 6.16). The theoretical errors provide

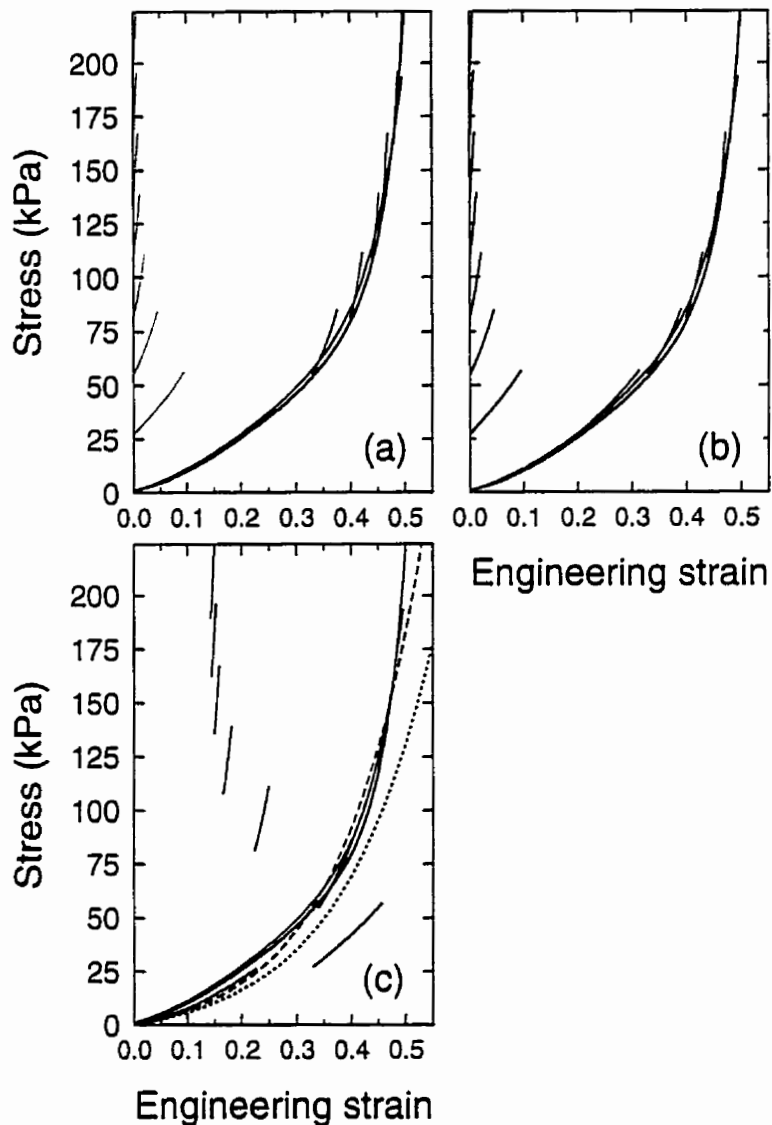


Figure 6.10. Incremental tensile stress-strain data for porcine aorta. (a) shows that strain of incremental data always starts at zero. A linear shift applied to ϵ_{inc} reveals that the slope of the incremental data is always higher than the slope of the full stress-strain curve at similar stress levels. By using Eq. 6.11a with ϵ , chosen as the linear shift value used in (a), the results in (b) match closely to the stress-strain curve. The results from using Eq. 6.13 are reported in (c). The solid lines are the actual data. The dashed line is the best fit by Eq. 6.5b to the full stress-strain data; and the dotted line is from Eq. 6.5b with $\alpha=5.87$ (i.e. average value for porcine aortas).

Table 6.3. Typical incremental tensile data for porcine aortas.

The values in brackets are percent deviation from the actual value.

Load range, g	Mean Stress, kPa	E_{inc} , kPa, (% from E)	E, kPa from full stress-strain curve	E_m , kPa, (% from E)	estimated α	actual % error in α relative to $\alpha_{theor}=5.55$	% α_{est} as predicted by Eq. 6.16	ϵ_1 , fitted (% from theoretical value)	ϵ_1 , theory
0-50	11.5	123 (-10)	136	131 (-4)	6.98	26	-5	0.02 (2)	0.00
50-100	41.1	306 (37)	224	228 (2)	4.71	-15	1	0.33 (65)	0.20
100-150	68.5	647 (75)	370	472 (28)	6.22	12	24	0.34 (3)	0.33
150-200	94.8	1389 (110)	663	1137 (71)	11.1	100	84	0.22 (-45)	0.40
200-250	122	2490 (151)	994	2137 (115)	16.5	197	159	0.17 (-61)	0.44
250-300	150	3677 (157)	1432	3113 (117)	19.8	257	192	0.15 (-67)	0.46
300-350	178	4731 (182)	1680	4024 (140)	21.7	291	228	0.14 (-71)	0.48
350-400	205	5720 (213)	1826	4867 (167)	23.0	314	258	0.14 (-71)	0.49

a guide on how the order of magnitude in the errors escalates with the absolute differences in the slope of the fit stress-strain curve and the real data. Since the differences in slopes increase at high stress levels, an improved estimated of α can be obtained for the high stress regime only if the mathematical model could be adjusted so that the fit is more accurate at higher stress levels.

From Table 6.3, it can be seen that at stress levels below 75 kPa, the error in predicting α ranges from -15 to +26% of the actual value of $\alpha_{full}=5.55$. Thus the extrapolation of incremental data to a full stress strain curve represented by a single α value (with a fixed β) is reasonable only at low stress levels. Even though the single exponential model is very simplistic, I have demonstrated that the technique does an adequate job in handling the biological variations found in the porcine aortic stress-strain curves.

Table 6.3, shows that E_{fit} is a good estimate of the elastic modulus E . At stress levels below 75 kPa, E_{fit} is always within 28% of the actual elastic modulus. Without performing the extrapolation procedure, the error in E_{inc} varies up to 75% over the same stress range. Table 6.3 also reveals that the differences between E_{inc} and E increases quite rapidly as the stress is increased. Clearly, E_{inc} cannot be considered to be the same as E .

6.4.D Incremental Data From MR Imaging

6.4.D.i Incremental Data from Cosine Stenosis Phantom

The results from the cosine stenosis phantom experiments demonstrate the limitations in reporting E_{inc} values. Fig. 6.11 shows the longitudinal MR image of this cosine stenosis phantom. Two separate series of cross-sectional MR images were made: one at the thick section and the other at the thin section of the phantom. In each series, 33 gated MR images corresponding to cross-sectional views at various times throughout the cardiac cycle were obtained. Images at the two separate locations are shown in Fig. 6.12. Figs. 6.12 (c) and (d) also show an example of how 12 consecutive tag points on the outer boundary of the phantom are used to form 11 different lines that can be tracked from image to image. By following the lengths of each line, the incremental strains can be calculated using

Eq. 6.8 where the first image (diastole) contains the lengths L_1 .

By using Eq. 6.17 to calculate the incremental circumferential stress for each image. A typical plot of average L_1 versus $\ln(T/\beta+1)$ for the thick and thin walled regions of a PVA stenosis phantom is shown in Fig. 6.13a. The extrapolation process described in the theory section predicts that the intercept is L_0 and the slope is L_0/α . From this information, ϵ_{inc} can be adjusted using Eqs. 6.11a and 6.11b so that Fig. 13b can be made. Typical stress-strain curves for the thick wall section (at the stenosis) and thin wall sections (2.5 cm down stream from the stenosis) are shown in Fig. 6.13b. Note that in Fig. 6.13b, the incremental data is shown on the left side starting with an incremental strain of zero. The average E_{inc} for the thin wall section was 209 kPa, and the average E_{inc} for the thick walled

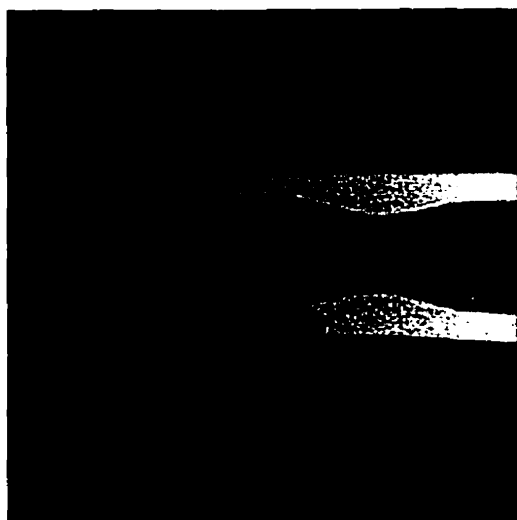


Figure 6.11. MR image of the longitudinal cross section of a PVA cryogel tube with a cosine stenosis (4.8 cm FOV).

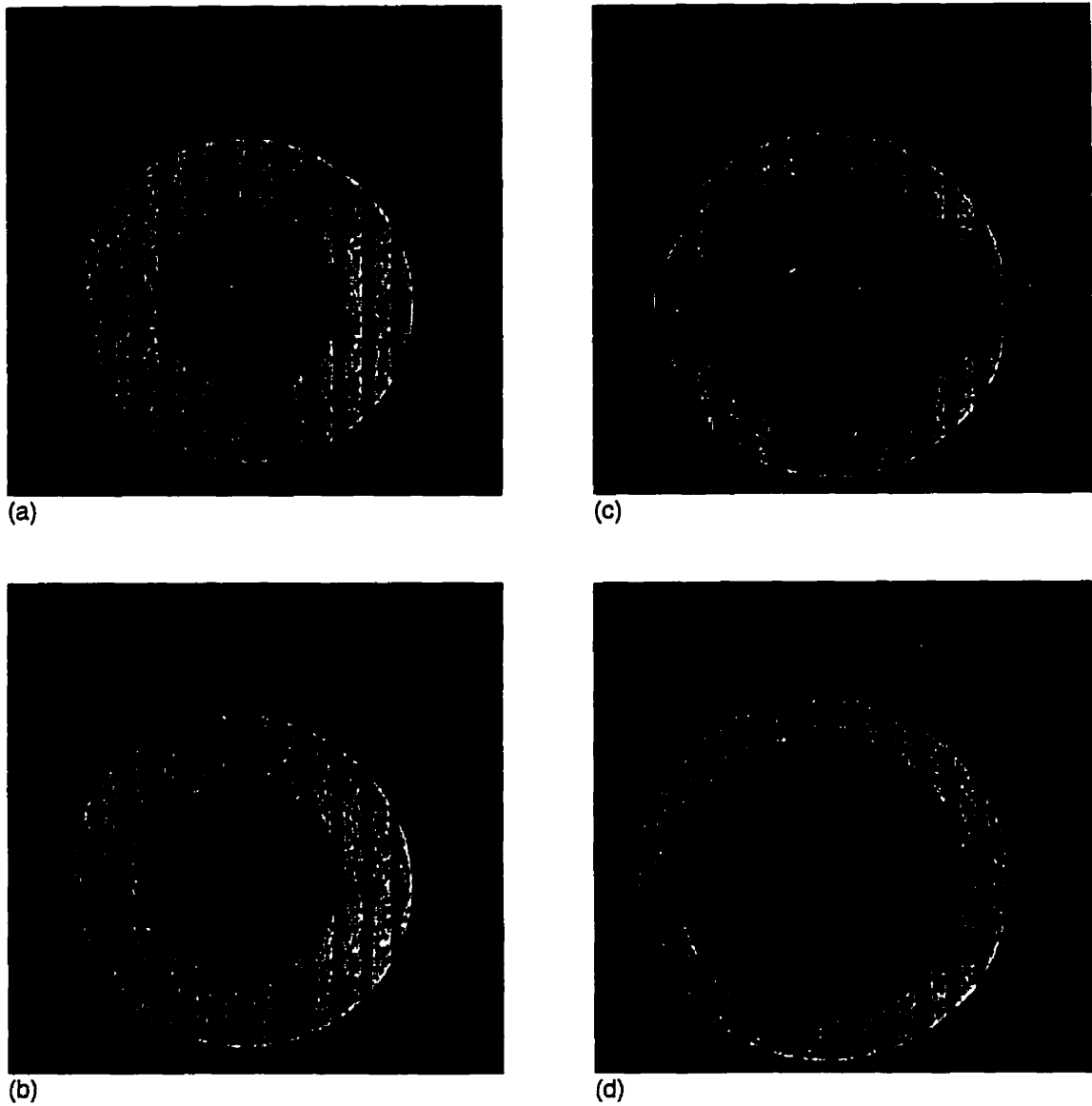


Figure 6.12. Circular cross sections of cosine stenosis phantom at the thick wall region in the centre of the stenosis (a and b), and in the thin wall region 2.5 cm upstream of the stenosis (c and d). Images (a) and (c) were obtained 70 ms after the gating signal (diastole) while (b) and (d) were obtained 406 ms after the gating signal (systole). A few tag points are shown on the outer top half of the thin wall images (c) and (d). P_m at diastole and systole were 11.8 kPa and 14.5 kPa, respectively. The mean pressure was the same for both the thick and thin wall sections.

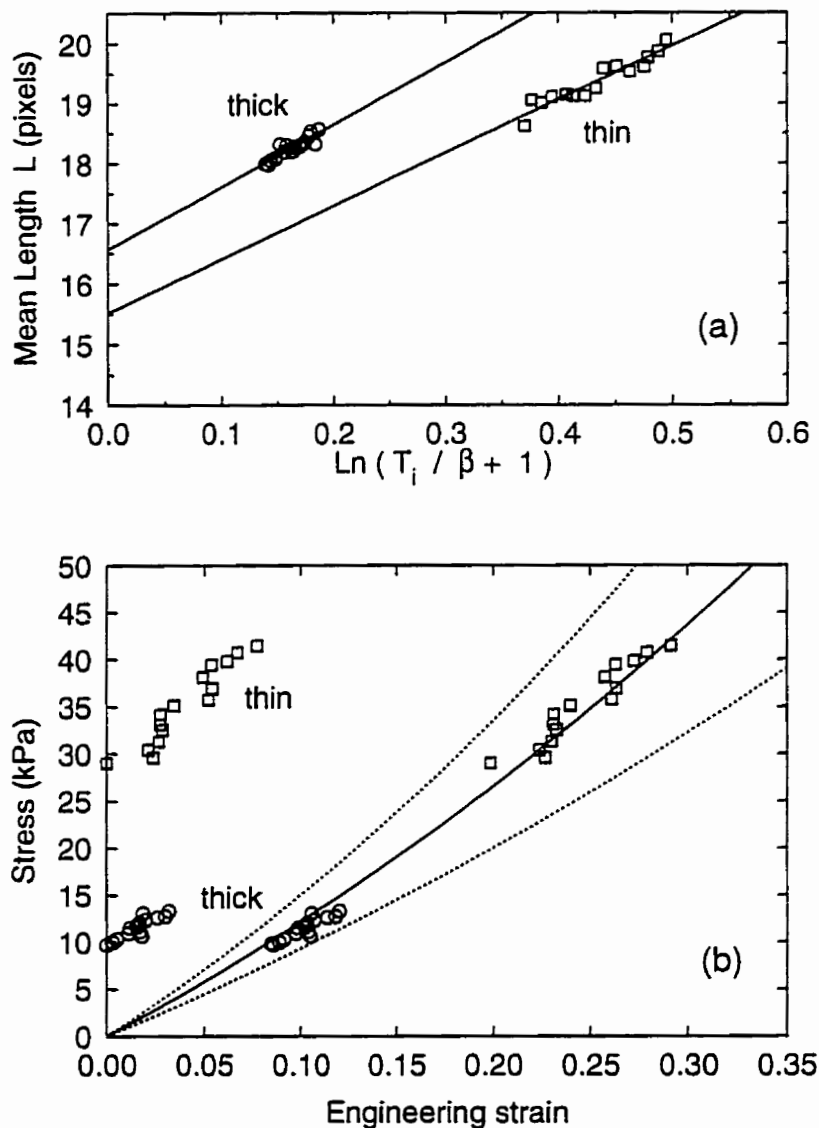


Figure 6.13. A typical plot of mean L , versus $\ln(T/\beta+1)$ for the thick and thin walled regions of a PVA stenosis phantom (a). The results from the thin wall section are given by squares, while the thick walled stenosed results are given by the circles. A linear least squares fit to each data set gives an intercept of L_0 and the slope is L_0/α . When the data is plotted as average T_{inc} versus ϵ_{inc} , the results are shown below in (b). The strain values of actual incremental data starts at zero. The adjusted data is shown to the right of the incremental data. The best fit solution is presented as the solid line. The dashed line is for the mean value for PVA cryogel frozen twice ($\alpha=1.72$). The dotted line represents $\alpha \pm 0.37$ (one standard deviation).

section was 132 kPa. The average pressure was essentially the same (13.2 kPa or 99 mm Hg) for both measurements. These different E_{inc} values imply that the thin wall section is approximately 1.6 times stiffer than the thick wall section. Yet subsequent tensile tests performed after MR imaging using the same phantom, at the thin and thick wall locations, reveal that the stress-strain curves are nearly identical for both the thin and thick wall sections (not shown). The discrepancy in reporting E_{inc} is from not knowing the associated stress levels for each E_{inc} value. However, just by knowing the associated stress value still limits the understanding of the full stress-strain characteristics. For example, if one were to report that the thin section had a $E_{inc} = 209$ kPa at an average stress of 35.2 kPa, and the thick section had a $E_{inc} = 132$ kPa at an average stress of 11.4 kPa, is the additional stress information significantly more useful? I address the answer to this question as follows.

By using *a priori* knowledge of the material's scaling parameter β , it is possible to estimate α from incremental data. Fig. 6.13b shows a plot of T_{inc} versus ϵ_{inc} as well as T_{inc} versus ϵ_i (shown on the right side of Fig. 6.13b). The exponential stiffness parameter for the thin and thick wall sections was estimated to be 1.74 and 1.59, respectively. Since the cosine stenosis phantom was made from PVA cryogel frozen twice, these α results are well within the average \pm standard deviation of 1.72 ± 0.37 for PVA cryogel reported in Section 6.4.B.1 above. A graphical representation of the full stress-strain curves given by these α parameters is shown in Fig. 6.13b as the dashed lines. The α parameter for thick and thin sections describe a full exponential stress-strain curve, whereas the E_{inc} values reported earlier are only valid at the stress level the measurements were made. Thus I conclude that α is a much more descriptive in characterizing the stress-strain behaviour of arteries compared to E_{inc} .

^c Having E_{inc} and T_{avg} are not sufficient for estimating the associated strain because the stress-strain curve is not linear. Only for the case of Hookean materials does strain=stress/modulus.

A total of four different stenosis phantoms were evaluated and the average α for all eight series of images was 2.1 ± 0.5 . Again, this is within the average \pm standard deviation of PVA cryogel frozen twice.

6.4.D.ii PVA phantom With Dual Elastic Properties

The unique characteristics of PVA cryogel permitted me to fabricate a simple elastic tube with two physically different stiffnesses in the azimuthal direction.⁶ Cross-sectional MR images of one such tube is in Fig. 6.14, and the two distinctly different PVA regions can be seen. At diastolic pressure the tube expands from its no-load state. The stiff PVA region shows a larger wall thickness than the flexible region because the former does not distend circumferentially nearly as much as the flexible PVA region. The incremental stress-strain data are plotted in Fig. 6.15. The average E_{inc} for the stiff region was 277 kPa with an average stress level of 17.7 kPa. Similarly, the flexible region had a E_{inc} of 176 kPa, and a stress level of 24.6 kPa. It is apparent that incremental modulus does reveal some insight to the materials true physical characteristics since the stiff PVA has a E_{inc} approximately 1.6 times higher than that for the flexible PVA. However, because the stress levels are different, one cannot simply compare the E_{inc} values. Because the stiff region wall thickness remains much larger than that of the thin region, the circumferential load on the thick region is carried over a larger area, and this results in a lower circumferential stress for the stiff region.

When the extrapolation method is applied, I find that the stiff PVA region has a mean $\alpha=3.20$, while the flexible region has a mean $\alpha=1.79$. These values are, respectively, within 6% and 4% of the PVA values reported in Table 6.1. Fig. 6.15 qualitatively shows that the extrapolated curves are reasonable fits. Since α is not dependent on any particular stress level, I can compare these two values directly, and get a more quantitative estimate of the materials' circumferential stress-strain characteristics.

It should be noted that in the stiff region, the maximum strain was found to be less than 3% from diastole to systole. Hence, with errors by ± 1 pixel and total lines lengths of approximately 10 pixels, this was enough to severely compromise

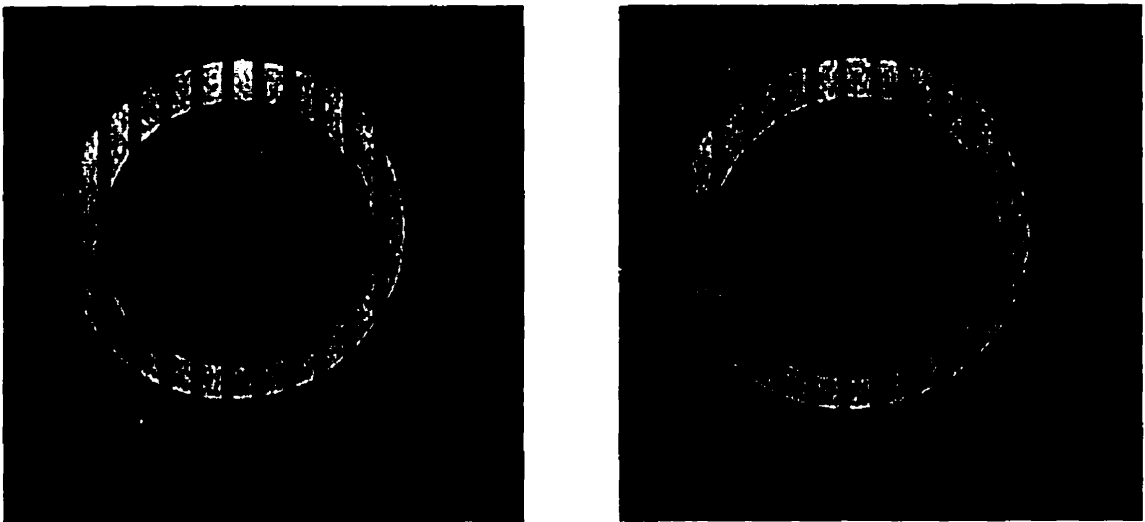


Figure 6.14. Cross sectional MR image of a PVA tube two distinct stiffness regions. The stiff region has been frozen and thawed 12 times, and the flexible region has been frozen only twice. The left image was taken 70 ms after the gating signal, and its corresponding diastolic pressure was 5.48 kPa. The image on the right was collected 406 ms after the gating signal and a systolic pressure of 9.3 kPa.

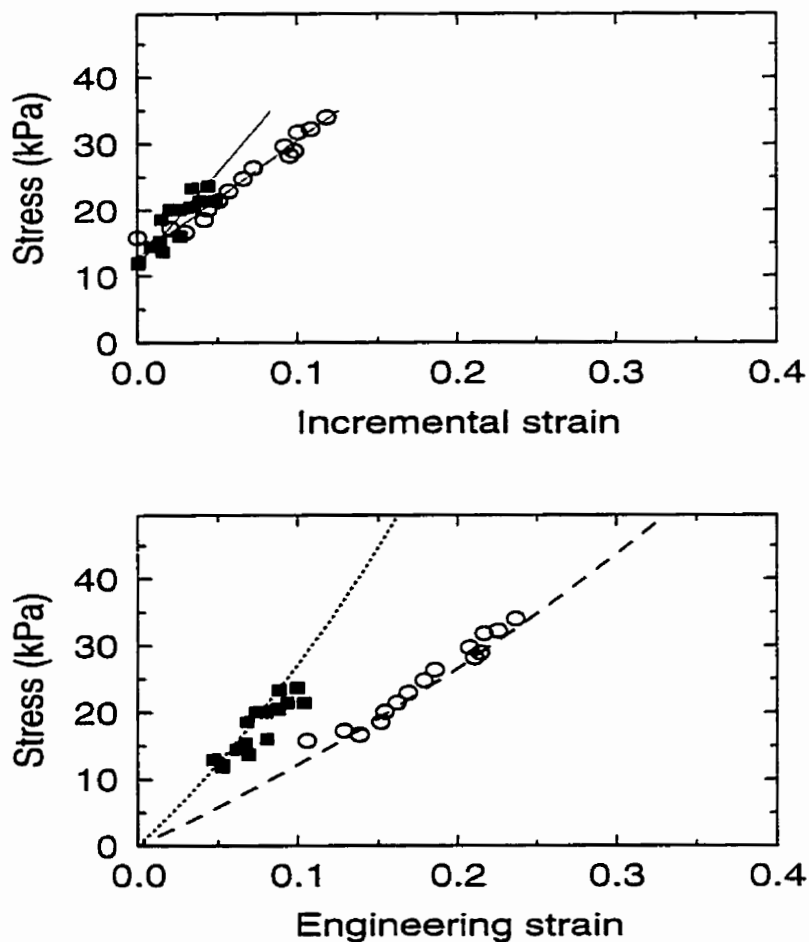


Figure 6.15 A typical stress-strain curve for the dual elastic phantom. The top graph shows the original incremental data. The slope of the linear least squares fit line (solid lines) is E_{mc} . The solid squares represent the average data from the stiff region, and the open circles represent the average data from the flexible region. The extrapolated data are also shown in the lower plot. The dashed line is $\alpha=1.72$ for PVA cryogel frozen twice, and the dotted line is $\alpha=3.5$ for PVA cryogel frozen 12 times.

the overall accuracy of the strain measurements. Often the strains in the stiff regions were found to be negative due to errors in the manually selected tag intersections. In these cases, the adjacent strains from 3 or more lines were summed together having the effect of measuring the strains from a line length of 30 or 40 pixels. This significantly improved the incremental strain values. Because the strain measurements were more susceptible to errors than the stress measurements, I did not calculate E_{inc} as the slope of a stress-strain plot, but instead I plotted strain versus stress, and calculated E_{inc} as the reciprocal of the slope of this new plot.

It should be noted that my semi-manual grid point selection method described in Section 6.3.E is only accurate to approximately ± 1 pixel. This accuracy can be improved ten fold by using sophisticated computer algorithms.^{41,43,44,45,46} For example, in all of my images, the radius and outer circumference were measured to be at least 50 and 314 pixels, respectively. Assuming there are 10 evenly spaced tag intersections around the circumference, each arc length will be approximately 31 pixels long. When the measurement technique can detect a 1 pixel change in 31 pixels, the measurable strain is approximately 3% (as I have found experimentally). However, if the measurement technique is accurate to 0.1 pixels, then the minimum measurable strain is 0.3%. Thus it is highly recommended that sub-pixel tag locating algorithms be used. This simple analysis describes the minimum length change that stiff arteries or plaques must undergo in order that its elastic properties be measured.

It was not possible to properly apply Eq. 6.1 to the data since the choice of a center reference point (the best circle to fit the lumen wall) forced both the stiff and flexible walls to appear to have equal displacements throughout the cardiac cycle. If Eq. 6.1 were applied to the data at various azimuthal angles, the numerical result of E_{inc} 's would indicate a higher value for the flexible wall. This is clearly incorrect. Most of the displacements were due to the flexible wall and not the stiff wall, but because of the choice of center, the radii measurements do not properly reflect the proper displacements. Alternatively, it may be possible to apply

Eq. 6.2 to the data assuming the specimen samples are circular with **thin walls** and that the variables c_i and c_o can be replaced with arc lengths; however, without proper markers on the inner and outer walls, accurate arc lengths may not be obtainable.

6.4.D.iii Tagging method with Porcine aorta

The concept of extrapolating incremental data derived from imaging data to full stress-strain curves was tested using porcine aortas. Figure 6.16 is a cross-sectional image of an aorta at diastole. In this example, the MR tags were applied in the horizontal direction. The image analyses remained the same as reported earlier. The average stress-strain data for one aorta is shown in Figure 6.17. The estimated α was 4.8 for this sample, which is -18% below the average α of 5.87 ± 0.72 for porcine aortas.

This sample was tested at a stress levels of 75 kPa to 118 kPa, which is at the limit of the applicability of the extrapolation method. The stress levels from three other porcine specimens tested were also near the 100 kPa range. One important aspect of this study is that a transmural pressure range of 12 to 17 kPa (90 to 130 mm Hg) caused the artery to have a very high strain of 50 to 65%. At porcine physiological pressures⁵³ of 19 to 24 kPa, the strains would even be higher. Strains in this range indicate that the artery expansion is limited by the collagen matrix straightening out from its normal crimped state. These high strains are twice as high as those for human arteries.⁵⁰ It is unclear whether the surrounding connective tissue bears some of the load induced by the lumen pressure in the *in vivo* case. If the connective tissue does support some of the load, then the proper stress level can be calculated only when the total thickness of both the artery wall and connective tissue is known. I suspect that the connective tissue does carry some of the load and that the normal wall stress for pigs *in vivo* is in the 75 kPa range. This can only be confirmed through a carefully designed set of experiments. It is In the mean time, it is suggested that future studies be performed at lower incremental pressure ranges (or several ranges starting from zero kPa).

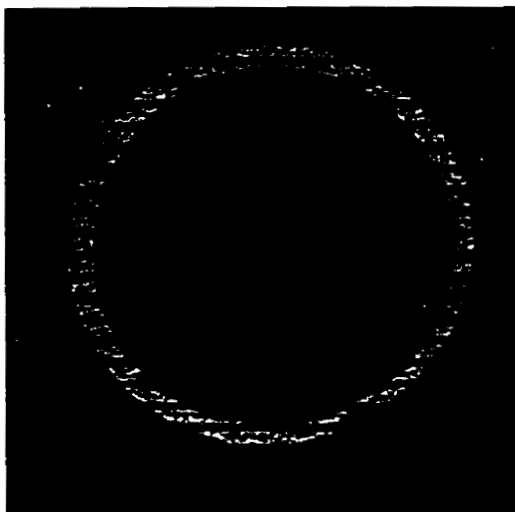


Figure 6.16. Ex-vivo porcine aorta undergoing pulsatile motion. Horizontal DANTE tags were applied at diastole ($P_m=12.2$ kPa). The 2.4 cm FOV image was acquired 70 ms after the gating signal.

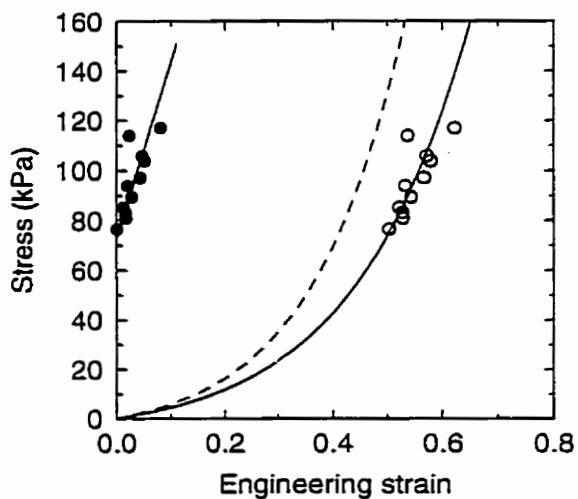


Figure 6.17. Average stress-strain curve for porcine aorta. The incremental data are shown as solid circles, and E_{inc} is the slope of the solid straight line. The extrapolated data are shown as hollow circles. The solid curved line is the best fit to this data. The dotted line is the average α for porcine aortas (i.e. $\alpha=5.87$).

6.5 General Discussion and Summary

The concept of using non-linear stress-strain analysis is not new. However, there are no reports on how incremental data from arterial specimens can be correlated to absolute stress strain curves from uniaxial tests. Stewart and Lyman⁵⁴ have attempted to correlate vascular compliance with stress-strain curves with limited success. In this chapter, a general method of extrapolating incremental data to full stress-strain curves is described. The method presented can be applied to **any** incremental data set (including previously published data) as long as the original stress and strain (or length) data are given. However, as with any extrapolation technique, the errors can be quite significant and caution is always required.

I have qualitatively demonstrated through several examples that it is possible to extrapolate incremental data from materials that show an exponential stress-strain behaviour. This technique requires that the scaling parameter β for the material be known with an accuracy of approximately 50%. The method appears to only be applicable when wall stresses are less than 75 kPa. The differences in the real stress-strain curve and the extrapolated curve from incremental data are most likely caused by differences between the model and real data. Differences in the slopes of the fitted and real curves at high stress levels above 75 kPa are suspected to propagate as significant errors in the extrapolation method. Improvements in the theory can be made by choosing a statistically appropriate β for a tissue type, and/or using an improved mathematical model.^{15,30,48}

The α values reported in this chapter are not so different from the stiffness parameter proposed by Hayashi⁷ who used a single exponential model to describe normalized pressure-radius curves of arteries. Hayashi⁷ reported the stiffness parameter for *ex vivo* human thoracic aortas to range from approximately 3 to 13 for 6 to 70 year olds, respectively. Hansen et al⁵⁵ found similar results in the stiffness parameter measured *in vivo* for human common carotid arteries and it ranged from 4.1 ± 0.7 for 15 year old males to 13.2 ± 3.6 for 70 year old males.

These results give an intuitive feeling of the different values and precision that one might expect from *in vivo* measurements of α .

The experimental data presented here is strictly for circumferential stress-strain data. Smooth muscle cell activity, bi-axial effects and viscous effects are assumed negligible. It should be kept in mind that the stress calculations assume there are no internal stress within the specimen wall. Clearly this is not correct for real arteries. Internal wall stresses are discussed elsewhere,³⁰ however, these are generally small compared to the applied stress induced by the lumen pressure.²⁶ In addition, since Eq. 6.17 assumes no shear stresses, the stress equation is only accurate for thick walled non-homogeneous specimens far away from areas of any discontinuities. Stress analysis in complex geometries⁵⁶ has been attempted by others. Incorporating more complex stress analysis is possible when the exact geometries are known, and may require numerical methods to solve. As discussed in the previous section, the actual wall stress for *in vivo* studies may require the exact vessel dimensions including its connective tissues. Otherwise, simple lumen pressures may overestimate the true wall stress and lead to errors.

General tagging techniques are necessary for measuring local strains. For *in vivo* studies, MR tagging is much less invasive than physically attaching markers²² onto the elastic material to be studied.^{57,58,59,60} Other researchers have reported success in using MR phase contrast methods^{61,62} to estimate cardiac strain from velocity measurements. Although phase contrast methods are not easily interpreted without significant post processing, they have an added advantage of being able to measure flow velocities within the lumen, as well as the wall itself. This would allow direct measurements of fluid shear,⁶³ as well as local wall motion. Other imaging modalities such as ultrasound can use speckle patterns as markers to measure strain. Since all of the techniques will require direct pressure measurements to obtain true stress levels, the described methods may not be fully non-invasive, unless the pressure can be estimated by other techniques.⁴⁸ Pulse wave velocity techniques^{48,64} have been shown to be able to estimate gross elastic modulus of arteries without requiring pressure

measurements. However, these techniques cannot measure local differences in elastic properties within the artery wall.

Alternatively, non-invasive tagging via MR techniques such as DANTE or SPAMM¹⁰ (Spatial Modulation of Magnetization) produce direct visual images showing wall motion, and are among the best techniques for future *in vivo* studies. In the last few years, several research groups have reported automatic tagging algorithms that can detect the center of tags with sub pixel accuracy. It is strongly recommended that these computer software techniques be applied to future studies. This would allow for improved strain estimates which is necessary for accurate results.

One problem with MR tagging methods is that the tags fade over the cardiac cycle. The fading depends on the T_1 relaxation time of the underlying tissue. In regions where there may be fibrous plaques, the T_1 is short, and the tags fade relatively quickly. This would again suggest MR velocity techniques may be useful. Others^{31,65} have correlated the relaxation times with the exponential stiffness parameter for excised human arteries. Although the correlation coefficient was relative low, it must be kept in mind that such a correlation given biological variations is impressive.

In summary, in this chapter, I have (1) introduced the use of the exponential stiffness factor α as the primary estimate of a materials stress-strain characteristics, (2) developed a new concept for extrapolating incremental data to full stress-strain curves, (3) demonstrated with tensile testing that the error in α can be significant, but within $\pm 30\%$ of the actual value when the stress is less than 75 kPa, (4) show that after the extrapolation method, E_{fit} is an improved estimate of the elastic modulus compared to E_{inc} , (5) used high resolution MR imaging in conjunction with DANTE tagging to determine the local incremental elastic properties and (6) demonstrated the extrapolation method using sophisticated PVA cryogel phantoms and excised porcine aortas.

The extrapolation method demonstrates the importance of using α instead of E_{inc} , and is a novel method of measuring and distinguishing differences in the

local elastic properties of a pulsating vascular phantom.

Further research is necessary in improving this work. With the improvement of medical imaging techniques, more researchers will be involved with the measurements of incremental elastic properties, and the concepts presented here will be of significant value in improving our overall understanding of the arterial behaviour during atherogenesis.

6.6 References

1. E.Falk, Why do plaques rupture?, *Circulation*, **86** (suppl. III), III-30 - III-42 (1992).
2. N.J.Severs and H.Robenek, Constituents of the arterial wall and atherosclerotic plaque: an introduction to atherosclerosis, in "Cell Interactions in Atherosclerosis" (H.Robenek, N.J.Severs, Eds.), CRC Press, Boca Raton, 1992.
3. K.Chu and B.K.Rutt, Quadrupole gradient coil design and optimization: a printed circuit board approach, *Mag. Res. Med.*, **31**, 652-659 (1994).
4. K.Chu and B.K.Rutt, MR gradient coil heat dissipation, *Mag. Res. Med.*, **34**, 125-132 (1995).
5. K.C.Chu, A.J.Martin, B.K.Rutt, Improved MR images of arterial specimens by submersion in trichlorotrifluoroethane, *Mag.Res.Med*, **35**, 790-796 (1996).
6. K.C.Chu, B.K.Rutt, Polyvinyl alcohol cryogel: an ideal phantom material for MR studies of arterial flow and elasticity, *Magnetic Resonance in Medicine*, **37**, 314-319 (1997).
7. K.Hayashi, Experimental approaches on measuring the mechanical properties and constitutive laws of arterial walls, *Journal of Biomechanical Engineering*, **115**, 481-488 (1993).
8. G.J.Langewouters, K.H.Wesseling, W.J.A.Goedhard, The static elastic properties of 45 human thoracic and 20 abdominal aortas in vitro and the parameters of a new model, *J.Biomechanics*, **17**, 425-435 (1984).
9. E.A.Zerhouni, D.M.Parish, W.J.Rogers, A.Yang, E.P.Shapiro, "Human heart: tagging with MR imaging - a method for noninvasive assessment of myocardial motion", *Radiology*, **169**, 59-63 (1988).

10. L.Axel, L.Dougherty, MR imaging of motion with spatial modulation of magnetization, *Radiology*, **171**, 841-845 (1989).
 11. J.L.Prince, E.R.McVeigh, Motion estimation from tagged MR image sequences, *IEEE transactions on Medical Imaging*, **11**, 238-249 (1992).
 12. A.A.Young, L.Axel, L.Dougherty, D.K.Bogen, C.S.Parenteau, Validation of tagging with MR imaging to estimate material deformation, *Radiology*, **188**, 101-108 (1993).
 13. G.A.Morris, R.Freeman, Selective excitation in fourier transform nuclear magnetic resonance, *J. Magnetic Resonance*, **29**, 433-462 (1978).
 14. T.J.Mosher, M.B.Smith, A DANTE tagging sequence for the evaluation of translational sample motion, *Mag. Res. Med.*, **15**, 334-339 (1990).
 15. Y.C.Fung, "Biomechanics: Mechanical Properties of Living Tissues", 2nd Ed., Springer-Verlag, New York, 1993.
 16. D.J.Patel, R.N.Vaishnav, "Basic Hemodynamics and Its Role in Disease Processes", University Park Press, Baltimore, 1980.
 17. D.H.Bergel, The static elastic properties of the arterial wall, *J.Physiol*, **156**, 445-457 (1961).
 18. D.H.Bergel, The dynamic elastic properties of the arterial wall, *J.Physiol.*, **156**, 458-469 (1961).
 19. S.Middleman, "Transport Phenomena in the Cardiovascular System", Wiley-Interscience, Toronto, 1972.
 20. U.Dinnar, "Cardiovascular Fluid Dynamics", CRC Press, Boca Raton, 1981.
 21. K.B.Chandran, "Cardiovascular Biomechanics", New York University Press, New York, 1992.
 22. M.Drangova, "Computed Tomography Scanner for Dynamic Vascular Imaging In Vitro", Ph.D. Thesis, University of Western Ontario, 1993.
 23. M.Drangova, D.W.Holdsworth, C.J.Boyd, P.J.Dunmore, M.R.Roach, A.Fenster, Elasticity and geometry measurements of vascular specimens using a high-resolution laboratory CT scanner, *Physiological Measurement*, **14**, 277-90 (1993).
-

24. C.J.Boyd, M.R.Roach, M.H.Sherebrin, R.N.Rankin, and A.Fenster, Demonstration of the need for the inclusion of parameter correlations in error estimation for non-linear curve fitting, *Med. & Biol. Eng. & Comput.*, **32**, 221-224 (1994).
 25. Y.C.Fung, K.Fronek, P.Patitucci, Pseudoelasticity of arteries and the choice of its mathematical expression., *Am. J.Physiol.*, **237**, H620-H631 (1979).
 26. W.R.Milnor. "Hemodynamics", 2nd Ed., Williams & Wilkins, Baltimore, 1989.
 27. P.B.Dobrin, Mechanical properties of arteries, *Physiological Reviews*, **58**, 397-460 (1978).
 28. Standard test method for tensile properties of plastics (metric), "Annual Book of ASTM Standards", Vol 08.01, ASTM D 638M-91a, American Society for Testing and Materials, Philadelphia, 1993.
 29. D.H.Touw, M.H.Sherebin, and M.R.Roach, The Elastic Properties of Canine Abdominal Aorta at its Branches, *Can. J. Physiol. Pharmacol*, **63**, 1378-1383 (1985).
 30. Y.C.Fung, "A First Course in Continuum Mechanics", 3rd Ed., Prentice-Hall, Englewood Cliffs, pp.285-298, 1994.
 31. P.Vinee, B.Meurer, A.Constantinesco, B.Kohlberger, K.Hauenstein, S.Petkov, Proton magnetic resonance relaxation times and biomechanical properties of human vascular wall: in vitro study at 4 MHz, *Invest. Radiol.*, **27**, 510-514 (1992).
 32. W.W.Nichols, M.F.O'Rourke, "McDonald's Blood Flow in Arteries", *Lea & Febiger*, Philadelphia, 1990.
 33. A.P.G.Hoeks, P.J.Brands, F.A.M.Smeets, R.S.Reneman, Assessment of the distensibility of superficial arteries, *Ultrasound in Med. & Bio.*, **16**, 121-128 (1990).
 34. T.Imura, K.Yamamoto,T.Satoh, K.Kanamori, T.Mikami, H.Yasuda, In vivo viscoelastic behaviour in human aorta, *Circulation Research*, **66**, 1412-1419 (1990).
 35. S.H.K.The, E.J.Gussenhoven, H.Pieterman, L.M.A.B.Van Bortel, W.Li, J.R.t.C.Roelandt, P.De Feyter, H.Van Urk, Assessment of regional vascular distensibility in diseased iliofemoral arteries by intravascular ultrasound, *Ultrasound in Med. & Biol*, **21**, 17-24 (1995).
-

36. R.H.Mohiaddin, S.R.Underwood, H.G.Bogren, D.N.Firmin, R.H.Klipstein, R.S.O.Rees, D.B.Longmore, Regional aortic compliance studied by magnetic resonance imaging: the effects of age, training, and coronary artery disease, *Br. Heart J.*, **62**, 90-96 (1989).
 37. R.W.Behling, H.K.Tubbs, M.D.Cockman, L.W.Jelinski, Stroboscopic NMR Microscopy of the Carotid Artery, *Nature*, 324-323, Sept. 28, 1989.
 38. S.M.Forbat, R.H.Mohiaddin, G.Z.Yang, D.N.Firmin, S.R.Underwood, Measurement of regional aortic compliance by MR imaging: a study of reproducibility, *JMRI*, **5**, 635-639 (1995).
 39. M.H.Sherebrin, H.A.Bernans, M.R.Roach, Extensibility changes of calcified soft tissue strips from human aorta, *Can. J. Physiol. Pharmacol.*, **65**, 1878-1883 (1987).
 40. Y.C.B.Fung, Elasticity of soft tissues in simple elongation, *American Journal of Physiology*, **213**, 1532-1544 (1967).
 41. E.R.McVeigh, E.Atalar, Cardiac tagging with breath-hold cine MRI, *Magn. Resonance in Medicine*, **28**, 318-327 (1992).
 42. C.M.Thompson, L.Shure, "Image Processing ToolBox: for use with MATLAB", The MathWorks, Natwick, 1995.
 43. L.Axel, R.C.Goncalves, D.Bloomgarden, Regional heart wall motion: two-dimensional analysis and functional imaging with MR imaging, *Radiology*, **183**, 745-750 (1992).
 44. S.Kumar, D.Goldgof, Automatic tracking of SPAMM grid and the estimation of deformation parameters from cardiac MR images, *IEEE transactions on Medical Imaging*, **13**, 122-132 (1994).
 45. M.G.Guttman, J.L.Prince, E.R.McVeigh, Tag and contour detection in tagged MR images of the left ventricle, *IEEE Transactions on Medical Imaging*, **13**, 74-88 (1994).
 46. E.Atalar, E.R.McVeigh, Optimization of tag thickness for measuring position with magnetic resonance imaging, *IEEE Transactions on Medical Imaging*, **13**, 152-160 (1994).
 47. S.K.Tadikonda, D.J.Fisher, J.C.Ehrhardt, W.T.C.Yuh, E.A.Hoffman, Echo planar SPAMM versus cine SPAMM: evaluation via sub pixel tag detection, "Proc., 12th SMRM Annual Meeting, 1993", p. 1243.
-

48. Y.Tardy, J.J.Meister, F.Perret, H.R.Brunner, M.Arditi, Non-invasive estimate of the mechanical properties of peripheral arteries from ultrasonic and photoplethysmographic measurements, *Clin. Phys. Physiol. Meas.*, **12**, 39-54 (1991).
49. F.L.Wuyts, V.J.Vanhuyse, G.J.Langewouters, W.F.Decraemer, E.R.Raman, S. Buyle, Elastic properties of human aortas in relation to age and atherosclerosis: a structural model, *Phys. Med. Biol.*, **40**, 1577-1597 (1995).
50. C.M.He, M.R.Roach, The composition and mechanical properties of abdominal aorta aneurysms, *Journal of Vascular Surgery*, **20**, 6-13 (1994).
51. J.H.Storkholm, G.E.Villadesen, K.Krogh, C.S.Jørgensen, H.Gregersen, Dimensions and mechanical properties of porcine aortic segments determined by combined impedance planimetry and high-frequency ultrasound, *Medical & Biological Engineering & Computing*, **35**, 21-26 (1997).
52. M.R.Roach, A.C.Burton, The effect of age on the elasticity of human iliac arteries, *Can. J. Biochem. Physiol.*, **37**, 557-570 (1959).
53. W.G.Pond, K.A.Houpt, "The Biology of the Pig", *Cornell University Press*, London, 1978.
54. S.F.C.Stewart, D.J.Lyman, Predicting the compliance of small diameter vascular grafts from uniaxial tensile tests, *J.Biomechanics*, **23**, 629-637 (1990).
55. F.Hansen, P.Mangell, B.Sonesson, T.Lanne, Diameter and compliance in the human common carotid artery - variations with age and sex, *Ultrasound in Med. & Biol.*, **21**, 1-9 (1995).
56. M.R.Piggott, "Load Bearing Fiber Composites", *Pergamon Press*, Toronto, 1980.
57. L.H.Peterson, R.E.Jensen, and J.Parnell, Mechanical properties of arteries in vivo, *Circulation Research*, **8**, 622-639 (1960).
58. B.S.Gow, C.D.Hadfield, The elasticity of canine and human coronary arteries with reference to postmortem changes, *Circulation Research*, **45**, 588-594 (1979).
59. D.J.Patel, F.M.De Freitas, J.C.Greenfield Jr., D.L.Fry, Relationship of radius to pressure along the aorta in living dogs, *J. Appl. Physiol.*, **18**, 1111-1117 (1963).

60. R.H.Cox, Passive mechanics and connective tissue composition of canine arteries, **234**, H533-H541, *Am. J. Physiol.* (1978).
61. A.Lingamneni, P.A.Hardy, K.A.Powell, N.J.Pelc, R.D.White, Validation of cine phase-contrast MR imaging for motion analysis, *J. Magn. Resonance Imaging*, **5**, 331-338 (1995).
62. N.J.Pelc, M.Drangova, L.R.Pelc, Y.Zhu, D.C.Noll, B.S.Bowman, R.J.Herfkens, Tracking of cyclic motion with phase-contrast cine MR velocity data, *Journal of Magnetic Resonance Imaging*, **5**, 339-345 (1995).
63. J.N.Oshinski, D.N.Ku, S.Mukundan, F.Loeh, R.I.Pettigrew, Determination of wall shear stress in the aorta using MR phase velocity mapping, *JMRI*, **5**, 640-647 (1995).
64. S.N.Urchuk, D.B.Plewes, A velocity correlation method for measuring vascular compliance using MR imaging, *JMRI*, **5**, 628-634 (1995).
65. A.Constantinesco, P.Gries, P.Vinee, B.Heckert, P.Carlier, In vitro 4 Mhz NMR proton relaxation times and in vitro mechanical behaviour at low extension of human common carotid arterial wall, *Magnetic Resonance Imaging*, **7**, 173-177 (1989).

CHAPTER 7 SUMMARY AND FUTURE APPLICATIONS

7.1 Overview

The goal of this research was to develop a magnetic resonance (MR) imaging system for dynamic imaging of arteries and phantoms *in vitro*. The system was used to study differences in the local elastic properties which may be important in the *early* detection of fibrous atherosclerotic plaques. The system and the *in vitro* data presented will aid in the long-term goal of being able to provide a method of early identification and management of people at high risk of vascular disease. In addition, such tools can be used to monitor the regression or progression of disease in people undergoing different drug therapies.

The tools developed in this thesis included i) the modification of a clinical MR scanner (1.5T GE Signa) to permit distortion free, fast high resolution (<100 μm pixels) images, ii) the application of a pumping fluid that is compatible with arterial specimens and does not introduce flow artifacts in the MR images, iii) the development of a synthetic phantom material that mimicked the properties of arteries in terms of biomechanical and MR properties iv) the modification of a GRE pulse sequence to permit non-invasive MR tagging of dynamic arterial specimens, and v) the measurement of local elastic properties of pulsatile arteries and arterial phantoms *in vitro*. The following is an recap on the development these tools presented in this thesis.

The concept of manufacturing and testing gradient coil designs with minimal time and expense was presented in Chapter 2. Chapter 3 discussed the practical issue of minimizing the temperature rise in gradient coils when they are used in high duty cycle applications. In Chapter 4, the application of a unique non-aqueous fluid that could keep biological specimens moist for MR imaging is reported. This fluid was trichlorotrifluoroethane (R-113) and MR images of specimens submersed in R-113 had improved SNR and CNR. As a pumping fluid, R-113 is ideal for *in vitro* MR studies since it does not produce flow artifacts. Unfortunately, R-113 cannot be used *in vivo*. The problem of flow artifacts for *in vivo* studies cannot be avoided and is addressed in Section 7.3.1. The introduction of the PVA cryogel

(Chapter 5) has been demonstrated to be the only known elastic phantom material with properties that mimic real tissue in mechanical and imaging properties. Due to its bio-compatibility, PVA cryogel shows tremendous promise for medical researchers beyond being utilized as phantoms. Finally, the concept of extrapolating incremental elastic data to full stress-strain curves was possible through the clarifications of basic stress-strain definitions and by using an exponential model of arterial stress-strain. The theory was also demonstrated using MR imaging of segments of porcine aortas and vascular phantoms made from PVA cryogel. The theory was presented in such a way that it can be applied to any clinical imaging modality and can be used to re-analyze and extrapolate exponential stress-strain curves from previously published incremental data.

7.2 Gradient Coils

7.2.1 PC Boards

In Chapter 2, I have presented a simple technique for accurately constructing a dual axis quadrupole gradient coil set that is necessary for fast high resolution MR imaging. The construction method used dual sided flexible PC board technology. Although I demonstrated the process on quadrupole designs, the methodology can be and has been used with more complicated design patterns.^{1,2} Traditionally, researchers have mathematically modeled gradient coil designs and had to hand wind wires into grooves milled or lathed in plastic formers.^{3,4,5} Numerically controlled milling machines have simplified the cutting of the grooves but the winding of the wires is often laborious and time consuming. For these reasons alone, some research papers report theoretical gradient coils years before any experimental verification.^{2,6,7} The PC board method described in Chapter 2 allows sophisticated gradient coil designs to be manufactured and tested within a few hours after completing a design. Typical material costs are less than a few hundred dollars.

7.2.2 Accuracy of Current Paths

A high degree of gradient accuracy and uniformity is desirable for MR gradient coils. In an image with 256x256 pixels, the gradient uniformity should

provide less than 1/256 or 0.4% deviation across the field of view in order that image warping algorithms not be needed to correct for spatial distortions. By numerical optimization of a 192 straight current path gradient coil, the volume having 0.4% gradient uniformity for MR imaging was shown to be a factor of 4.7 larger than the reference Webster^a quadrupole design.

The effect of imprecise wire position was investigated by comparing computer simulations with an image made from a coil constructed with a small error. Theoretical analysis shows that an error of -0.5% in all of the wire positions during construction will asymmetrically reduce the volume having 0.4% gradient uniformity by half. However, the volume having 5% gradient uniformity was less sensitive to systematic errors in the wire position and did not significantly change.

7.2.3 Heat Dissipation

Although the PC board technology is ideal in testing gradient coil designs, it is not recommended for permanent heavy duty applications. For these applications it is important to understand that the electrical power used for high resolution MR imaging must be removed by forced cooling. In small gradient coils, where the subject may be in close proximity to the coil, it is vital that the temperature of the coil be maintained at a comfortable level. For example, it is not unusual for the small customized gradient coils in high resolution MRI to continuously use 500 to 2000 watts of power; thus, the need for forced cooling becomes apparent. The mathematical model derived in Chapter 3 accurately predicted the transient temperature rise and its peak value to within 5°C. The model reveals that to minimize the temperature rise in gradient coils, the coil radius should be minimized and the copper thickness maximized. This latter requirement negates the use of copper PC boards for high duty cycle gradient coil applications. In addition, the use of a high thermal conductivity coil former along with circulating water will significantly enhance the cooling of the coil. When no forced cooling is used, both natural convection and radiation play significant roles in cooling. They are, however, limited in the amount of heat they can dissipate. The best method of cooling is a water cooling system. It is strongly recommended that a

recirculation water system be used with the water temperature maintained at 20°C. Colder water temperatures may cause the gradient coil to become uncomfortably cold for *in vivo* studies. The water should be doped with paramagnetic ions to minimize aliasing of extraneous signals back into the MR images.

7.2.4 Installation

Another aspect to consider is the installation of customized gradient coils in clinical MR scanners. Although briefly discussed in Chapter 2, it is important to realize that clinical MR scanners have sophisticated feed back circuitry installed on their amplifiers so that current rise times are critically dampened (i.e. the rise time to achieve maximum current output is just fast enough so that delivered output current does not exceed the requested amount). Customized gradient coils with inductances and resistances that are significantly different from the manufacturer's original gradient coils may cause the amplifiers to oscillate and result in significant damage. It is recommended that the manufacturer's service technician assist researchers in the initial installation of any customized gradient coil set.

7.2.5 Alternative Designs

Although I have found that the quadrupole design is an excellent choice as a small diameter gradient coil, these designs cannot be used for *in vivo* applications because the coil is perpendicular to the main magnetic field. Hence, there is no easy access to the gradient coil once installed in the center of the bore of a clinical superconducting magnet. However, quadrupole designs could be used in open vertical field MR scanners. For *in vivo* applications, it is recommended that the axis of the gradient coil be parallel to the bore of the superconducting magnet. Designs such as the "finger print" coils^{2,9} can be used for this purpose. This recommendation has been recently implemented at our research laboratories (Department of Medical Biophysics, University of Western Ontario).

7.3 Hydrogen Free Medium For Aortic Specimens

Excised arteries must be kept moist to prevent dehydration, otherwise the MR properties may be significantly different from the in-vivo

situation.^{10,11,12,13,14} Specimens are frequently submersed in an aqueous solution¹² or embedded into aqueous gels.¹¹ This results in a decreased contrast-to-noise ratio (CNR) since the surrounding fluid also yields an MR signal. In Chapter 4, I reported that R-113 can be used a medium for which porcine aortic specimens can be stored during MR imaging. Since there were no previous reports on the short and long term effects of arterial specimens submersed in R-113, the experiments in Chapter 4 were performed with the following results.

Biological samples were shown not to dehydrate while submersed in R-113 because of the immiscibility of water in R-113. An 11% higher SNR was obtained for MR images of specimens submersed in R-113 compared to saline solution. This is attributed to the fact that R-113 is non conductive; thus the RF coil loading and inductive noise are minimized. As a result of the nearly perfect match between the volume susceptibility χ_v of R-113 and water, MR images of arteries submersed in R-113 are not distorted. Another advantage in using R-113 instead of water or saline solutions is that there are fewer air bubbles adhering to the specimen. This is attributed to the extra buoyancy of the air bubbles in the denser and less viscous R-113.

Short term (<7 hours) submersion of porcine aortas in R-113 was found to have no significant effect on the artery's hydration level, relaxation time, tensile strength nor structure and quantity of elastin, collagen and smooth muscle cells. However, at longer periods of time, the arterial T_1 relaxation time starts to decrease.

Since R-113 has no hydrogen atoms, it does not yield a proton MR signal and thus, cannot contribute to flow artifacts when used as a pumping fluid to pulsate arterial specimens. R-113 is ideal for *in vitro* MR studies where it was necessary to keep specimens moist and have a pumping fluid that would not cause flow artifacts.

7.3.1 Practicality of using R-113

The novel application of R-113 for *in vitro* MR studies has been proven to have several benefits. Although R-113 is relatively non-toxic, it is suspected to be

harmful to the atmospheric ozone layer and is no longer manufactured in North America as a common refrigerant. Thus, care should be used when handling R-113, and the material redistilled for subsequent use. R-113 is still available for research applications (e.g. high-pressure liquid chromatography).

For *in vitro* MR experiments, it is ideal to have a signal free fluid to eliminate all flow artifacts. However, this situation does not exist for *in vivo* studies. For *in vivo* studies, flow artifacts can be minimized but never eliminated. Since flow artifacts only occur in the phase encode direction, it is feasible to perform two sets of experiments where the phase encode direction is swapped with the frequency encode direction in the second experiment. To avoid doubling the imaging time compared to a standard 256x256 k-space data matrix, the number of phase encode steps should be halved. By doing so, each k-space data is effectively 256x128 in size which results in lower spatial resolution in the phase encode direction. Since flow artifacts are present in the phase encode direction, one should not be concerned about losing some resolution in that direction. Thus high resolution quantitative motion can be studied in both directions without requiring any additional imaging time. In terms of MR tagging, the tag lines should be applied so that the tag widths are in the frequency encode direction where the resolution is highest. In addition, post processing to track single lines is significantly simplified compared to tracking tag intersections.¹⁵

7.4 PVA Cryogel

Over the years, several research groups^{16,17,18,19,20,21,22} have presented various phantoms that can mimic tissue. For applications where the phantom is stationary, agar and gelatin phantoms are adequate. However, there have been no published reports of an elastic material that has mechanical properties as well as MR imaging properties that are similar to vascular tissue.

In Chapter 5, I have developed a PVA cryogel material whose simple recipe and manufacturing technique along with its realistic properties such as signal intensity, relaxation times, elasticity and strength make it a near-ideal phantom material. Preliminary studies (not shown) suggest that PVA cryogel could also be

used as ultrasound imaging phantoms.²³

Although this study was limited to aortic phantoms, it is possible to create larger distensible phantoms for use in the study of cardiac motion and flow. The elastic properties can be manipulated to mimic most tissues whether healthy or diseased.

Not only is PVA cryogel very similar to real tissue, it is also fully biocompatible. For this reason, I predict that PVA cryogel will play a significant role in the other medical applications such as artificial breast implants, heart valves or arterial grafts. In addition, PVA cryogel's role as a controlled drug release medium²⁴ will be important as shown in preliminary studies.²⁵

7.5 Elastic Properties of Arteries

7.5.1 MR Tagging

Early detection of fibrous atherosclerotic plaques necessitates that local strain measurements be capable of detecting the development of patchy elastic changes in arteries during atherogenesis. This requirement suggests that general tagging techniques be used. For *in vivo* studies, MR imaging is capable of providing tags.^{26,27,28,29,30,31} These techniques are adaptable to *in vivo* studies and are much less invasive than physically attaching markers.^{32,33,34,35,36} In Chapter 6, I demonstrated that DANTE MR tagging used in conjunction with gated fast gradient recalled echo imaging can monitor dimension changes from image to image. This non-invasive tagging technique produces direct visual images showing wall displacement and is probably one of the best non-invasive techniques that can be used for future *in vivo* studies.

In the last few years, several research groups^{37,38,39,40} have reported the development of computer algorithms for automatic tag detection with sub pixel accuracy. It is strongly recommended that this type of algorithm be applied to future studies. This would allow for improved strain estimates necessary for accurate results.

7.5.2 Modelling Stress-Strain Data

In my analysis of stress-strain data and elastic modulus, the definition of incremental modulus is first clarified.^{41,42,43} That is, incremental elastic modulus is *not* equal to the slope of a full stress-strain curve at any stress level. Using this fact and other basic definitions, the difference between incremental stress-strain data and full stress-strain data was mathematically described. By using an exponential model to describe stress-strain curves, it is possible to extrapolate the full exponential stress strain curve from a limited amount of incremental data.

The general method of extrapolating incremental data to full exponential stress-strain curves has the advantage of being applicable to **any** incremental data set from arterial studies (including previously published data) as long as the original stress and strain data are given. However, as with any extrapolation technique, the errors can be quite significant and caution is always required.

7.5.3 Validation of Stress-Strain Model

I have demonstrated through several examples that it is possible to extrapolate stress-strain curves from incremental data of materials that have an exponential stress-strain behaviour. This technique requires *a priori* knowledge of the material scaling parameter β (in Eq. 6.5b). For example, the measured value of β for PVA cryogel and porcine aortas was 64759 Pa and 7357 Pa, respectively. By knowing β , the material's stress-strain characteristic is now represented by the exponential stiffness parameter α . Incremental tensile testing used in conjunction with the extrapolation method demonstrates the importance of α (Eq. 6.5b), instead of the more commonly reported incremental modulus E_{inc} .

Experiments using two different PVA cryogel phantoms mimicking vascular disease states resulted in E_{inc} values that appear to be contradictory to the true material properties. Only through local stress-strain measurements followed by the extrapolation method was it possible to understand the non-linear elastic character of these phantoms. A final demonstration of the extrapolation method using incremental data from MR images of pulsating porcine aortas resulted in full stress-strain curves similar to that obtained by direct tensile tests.

To the best of my knowledge, this is the first report of the measurement of *local* elastic properties of a pulsating vascular phantom using MR tagging.

7.5.4 Limitations

The extrapolation method appears to be applicable only when wall stresses are less than 75 kPa. At these stress levels, the estimates of α were within 30% of the actual value. At stress levels above 75 kPa, large differences in the slopes of the exponential model and actual data are suspected to propagate significant errors in the extrapolation method. Improvements in the theory can be made by choosing a statistically appropriate β for a tissue type, using a dual set of exponential equations as suggested by Fung,⁴³ or perhaps choosing a completely different mathematical model all together.⁴⁴

It should be kept in mind that the equation used for stress was for cylindrically symmetric tubes and assumes no shear stresses in the tube wall. Thus the stress from Eq. 6.17 is only accurate in areas without any discontinuities. Incorporating more complex stress analysis is possible when the exact geometries are known and may require numerical algorithms to solve. This will be left for future studies.

The minimum length change that stiff arteries or plaques must undergo in order that its elastic properties be measurable is 0.3%. This detection level requires that sub-pixel tag locating algorithms be implemented. Semi-manual tag locating methods can detect a minimum strain of 3%. Thus it is highly recommended that sub-pixel tag locating algorithms be used.

7.5.5 Future of Local Elasticity Measurements

MR tagging techniques are probably one of the best non-invasive techniques that can be used for future *in vivo* studies of local elastic properties. One problem with MR tagging methods is that the tags fade over the cardiac cycle. The fading depends on the T_1 relaxation time of the underlying tissue. In regions where there may be fibrous plaques the T_1 is short and the tags fade relatively quickly. This would suggest MR velocity techniques may be useful (i.e. MR phase contrast).^{45,46} Although phase contrast images are not easily interpreted without

significant post processing, they have an advantage of being able to measure flow velocities within the lumen as well as the wall itself. This would allow direct measurements of fluid shear.⁴⁷ The dynamic range of phase contrast methods may prove to be a limiting factor, but these methods deserve further investigation.

Others^{48,49} have correlated the relaxation times with the exponential stiffness parameter for excised human arteries. Although the correlation coefficient was relatively low ($r < 0.6$), the results are quite impressive considering biological variations in the data. I believe that this concept warrants further evaluation.

Since SNR is proportional to voxel size in high resolution MR imaging, customized RF coils will be required to maximize the SNR. Future *in vivo* research will probably involve the carotid arteries because customized RF coils can be easily placed in close proximity to these arteries. It is anticipated that SNR will be improved in the future years ahead.

Since most of the techniques require direct pressure measurement to obtain true stress levels, the described methods may not be fully non-invasive, unless the blood pressure can be estimated by other techniques as suggested by Tardy et al.⁴⁴

7.6 Overall Conclusions

This thesis demonstrated that it was possible to measure the elastic properties of pulsatile arteries and arterial phantoms *in vitro* by modifying a clinical MR scanner. Custom designed high strength gradient coils provided image resolution with 94 μm pixel size. Fast GRE imaging with DANTE tagging produced 33 images in 64 seconds. Signal averaging of 8 sets of data required 8.5 minutes. These imaging times are practical for *in vitro* imaging, and more importantly, for future *in vivo* studies.

As medical imaging techniques improve, more researchers will be involved with the measurement of incremental elastic properties. The concepts presented here will be significant to improving the overall understanding of the complete elastic behaviour of healthy and diseased arteries.

7.7 References

1. C.F.Maier, K.C.Chu, B.A.Chronik, B.K.Rutt, A novel transverse gradient coil design for high-resolution MR imaging, *Magnetic Resonance in Medicine*, **34**, 604-611 (1995).
2. B.A.Chronik, B.K.Rutt, A target field gradient coil design for blood flow imaging in the neck, in "Proc. of the 4th International Society for Magn. Reson. in Medicine Meeting, 1996", p.122.
3. A.Jasinski, T.Jakubowski, M.Rydzy, P.Morris, I.C.Smith, P.Kozlowski, J.K.Saunders, Shielded gradient coils and radio frequency probes for high resolution imaging of rat brains. *Magn. Reson. Med.* **24**, 29-41 (1992).
4. J.S.Schoeniger, "Theory and Equipment Design for Nuclear Magnetic Resonance Microscopy and its Application to the Study of Water Properties in Isolated Neurons," PhD Thesis, The Johns Hopkins University, 1992.
5. C.D.Eccles, "Microscopic NMR Imaging", PhD Thesis, Massey University, 1987.
6. D.E.Lobb, Properties of some useful two-dimensional magnetic fields. *Nuclear Instruments and Methods.* **64**, 251-267 (1968).
7. S.Crozier, L.K.Forbes, D.M.Doddrell, The design of transverse gradient coils of restricted length by simulated annealing, *Journal of Magnetic Resonance, Series A*, **107**, 126-128 (1994).
8. D.S.Webster, K.H.Marsden, Improved apparatus for the NMR measurement of self-diffusion coefficients using pulsed field gradients. *Rev. Sci. Instruments.* **45**, 1232-1234 (1974).
9. R.Turner, Gradient coil design: a review of methods, *Magnetic Resonance Imaging*, **11**, 903-920 (1993).
10. L.Arnder, X.Zhou, G.P.Cofer, L.W.Hedlund, G.A. Johnson, Magnetic resonance microscopy of the rat carotid artery at 300 megahertz, *Investigative Radiology*, **29**, 822-826 (1994).
11. G.E.Gold, J.M. Pauly, G.H.Glover, J.C. Moretto, A.Macovski, R.J.Herfkens, Characterization of atherosclerosis with a 1.5-T imaging system, *JMRI*, **3**, 399-407 (1993).
12. C.Yuan, J.S.Tsuruda, K.N.Beach, C.E.Hayes, M.S.Ferguson, C.E.Alpers, T.K.Foo, and D.E.Strandness, Techniques for high-resolution MR imaging of atherosclerotic plaque, *JMRI*, **4**, 43-49 (1994).

13. K.C.Chu and B.K.Rutt, An in-vitro method of measuring local arterial elasticity under pulsatile motion, in "Proc of the 11th SMRM Ann. Meeting, 1992", p.829.
14. A.J.Martin, A.I.Gottlieb, R.M.Henkelman, High-resolution MR imaging of human arteries, *JMRI*, **5**, 93-100 (1995).
15. Personal discussions with E.R.McVeigh of Johns Hopkins University visiting University Hospital, London, Ontario, April 18, 1996.
16. D.C.Goldstein, H.L.Kundel, M.E.Dube-Witherspoon, L.E.Thibault, E.J.Goldstein, A silicone gel phantom suitable for multimodality imaging, *Investigative Radiology*, **22**, 153-157 (1987).
17. E.L.Madsen, Prospective tissue-mimicking materials for use in NMR imaging phantoms, *Mag. Res. Imaging*, **1**, 135-141 (1982).
18. R.Frayne, L.M.Gowman, D.W.Rickey, D.W.Holdsworth, P.A.Picot, M.Drangova, K.Chu, C.B.Caldwell, A.Fenster, B.K.Rutt., A geometrically accurate vascular phantom for in-vitro x-ray, ultrasound and MR flow studies: construction and geometric verification, *Med. Phys.* **20**, 415-425 (1993).
19. M.D.Mitchell, H.L.Kundel, L.Axel, P.M.Joseph, Agarose as a tissue equivalent phantom material for NMR imaging, *Mag. Res. Imaging*, **4**, 263-266 (1986).
20. M.W.Groch, J.A.Urbon, W.D.Erwin, S.AI-Doohan, An MRI tissue equivalent lesion phantom using a novel polysaccharide material, *Mag. Res. Imaging*, **9**, 417-421 (1991).
21. K.A.Kraft, P.P.Fatouros, G.D.Clarke, P.R.S.Kishore, An MRI phantom material for quantitative relaxometry, *Mag.Res.Med.*, **5**, 555-562 (1987).
22. J.C.Blechinger, E.L.Madsen, G.R.Frank, Tissue-mimicking gelatin-agar gels for use in magnetic resonance imaging phantoms, *Med. Phys.*, **15**, 629-636 (1988).
23. M.Nambu, T.Watari, T.Sakamoto, K.Akojima, Method for applying electromagnetic wave and ultrasonic wave therapies, U.S.Patent 4,958,626, 25 September 1990.
24. L.L.Wood, G.J.Calton, Cryogel bandage containing therapeutic agent, U.S.Patent 5,260,066, November 9, 1993.

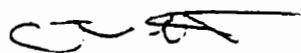
25. M.J. Gordon, "The Diffusion of Paramagnetic Tracers Through Tissue Mimicking Materials", B.E.Sc. Thesis, Department of Chemical Engineering, University of Western Ontario, 1997.
26. E.A.Zerhouni, D.M.Parish, W.J.Rogers, A.Yang, E.P.Shapiro, Human heart: tagging with MR imaging - a method for noninvasive assessment of myocardial motion, *Radiology*, **169**, 59-63 (1988).
27. L.Axel, L.Dougherty, MR imaging of motion with spatial modulation of magnetization, *Radiology*, **171**, 841-845 (1989).
28. J.L.Prince, E.R.McVeigh, Motion estimation from tagged MR image sequences, *IEEE transactions on Medical Imaging*, **11**, 238-249 (1992).
29. A.A.Young, L.Axel, L.Dougherty, D.K.Bogen, C.S.Parenteau, Validation of tagging with MR imaging to estimate material deformation, *Radiology*, **188**, 101-108 (1993).
30. G.A.Morris, R.Freeman, Selective excitation in fourier transform nuclear magnetic resonance, *J. Magnetic Resonance*, **29**, 433-462 (1978).
31. T.J.Mosher, M.B.Smith, A DANTE tagging sequence for the evaluation of translational sample motion, *Mag. Res. Med.*, **15**, 334-339 (1990).
32. M.Drangova, "Computed Tomography Scanner for Dynamic Vascular Imaging In Vitro", Ph.D. Thesis, University of Western Ontario, 1993.
33. L.H.Peterson, R.E.Jensen, J.Parnell, Mechanical properties of arteries in vivo, *Circulation Research*, **8**, 622-639 (1960).
34. B.S.Gow, C.D.Hadfield, The elasticity of canine and human coronary arteries with reference to postmortem changes, *Circulation Research*, **45**, 588-594 (1979).
35. D.J.Patel, F.M.De Freitas, J.C.Greenfield Jr.,D.L.Fry, Relationship of radius to pressure along the aorta in living dogs, *J. Appl. Physiol.*, **18**, 1111-1117 (1963).
36. R.H.Cox, Passive mechanics and connective tissue composition of canine arteries, **234**, H533-H541, *Am. J. Physiol.* (1978).
37. S.Kumar, D.Goldgof, Automatic tracking of SPAMM grid and the estimation of deformation parameters from cardiac MR images, *IEEE transactions on Medical Imaging*, **13**, 122-132 (1994).

38. M.G.Guttman, J.L.Prince, E.R.McVeigh, Tag and contour detection in tagged MR images of the left ventricle, *IEEE Transactions on Medical Imaging*, **13**, 74-88 (1994).
39. E.Atalar, E.R.McVeigh, Optimization of tag thickness for measuring position with magnetic resonance imaging, *IEEE Transactions on Medical Imaging*, **13**, 152-160 (1994).
40. S.K.Tadikonda, D.J.Fisher, J.C.Ehrhardt, W.T.C.Yuh, E.A.Hoffman, Echo planar SPAMM versus cine SPAMM: evaluation via sub pixel tag detection, "Proc., 12th SMRM Annual Meeting, 1993", p. 1243.
41. Y.C.Fung, K.Fronek, P.Patitucci, Pseudoelasticity of arteries and the choice of its mathematical expression., *Am. J.Physiol.*, **237**, H620-H631 (1979).
42. P.B.Dobrin, Mechanical properties of arteries, *Physiological Reviews*, **58**, 397-460 (1978).
43. Y.C.Fung, "Biomechanics: Mechanical Properties of Living Tissues", 2nd Ed., Springer-Verlag, New York, 1993.
44. Y.Tardy, J.J.Meister, F.Perret, H.R.Brunner, and M.Arditi, Non-invasive estimate of the mechanical properties of peripheral arteries from ultrasonic and photoplethysmographic measurements, *Clin. Phys. Physiol. Meas.*, **12**, 39-54 (1991).
45. A.Lingamneni, P.A.Hardy, K.A.Powell, N.J.Pelc, R.D.White, Validation of cine phase-contrast MR imaging for motion analysis, *J. Magn. Resonance Imaging*, **5**, 331-338 (1995).
46. N.J.Pelc, M.Drangova, L.R.Pelc,Y.Zhu, D.C.Noll, B.S.Bowman, R.J.Herkens, Tracking of cyclic motion with phase-contrast cine MR velocity data, *Journal of Magnetic Resonance Imaging*, **5**, 339-345 (1995).
47. J.N.Oshinski, D.N.Ku, S.Mukundan, F.Loeth, R.I.Pettigrew, Determination of wall shear stress in the aorta using MR phase velocity mapping, *JMRI*, **5**, 640-647 (1995).
48. P.Vinee, B.Meurer, A.Constantinesco, B.Kohlberger, K.Hauenstein, S.Petkov, Proton magnetic resonance relaxation times and biomechanical properties of human vascular wall: in vitro study at 4 MHz, *Invest. Radiol.*, **27**, 510-514 (1992).

49. A.Constantinesco, P.Gries, P.Vinee, B.Heckert, P.Carlier, In vitro 4 Mhz NMR proton relaxation times and in vitro mechanical behaviour at low extension of human common carotid arterial wall, *Magnetic Resonance Imaging*, **7**, 173-177 (1989).
-

APPENDIX PERMISSION FROM CO-AUTHOURS AND PUBLISHER

We the undersigned hereby grant permission to K.C.Chu to include in or adapt for his Ph.D. thesis the paper entitled "Improved MR Images of Arterial Specimens by Submersion in Trichlorotrifluoroethane" by K.C.Chu, A.J.Martin and B.K.Rutt, which appeared in *Magnetic Resonance in Medicine*, Vol. 35, pp. 790-796 (1996).



ALASTAIR J. MARTIN

April 22 '97

DATE



BRIAN K. RUTT

MAY 22 '97

DATE


Waverly

Williams & Wilkins • Urban & Schwarzenberg

October 31, 1996

Invoice: 9610-171

Kenneth Chu
 Imaging Research Laboratories
 The John P. Robarts Research Ins
 PO Box 5015
 100 Perth Drive
 London, Ontario
 CANADA N6A 5K8

Dear Mr Chu:

Permission is granted for one time usage of the material listed in your letter to include in your material the following:

MAGNETIC RESONANCE IN MEDICINE 1994;31:652-659
 MAGNETIC RESONANCE IN MEDICINE 1995;34:125-132
 MAGNETIC RESONANCE IN MEDICINE 1996;35:790-796
 MAGNETIC RESONANCE IN MEDICINE ref # MRM-96-2750

There is no fee for this request. The requestor guarantees to reprint the material exactly as originally published. Please sign below to confirm this rights agreement. If you have any further questions, please call Debbie Heise at (410)528-4016.

Sincerely,

Debbie Heise

Permission is granted upon receipt of this signed agreement with payment (if applicable) by Waverly. Requestor agrees to secure written permission from the author (Books only). Please retain a copy for your files.

Requestor accepts: Kenneth Chu Date: Dec 16, 96 .

351 West Camden Street • Baltimore, Maryland 21201-2436 • 410-528-4000
 The Global Information Resource for Medicine and the Health Sciences

VITA: **Kenneth C. Chu**

DATE AND PLACE OF BIRTH: August 30, 1960; Toronto, Ontario, Canada

UNIVERSITY EDUCATION:

B.A.Sc.

Sept. 1979 - May 1983

Supervisor:

Thesis:

Engineering Science, University of Toronto

Dr. R.T.Woodhams

Anhydride coupling agents in mica filled polypropylene

M.A.Sc.

May 1983 - May 1985

Supervisor:

Thesis:

Chemical Engineering, University of Toronto

Dr. R.T.Woodhams

High intensity mixing of mica filled polypropylene composites using a Gelimat mixer

Ph.D.

Jan. 1991 - May 1997

Supervisor:

Thesis:

Medical Biophysics, University of Western

Dr. Brain K. Rutt

High resolution MRI system to measure arterial elasticity *in vitro*

RESEARCH AND INDUSTRIAL EXPERIENCE:

May 1981-Sept. 1982

Research Assistant: Medical Physics

Ontario Cancer Institute

Toronto, Ontario

Supervisor: A.Fenster

Apr. 1985-Nov. 1990

Research Scientist: Polymer Processing

DuPont Canada Inc.

Kingston, Ontario

Manager: B.Kershaw

TEACHING EXPERIENCE:

Sept. 1983-May 1995

Teaching Assistant: Polymer Chemistry,

Mass Transport, Kinetics

University of Toronto

Sept. 1983-June 1985

Private Tutor: Chemical Engineering

Toronto, Ontario

Sept. 1992-Dec. 1992

Teaching Assistant: Biomechanics

University of Western Ontario

HONOURS AND AWARDS - ACADEMIC:**Undergraduate**

1979-80	UofT	J.W.Billes Scholarship
1980-81	UofT	B.P.Canada Scholarship
1981-82	UofT	J.W.Billes Scholarship
1982-83	UofT	J.W.Billes Scholarship

Graduate

1983-84	UofT	J.R.Bradfield Graduate Fellowship
1983-84	UofT	NSERC Post Graduate Scholarship
1983 (Declined)	UofT	Ontario Graduate Scholarship
1983 (Declined)	UofT	Open Master's Fellowship
1984-85	UofT	J.R.Bradfield Grad. Fellowship
1984-85	UofT	NSERC Post Graduate Scholarship
1985 (Declined)	UofT	NSERC Post Graduate Scholarship
1991 (Declined)	UWO	Ontario Graduate Scholarship
1991 (Declined)	UWO	NSERC Post Graduate Scholarship
1991-93	UWO	Entrance Scholarship
1991-94	UWO	Medical Research Council Studentship
1991-94	UWO	Medical Research Council Travel Stipend
1992	UWO	Dean's Research Travel Award
1993-94	UWO	Meloche-Monnex Scholarship
1993	UWO	Soc. of Magn. Res. in Med. Student Stipend
1993	UWO	Sunnybrook Invited Speaker Honorarium
1994	UWO	Neille Farthing Fellowship Nominee
1994	UWO	Dean's Research Travel Award

AWARDS - INDUSTRIAL:

1987	DuPont Canada, Inc.	Research Center Dedication Award
1988	DuPont Canada, Inc.	Research Center Innovation Award

GRANTS:

1996	University Hospital-CAMDT PVA cryogel development
------	---

MEMBERSHIPS IN PROFESSIONAL ORGANIZATIONS:

1983-1991	Society of Plastic Engineers (SPE), Member
1987-	Professional Engineers of Ontario (PEO), Member
1991-1993	Society of Magnetic Resonance in Medicine (SMRM), Student Member
1994-	International Society of Magnetic Resonance in Medicine (ISMRM), Student Member
1994-	International Brotherhood of Magicians (IBM), Member
1994-	Canadian Organization of Medical Physicists (COMP), Student Member

COMMITTEE APPOINTMENTS:

1985-86	Society of Plastics Engineers Student Chapter, University of Toronto, President
1987-90	Recreation Committee of Big Brothers of Kingston, Member
1990-91	Recreation Committee of Big Brothers of Kingston, Chairman
1991-94	Activities Committee of Big Brothers of London Member
1991-95	Fund Raising Committee of Big Brothers of London Member
1991-93	Society of Graduate Students, UWO Representative
1992-93	Society of Graduate Students Athletic Coordinator
1992-93	University Student Council Athletics Liaison

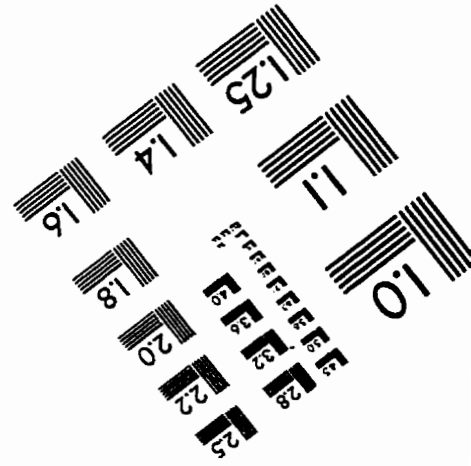
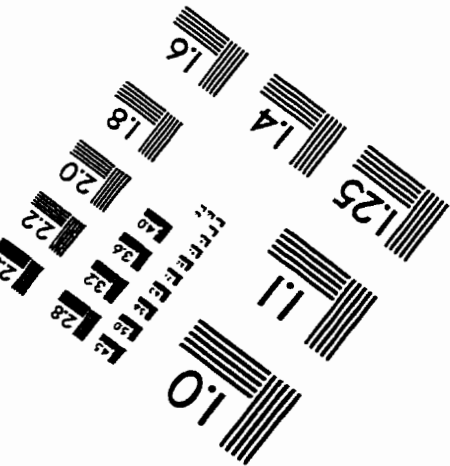
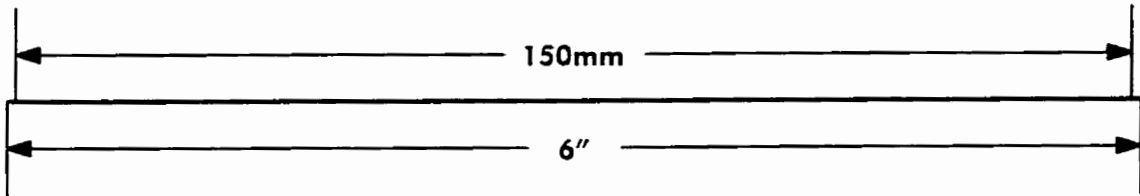
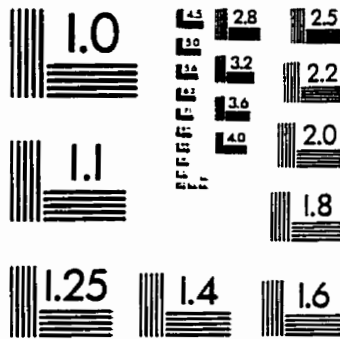
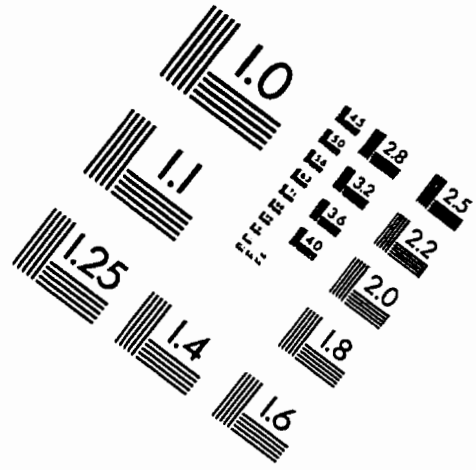
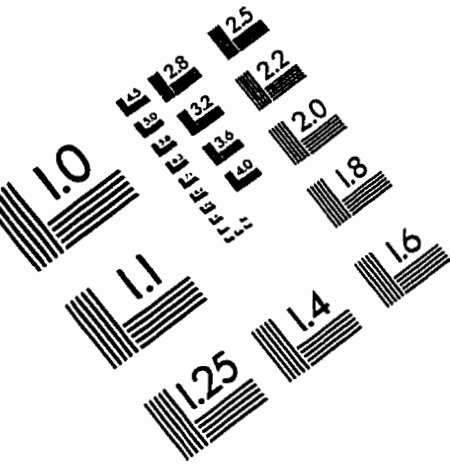
PATENTS:

1. **K.Chu**, "Polyolefin Concentrate - Melt Mixing of Polyolefins and Polyisobutylene", U.S. Patent No. 4,877,840 (31 October 1989).
2. **K.Chu**, "Polyolefin Concentrate - Melt Mixing of Polyolefins and Polyisobutylene", Canadian Patent No. 1 289 711 (1 October 1991).
3. **K.Chu**, "Concentrate of Polyolefins and Modifying Agent", Canadian Patent No. 1 323 123 (October 12, 1993).
4. **K.Chu**, "Polyolefin Concentrate", British Patent Application No. 87.01914
5. **K.Chu** and B.J.Kershaw, "Coated Synthetic Polymer Pellets", U.S. Patent Application No.07/202,230 (filed June 1, 1988), and European Patent Application No. EP 294,141 (filed Dec. 7, 1988.)
6. S.Dykes, **K.Chu** and G.White, "Concentrate Capsules", European Patent Application No. EP320,120 (filed Sept. 11, 1988).
7. B.K.Rutt, C.F.Maier and **K.Chu**, "Transverse Magnetic Gradient Coil", Disclosure submitted to University Hospital, London, March 10, 1994.

PUBLICATIONS:

1. **K.Chu** and A.Fenster, Determination of x-ray spectral distribution from transmission measurements using k-edge filters, *Medical Physics*, **10**, 772-777, 1983.
 2. **K.Chu**, A.N.Wright, and R.T. Woodhams, One step delamination and compounding of mica for optimum reinforcement of polypropylene, Proc. 41st Annual Conference, Reinforced Plastics/Composites Institute, The society of the Plastics Industries, 21C1-4, Jan. 1986.
 3. **K.Chu**, "Powder coating of molten pellets to prevent blocking (sticking)", DuPont World Wide Compounding Conference, 2.3.1-2 (Proprietary), 1989.
 4. R.Frayne, L.M.Gowman, D.W.Rickey, D.W.Holdsworth, P.A.Picot, M.Drangova, **K.Chu**, A.Fenster, B.K.Rutt., An in-vitro multi-modality phantom for the assessment of vascular imaging systems, *Med. Phys.*, **19**, 798, 1992.
 5. R.Frayne, L.M.Gowman, D.W.Rickey, D.W.Holdsworth, P.A.Picot, M.Drangova, **K.Chu**, C.B.Caldwell, A.Fenster, B.K.Rutt., A geometrically accurate vascular phantom for in-vitro x-ray, ultrasound and MR flow studies: construction and geometric verification, *Med. Phys.* **20**, 415-25, 1993.
 6. **K.C.Chu** and B.K.Rutt, Quadrupole gradient coil design and optimization: A printed circuit board approach, *Magnetic Resonance in Medicine*, **31**, 652-659, 1994.
 7. **K.C.Chu** and B.K.Rutt, MR gradient coil heat dissipation, *Magnetic Resonance in Medicine*, **34**, 125-132, 1995.
 8. C.F.Maier, **K.C.Chu**, B.A. Chronik, B.K.Rutt, A novel transverse gradient coil design for high-resolution MR imaging, *Magnetic Resonance in Medicine*, **34**, 604-611, 1995.
 9. **K.C.Chu**, A.J.Martin, B.K.Rutt, Improved MR images of arterial specimens by submersion in trichlorotrifluoroethane, *Magnetic Resonance in Medicine*, **35**, 790-796, 1996.
 10. **K.C.Chu**, B.K.Rutt, Polyvinyl alcohol cryogel: an ideal phantom material for MR studies of arterial flow and elasticity., *Magnetic Resonance in Medicine*, **37**, 314-319 (1997).
 11. C.F.Maier, H.N.Nikolov, **K.C.Chu**, B.A.Chronik, B.K.Rutt, Practical design of a high-strength gradient coil for diffusion/microvascular imaging of breast tumours, *Magnetic Resonance in Medicine*, Submitted March 7, 1997.
-

IMAGE EVALUATION TEST TARGET (QA-3)



APPLIED IMAGE, Inc
1653 East Main Street
Rochester, NY 14609 USA
Phone: 716/482-0300
Fax: 716/288-5989

© 1993, Applied Image, Inc., All Rights Reserved